Constance Rost-Bietsch

Ambipolar and Light-Emitting Organic Field-Effect Transistors

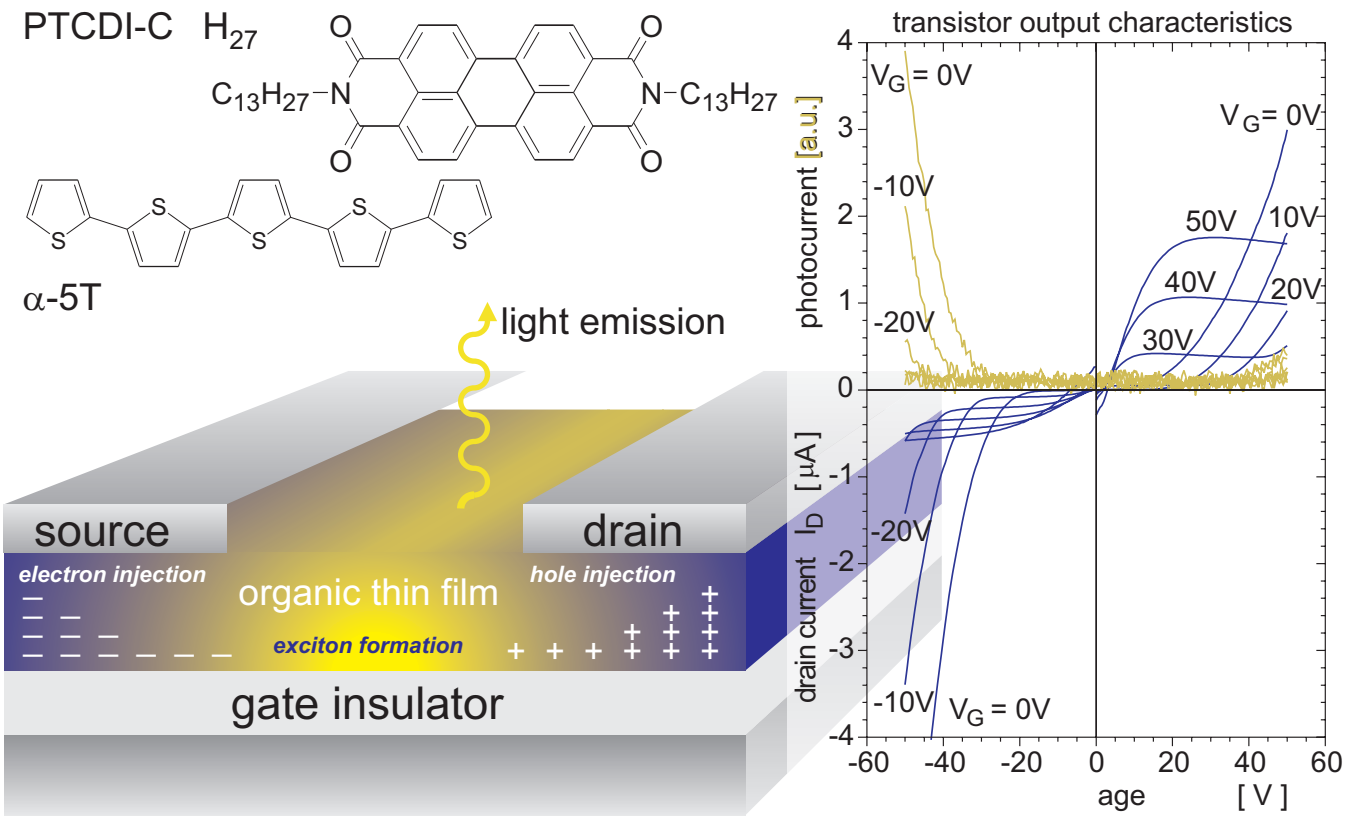

Cuvillier Verlag Göttingen

Ambipolar and Light-Emitting Organic Field-Effect Transistors

A dissertation submitted to the
University of Bayreuth
for the degree of
Doktor der Naturwissenschaften (Dr. rer. nat.)

presented by
CONSTANCE ROST-BIETSCH
Dipl.-Phys.
born May 17th, 1975 in Erlabrunn/Erzgeb.

Prof. Dr. Markus Schwoerer, examiner
Prof. Dr. Werner Köhler, co-examiner

day of submission: 17.12.2004
day of colloquium: 03.05.2005

Bibliografische Information Der Deutschen Bibliothek
Die Deutsche Bibliothek verzeichnet diese Publikation in der Deutschen Nationalbibliografie; detaillierte bibliografische Daten sind im Internet über http://dnb.ddb.de abrufbar.
1. Aufl. - Göttingen : Cuvillier, 2005
Zugl.: Bayreuth, Univ., Diss., 2005
ISBN 3-86537-535-9

© CUVILLIER VERLAG, Göttingen 2005
Nonnenstieg 8, 37075 Göttingen
Telefon: 0551-54724-0
Telefax: 0551-54724-21
www.cuvillier.de

Alle Rechte vorbehalten. Ohne ausdrückliche Genehmigung des Verlages ist es nicht gestattet, das Buch oder Teile daraus auf fotomechanischem Weg (Fotokopie, Mikrokopie) zu vervielfältigen.
1. Auflage, 2005
Gedruckt auf säurefreiem Papier

ISBN 3-86537-535-9

Contents

Zusammenfassung **v**

1 Introduction **1**
1.1 State of the Art of OFETs 1
1.2 Concept of Light Emission from OFETs 6
1.3 Outline 9

2 Physical Background **11**
2.1 Organic Semiconductor Devices 11
2.1.1 MIS Diode 11
2.1.2 Unipolar Field-Effect Transistor 15
2.1.3 Ambipolar Field-Effect Transistor 20
2.1.4 Organic Light-Emitting Diodes 22
2.2 Charge-Carrier Injection, Transport and Recombination 22
2.2.1 Charge-Carrier Injection 22
2.2.2 Charge-Carrier Transport 23
2.2.3 Charge-Carrier Recombination 24

3 Experimental Methods **25**
3.1 Device Preparation 25
3.1.1 Substrate Preparation 25
3.1.2 Purification of Organic Materials 27
3.1.3 Thin-Film Growth 28
3.2 Device Characterization 30
3.2.1 Electrical Characterization 30
3.2.2 Optical Properties 36
3.2.3 Surface Characteristics and Film Morphology 37

4 Single-Layer Devices **39**
4.1 Film Growth and Morphology 39

4.2 Charge-Carrier Injection by CV-Measurements . . . 46
4.2.1 Influence of Contact Metal . . . 47
4.2.2 Frequency-Dependent Capacitance . . . 50
4.3 Transport Properties at Room Temperature . . . 53
4.3.1 Charge-Carrier Mobility . . . 53
4.3.2 Influence of Contact Metal . . . 53
4.4 Temperature-Dependence of Charge-Carrier Mobility . . . 56
4.5 Conclusion . . . 58

5 Ambipolar Organic Field-Effect Transistor 59
5.1 Pentacene/PTCDI-$C_{13}H_{27}$ OFET . . . 59
5.2 *p*-4P/PTCDI-$C_{13}H_{27}$ OFET . . . 66
5.3 α-5T/PTCDI-$C_{13}H_{27}$ OFET . . . 71
5.4 Simulation of Ambipolar OFET Characteristic . . . 76
5.4.1 Model Based on a Modified Shockley Equation . . . 76
5.4.2 Advanced Simulation using the Drift-Diffusion Model . . . 81
5.5 Conclusion . . . 88

6 Light-Emitting Organic Field-Effect Transistor 91
6.1 Unipolar Light-Emitting OFETs . . . 92
6.1.1 p-6P Light-Emitting OFET . . . 92
6.1.2 *p*-4P/*p*-4P:Ir(btp)$_2$acac Light-Emitting OFET . . . 97
6.2 Ambipolar Light-Emitting OFET . . . 103
6.2.1 α-5T/PTCDI-$C_{13}H_{27}$ Light-Emitting OFET . . . 104
6.2.2 Modelling the Electroluminescence of Ambipolar OFETs . . . 120
6.3 Conclusion . . . 125

Summary 127

Appendix 130

A Transistor Characteristics - Experimental Data 131

B Optical Properties - Experimental Data 139

C Simulation of Ambipolar Transistor Characteristic 143

D Simulation of Electroluminescence from OFETs 145

Abbreviations 147

Bibliography **151**

List of Publications **161**

Acknowledgements **163**

Curriculum Vitae **165**

Zusammenfassung

Ziel dieser Arbeit war die Herstellung und Charakterisierung eines lichtemittierenden ambipolaren organischen Feldeffekttransistors (OFET). In der Literatur wurden lichtemittierende ambipolare Feldeffekttransistoren auf der Basis organischer Moleküle, die von Interesse für neue elektro-optische Bauelemente sind, bisher noch nicht beschrieben. Für die Realisierung eines lichtemittierenden ambipolaren OFETs wurden drei verschiedenene Strategien verfolgt: Zum einen wurden konventionelle Einschichtstrukturen auf ihre Elektrolumineszenzeigenschaften hin untersucht. Desweiteren wurden Zweischichtstrukturen auf der Basis eines Elektronen- und eines Löchertransportmaterials hergestellt. Schließlich wurde ein völlig neues Konzept basierend auf koverdampften, d.h. gemischten Filmen bestehend aus Löcher- und Elektronentransportmaterial, realisiert. Die Einschichtstrukturen für sich waren zwar emittierend, doch ist aufgrund der unipolaren Transporteigenschaften der organischen Materialien die Lichtemission auf einen Bereich an einem Kontakt beschränkt. Im Gegensatz dazu wurde an den Zweischichtstrukturen eine ambipolare Transportcharakteristik gemessen, jedoch keine Elektrolumineszenz beobachtet. Schließlich konnte über das neue Konzept der koverdampften Bulk-Heterostruktur erstmals Elektrolumineszenz in einem ambipolaren OFET beobachtet werden.

Im Rahmen dieser Arbeit wurden in den Einschichtstrukturen verschiedene organische Halbleitermaterialien auf ihre Transporteigenschaften hin untersucht: Tetracen, Pentacen, *p*-4P [1], *p*-6P [2], α-4T [3], α-5T [4] and PTCDI-$C_{13}H_{27}$ [5]. Dabei wurde die Ladungsträgerinjektion und Ausbildung eines leitfähigen Kanals aufgrund akkumulierter Ladungsträger an Metall-Isolator-Halbleiter (metal-insulator-semiconductor: MIS) Kondensatorstrukturen untersucht. Für die charakterisierten Materialien Oligoacene, α-Oligothiophene und *para*-Oligophenyle wurde Löcherinjektion beobachtet, für das Perylenederivat dagegen Elektroneninjektion. Variationen in der Austrittsarbeit des Kontaktmetalls haben zu folgenden Erkenntnissen geführt: (i) Trotz hoher Barrieren von bis zu 2 eV am injizierenden Kontakt kommt es zur Ladungsträgerinjektion. (ii) In organischen Filmen, deren

[1] *para*-Quaterphenyl
[2] *para*-Sexiphenyl
[3] α-Quaterthiophen
[4] α-Quinquethiophen
[5] N,N'-Ditridecylperylene-3,4,9,10-tetracarboxylic diimide

räumliche Ausdehnung größer als die Kontaktfläche ist, kommt es zur Akkumulation von Ladungsträgern und damit zur Ausbildung eines leitfähigen Kanals auch in Bereichen des organischen Films, die nicht direkt mit der Metallelektrode kontaktiert sind. (iii) Bei höherer Kontaktbarriere ist die räumliche Ausdehnung des ausgebildeten Kanals geringer. (iv) Anzeichen für Inversion von Ladungsträgern in einem organischen Halbleiter konnten nur unter Inertatmosphäre für Pentacene in Kombination mit Ca als Kontaktmetall beobachtet werden. Allerdings findet die Inversion der Ladungsträger nur unmittelbar unterhalb des Kontaktes statt, d.h. ein ausgedehnter Kanal wird nicht ausgebildet. Anhand von frequenzabhängigen Kapazitäts-Spannungs-Messungen (capacitance-voltage: CV) konnten die MIS-Kondensatorstrukturen mittels eines Ersatzschaltbildes modelliert werden. Daraus erhält man die Kapazität aufgrund des ausgedehnten Kanals und damit auch die Kanallänge als Funktion der angelegten Spannung. Bei Untersuchungen der Transporteigenschaften und Transistorcharakteristik wurde besonderes Augenmerk auf den Parameter Beweglichkeit gelegt. Die Beweglichkeit der Ladungsträger in einem organischen Dünnfilm hängt stark von dessen molekularer Ordnung ab, und diese wiederum von den Aufdampfparametern, wie Substrattemperatur und Aufdampfrate. Deshalb wurden Strukturuntersuchungen an den aufgedampften Filmen mittels Röntgenbeugung (X-ray diffraction: XRD) vorgenommen, um die Kristallinität der Filme zu überprüfen. Filme aus Pentacene, einem planaren Molekül, weisen eine hohe Kristallinität mit einer Molekülorientierung nahezu senkrecht zum Substrat auf. Selbst Filme aus *para*-Oligophenyl, d.h. nicht planaren Molekülen, welche weitaus schlechter geordnete Filme bilden, weisen im XRD-Spektrum Strukturen auf, die auf texturierte, polykristalline Filme schließen lassen. Da *p*-4P am empfindlichsten auf Veränderungen der Aufdampfparameter reagiert, wurde anhand dieses Moleküls die Abhängigkeit der Beweglichkeit von der Aufdampfrate untersucht. Die Löcherbeweglichkeit in *p*-4P konnte dabei zwischen 1.5×10^{-5} cm^2/Vs und 4.8×10^{-4} cm^2/Vs variiert werden. Temperaturabhängige Messungen der Transistorkennlinien geben Aufschluss über den Ladungsträgertransport. Sowohl die Beweglichkeit der Löcher in Pentacen, als auch die Elektronenbeweglichkeit in PTCDI-$C_{13}H_{27}$ ist thermisch aktiviert, und in beiden Materialien nimmt die Beweglichkeit ausgehend von Raumtemperatur mit sinkender Temperatur ab. Unter der Annahme von thermisch aktiviertem Hopping-Transport wurden für die Löcherbeweglichkeit in Pentacene Aktivierungsenergien von $E_a = 41$ meV und 71 meV für entsprechende Raumtemperaturbeweglichkeiten von 6×10^{-2} cm^2/Vs und 4.4×10^{-3} cm^2/Vs bestimmt. Die Elektronenbeweglichkeit in PTCDI-$C_{13}H_{27}$ weist eine Aktivierungsenergie von 87 meV auf.

Da in allen untersuchten Materialien nur unipolarer Transport festgestellt werden konnte, wurden OFETs bestehend aus Zweischichtstrukturen, in denen ein ausgewähltes Löcher- und ein Elektronentransportmaterial kombiniert wurden, präpariert und auf ihre Transporteigenschaften hin untersucht. Um effiziente Ladungsträgerinjektion zu gewähr-

leisten, wurden Metalle mit verschiedener Austrittsarbeit für den Quellen- und den Senkenkontakt (source and drain contact) verwendet. Das Elektronentransportmaterial PTCDI-$C_{13}H_{27}$ wurde jeweils mit dem Löchertransportmaterial Pentacene, *p*-4P oder α-5T kombiniert. In allen Fällen wurde eine ambipolare Transportcharakteristik beobachtet. Zur elektrischen Simulation dieser Charakteristik wurden zwei verschiedene Ansätze gewählt: Zum einen wurden die experimentellen Daten basierend auf einer modifizierten Shockley-Gleichung mit den freien Parametern Elektronen- und Löcherbeweglichkeit, sowie Schwellenspannung für den Elektronen- und den Löchertransport simuliert. Zum anderen wurden die experimentellen Daten unter Annahme des Drift-Diffusionsmodells simuliert. Beide Ansätze können den qualitativen Verlauf der Charakteristik erklären. Zusätzlich zu den Parametern Beweglichkeit und Schwellenspannung liefert die numerische Simulation auch Informationen über den Potentialverlauf und die Ladungsträgerdichten zwischen Quelle und Senke, sowie über die Rekombination im ambipolaren Transistor. In keiner der OFET-Zweischichtstrukturen konnte Lichtemission beobachtet werden, was unter anderem auf zu schwache Coulomb-Wechselwirkung zwischen den akkumulierten Ladungsträgern in beiden Filmen zurückgeführt werden kann. Deshalb wurden unipolare OFETs auf ihre Elektrolumineszenzeigenschaften hin untersucht. Verwendet wurden effizient emittierende Transportmaterialien, wie *p*-6P, oder dotierte Filme, wie mit $Ir(btp)_2acac$ [6] dotierte *p*-4P Filme. Im letzteren Fall konnte Lichtemission in der Nähe des Senkenkontaktes nachgewiesen werden, was auch mit den Resultaten der numerischen Simulation übereinstimmt.

Erst mit dem für OFETs basierend auf kleinen Molekülen völlig neuen Ansatz, dem Koverdampfen eines Löcher- und eines Elektronentransportmaterials, konnte erstmals Lichtemission in ambipolaren OFETs beobachtet werden. Hierfür wurde das Elektronentransportmaterial PTCDI-$C_{13}H_{27}$ mit dem Löchertransportmaterial α-5T kombiniert. Entscheidend für die Wahl von α-5T war dabei zum einen die Energielücke, zum anderen die Planarität des Moleküls, welche auch im koverdampften Film eine möglichst hohe Ordnung auf molekularer Ebene gewährleistet. Es konnte gezeigt werden, daß durch variieren der Anteile beider Materialien im koverdampften Film es möglich ist, die Elektronen- und Löcherbeweglichkeit gezielt zu beeinflussen und aufeinander abzustimmen. Die Löcherbeweglichkeit in koverdampften Filmen konnte zwischen 2.2×10^{-3} cm^2/Vs und 4×10^{-5} cm^2/Vs variiert werden, die Elektronenbeweglichkeit zwischen 6.7×10^{-3} cm^2/Vs und 5.5×10^{-4} cm^2/Vs. Die Lichtemission in OFETs wurde mit Hilfe der bereits vorgestellten modifizierten Schockley-Gleichung unter Annahme von Langevin-Rekombination modelliert.

Darüberhinaus wurde im Rahmen dieser Arbeit zur Herstellung und Charakterisierung der OFETs eine kombinierte Vakuumanlage zur Deposition und elektrischen Cha-

[6] Iridium(III)bis(2-(2.-benzothienyl)pyridinato-N,C^3)(acetylacetonate)

rakterisierung, sowie ein Messplatz zur elektro-optischen Charakterisierung von OFETs konzipiert und aufgebaut. Die elektro-optische Charakterisierung der Filme wird in einer Handschuhbox unter Argonatmosphäre vorgenommen. Die hier untersuchten OFETs wurden ausschließlich auf Siliziumsubstraten präpariert, d.h. ein hochdotierter Silizium-Wafer diente als Substrat und leitfähige Gate-Elektrode. Der Gate-Isolator SiO_2 wurde durch thermische Oxidation hergestellt.

Der lichtemittierende ambipolare OFET basierend auf einem koverdampften Dünnfilm eines Elektron- und eines Löchertransportmaterials ist ein vielversprechendes Konzept. Die Arbeit wurde im Rahmen des EU Projektes ILO[7] angefertigt. Basierend auf den Ergebnissen des hier vorgestellten lichtemittierenden ambipolaren OFETs wurde ein Anschlussprojekt beantragt.

[7] **I**njection **L**asing in **O**rganic Thin Films; Vertrag IST-2001-33057

Chapter 1

Introduction

1.1 State of the Art of OFETs

The principle of the field-effect transistor (FET) was introduced by Lilienfield in 1930 [Lil30] and applied to organic semiconductors for the first time in 1970 for phthalocyanine single crystals [Bar70] as well as for the organic semiconductor chloranil [Pet70], followed by field-effect measurements of organic dye films in 1984 [Kud84]. In the late 80's, several researchers began investigating small-molecule organic materials with highly delocalized π-electron systems. The strategy to increase intermolecular transport was to improve the π-orbital overlap of adjacent molecules in highly oriented thin films of these materials.

Since then, organic materials have been successfully incorporated as active layers in electronic thin-film devices, such as organic light-emitting diodes (OLEDs) [Tan87, Bur90, Bei02, Rie03], organic solar cells [Peu03, Sha01], and organic field-effect transistors (OFETs) [Ebi83, Kud84, Hor89, Tsu86, Koe87, Sir98]. The devices are based on either conjugated polymers [Bur90, Sha01, Ebi83, Tsu86, Koe87, Sir98] or small molecules [Tan87, Peu03, Kud84, Hor89, Bei02, Rie03]. For example, OLEDs find broad application in display devices [Raj00, Ter03]. The progress was recently highlighted by the demonstration of a 20-inch full-color active-matrix OLED display driven by a-Si thin-film transistors [Tsu03, Rie04]. OFETs are being developed as switching devices for active-matrix OLED displays [Jac98] and for low-cost electronics, such as low-end smart cards and electronic identification tags [Gmb04]. The growing interest in organic-based thin-film electronics is not only due to its immense progress in performance, but also due to the potential flexibility of the devices, their relatively easy processing and low production costs. Organic thin films can be deposited and processed by thermal evaporation, spin-coating, micro-contact printing, self-assembly or screen-printing.

Typically, in organic materials unipolar transport is observed, i.e. one type of charge carrier is transported preferentially, therefore a transistor operates either as *p*- or *n*-

channel device. In Figure 1.1 the molecular structures of materials used for charge-transport layers in OFETs are shown. The prime example for materials used in *p*-type OFETs is pentacene: For evaporated thin films, mobilities of up to 2.2 cm^2/Vs have been reported [Lin97] with a corresponding on/off current ratio of more than 10^8. For devices with such a high mobility, nearly temperature-independent transport has been reported [Nel98], indicating that a simple transport model of thermally activated hopping cannot be applied. These values can easily compete with those of devices fabricated from amorphous silicon, which have a charge-carrier mobility of about 1 cm^2/Vs [Tsu03] and are limited to on/off current ratios of 10^6. However, it has to be noted that OFETs are typically driven at much higher voltages, i.e. up to ± 100 V, than amorphous silicon thin-film transistors (TFTs). Another group of well-studied hole-transport materials are oligothiophenes (see Fig. 1.1): the first α-6T [1] based OFET was reported already in 1989 [Hor89]. The extracted hole mobility increased due to improvements in film preparation from initially 2.2×10^{-2} cm^2/Vs [Gar89] to 1×10^{-1} cm^2/Vs [Hal03]. Oligophenyl, another class of small molecules with a relatively high hole mobility, were introduced for OFETs in 1997 [Gun97]. Here, the mobility increases with the chain length, that is from *p*-4P [2], *p*-5P [3] to *p*-6P [4] from 1×10^{-2} cm^2/Vs, 4×10^{-2} cm^2/Vs to 7×10^{-2} cm^2/Vs, respectively, and on/off current ratios of 10^5 to 10^6 have been reported. The increase in mobility with increasing chain length was also observed for the other systems discussed above and was explained by an increased molecular order within the thin film. A detailed study of the relation between molecular order and charge-carrier mobility can be found in [Mue01]. Furthermore, *p*-channel devices have been fabricated from nickel phthalocyanine [Gui89] and copper-phthalocyanine [Bao96] with hole mobilities of 7×10^{-4} cm^2/Vs and 2×10^{-2} cm^2/Vs, respectively. The highest hole mobility in organic materials reported so far is up to 20 cm^2/Vs for rubrene single crystals [Pod03, Pod04, Sta04].

The choice of electron-transport materials is rather limited and in general, the charge-carrier mobilities are lower. *n*-channel devices have been fabricated using C_{60}, naphthalene and perylene derivatives, fluorinated copper-phthalocyanine and fluorinated oligothiophene derivatives. For the perylene derivative PTCDI-C_8H_{17} [5] an electron mobility of 0.6 cm^2/Vs with a corresponding on/off current ratio $> 10^5$ was reported [Mal02]. The first *n*-type sexithiophene was published in 2000 [Fac00], and electron mobilities of 10^{-3} cm^2/Vs and 4.8×10^{-2} cm^2/Vs were reported for DFH-6T [6] and DFH-4T [7], respec-

[1] α-sexithiophene
[2] *para*-quaterphenyl
[3] *para*-quinquephenyl
[4] *para*-sexiphenyl
[5] N,N'-dioctyl-3,4,9,10-perylene tetracarboxylic diimide
[6] α,ω-diperfluorohexylsexithiophene
[7] α,ω-diperfluorohexylquaterthiophene

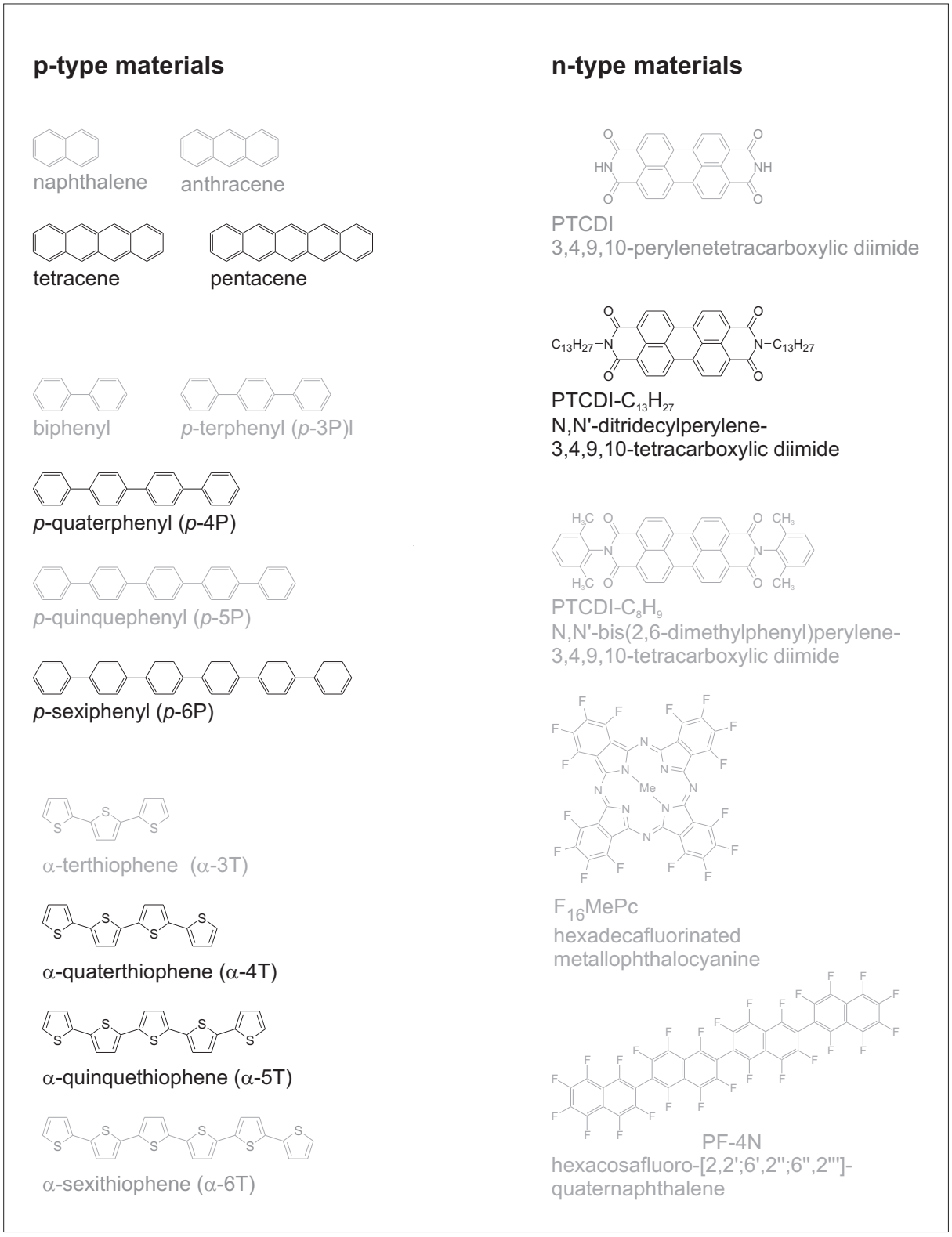

Figure 1.1: *Molecular structures of materials used for charge-transport layers in OFETs. The compounds investigated in this work are shown in black.*

tively [Fac03]. Moreover, fluorinated copper-phthalocyanine *n*-channel transistors [Bao98] have been combined with *p*-channel devices in integrated circuits [Cro01]. Perfluorinated *n*-type oligophenylenes [Hei00] have not yet been successfully employed in OFETs so far.

Extensive reviews on unipolar organic field-effect devices can be found in Refs. [Hor90, Kat97, Hor98, Dim01, Dim02]. Further improvement of single-layer OFETs will depend on the design and synthesis of new transport materials, improvements in device geometry, as well as optimization of device fabrication. The main disadvantage of OFETs as compared with conventional amorphous Si TFTs does not originate in its intrinsic material properties, but in the high contact resistance that requires relatively large device dimensions, i.e. in the micrometer range, leading to high operation voltages. In the case of shorter channel dimension, the device characteristics are dominated by the contact resistance instead of the channel properties.

In contrast to inorganic materials, where ambipolar device characteristic is well understood and described in detail, e.g. for amorphous silicon FETs [Pfl86a, Pfl86b, Neu87a], in organic devices typically unipolar transport is observed. Because pure organic semiconductors are intrinsic and exhibit no significant difference between the electron and the hole mobility, the unipolar transport characteristic observed in organic semiconductors has been attributed to impurities [Kar03]. Ambipolar transport in a single organic material [8] has so far been reported only for titanyl-phthalocyanine [Tad00], DCMT [9] [Che03b] and pentacene [Mei03] thin films as well as for carbon nanotubes (CNTs) [Mar01, Lin04a, Shi04]. The ambipolarity of CNTs has been proposed for application in nonvolatile molecular memory elements [Rad02]. In case of titanyl-phthalocyanine, ambipolar transport was observed in a transition state between unipolar electron and hole transport, initiated by oxygen exposure. The unipolar electron mobility was 9×10^{-6} cm^2/Vs, and the unipolar hole mobility 1×10^{-5} cm^2/Vs. The ambipolar electron and hole mobilities were even lower, with 2.7×10^{-6} cm^2/Vs and 2×10^{-6} cm^2/Vs, respectively. Thus, the ambipolarity in titanyl-phthalocyanine has no potential application in integrated circuits. Also for DCMT, the ambipolar mobilities, with $< 10^{-4}$ cm^2/Vs, were much lower than in the unipolar *n*-channel device, for which an electron mobility of 0.2 cm^2/Vs has been reported. In the case of pentacene the reported electron mobility of 10^{-6} cm^2/Vs could be observed only in vacuum; its hole mobility is 10^{-2} cm^2/Vs [Mei03]. This result is consistent with the observation of electron accumulation below the contact in in-situ characterized pentacene thin films described in Chapter 4 of this thesis.

[8] Previously reported results on ambipolarity and light emission combined with observed lasing in organic single crystals had to be withdrawn due to scientific misconduct. For details see also *Report on the investigation committee on the possibility of scientific misconduct in the work of Hendrik Schön and coauthors*, September 2002. http : //www.lucent.com/news_events/pdf/researchreview.pdf

[9] 3'4'-dibutyl-5,5"bis(dicyanomethylene)-5,5"dihydro-2,2':5',2"-terthiophene

Another approach for the fabrication of ambipolar OFETs was therefore the combination of an electron- and a hole-transport material in a bilayer heterostructure, as it has been shown for the combination of C_{60} and α-6T as well as PTCDA [10] and H6T [11] [Dod95, Dod96]. A drawback of this structure is the limitation to symmetrical source and drain contacts, leading to a large injection barrier for at least one type of charge carrier. A pronounced ambipolar characteristic for a bilayer heterostructure OFET consisting of pentacene and PTCDI-$C_{13}H_{27}$ [12], which uses different contact metals for the source and the drain electrode to achieve efficient electron and hole injection [Ros04a], is discussed in detail in Chapter 5 of this thesis. This work has triggered further research on the influence of injection barriers and the contact resistance on the ambipolar characteristic of bilayer heterostructure OFETs [Kuw04].

For future technological application it would probably be advantageous to combine both materials in a single layer. An ambipolar transistor based on a blend of a *p*-type polymer, MDMO-PPV [13], and a soluble derivative of C_{60}, PCBM [14], i.e. a blend of two otherwise unipolar materials, was reported for the first time in 2000 [Gee00]. The composition of blend films has an influence on the electron and hole mobility, as shown in [Pac03] for the combination of polyfluorene and PCBM. The ambipolar characteristic of a film consisting of the *n*-type-polymer BBL [15] and the *p*-type small-molecule copper-phthalocyanine was improved by increasing the crystallinity of the copper-phthalocyanine phase [Bab04]. Very recently, CMOS inverter circuits were fabricated using a blend of PCBM and OC_1C_{10}-PPV [16] [Mei03].

Ambipolar transport in a mixture of small molecules has been shown for single crystals of the quasi-one-dimensional Mott-Hubbard insulator (BEDT-TTF)[17](F_2TCNQ)[18] [Has04]. The hole mobility in these crystals is $\sim$1.5 times larger than the electron mobility and shows at a temperature of $T = 40$ K a value of $\mu = 2 \times 10^{-3}$ cm^2/Vs. For coevaporated thin films ambipolar transport was reported for the first time for α-5T [19] and PTCDI-$C_{13}H_{27}$ [Ros04b]. The striking feature, however, was the simultaneous observation of electroluminescence (EL), which could be tuned by the applied gate bias. This concept will be discussed in detail in Chapter 6 of this thesis.

[10] perylene-3,4,9,10-tetracarboxylic-3,4,9,10-dianhydride
[11] α,ω-dihexylsexithiophene
[12] N,N'-ditridecylperylene-3,4,9,10-tetracarboxylic diimide
[13] poly(2-methoxy-5-(3,7-dimethyloctyloxy)-1,4-phenylenevinylene
[14] (6,6)-phenyl C61-butyric acid methyl ester
[15] poly(benzobisimidazobenzophenanthroline)
[16] poly[2-methoxy-5-(3',7'-dimethyloctyloxy)]-*p*-phenylene vinylene
[17] bis(ethylenedithio)tetrathiafulvalene
[18] 2.5-difluorotetracyanoquinodimethane
[19] α-quinquethiophene

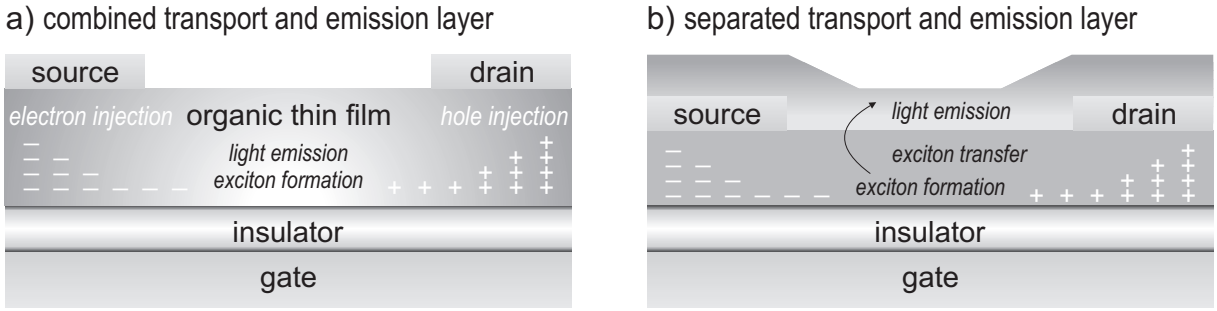

Figure 1.2: *Device structures of light-emitting field-effect transistors. (a) Within a one-layer structure, charge-carrier transport and light emission occurs in the same film. (b) In a two-layer structure, charge-carrier transport and exciton formation are spatially separated from light emission. This requires efficient energy transfer between the two layers. It should be noted that the device dimensions are not shown in scale: the active device thickness is typically in the order of 100 nm and the source-drain contact distance, i.e. the channel length L is typically in the order of 100 μm).*

1.2 Concept of Light Emission from OFETs

Combining light emission with switching characteristics in a single device, i.e. a light-emitting field-effect transistor, is interesting from both a scientific aspect as well as a technical point of view. On one hand it can give further insight into the understanding of fundamental device physics, on the other hand it would increase the number of potential applications of organic opto-electronic devices. Similarly to light emission in an OLED, light emission from an OFET requires electron and hole injection and transport as well as exciton formation followed by efficient radiative decay. Thus, ambipolar charge-carrier injection and transport are thought to be required for an efficient light-emitting OFET. Recently, in unipolar *p*-type tetracene thin-film OFETs [Hep03, San04] as well as in unipolar polymer OFETs [Ahl04, Sak04] EL was reported. However, the recombination zone and therefore also the EL in these unipolar OFETs is restricted to a region in close vicinity of the drain contact [Hep03, Rey04], resulting in quenching by the metal drain contact. In ambipolar devices, the recombination zone can be shifted between source and drain contact by the gate voltage, as it has been reported for ambipolar carbon nanotube FETs [Fre04].

The emitting material can either function as both emitting and transport material, or it can be placed on top of the transport layer and EL is based on exciton transfer. Figure 1.2 shows the two different concepts of light emission from a FET. From an electrical point of view both devices function identically: Electrons and holes are injected at source and drain contacts and the accumulation of both types of charge-carriers in a conductive channel is controlled by the gate electrode. In Figure 1.2(a), charge-carrier

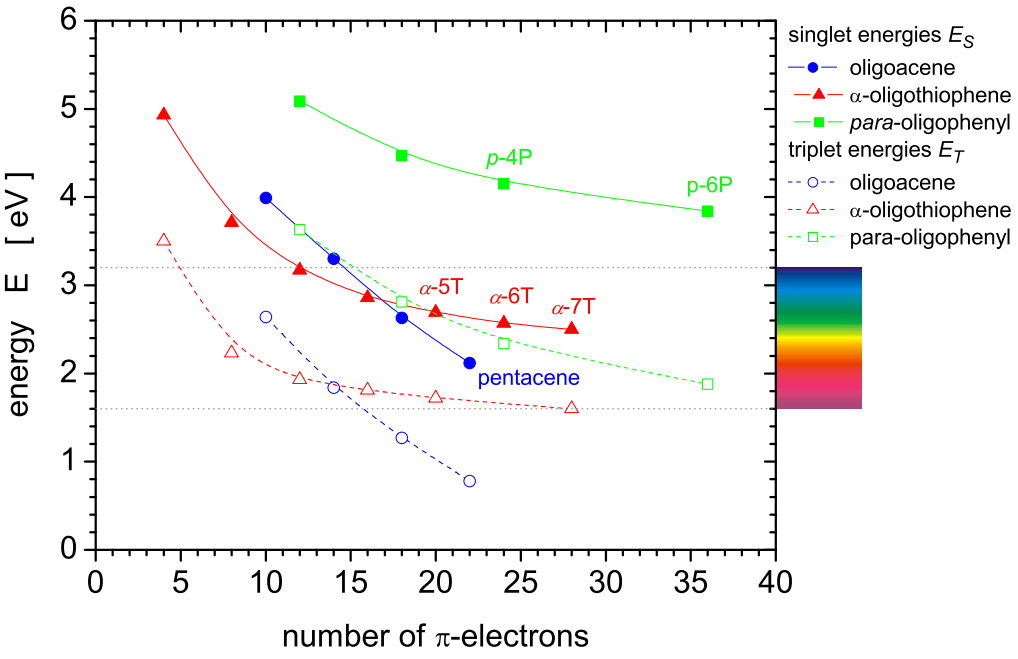

Figure 1.3: *Singlet (filled symbols) and triplet (hollow symbols) energies of materials for charge-transport layers in a light-emitting field-effect transistor. The values are taken from Table 1.1. The groups of materials considered are oligoacenes, α-oligothiophenes and para-oligophenyls. In addition, the spectral range of visible light is indicated.*

transport and light emission is allocated to a single layer. Thus, the EL is quenched by free charge carriers. In Figure 1.2(b), the charge-carrier transport is spatially separated from light emission occurring in a second layer on top of the transport layer. Thus, quenching by free charge-carriers is prevented, however, the EL is decreased by transfer losses. The transfer rate depends on the intermolecular distance of donor and acceptor and can be improved by decreasing the thickness of the transport layer, which however as a consequence impairs the transport properties. Typical transfer radii for Förster and Dexter transfer are a 5−10 nm or 1.5−2 nm, respectively. If the emission layer comprises a sufficient concentration of a phosphorescent dye, the diffusion length of triplet excitons will also contribute to the EL. The concept of separating the transport and the emission layer is one of the subject of a European Project (ILO[20]).

Figure 1.3 shows the singlet and triplet energies for typical hole-transport materials, which are also listed in Table 1.1. In addition, the spectral range of the visible spectrum is presented. In general, the energy gap of the transport material has to be larger than or within the visible spectrum. From an energetic point of view, materials from the class of *para*-oligophenyls are the most promising ones. However, their transport properties

[20]**I**njection **L**asing in **O**rganic Thin Films; contract number IST-2001-33057

Material	E_S [eV]	ϕ_{fl}	E_T [eV]	ϕ_T	Ref.	LUMO [eV]	HOMO [eV]	E_g [eV]	Ref.
naphthalene	3.99	0.19	2.62	0.75	[Mur93]	1.2-1.4	6.5-6.7	5.1-5.5	[Kar01a]
anthracene	3.30	0.30	1.84	0.71	[Mur93]	2.0-2.2	5.8-5.9	3.6-3.9	[Kar01a]
tetracene	2.63	0.17	1.27	0.62	[Mur93]	2.2-2.3	5.2-5.4	2.9-3.2	[Kar01a]
pentacene	2.12	0.08	0.78	0.16	[Mur93]	2.6-2.8 3.22	5.0-5.2 5.07	2.2-2.6 1.85	[Kar01a] [Sch02a]
thiophene	4.93	–	3.50	–	[dM99]				
α-2T	3.71	–	2.23	0.94	[dM99]				
α-3T	3.17	–	1.93	0.93	[dM99]				
α-4T	2.86	–	1.81	0.71	[dM99]				
α-5T	2.69	–	1.72	0.60	[dM99]		5.3		[Jon90]
α-6T	2.57	–	1.73	–	[Pog02]				
α-7T	2.50	–	1.60	0.60	[dM99]				
biphenyl	5.09	–	3.63	–	[Pog02]				
p-3P	4.47	–	2.81	–	[Pog02]				
p-4P	4.15	–	2.34	–	[Pog02]				
p-6P	3.84	–	1.88	–	[Pog02]	2.27	6.07	3.8	[Sch02b]
perylene	2.85	0.75	1.53	0.014	[Mur93]				
PTCDI-CH_3						3.4	5.4	2.0	[Hir95]

Table 1.1: *Singlet (E_S) and triplet (E_T) energies, fluorescence quantum yield (ϕ_{fl}), triplet quantum yield (ϕ_T), HOMO and LUMO levels of materials to be used as charge-transport layer in a light-emitting field-effect transistor. The groups of materials considered are oligoacenes, α-oligothiophenes and para-oligophenyls, all of which are p-type materials, and PTCDI-CH_3 with a similar molecular structure as PTCDI-$C_{13}H_{27}$ as n-type material. Values cited from [Mur93] and [dM99] were derived in solution from optical absorption measurements. Thus, these values depict only an indication for the actual HOMO-LUMO separation E_g, since they do not account for exciton binding energies. The same counts for the value of E_g in case of p-6P [Sch02b] and PTCDI-CH_3 [Hir95]. Values cited from [Pog02] are excitation energies calculated with time-dependent DFT. HOMO levels have been determined using XPS and UPS measurements.*

are difficult to control owing to the non-planar molecular structure, which results in a low degree of molecular order. Oligoacenes show the best transport properties, with a trade-off regarding the energy gap. α-Oligothiophenes exhibit good transport properties, while having singlet and triplet energies within the visible spectral range.

1.3 Outline

In Chapter 2, the physics of organic semiconductor devices, i.e. the metal-oxide-semiconductor (MOS) capacitor, the FET in unipolar and ambipolar function as well as organic light-emitting devices are introduced. Furthermore, an overview of the theoretical concepts of charge-carrier injection, transport and recombination in organic semiconductors is given. The application of inorganic semiconductor theory to organic semiconductors is briefly discussed.

Chapter 3 describes the device preparation and characterization, including gate-oxide growth and substrate cleaning, purification of organic semiconductors as well as thin-film growth by vacuum deposition. An integrated chamber for in-situ device preparation and characterization, which was designed and set up during this thesis work, is described in detail. It allows device preparation and characterization without transfer through and thus exposure to air. For device characterization, special emphasis is put on the electrical characterization, including capacitance-voltage (CV) measurements and impedance spectroscopy on metal-insulator-semiconductor (MIS) diodes, as well as on the current-voltage characteristic of organic field-effect transistors. A cryogenic probe station that was designed with and purchased from CryoVac, allows the temperature-dependent characterization of the organic thin films. Of special interest hereby is the temperature dependence of the mobility. Also, the electrical characterization of OLEDs is discussed briefly. In addition, optical characterization methods as well as X-ray diffraction (XRD) and atomic force microscopy (AFM) were used for studying the film morphology.

In Chapter 4, experimental results on *n*- and *p*-type single-layer devices are presented. This includes film growth and morphology, as well as a detailed description of charge-carrier injection and channel formation as obtained by CV measurement in *p*-type and *n*-type materials. These results are related to field-effect mobilities extracted from the characterization of field-effect devices. The transport mechanism is discussed based on temperature dependent transport measurements.

The combination of appropriate *n*-type and *p*-type materials results in an ambipolar OFET, which is described in detail in Chapter 5. Different material combinations are discussed, including pentacene and PTCDI-$C_{13}H_{27}$, *p*-4P and PTCDI-$C_{13}H_{27}$ as well as α-5T and PTCDI-$C_{13}H_{27}$. A model for the current-voltage characteristic of ambipolar

field-effect transistors is presented.

Chapter 6 deals with light-emitting OFETs. Two unipolar light-emitting OFETs based on *p*-4P and *p*-6P are presented in detail. A third system, based on a coevaporated thin film of α-5T and PTCDI-$C_{13}H_{27}$, which is an ambipolar light-emitting OFET, is also studied. Evaporating the *n*- and *p*-type materials simultaneously from two different sources allows the electron and hole mobility to be tuned. Finally, a model for the electroluminescence-current-voltage (EL-IV) characteristic of light-emitting transistors is introduced.

Chapter 2

Physical Background

2.1 Organic Semiconductor Devices

Specific material parameters of inorganic semiconductors can be studied by varying device geometries and measurement methods. Three device geometries will be introduced: metal-insulator-semiconductor (MIS) diodes, organic field-effect transistors (OFETs) and organic light-emitting diodes (OLEDs). MIS diodes are used to study the charge-carrier accumulation by capacitance-voltage (CV) measurement. The transport properties of organic semiconductors are extracted from current-voltage characteristics of thin-film transistors (TFTs) and OLEDs are used to investigate the electroluminescence of organic semiconductors.

2.1.1 MIS Diode

In a MIS diode the gate electrode is electrically isolated from the (organic) semiconductor by a gate insulator. Thus, a MIS diode can be understood as a fragment of a top-contact transistor structure, namely the source and the gate contact together with the (organic) semiconducting thin film and the gate insulator. A schematic drawing of a MIS diode is shown in Figure 2.1(a). Applying a voltage between gate and the semiconducting thin film leads to the accumulation of charges on both sides. The number of accumulated charges at a defined gate voltage is a function of the capacitance of the device, which is determined by the contact area A, the insulator and semiconductor layer thicknesses, d_{ox} and d_s, as well as the dielectric constants ϵ_{ox} and ϵ_s, respectively. The capacitance itself depends on the charge-carrier distribution. Therefore, the measured capacitance as a function of applied voltage provides information about the charge-carrier distribution within the device. Due to the analogies of the device structures, the charge-carrier accumulation in a MIS diode is equivalent to the channel formation in a transistor.

Basic characteristics of organic MIS diodes can be understood by the theory of inor-

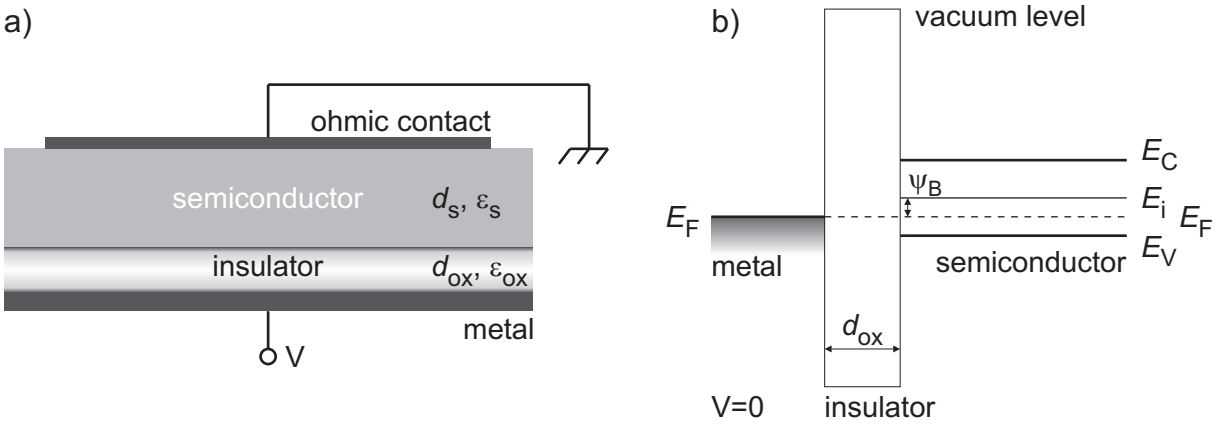

Figure 2.1: *(a) Schematic drawing of a metal-insulator-semiconductor (MIS) diode. (b) Energy band diagram of an ideal MIS diode at flat-band condition. The semiconductor is p-type. E_C, E_V, E_F, and E_i denote the energy levels of the conduction band, valence band, Fermi level and intrinsic Fermi level, respectively. Ψ_B is the potential difference between the Fermi level E_F and the intrinsic Fermi level E_i.*

ganic semiconductors. Deviations for organic semiconductors will be addressed later. The most intensively studied MIS diode is the metal-oxide-silicon (MOS) capacitor. The energy band diagram for a MOS capacitor consisting of *p*-doped silicon is shown for flat-band condition in Figure 2.1(b).

The characteristic of the device can be understood by the energy band diagram of the device under bias condition, as it is shown in Figure 2.2. Applying a negative voltage, as shown in Figure 2.2(a), leads to an increase of the Fermi level of the gate electrode by $+qV$. The negative charge at the gate electrode results in an accumulation of positive charges in the semiconductor/insulator interface. In the energy band diagram this is equivalent with an upwards bending of the valence band, whereas the Fermi level remains constant. The carrier density depends exponentially on the energy difference of valence band and Fermi level, thus the band bending leads to an *accumulation* of majority carriers at the insulator-semiconductor interface. The corresponding device capacitance C_{acc} is equivalent to the geometric capacitance of the plate capacitor formed by charges on both sides of the gate oxide C_{ox} with

$$C_{acc} = C_{ox} = \epsilon_0 \epsilon_{ox} \frac{A}{d_{ox}} \tag{2.1}$$

Here, A is the device area, ϵ_{ox} the dielectric constant and d_{ox} the thickness of the gate insulator. Applying a small positive voltage, as shown in Figure 2.2(b), decreases the Fermi level of the gate electrode by $-qV$. Overall charge neutrality leads to a negative charging of the semiconductor at the interface, i.e. mobile positive charges are pushed into the bulk material and negatively charged immobile acceptors remain at the interface.

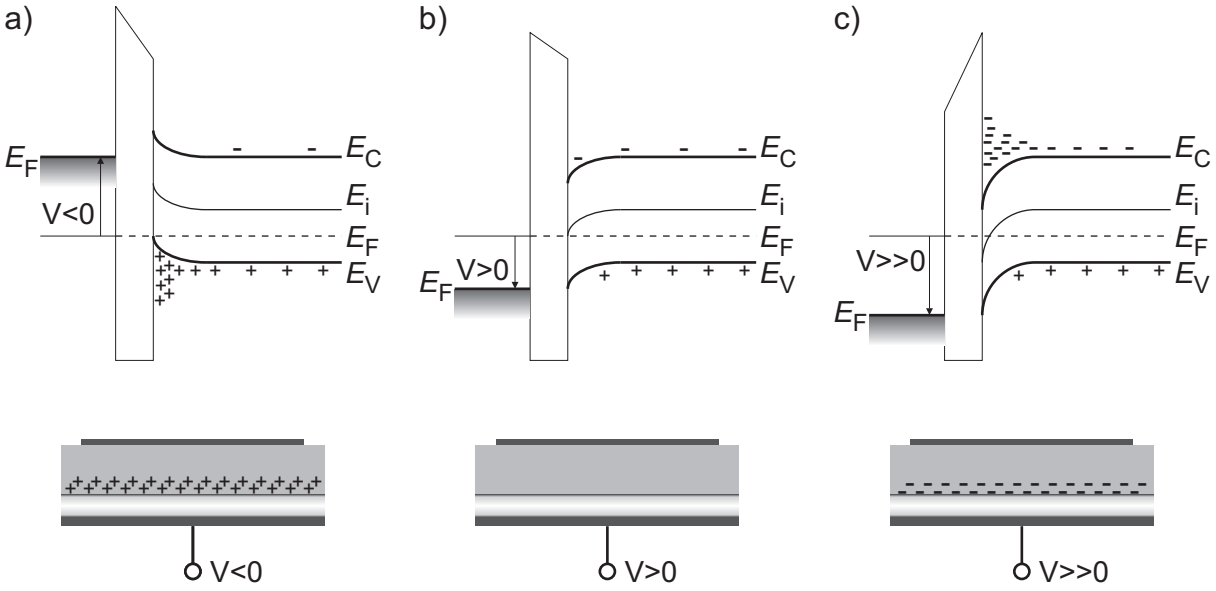

Figure 2.2: *Energy band diagrams and schematic drawing of charge-carrier distribution for p-type silicon in (a) accumulation, (b) depletion and (c) inversion.*

This is equivalent with a downward bending of the conduction and valence band of the semiconductor. Due to the only weak band bending, the electron density can be neglected at the interface and the negative charge at the insulator/semiconductor interface is formed only by immobile acceptors. This case is called *depletion* and the geometric capacitance is a serial connection of the gate oxide capacitance C_{ox} and the capacitance of the depleted semiconductor C_s:

$$\frac{1}{C_{depl}} = \frac{1}{C_{ox}} + \frac{1}{C_s} \tag{2.2}$$

with

$$C_s = \frac{\epsilon_0 \epsilon_s}{x_d} \tag{2.3}$$

Here, ϵ_s the dielectric constant of the semiconductor and x_d is the width of the depletion zone. The minimum capacitance C_{min} for maximum depletion width x_{dmax} is

$$C_{min} = \frac{\epsilon_{ox}}{d_{ox} + (\epsilon_{ox}/\epsilon_s) x_{dmax}} \tag{2.4}$$

with [Sze81]

$$x_{dmax} = \sqrt{\frac{4\epsilon_s kT \ln(N_A/n_i)}{e^2 N_A}} \tag{2.5}$$

Here, N_A is the acceptor impurity density and n_i is the intrinsic charge-carrier concentration. Increasing the applied gate voltage further leads to a stronger band bending and the

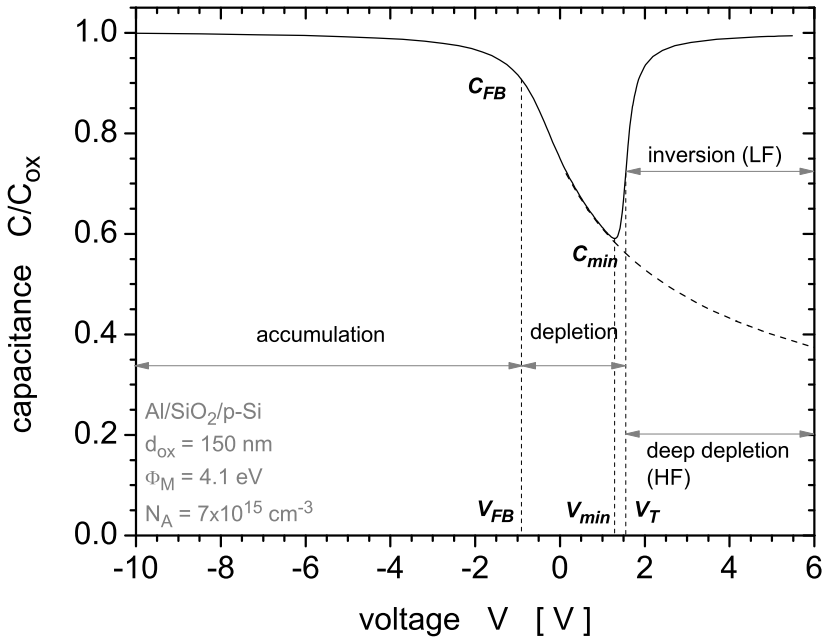

Figure 2.3: *Simulation of the normalized capacitance as a function of applied gate voltage for a p-type MOS capacitor with $d_{ox} = 150$ nm, $\Phi_M = 4.1$ eV and $N_A = 7 \times 10^{15}$ cm^{-3} in both high-frequency (HF) and low-frequency (LF) measurement mode with Φ_M being the metal work function.*

intrinsic Fermi level E_i falls below the Fermi level E_F of the semiconductor (Figure 2.2(c)). At this point, the electron density at the interface is larger than the hole density, which is called *inversion*. The case of the electron density at the surface being larger than the hole density in the bulk is called *strong inversion*. The threshold voltage, i.e. the onset of strong inversion, depends on the doping level of the semiconductor [Sze81]:

$$V_T = 2\psi_B + \frac{\sqrt{2\epsilon_s e N_A (2\psi_B)}}{C_i} \tag{2.6}$$

Here, ψ_B denotes the potential difference between the Fermi level E_F and the intrinsic Fermi level E_i; see also Figure 2.1. C_i is the capacitance per unit area of the insulator. The CV characteristic of a MOS diode device is shown in Figure 2.3. CV measurements are usually performed by applying a DC voltage, which is modulated by a small AC amplitude of a defined frequency. A detailed description of the measurement technique is given in Chapter 3.

For negative applied gate voltages, the normalized device capacitance is 1. Increasing the gate voltage, the capacitance decreases. In case of low frequency measurement, the capacitance has a minimum value C_{min} at the corresponding bias voltage V_{min} and returns to the initial value of 1 for even larger gate voltage. In case of high-frequency measurement,

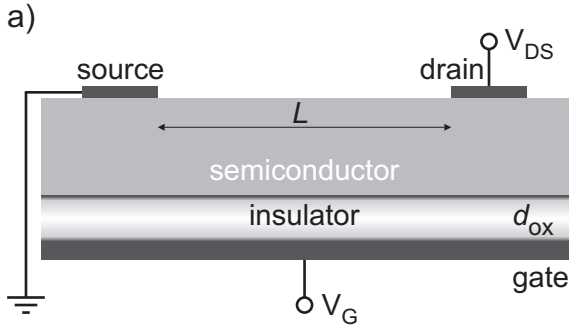

Figure 2.4: *Schematic device structure of an organic field-effect transistor. Additionally to source, drain and gate contact the channel width L and the gate oxide thickness d_{ox} are shown. The channel width W describes the dimension of the field-effect transistor perpendicular to the drawing plane but is not shown in the figure.*

the capacitance does not show a minimum but decreases continuously for large positive gate bias. C_{FB} denotes the capacitance at the flat-band voltage V_{FB}.

The formation of the accumulation layer by majority charges is a fast process and depends only on the mobility of charge carriers. Thus, no dependence on the frequency is observed. Contrary, the formation of an inversion layer and thus the increase of capacitance depends on the ability of the minority carrier concentration to follow the applied AC signal. The minority carriers are thermally generated and inversion is only observed for frequencies smaller than the generation-recombination rate of the minority carriers.

A major relevant difference in the CV characteristic of organic and inorganic semiconductors is its frequency-dependence. Whereas for inorganic semiconductors inversion is observed at frequencies $f \leq 100$ Hz, in organic semiconductors the measurement has to be performed under almost steady state conditions and in most cases it is difficult to observe inversion at all. Even accumulation in organic semiconductors shows a strong frequency-dependence and measurements are performed typically at 1 Hz. Firstly, organic semiconductors contain a much smaller density of thermally generated charge carriers and therefore the generation-recombination rate is much smaller than in inorganic semiconductors. Thus, accumulated charges as well as inverted charges need to be injected at the semiconductor/metal interface. Secondly, the charge-carrier mobility in organic semiconductors is generally smaller than in inorganic semiconductors due to hopping transport compared to band-like transport.

2.1.2 Unipolar Field-Effect Transistor

The schematic device architecture of an organic field-effect transistor (OFET) is shown in Figure 2.4. The device consists of two electrodes, named source and drain, in direct

contact with the semiconductor. A third electrode is separated by the gate insulator. The device shown here is called a *top-contact* architecture. Alternatively, source and drain contact can also be placed in between the gate insulator and the semiconductor. This device architecture is called *bottom contact*. In analogy to MIS diodes, applying a voltage at V_G results either in accumulation or inversion of charge carriers at the semiconductor/insulator interface. These accumulated or inverted charges, depending on the operation mode, form the conductive channel in which the transport of charge carriers between source and drain takes place. Thus, for the charge-carrier transport in a FET structure the semiconductor/insulator interface is crucial. Normally, MOS field-effect transistors (MOSFETs) are operated in *enhancement mode*, i.e. a voltage has to be applied to the gate contact in order to form a conductive channel. In case a channel is formed already at 0 V gate bias, the transistor operation is called *depletion mode*.

OFETs are operated typically in accumulation mode, since inversion is difficult to achieve (see also Section 2.1.1). Depending on the threshold voltage of the device, OFETs are operated either in enhancement or depletion mode.

Current Voltage Characteristic

FETs are characterized by two kinds of current-voltage characteristics, the output and the transfer characteristic. For measuring the *output characteristic*, a constant voltage is applied between source and gate contact and the drain current I_D is measured as a function of the drain voltage V_{DS}. The *transfer characteristic* is obtained by measuring the drain current I_D as a function of the gate voltage V_G for a constant drain-source voltage. Measuring each characteristic for several constant V_G or V_{DS} leads to a set of characteristic curves. In the following, such a set of characteristic curves will be denoted as output or transfer characteristic.

In inorganic FETs the drain current is described by the Shockley equation, as it is derived in detail in [Sze81]:

$$I_D = \frac{W}{L}\mu C_i\left[(V_G - V_T)V_{DS} - \frac{1}{2}{V_{DS}}^2\right]; \qquad V_{DS} \leq V_G - V_T \tag{2.7}$$

Here, W and L are the channel width and channel length, μ is the field-effect mobility and C_i the capacitance per unit area of the gate dielectric, described the the geometric capacitance of the gate insulator. For very small V_{DS} we observe a linear region for the drain current I_D:

$$I_D = \frac{W}{L}\mu C_i(V_G - V_T)V_{DS}; \qquad V_{DS} \ll V_G - V_T \tag{2.8}$$

For large V_{DS} with $V_{DS} \geq V_G - V_T$, the drain current I_D saturates and depends only on V_G:

$$I_{Dsat} = \frac{W}{2L}\mu C_i (V_G - V_T)^2; \qquad V_{DS} \geq V_G - V_T \tag{2.9}$$

The simulated output and transfer characteristic for a FET with an electron mobility $\mu_n = 10^{-2}$ cm^2/Vs, an oxide thickness of $d_{ox} = 100$ nm, resulting in an oxide capacitance $C_i = 3.45 \times 10^{-8}$ F/cm^2, and a threshold voltage $V_T = 0$ V is shown in Figure 2.5. The channel width-to-length ratio has been set to 8, a typical value for transistors studied within this thesis work.

The output characteristic features a linear current increase for small V_{DS} and a saturation region for large V_{DS}. At $V_{DS} = 0$ V the charge-carrier density in the conductive channel is constant between source and drain contact. Thus, the device behaves in case of ohmic contacts like a resistor with linear current increase. With increasing V_{DS} the charge-carrier density in the channel in close vicinity to the drain contact decreases due to a decrease in potential difference between drain and gate. Thus, the conductivity of the channel near the drain contact decreases with increasing V_{DS} and increase in current turns out to be sub-linear. For large V_{DS} with $V_{DS} \geq V_G - V_T$, the charge-carrier density close to the drain contact is zero. This situation is also called pinch-off. Additionally applied voltage drops over this pinch-off region and despite the voltage increases, the current I_{DS} is constant.

Field-Effect Mobility

The saturation field-effect mobility is extracted from the saturated drain current in transfer characteristic, i.e. applying a large drain-source bias V_{DS} and measuring I_D as function of V_G. By plotting the square root of drain current as function of gate voltage, the field-effect mobility can be extracted from the slope m_{sat} of the curve using the following relation:

$$\mu = \mu_{sat} = m_{sat}^2 \cdot \frac{2L}{W} \cdot \frac{1}{C_i}, \tag{2.10}$$

as shown in Figure 2.5(b). Additionally, the field-effect mobility can be extracted from the linear region, i.e. applying a small drain-source bias V_{DS} and measuring I_D as a function of V_G. From the slope m_{lin} of the linear fit the field-effect mobility is calculated using the following relation:

$$\mu = \mu_{lin} = m_{lin} \cdot \frac{L}{W} \cdot \frac{1}{C_i} \tag{2.11}$$

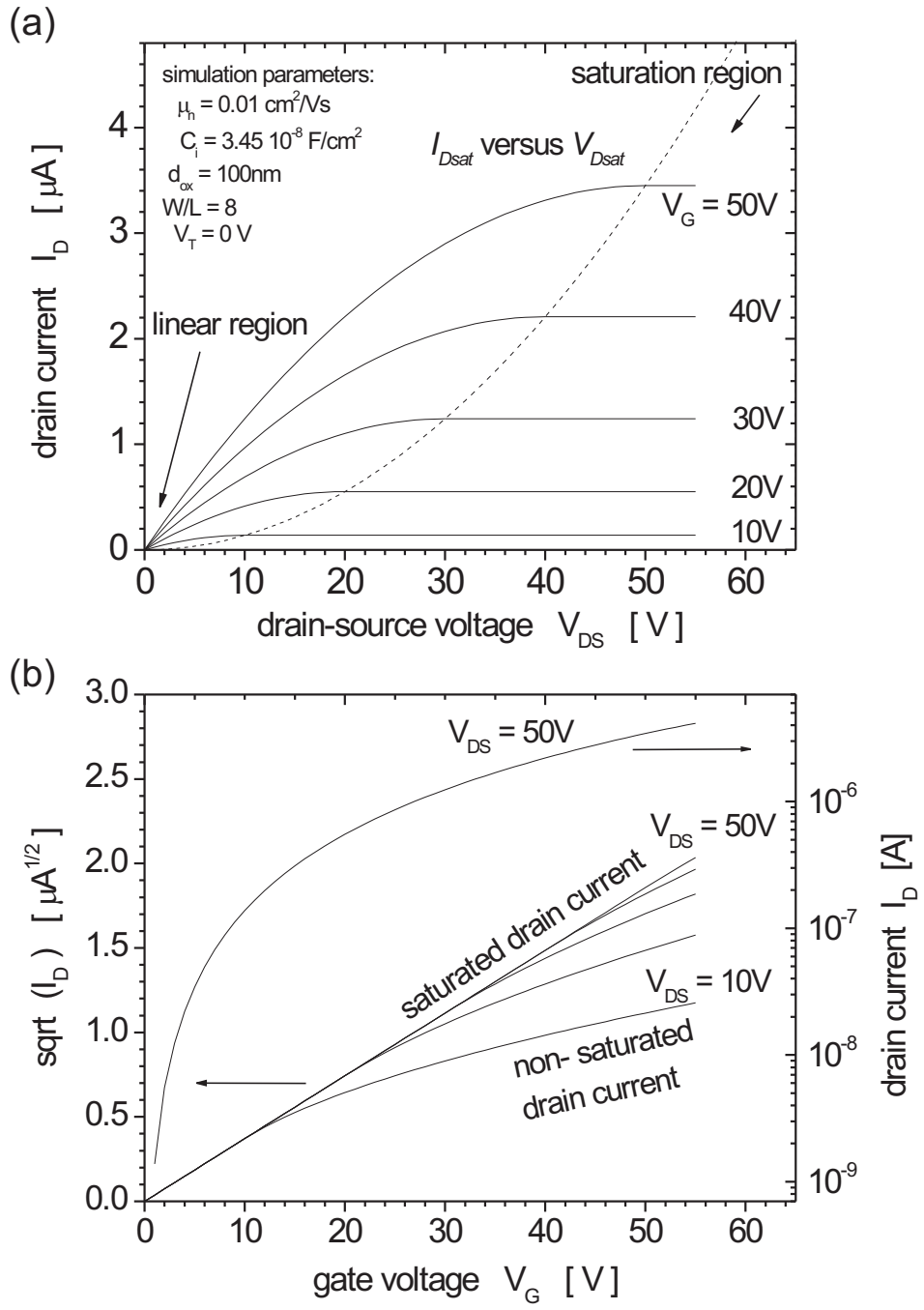

Figure 2.5: *(a) Simulated output characteristic of a n-channel OFET. Shown is the linear region for small V_{DS}, the saturation region for large V_{DS} and the locus of the saturation drain-source voltage V_{Dsat}. (b) Simulated transfer characteristic of the same device. The graph shows the semi-logarithmic plot of the drain current and the square root of the drain current as a function of V_G. In the simulation, the threshold voltage has been set to $V_T = 0$ V.*

Extracting the field-effect mobility directly from the linear region of the output characteristic might yield larger values for the field-effect mobility than the actual one, since the drain current is linear only for very small V_{DS} and large V_G. In contrast, extracting the field-effect mobility from the saturated region might yield rather conservative values for the field-effect mobility, since the drain-current dependence from the gate-voltage becomes sub-quadratic for large V_G as well as for small V_{DS} (see also Fig. 2.5). If not stated otherwise, field-effect mobilities have been extracted from the saturated drain current.

Threshold Voltage

The threshold voltage, i.e. the gate voltage required to accumulate enough charges to form a conductive channel, is for an inorganic MOSFET defined in equivalence with the threshold voltage for an MOS capacitor as in Equation 2.6 [Sze81]:

$$V_T = 2\psi_B + \frac{\sqrt{2\epsilon_s e N_A (2\psi_B)}}{C_i} \tag{2.12}$$

By plotting the square root of the saturated drain current I_D versus the gate voltage V_G, the threshold voltage V_T is derived from the intercept of the linear fit with the abscissa. Similarly, in the linear region, the threshold voltage can be derived from the intercept of linearly extrapolated value of the drain current with the gate voltage V_G. The threshold voltage in OFETs is extracted by the same method, although the theoretical description is still incomplete [Hor98].

On/Off Current Ratio

The on/off current ratio, which is derived from the semi-logarithmic plot of I_D versus V_G, is a crucial device parameter considering application in integrated circuity. For a low doping level of the semiconductor, the on/off current ratio is given by [Bro97]:

$$\frac{I_{on}}{I_{off}} = \frac{\mu}{\sigma} \frac{C_i^2 V_{DS}^2}{e N_A d_s^2} \tag{2.13}$$

Here, σ is the conductivity and d_s the thickness of the semiconductor thin film. Thus, the on/off current ratio depends not only on the mobility to conductivity ratio, but can be increased by decreasing the gate insulator thickness, the semiconductor thickness and the semiconductor doping level.

Subthreshold Characteristics

The drain current at gate voltages below the threshold voltage is called subthreshold current. This situation corresponds to the semiconductor in *weak accumulation*, where

the drain current is dominated by diffusion. The subthreshold swing S, which is gate-voltage required to increase or reduce the drain current I_D by one decade, is defined as the inverse subthreshold slope [Sze81]:

$$S \equiv \left(\frac{d(\log_{10} I_D)}{dV_G} \right)^{-1} \tag{2.14}$$

$$S \simeq 2.3 \frac{k_B T}{q} \cdot \left(1 + \frac{C_d}{C_i} \right) = 57.5\,\mathrm{meV} \cdot \left(1 + \frac{C_d}{C_i} \right) \tag{2.15}$$

Here, C_d is the depletion layer capacitance and C_i is the capacitance of the gate oxide. Additionally, interface charges Q_{it} due to traps with energy states in the band gap of the semiconductor are associated with a capacitance C_{it}, which is parallel to the depletion layer capacitance C_d. Therefore, the traps influence the subthreshold slope according to:

$$S \simeq 2.3 \frac{k_B T}{q} \cdot \left(1 + \frac{C_d + C_{it}}{C_i} \right) \tag{2.16}$$

Effects of Contact Resistance

The contact resistance can be determined by the transition line method (TLM). For small drain-source voltages V_{DS} and high gate voltage V_G it is assumed that the overall device resistance R consists of the channel resistance R_{ch} plus the parasitic source-to-channel and channel-to-drain resistance R_p [Bus89], [Lua92].

$$R = \left. \frac{\partial V_{DS}}{\partial I_D} \right|_{V_{DS} \to 0}^{V_G} = R_{ch} + R_p \tag{2.17}$$

The channel resistance R_{ch} is given by [Sze81]:

$$R_{ch} = \frac{L}{W \mu C_i} \frac{1}{(V_G - V_T)} \tag{2.18}$$

By plotting $R \cdot W$ as a function of the channel length L, a straight line is obtained, whereas the intercept with the ordinate is at $R_p \cdot W$ and the slope is $R_{ch} \cdot W/L$. Thus, TLM involves measuring the device characteristic of various OTFTs with different channel length versus the channel length, and then extrapolating back to zero channel length to extract the contact resistance.

2.1.3 Ambipolar Field-Effect Transistor

Evidence of the ambipolar behavior of a-Si:H thin-film transistors (TFTs) was observed almost thirty years ago by Neudeck and Malhotra [Neu75]. Detailed investigations have been presented early by Pfleiderer *et al.* [Pfl85b, Pfl85a, Pfl86a, Pfl86b], Hack *et al.*

[Hac86], and Neudeck *et al.* [Neu87a, Neu87b]. Hack *et al.* emphasized that one obtains much larger currents than in a conventional a-Si:H TFT and proposed the possibility of fabricating light-emitting transistors in the visible spectrum whose emission can be modulated at high speed. However, a-Si:H does not efficiently emit light and this new type of device did not find applications. Recently, an ambipolar Schottky barrier silicon-on-insulator metal-oxide-semiconductor (MOS) transistor with promising electrical properties has been presented [Lin03].

The most common TFTs based on amorphous hydrogenated silicon operate as unipolar devices with the formation of either a *n*-channel or a *p*-channel. The operation in inversion or accumulation mode is determined by the contacts, which are chosen either rectifying or ohmic, respectively. If source and drain contact are ohmic for both, majority and minority carriers, TFTs exhibit *n*-channel, *p*-channel and ambipolar operation, depending on the applied gate-source and drain-source voltages, and have been studied in detail also in Refs. [Hac86, Neu87a, Neu87b].

The essential feature in the output characteristic of the ambipolar device is a strong increase of the drain current for large drain-source voltages in addition to the linear and saturation regions. This can be understood as follows. For a negative effective gate-source voltage $V_{G,eff}$ with $V_{G,eff} = V_G - V_T < 0$, where V_G is the applied gate voltage and V_T is the threshold voltage, a hole accumulation layer is formed due to hole injection at source and drain contacts if these contacts are ohmic for holes. The electron inversion layer for $V_{G,eff} > 0$ cannot be formed if these contacts are blocking ones for electrons. For small negative drain-source voltage $V_{DS} < 0$ the drain current I_D is in the active or linear regime. Thereby the gate-drain voltage is effectively reduced to $V'_{GD} = V_{G,eff} - V_{DS}$. With V_{DS} approaching $V_{G,eff}$ the region close to the drain becomes depleted and I_D saturates. For even larger negative V_{DS} the condition for inversion is fulfilled at the drain contact but owing to the electron blocking drain contact this channel is not formed. Replacing this contact by one which is ohmic for electrons [Pfl85b, Pfl85a, Pfl86a, Pfl86b] leads to the electron inversion channel near the drain contact for $-V_{DS} > -V_{G,eff}$ in addition to the hole channel near source. The additional electron current leads to a strong increase of the total drain current I_D. If both source and drain are ohmic for electrons and holes, the transfer characteristics does not consist only of an "on"and an "off"region, as it is known from unipolar device operation. Instead "on-off-on"states are observed for increasing gate voltage.

Proposed circuit applications of these devices utilizing the peculiarities arising from the ambipolar transport have not been realized until now. With hole injection at one contact and electron injection at the other one, recombination becomes important for the operation. Combining switching with light-emission by radiative recombination as proposed in Ref. [Hac86] requires the replacement of a-Si:H by a suitable emitter.

The state of the art of ambipolar OFETs has been discussed in detail in Chapter 1. In Chapter 5 of this thesis a detailed simulation on the ambipolar characteristic in OFETs is presented. The simulation itself was performed in collaboration with Dr. Thomas Lindner and Dr. Gernot Paasch from the IWF in Dresden. Special emphasis is put on the potential distribution, the charge-carrier density and recombination between source and drain contact. In Chapter 6, the first ambipolar light-emitting OFET is presented [Ros04b], being the first step towards new opto-electronic applications.

2.1.4 Organic Light-Emitting Diodes

In an organic light-emitting diode (OLED) at least one organic semiconductor is sandwiched between to electrodes, one of them is semitransparent. Applying a voltage leads to the injection of charge carriers at both electrodes. Electrons and holes can form excited states, followed by radiative emission. The efficiency of OLEDs can be improved by introducing multi-layer devices, improving the charge-carrier injection or the light outcoupling. A detailed description of OLEDs, including preparation and characterization methods which are relevant for this thesis can be found in [Rie02, Bei03].

2.2 Charge-Carrier Injection, Transport and Recombination

The characteristic of a light-emitting transistor is determined by three important processes: charge-carrier injection, charge-carrier transport and charge-carrier recombination.

2.2.1 Charge-Carrier Injection

The charge-carrier injection is more crucial for an OLED than for an OFET device. The thickness of the organic thin-film stack in an OLED is in the order of 100 nm, in an OFET the distance between source and drain is more than 1 μm. Thus, the IV characteristic of an OLED is mainly determined by the injection barriers at cathode and anode, the characteristic of an OFET is governed by the properties of the organic thin film. Nevertheless, when downscaling of OFETs is required, e.g in order to reduce the operating voltage, contact engineering becomes more important.

Since organic semiconductors typically have a large bandgap and only few intrinsic carriers, they can be treated similar to wide bandgap semiconductors in inorganic semiconductor theory. Here, the injection barrier Φ_B depends only on the work function Φ_M

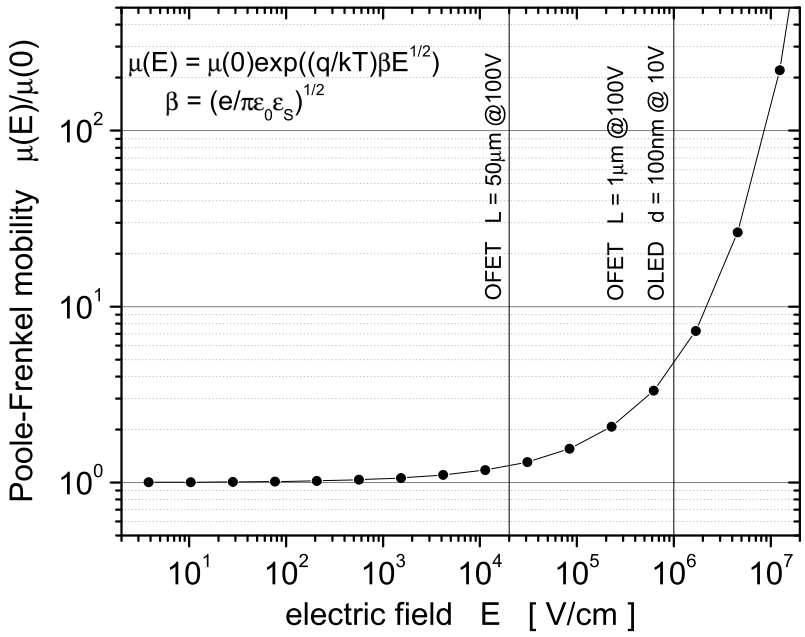

Figure 2.6: *Field dependence of mobility in organic semiconductors according to Poole-Frenkel. For electric fields larger than 10^5 V/cm, the mobility increases significantly with the applied electric field. L denotes the channel length of an OFET and d the thickness of an OLED.*

of the metal contact, and the electron affinity χ_S of the semiconductor:

$$\Phi_B = \Phi_M - \chi_S \tag{2.19}$$

Ideally, the resulting injection barrier is small. In this case, the charge-carrier density at the contact is always larger than in the bulk of the organic semiconductor and the contact behaves like an ohmic one.

2.2.2 Charge-Carrier Transport

In conventional semiconductors having delocalized states, transport is limited by phonon scattering. Therefore, the mobility decreases with temperature. In amorphous or organic semiconductors transport occurs by hopping of charges between localized states and is phonon-assisted. Here, the mobility increases with temperature. The transition between delocalized and localized processes occurs typically at a mobility around 0.1 and 1 cm^2/Vs. Even in highly ordered molecular crystals, the mobility is close to that limit, and therefore the mobility is in most cases described by localized states.

The temperature dependence of the mobility can be described in analogy to the temperature-dependent charge-carrier transport in amorphous silicon by the multiple

trapping and release model [Hor98]:

$$\mu = \mu_0 exp(-E_a/kT) \tag{2.20}$$

where in case of a single trapping level E_a corresponds to the distance between the trap level and the delocalized band edge.

According to Poole-Frenkel, the mobility in organic semiconductors is field-dependent. The with respect to $\mu(0)$ normalized Poole-Frenkel mobility $\mu(F)$ is shown in Figure 2.6. Considering OFETs with channel length larger than 50 nm, i.e. in devices structures studied within this thesis, the field-dependence of the mobility can be neglected.

2.2.3 Charge-Carrier Recombination

Recombination is discussed in the Langevin model [Pop99]. Here, recombination is considered as a random process due to statistically independent injected electrons and holes. An important value is the coulomb capture radius r_c, for which the kinetic energy of the particle is equal to the attractive coulomb potential. For $\epsilon_s = 3.5$ it is

$$r_c = \frac{e^2}{4\pi\epsilon_0\epsilon_s kT} \simeq 16 \text{ nm}. \tag{2.21}$$

The coulomb capture radius r_c determines the maximum thickness of the bottom transport layer in bilayer heterostructure OFETs, for which recombination of both charge carriers can occur.

For energy transfer from the transport to the emitting layer in a light-emitting OFET, Förster transfer and Dexter Transfer are the two important processes [Bul01]. Transfer radii are 5 to 10 nm and 1.5 to 2 nm, respectively. The transfer radius determines the maximum thickness of the transport layer in light-emitting OFET structures, for which the transport is spatially separated from the emission layer.

Chapter 3

Experimental Methods

3.1 Device Preparation

3.1.1 Substrate Preparation

If not stated explicitly, Phosphor-doped (100) *n*-type silicon wafers with a resistivity of 1-10 mΩcm were used. This is equivalent to a doping density of 4×10^{18} to 8×10^{19} cm^{-3}. Additionally, Boron-doped (100) *p*-type silicon wafers with an equivalent resistivity were used, which is equivalent to a doping density of about 8×10^{18} to 1×10^{20} cm^{-3}.

Oxide Growth

The silicon wafers were oxidized at 1050 ℃ for 4 h in order to obtain an oxide thickness of 150 nm. After oxidation, the oxide thickness was measured by spectral ellipsometry, using an WOOLAM VASE© variable-angle spectroscopic ellipsometer. The oxide capacitance was characterized by impedance spectroscopy.

Surface Treatment

Before further processing, the oxide was removed from the backside using HF, thus the highly conductive wafer could be used as gate contact. In order to protect the gate oxide against etching, it was covered by photoresist. The substrates were then cut and cleaned by an acetone/IPA process, followed by piranha (H_2SO_4/H_2O_2) cleaning for about 10 min at 125 ℃.

Contact Processing

The source and drain contacts were evaporated through shadow masks, whereas three different mask designs were used for different purposes. The mask set shown in Figure 3.1(a), fabricated by nickel electroforming (Tecan Ltd., Dorset, UK), comprises a set

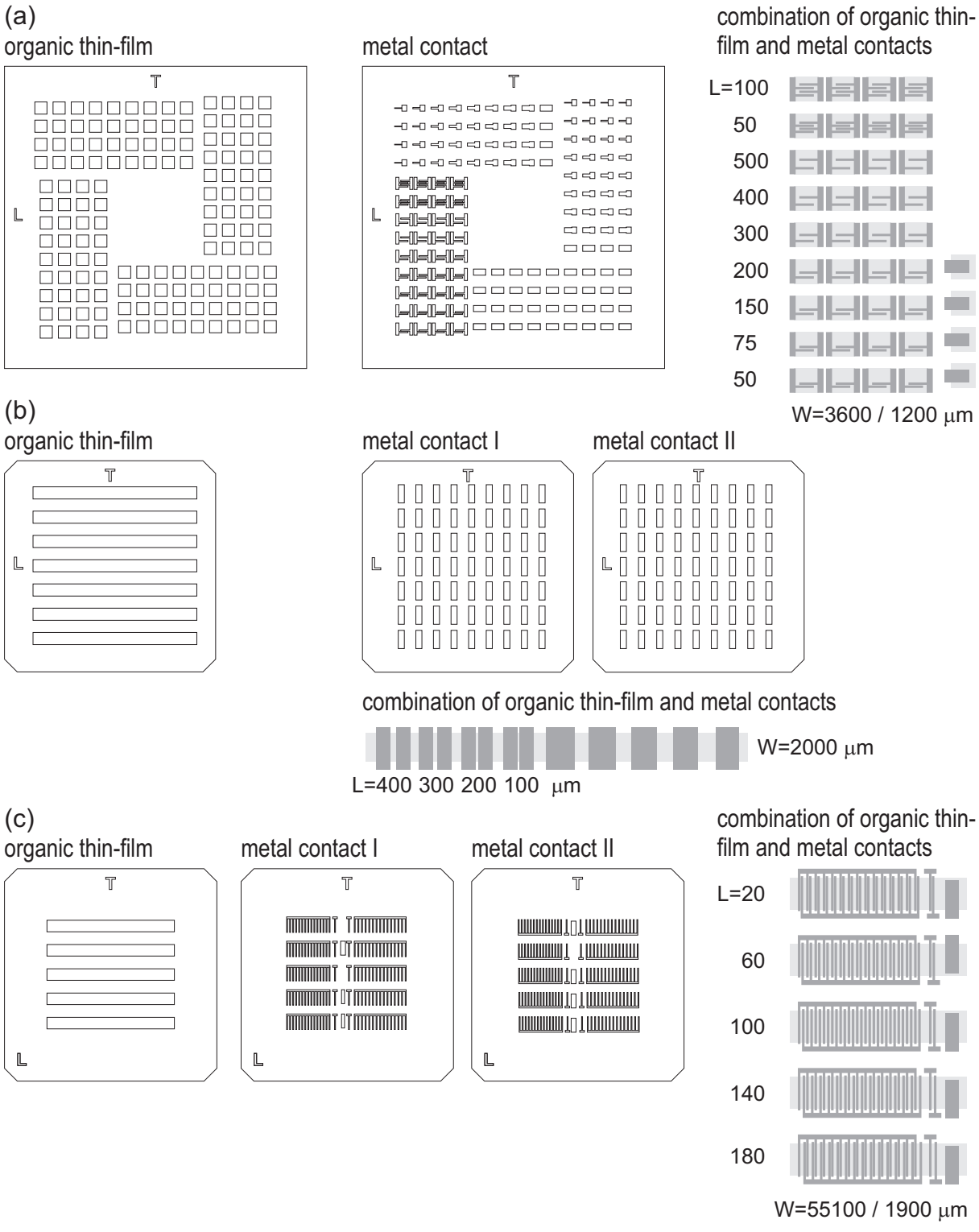

Figure 3.1: *Shadow mask design for capacitor and transistor structures. (a) The substrate size is 50×50 mm^2 and the masks allow the preparation of transistor structures with different channel length L. (b) The substrate size is 35×35 mm^2. Two masks which are out-of-tune by 100 μm are used for the deposition of different metals for source and drain contact. (c) The substrate size is 35×35 mm^2. Two masks, which are out-of-tune by 40 μm (left part) and 60 μm (right part) are used for the deposition of different metals for source and drain contact. The transistor structures are designed interdigitally in order to increase the channel width W.*

of capacitor and transistor structures with different dimensions. The capacitor structures consist of squares with a dimension of 2×2 mm^2 (light grey) for the organic thin film and an overlapping structure of 1×2 mm^2 (dark grey) for the metal contacts. The transistor structures have varying channel lengths of 100, 50, 500, 400, 300, 200, 150, 75 and 50 μm. The channel width is 3600 μm for the devices with a channel length of 100 and 50 μm and 1200 μm for all other channel length. For each combination, four identical devices are fabricated.

A second set of masks, shown in Figure 3.1(b), was used to evaporate different metals for source and drain contact. Therefore, it consists of three different masks, one for the organic thin film and two different ones for the metal contacts. Source and drain contacts were evaporated in two subsequent steps. In order to obtain short channel length in the range of 100 μm despite of the mask-holder tolerance of 0.2 mm, the two metal-contact masks were intentionally misaligned, leading to devices with varying channel length in 100 μm steps, starting at a random sub-100 μm value. The exact channel length was measured after evaporation using a microscope. For each channel length, seven identical devices were fabricated.

A third set of masks, similar to the previous one and shown in Figure 3.1(c), was used in order to increase the channel width by a interdigitated contact pattern. Additionally, reduced tolerances of the mask holder allowed the processing of shorter channel length down to 40 μm. The masks shown in Figure 3.1(b) and (c) were fabricated by laser cutting of 0.1 mm thick steel sheets (Digipack AG, Wetzikon, Switzerland).

3.1.2 Purification of Organic Materials

Pentacene, *p*-4P [1] and PTCDI-$C_{13}H_{27}$ [2] were purchased from Fluka (Switzerland), *p*-6P [3] was purchased from TCI (Europe). As purchased organic materials were purified prior thin film deposition, either by temperature gradient sublimation, similar to the system described in [Kar01b] or by resublimation onto a cold finger. Whereas the resublimation leads to the deposition of polycrystalline bulk material, in the tubular temperature gradient sublimation polycrystalline thin films are obtained. Tetracene, α-4T [4] and α-5T [5] were processed by Dr. Mauro Murgia at the ISMN-CNR in Bologna. Whereas tetracene and α-4T were obtained commercially, α-5T was synthesized by the group of Dr. Giovanna Barbarella, ISOF-CNR Bologna, Italy.

[1] *para*-quaterphenyl
[2] N,N'-ditridecylperylene-3,4,9,10-tetracarboxylic diimide
[3] *para*-sexiphenyl
[4] α-quaterthiophene
[5] α-quinquethiophene

3.1.3 Thin-Film Growth

Thin films were grown by thermal sublimation of the organic materials from an effusion cell using quartz crucibles.

Deposition Chamber

Two different deposition chambers were used. One is a stand-alone chamber, comprising three sources centered towards the sample, which is fixed to a sample holder that can be heated. Normally, substrate temperatures were varied between of 60 to 90 ℃. The thickness was monitored by a quartz balance. The second chamber, which I designed and set up during my thesis, is an integrated system with two separate deposition chambers - one for organic materials and one for metals - connected to an electrical characterization chamber via a transfer backbone, see Figures 3.2 and 3.3(b). It allows the characterization of samples without transfer through air. Here, both sample holders can be heated or cooled. For cooling, either cooling water or liquid nitrogen can be used. Each deposition chamber has four different sources, which are directed towards the center of the chamber, where the sample holder is placed. The masks can be changed independent of the samples and the film thickness is again monitored by a quartz balance.

Sample Holder

A photograph of the sample holder is shown in Figure 3.3(a). The sample holder was designed such that it allows heating and cooling over a wide temperature range between 70 and 400 K. The heating is done by a heating wire, for cooling liquid nitrogen is used. The temperature is controlled by a Eurotherm 2408 temperature controller. The temperature is measured directly on the sample to assure accurate measurement. Furthermore, a mask holder has been designed to allow the use of four different masks. The technological challenge was to keep the distance between mask and sample as short as possible. Due to the evaporation from tilted effusion cells, a distance between mask and sample surface of e.g. 0.1 mm leads to significant variations in the channel length of about 20 μm.

Effusion Cell

The effusion cells for deposition of organic materials (WEZ 40-10-KS; Eberl MBE-Komponenten GmbH, Germany) containing quartz crucibles are mounted on a CF35 flange and are actively water cooled, in order to obtain temperature stability even at low temperatures, as needed for the evaporation of organic materials. For metal deposition, high-temperature cells with a pyrolytic boron nitride crucible were used.

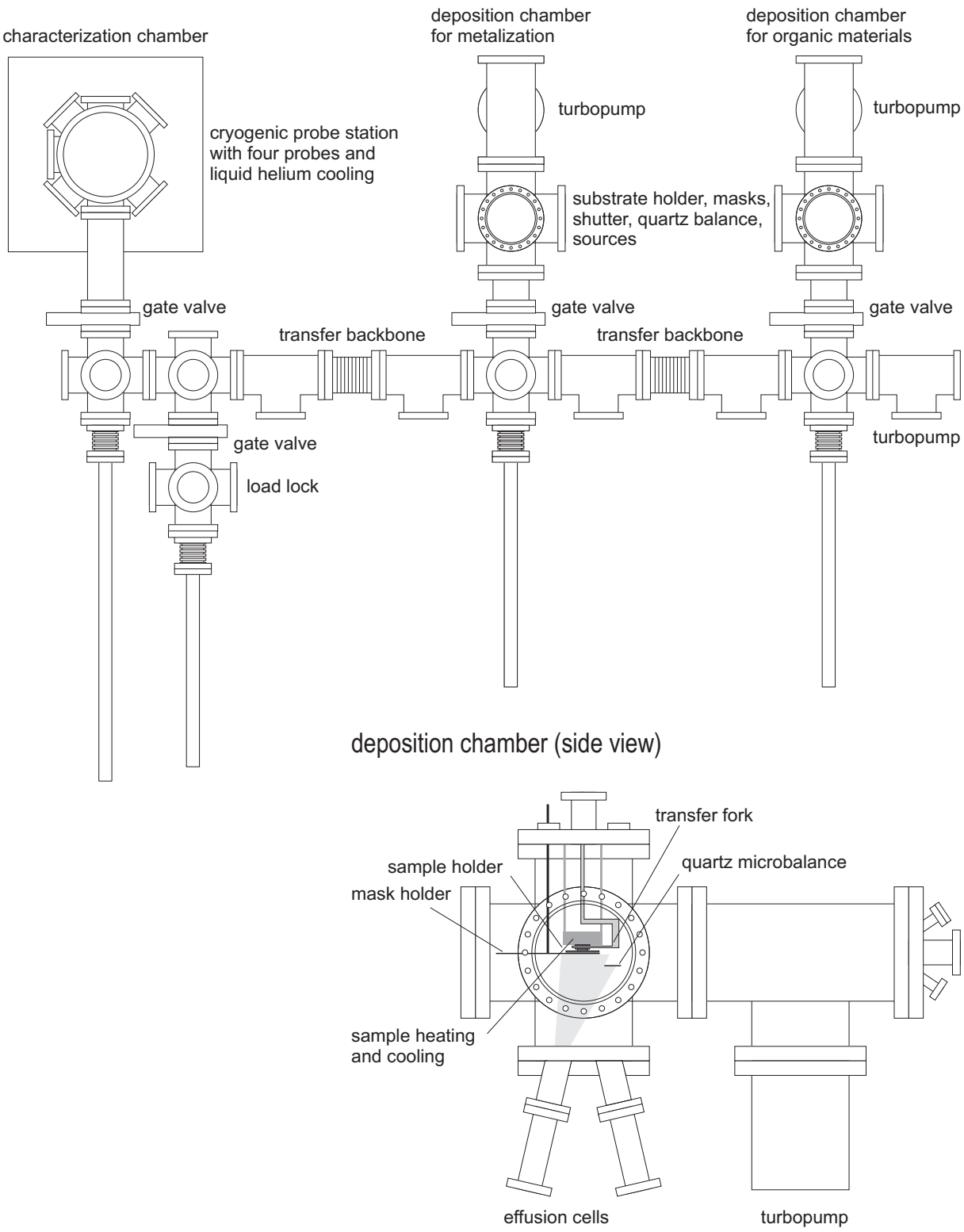

Figure 3.2: *Deposition and characterization chamber, which is an integrated system, where two separate deposition chambers - one for organic materials and one for metals - are connected to an electrical characterization chamber via a transfer backbone.*

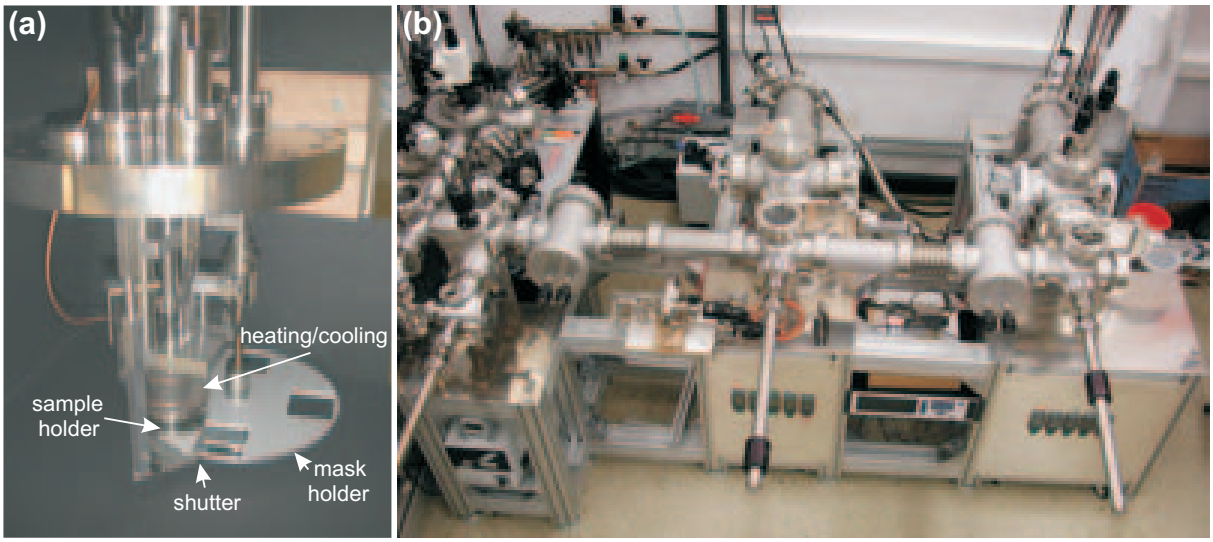

Figure 3.3: *(a) Sample holder and (b) deposition and characterization chamber.*

3.2 Device Characterization

The device characterization includes electrical, electro-optical and optical methods. The electrical characterization of the devices was performed solely under inert conditions, either in an Argon filled glove box or under vacuum, in order to prevent device degradation due to oxidation. Optical characterization was performed under ambient conditions. Additionally, the topology and morphology of the thin films has been investigated by atomic force microscopy (AFM), laser scanning confocal microscopy (LSCM) and X-ray diffraction (XRD).

3.2.1 Electrical Characterization

CV-Measurement and Impedance Spectroscopy

Capacitance-voltage (CV) measurement and impedance spectroscopy are powerful methods to study charge-carrier injection across interfaces and accumulation of charges at barriers. A detailed description of the method can be found in [Mac87]. The CV characteristic of metal-oxide semiconductor (MOS) capacitor structures was measured using a Solartron 1260 impedance analyzer combined with the Solartron 1296 dielectric interface (Solartron Analytical, UK) to extend the measurement range. Therefore, high impedance samples up to 10^{14} Ω could be measured with a frequency range from 10 μHz to 10 MHz. Measurements were carried out in the reference mode, using an internal reference, and data were averaged over five cycles. Typically, a voltage scan between -40 and $+40$ V at different discrete frequencies and a frequency scan between 0.1 Hz and 10^6 Hz at dif-

ferent discrete voltages was performed. The impedance data has been further analyzed with the ZView© modelling software (Scribner Associates, Inc., NC) using an appropriate equivalent circuit model.

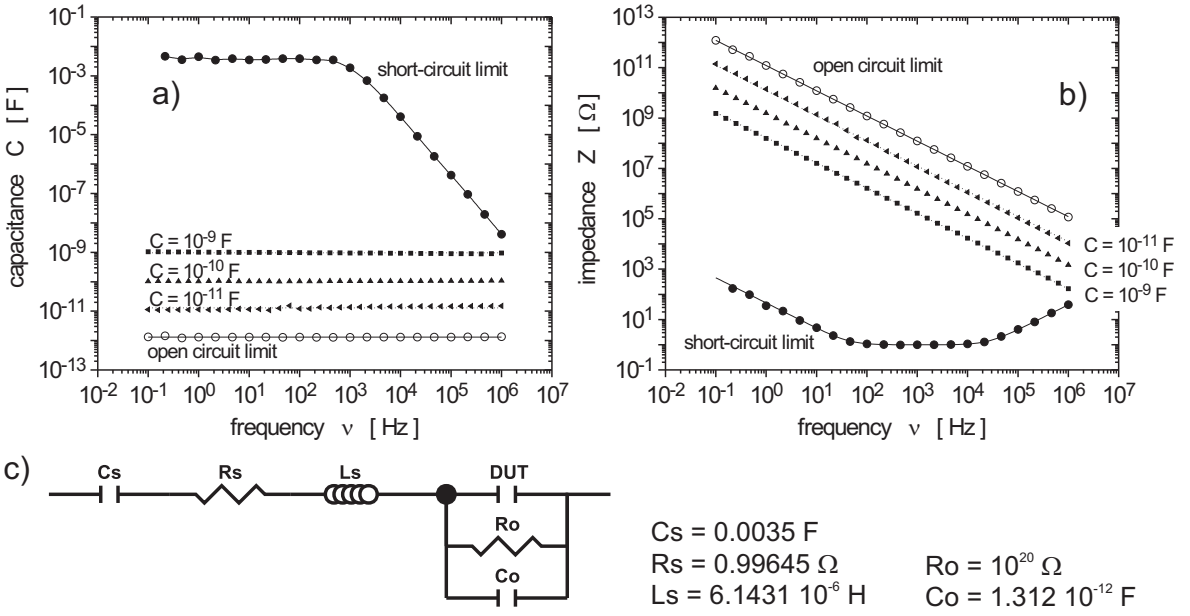

Figure 3.4: *Open circuit and short-circuit limit for (a) the capacitance, and (b) the impedance of the setup. The measurement has been performed at 0 V dc bias and an applied ac voltage of 0.1 V. (c) Equivalent circuit model for the set-up, where DUT denoted the device under test. Additionally, the data for three reference capacitors with the capacities of 10^{-11}, 10^{-10} and 10^{-9} F are shown in the diagram. The increase in the short-circuit impedance for low frequencies is due to ac coupling, but is not relevant for the characterization of high-impedance samples.*

No additional electrostatic shielding was used. Therefore the measurement setup itself was characterized by open-circuit and short-circuit measurements. The open-circuit capacitance of the setup was 2 pF and constant over the measured frequency range of 10^{-1} to 10^{6} Hz, as it is shown in Figure 3.4(a). The impedance of the setup is shown in Figure 3.4(b). Additionally, three capacitors of known capacitance were measured, in order to elaborate whether the experimental data on metal-insulator-semiconductor (MIS) diodes had to be corrected by the setup parasitics in order to be modelled correctly, according to Figure 3.4(c). The impedance shows for high frequency larger 10^4 Hz an inductive component, for low frequencies smaller 10^2 Hz a capacitive component. The the characteristic values of the short-circuit and open circuit limit can be fitted by using a serial and parallel equivalent circuit, as shown in Figure 3.4(c). Here, C_S, R_S, and L_S denote short-circuit capacitance, resistance and inductance, respectively. Analogous, R_O and C_O are the open-circuit resistance and capacitance. The device-under-test is labelled

reference value	10^{-11} F	10^{-10} F	10^{-9} F
uncorrected	$1.28(2) \times 10^{-11}$ F	$1.027(2) \times 10^{-10}$ F	$0.962(6) \times 10^{-9}$ F
corrected	$1.15(2) \times 10^{-11}$ F	$1.041(2) \times 10^{-10}$ F	$0.944(9) \times 10^{-9}$ F

Table 3.1: *Reference capacitance values extracted from experimental data using the uncorrected and the corrected model.*

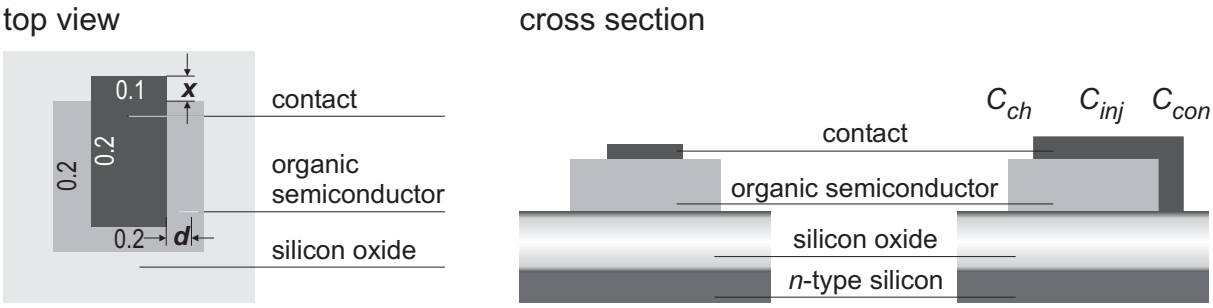

Figure 3.5: *Top view and cross sections of the MIS device structure. x denotes the overlap of the metal contact and d the spread distance of charge carriers accumulated in the organic thin film that is not directly top contacted, also referred to as* d_{spread}.

DUT. For the fit, either only open circuit or only short-cut compounds were taken into account. In order to be able to judge, whether setup correction is necessary, the data for three defined capacitances have been fitted with and without setup correction. The obtained results are summarized in Table 3.1. For small capacitances, the corrected value is closer to the reference value, however, for capacitances between 10^{-10} and 10^{-9} F, the correction does not correct the data appropriately. Thus, in order to keep the corresponding equivalent circuit as simple as possible, uncorrected data were used for the fit of the actual experimental data.

In order to derive an equivalent circuit model used for the fitting of the experimental data, the device architecture and geometry were considered. The MIS device architecture, fabricated with the shadow masks discussed previously, is shown in top view and cross section in Figure 3.5. Three areas of interest can be distinguished with the circuit model shown in Figure 3.6.

First, there is a region where the metal is in direct contact with the gate insulator SiO_2. The capacitance contributes to the overall capacitance with $C_1 \equiv C_{con}$, which is the oxide capacitance defined by the contact area of the metal with the silicon oxide surface, A_{con}, and the silicon oxide thickness d_{ox}:

$$C_1 \equiv C_{con} = \epsilon_0 \epsilon_{ox} \cdot \frac{A_{con}}{d_{ox}} \tag{3.1}$$

with ϵ_0 being the permittivity of free space and ϵ_{ox} the permittivity of the silicon oxide.

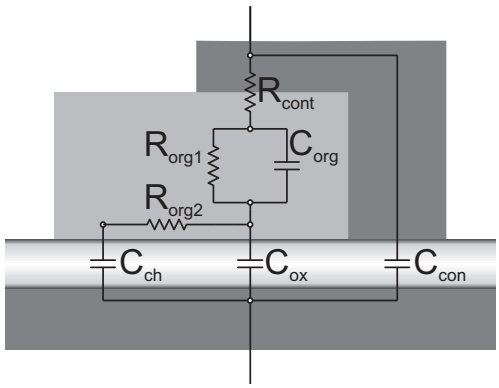

Figure 3.6: *Equivalent circuit for the characterization of a silicon wafer and the organic thin film. The bias voltage is applied with respect to the metal contact.*

Second, there is the actual injecting contact, where the metal contact is directly on top of the organic thin film, contributing to the overall capacitance with a capacitance C_{inj}, which is a serial composition of the organic thin film capacitance and the oxide capacitance:

$$\frac{1}{C_{inj}} = \frac{1}{C_{org}} + \frac{1}{C_{ox}} \tag{3.2}$$

$$C_{inj} = C_{ox} \cdot \frac{1}{1 + \frac{\epsilon_{ox}}{\epsilon_{org}} \cdot \frac{d_{org}}{d_{ox}}} = \epsilon_0 \epsilon_{ox} \cdot \frac{A_{inj}}{d_{ox}} \cdot \frac{1}{1 + \frac{\epsilon_{ox}}{\epsilon_{org}} \cdot \frac{d_{org}}{d_{ox}}} \tag{3.3}$$

The third interesting area of the device, which is covered only by the organic thin film, contributes in the case of very strong accumulation, where charge carriers are not only accumulated below the contact, but also besides the area covered with the metal contact:

$$C_{ch} = \epsilon_0 \epsilon_{ox} \cdot \frac{A_{ch}}{d_{ox}} \tag{3.4}$$

A_{ch} is variable and depends on the degree of accumulation. Its maximum value is given by the size of the organic thin film. The special device architecture allows not only to study the charge-carrier accumulation below the contact, but also in regions of the organic thin film that are not directly top-contacted. This situation is equivalent to the formation of a channel of accumulated charges in an OFET. The overall measured capacitance is a serial combination of C_{con}, C_{inj} and C_{ch}:

$$C = C_{con} + C_{inj} + C_{ch} \tag{3.5}$$

whereas in depletion it is $C_{dep} = C_{con} + C_{inj}$, in accumulation $C_{acc} = C_{con} + C_{ox}$ and in strong accumulation $C_{spread} = C_{con} + C_{ox} + C_{ch}$. The areas A_{con}, A_{inj} and A_{ch} can be

expressed as following:

$$\begin{aligned} A_{con} &= 0.1 \cdot x \\ A_{inj} &= 0.1(0.2 - x) \\ A_{ch} &= (0.5 - 2x)d_{spread} + (\pi d_{spread}^2/2) \\ A_{chmax} &= 0.04 + 0.1(0.2 - x) \end{aligned} \tag{3.6}$$

Here, d_{spread} is the spread distance of charge carriers accumulated in the organic thin film that is not directly top contacted.

Depending on the applied voltage, also the capacitance of the silicon wafer is modulated due to accumulation, depletion and inversion of charge carriers at the silicon/silicon oxide interface. However, due to the high doping level of the silicon wafer, depletion occurs at much higher voltages than 40 V and can therefore be be neglected.

The equivalent circuit model is summarized in Figure 3.6: the three previously discussed capacitances are shown in parallel. The capacitance of the organic thin film is in parallel with a resistor R_{org1}. A contact resistance for charge-carrier injection is considered and in series to the channel capacitance C_{ch} the resistor R_{org2} is introduced. Using the modelling software ZView©, the geometric capacitances C_{con}, C_{ox} and C_{org} are set constant and only the channel capacitance C_{ch} and the resistors are assumed to depend on the bias voltage.

Current-Voltage Characteristic of OFETs

The electro-optical characterization of the OFETs was done on a probe station inside a glove box under argon atmosphere, using an Agilent semiconductor parameter analyzer (Agilent 4155C), see Figure 3.7. For the output characteristic of an OFET, the drain current was measured during drain-source voltage ramps from 0 to 100 V in 0.5 V steps at discrete gate voltages, which were varied in 10 V steps. In order to reach equilibrium after changing the gate voltage, a hold time of 5 s was used. The integration time for the drain-source voltage scan was selected to "medium". The transfer characteristic was measured by scanning the gate voltage in 0.5 V steps for discrete drain-source voltage changed in 10 V steps. A silicon photodiode (Hamamatsu S1337-1010BR) is placed on top of the sample to measure the intensity of the emitted light. By shading the glove box, the background current of the photodiode was reduced to values below 1 pA.

Temperature Dependence

Temperature-dependent current-voltage (IV) measurements were taken using a helium-pumped flow-cryostat probestation in the temperature range of 50 - 450 K. The temperature is measured at the sample holder by a silicon diode (DT-470-CO-13, Lakeshore,

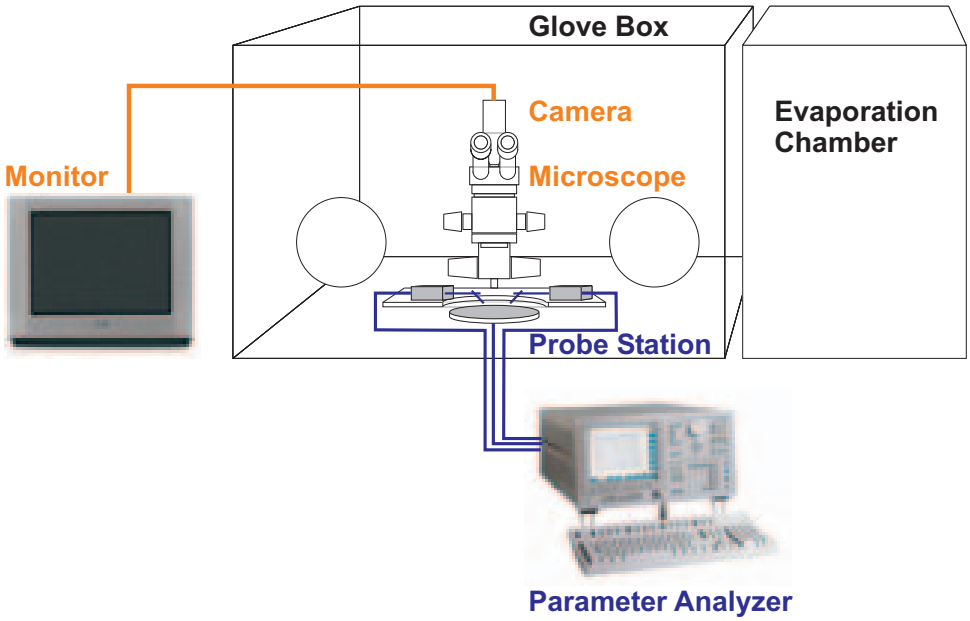

Figure 3.7: *Setup for the current-voltage characteristics of OFETs.*

OH) and is controlled via a TIC 304-MA temperature controller (CryoVac, Germany). The sample is fixed on the sample holder by mechanical clamps and thermal contact is improved by using a thermally conducting paste (AIT Cool Grease 7016, AI Technology, Inc., NJ). The setup is shown in Figure 3.8. To measure the temperature correctly, a second silicon diode (DT-471-CO, Lakeshore, OH) is placed on top of the sample in order to measure the device temperature as accurate as possible. The IV characteristics is measured with an Agilent 4155C semiconductor parameter analyzer, as described above. The data acquisition is automated using a Labview program, which controls both, the temperature controller and the parameter analyzer.

Device Characterization of Organic Light-Emitting Diodes

Current-voltage (IV) and electroluminescence-voltage characteristics of organic light-emitting diodes were measured inside a glove box using a Hewlett Packard semiconductor parameter analyzer (HP 4145B) together with a test fixture HP 16058A. The latter shields the sample electrostatically and optically and records the EL intensity with a silicon photodiode (Hamamatsu S2281), which is placed in front of the OLED.

The spectral characteristic of the electroluminescence spectrum is recorded using a calibrated spectroradiometer (Spectra Scan PR704, Photo Research, CA). The system consists of a diffraction grating and a photodiode array, allowing measurements in the spectral range of $380 - 780$ nm with 2 nm resolution. The EL spectra is analyzed to determine the CIE1931 x and y color coordinates are obtained.

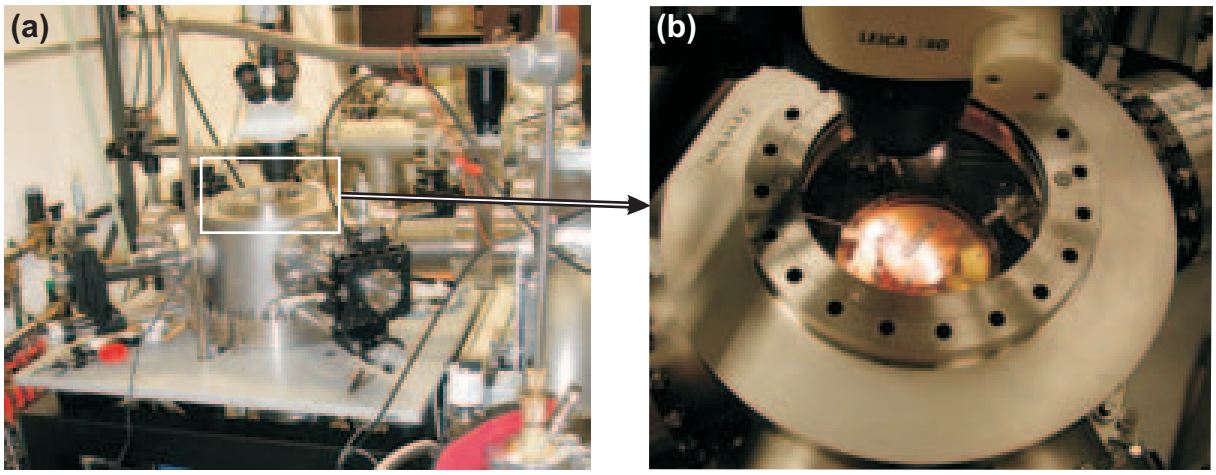

Figure 3.8: *Setup of the temperature-dependent current-voltage measurement. (a) The recipient with four manipulators, the helium transfer line, and the microscope. (b) Top view into the chamber with the sample holder and prober needles.*

3.2.2 Optical Properties

UV-VIS Absorption Spectroscopy

The absorption of organic thin films prepared on quartz substrates was measured using a UV/Vis/NIR spectrophotometer (Lambda 900, Perkin Elmer, MA), offering a spectral range of 175 - 3300 nm. Typically, a resolution of 1 nm was chosen.

Photoluminescence

The photoluminescence (PL) spectrum of the organic thin films was studied by using a Hitachi F-4500 fluorescence spectrophotometer, which offers a spectral range for the excitation and emission wavelength between 200 and 900 nm. Typically, measurements were performed with a resolution of 0.2 nm. For PL measurements, the organic thin film was prepared on quartz substrates, in order to acquire optical data on identical films. Silicon/SiO_2 wafers were not used as substrates here, because this would lead to a shift in the spectrum due to interference effects.

Additionally, PL excitation spectra were recorded. Here, the emission wavelength is kept constant and the emission intensity is recorded as a function of excitation wavelength. Thus, the PL excitation spectrum resembles the absorption spectrum.

3.2.3 Surface Characteristics and Film Morphology

Variable Angle Spectroscopic Ellipsometry

The organic thin-film thickness d was determined using variable angle spectroscopic ellipsometry (VASE). Additionally, the optical constants n and k of the organic thin film were obtained. The ellipsometer (WVASE32©, J. A. Woollam Co., Inc., NE) allows characterization within the wavelength range of $240 - 1700$ nm. Typically, measurements were performed with a resolution of 10 nm.

Atomic Force Microscopy

The surface morphology of the organic thin films was studied by atomic force microscopy (AFM). Tapping mode AFM images were obtained using Pointprobe silicon cantilevers (Nanosensors) with a Dimension 3000 Instrument (Digital Instruments). Contact mode images were recorded by Dr. Franco Dinelli at the ISMN-CNR in Bologna, Italy, using silicon cantilevers having a spring constant of 0.02 to 0.2 N/m (PARK Scientific) with a PARK Scientific model CP AFM.

Laser Scanning Confocal Microscopy

LSCM was used to obtain high-resolution images of fluorescent samples. A focused laser beam is scanned over the sample in x and y direction. The corresponding PL intensity is recorded by a photomultiplier. A confocal aperture, i.e. a pinhole, is placed in front of the photodetector in order to avoid out-of-focus contribution to the PL intensity in z direction. Here, LSCM was applied to study a coevaporated thin film of two materials having different PL spectra. By using appropriate optical filters, information about the spatial distribution of both materials can be obtained. The measurements were performed by Dr. Maria Antonietta Loi at the ISMN-CNR in Bologna, Italy.

X-ray Diffraction

The crystallinity of pentacene thin films and the crystal orientation with respect to the surface was studied by grazing incidence X-ray diffraction (GID) at the BW2 beamline at Hasylab in Hamburg in collaboration with Dr. Dag Werner Breiby from the Danish Polymer Centre at the Risø National Laboratory, Roskilde, Denmark [Bre04]. The wavelength was $\lambda = 1.2398$ Å corresponding to a photon energy of $E = 10.00$ keV. Figure 3.9 shows the geometry of the experiment. The incidence angle α_i is kept fixed at a value of $\sim 0.18°$, which is below the critical angle of reflection of the substrate, thus giving total reflection of the beam, effectively suppressing scattering from the substrate. The angle $2\theta_z$ denotes the vertical angular displacement of the point detector from the direct beam.

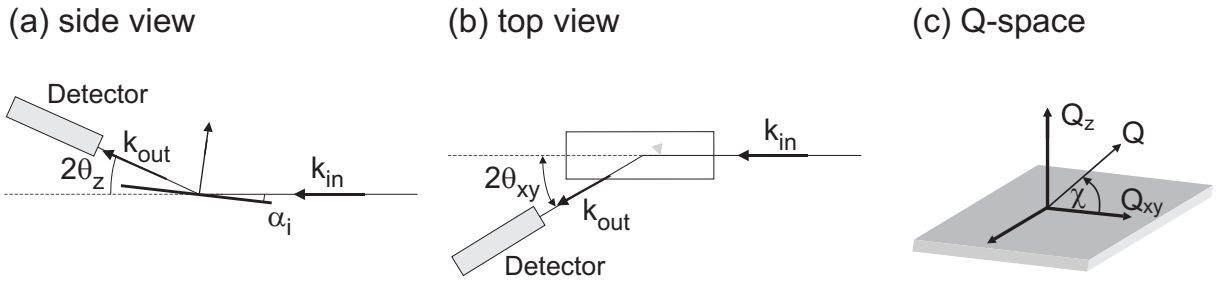

Figure 3.9: *Geometry of grazing incidence X-ray diffraction setup in (a) side view and (b) top view. (c) The scattering vector Q can be decomposed in an in-plane component Q_{xy} and an out-of-plane component Q_z.*

Similarly, $2\theta_{xy}$ is the horizontal displacement. For the total scattering angle 2θ it holds $cos2\theta = cos2\theta_z cos2\theta_{xy}$. The in- and out-going wave vectors, k_{in} and k_{out}, respectively, define the scattering vector Q by $Q \equiv k_{out} - k_{in}$. Because of random in-plane orientation of the crystallites, i.e. 2D cylindrical symmetry of the sample, the scattering becomes independent of the rotation angle of the sample around the film normal. The scattering vector Q can therefore be conveniently described by an in-plane component Q_{xy} and an out-of-plane component Q_z. The angle χ denotes the angle between Q and the sample plane.

The crystallinity of oligophenyl thin films was analyzed in-house using a D8 Discover diffractometer (Bruker), equipped with a rotating anode generator (RAG). The measurements were performed in $\theta - 2\theta$ geometry 0.02° steps with an integration time of 5 s per step. In order to increase the intensity, the Cu Kα1 (1.54056 Å) and Kα2 (1.54439 Å) lines were used, resulting in a CuKα weighted average wavelength of 1.5418 Å. The distance d_{hkl} between molecular layers is determined using the Bragg equation:

$$n\lambda = 2d_{hkl} sin\theta. \tag{3.7}$$

Here, n is the diffraction order, λ the wavelength and θ the incident angle relative to the substrate surface. (h,k,l) denote the Miller indices, which are related to the lattice parameters a, b, and c in case of orthorhombic cells by the following relation:

$$\frac{1}{d^2} = \frac{h^2}{a^2} + \frac{k^2}{b^2} + \frac{l^2}{c^2}. \tag{3.8}$$

Chapter 4

Single-Layer Devices

The device characteristic of an OFET is determined not only by the transport properties of the organic semiconductor, but also by charge-carrier injection and channel formation. In addition to the intrinsic material and contact properties, also the device architecture and geometry influence the IV characteristic. In this chapter the transport properties of various organic semiconductors in combination with different contact metals are studied by means of impedance spectroscopy and current-voltage scans. The materials investigated are tetracene, pentacene, *p*-4P [1], *p*-6P [2], α-4T [3], α-5T [4] and PTCDI-$C_{13}H_{27}$ [5]. Different metals are applied as top or bottom contacts: Ca, Mg, and Au. Temperature-dependent mobility measurements provide further insight into the transport properties. Moreover, the transport properties are related to the thin film structure, which is investigated by AFM and X-ray diffraction.

4.1 Film Growth and Morphology

Organic semiconductors can be prepared as single crystalline, polycrystalline or amorphous films. The highest charge-carrier mobilities are obtained in single crystals. Evaporated thin films generally are polycrystalline or amorphous. For application in OFET devices, rod-like molecules, such as oligoacene, oligophenyls or oligothiophenes are preferred because of their relatively high degree of molecular order even in evaporated thin films. The overlap of π-orbitals, which is optimized in the crystalline order, is decisive for charge-carrier transport. When aiming for transport parallel to the organic thin film/SiO_2 interface, as in OFETs, it is favorable that the aromatic rings of the molecules are ori-

[1] *para*-quaterphenyl
[2] *para*-sexiphenyl
[3] α-quaterthiophene
[4] α-quinquethiophene
[5] N,N'-ditridecylperylene-3,4,9,10-tetracarboxylic diimide

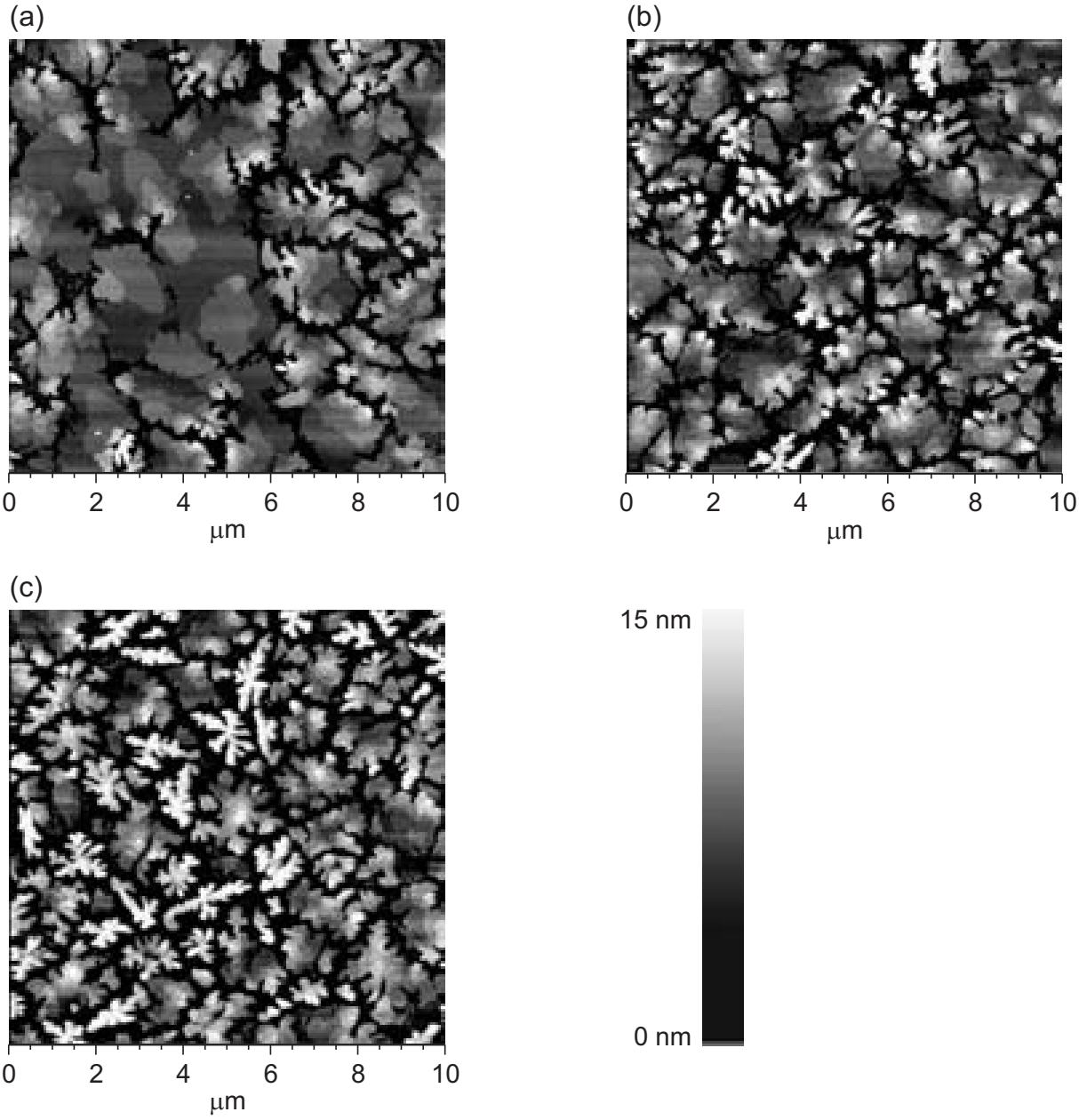

Figure 4.1: *AFM tapping-mode images of pentacene on SiO_2. Shown are films with different nominal thicknesses of (a) 3 nm, (b) 5 nm, and (c) 7 nm. The greyscale bar quantifies the topography of the film between 0 and 15 nm. The thinnest film shows more terrace-like islands, which are partially connected. Additional evaporated material tends to agglomerate in isolated dendritic structures rather than to complete the first few monolayers of the film. The grey-scale bar quantifies the topology between 0 and 50 nm.*

ented perpendicular to that interface instead of lying flat on the SiO_2 surface. The growth of organic semiconducting polycrystalline films can be influenced by parameters such as substrate pretreatment, substrate temperature and evaporation rate. In the following section the growth of pentacene and *p*-4P is studied.

In Figure 4.1 atomic force microscopy (AFM) images of pentacene on silicon oxide are shown for different nominal film thicknesses of 3, 5 and 7 nm. The film (a) with a nominal thickness of 3 nm shows large interconnected islands indicating terrace-like growth. In the upper right area of the image tendencies towards more dendritic growth are observed, which are also present in the 5 nm sample of Figure 4.1(b). In the image of the film with 7 nm nominal thickness, mainly dendritic growth is observed having topographical peaks of 15 nm. The large interconnected islands of only few monolayers thickness cannot be distinguished from the background anymore. In an OFET the lateral charge-carrier transport between source and drain takes place within the first few monolayers of the organic thin film. Thus, the dendritic growth after few deposited monolayers has little effect on the charge-carrier transport. Nevertheless, measuring the mobility as a function of layer thickness, nominally much thicker layers are needed for a saturation of the mobility. This is due to the voids, which are still observed in the 3 nm thick film. Due to the preferred dendritic growth, these voids are not completely filled and it requires nominally thicker films to achieve a largely continues film of a few monolayers thickness. With respect to impedance spectroscopy discussed later on, the film roughness is neglected and an effective film thickness is used for all data analysis and discussion.

Figure 4.2 shows the X-ray diffractogram in Q-space of a pentacene thin film deposited at standard conditions. Using grazing-incidence XRD, the pentacene thin film exhibits several strong and sharp diffraction peaks, indicating a high degree of crystallinity. Comparing Figure 4.2 (a) and (b), which show the in-plane and out-of-plane intensity, respectively, reveals a high degree of preferential crystal orientation, with the *c*-axis of the unit cell tending to orient perpendicularly to the sample surface. The data indicate that the molecules are tilted by about $25 - 30^\circ$ with respect to the surface normal. Furthermore, the film is found to have domains with random in-plane orientation. Considering the deposition method of thermal evaporation onto a thermally grown SiO_2 surface, random in-plane orientation is expected.

In Figure 4.2(b), a peak splitting is observed with harmonics of $Q = 0.407$ Å^{-1} and $Q = 0.436$ Å^{-1}, which is equivalent to $d_{001} = 15.4$ Å and $d_{001} = 14.4$ Å. Attempts to relate the observed peaks to reported crystal structures of pentacene [Bri03, Mat01] showed that this splitting can be interpreted as being due to a coexistence of two phases. This is in agreement with other reports of vacuum deposited pentacene structures [Sch99]. The various crystal structures of pentacene are all similar in having two molecules per unit cell, rotated with respect to each other to form a herringbone-like arrangement. The

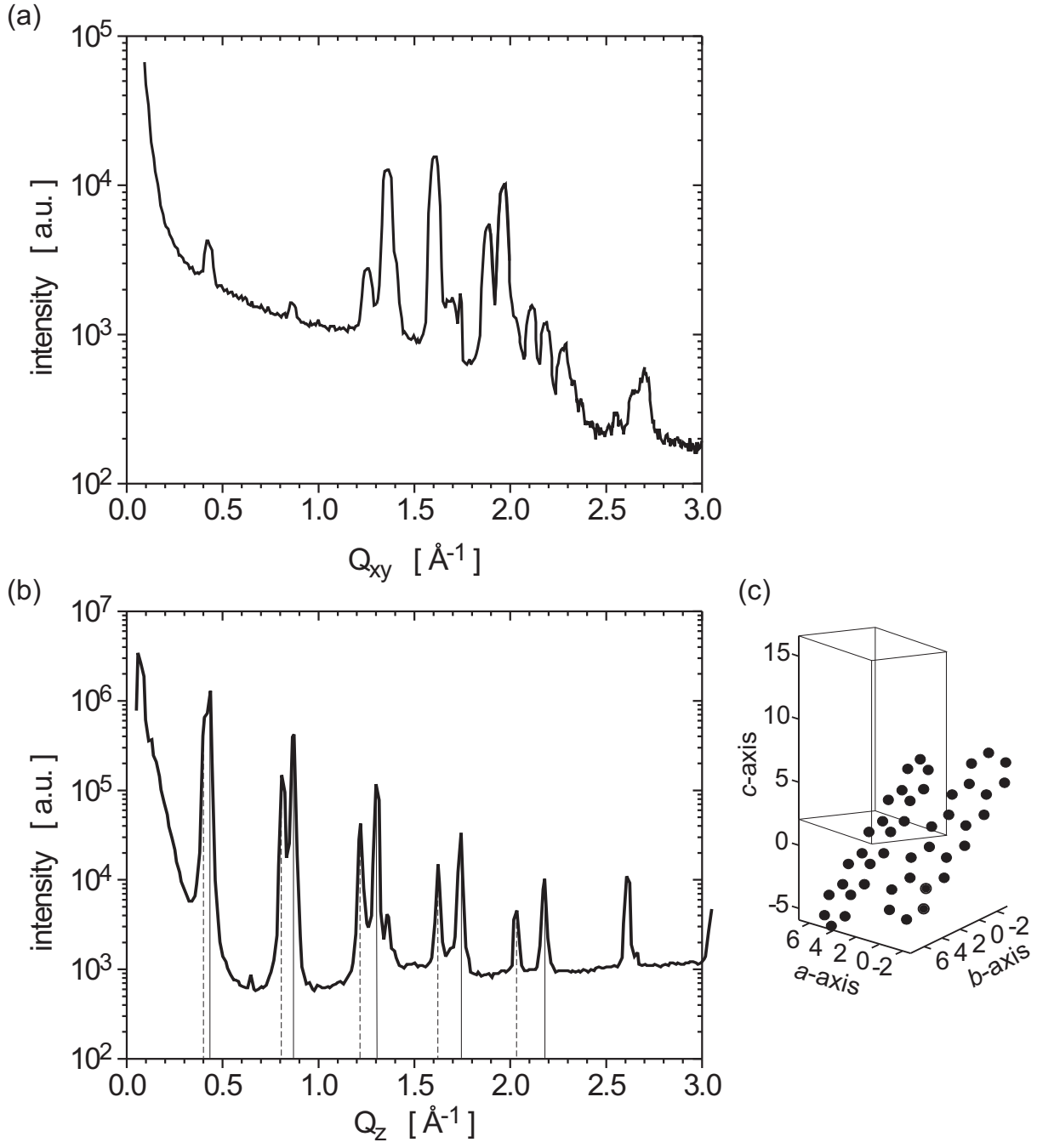

Figure 4.2: *In-plane (a) and out-of-plane (b) grazing-incidence X-ray diffraction pattern for a pentacene thin film deposited under standard conditions. The intensity is shown as a function of the in-plane and out-of plane component of the scattering vector Q. (c) Herringbone crystalline structure of pentacene.*

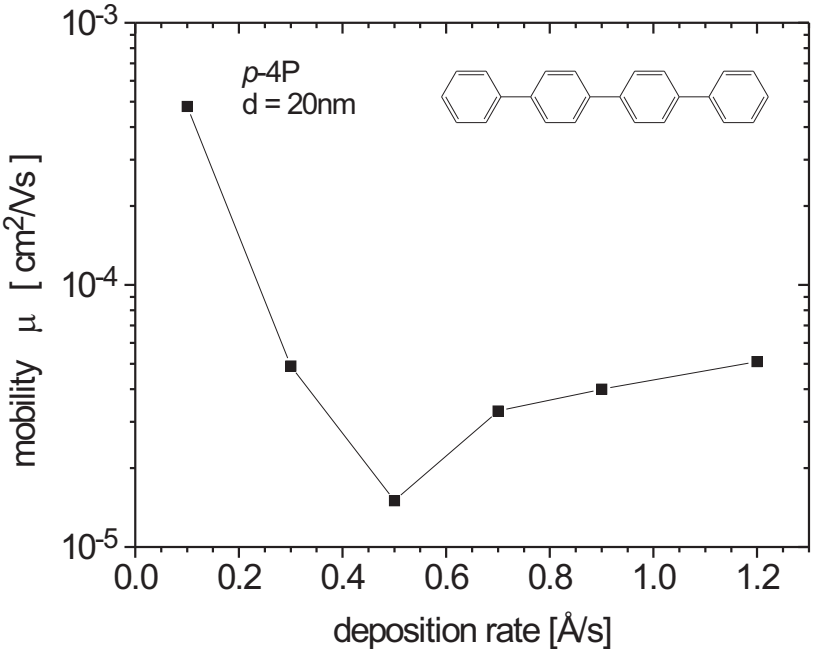

Figure 4.3: *Hole mobility in 20 nm thick p-4P films as a function of the deposition rate.*

corresponding model is given in Figure 4.2(c). In order to check, whether the pentacene thin film was partially oxidized, the diffractograms were also compared with the reported structure for 6,13-pentacene-quinone, however, no indication for oxidation could be found.

The hole mobility in *p*-4P was found to depend much stronger on substrate temperature and deposition rate then the one in pentacene. Thus, the hole mobility was measured in devices deposited at different deposition rates at a substrate temperature of 90 °C. The extracted field-effect mobility of holes was minimal for a deposition rate of 0.5 Å/s. This is most likely due to two competing processes: at a low deposition rate the films show a better crystallinity, at higher deposition rates, the substrate coverage is better.

Figure 4.4 shows AFM images of *p*-4P thin films of different thicknesses. The substrate temperature during evaporation was kept at 90 °C and the evaporation rate was 0.1 Å/s. Starting at 3 nm (a), well separated nucleation centers with a density of 10^7 cm^{-2} are observed. Increasing the nominal film thickness to 5 nm, the density of nucleation centers increases, but no significant growth in maximum thickness is noticed. Increasing the nominal film thickness further to 7 nm, the substrate coverage appears to be almost complete and a granular structure is observed, which is even denser at a film thickness of 50 nm.

Figure 4.5 shows the out-of-plane XRD pattern measured in-house of a *p*-4P thin film deposited under standard conditions. The film exhibits sharp diffraction peaks, indicating a high crystallinity of the vacuum-deposited thin film. Analysis of the peak-to-peak

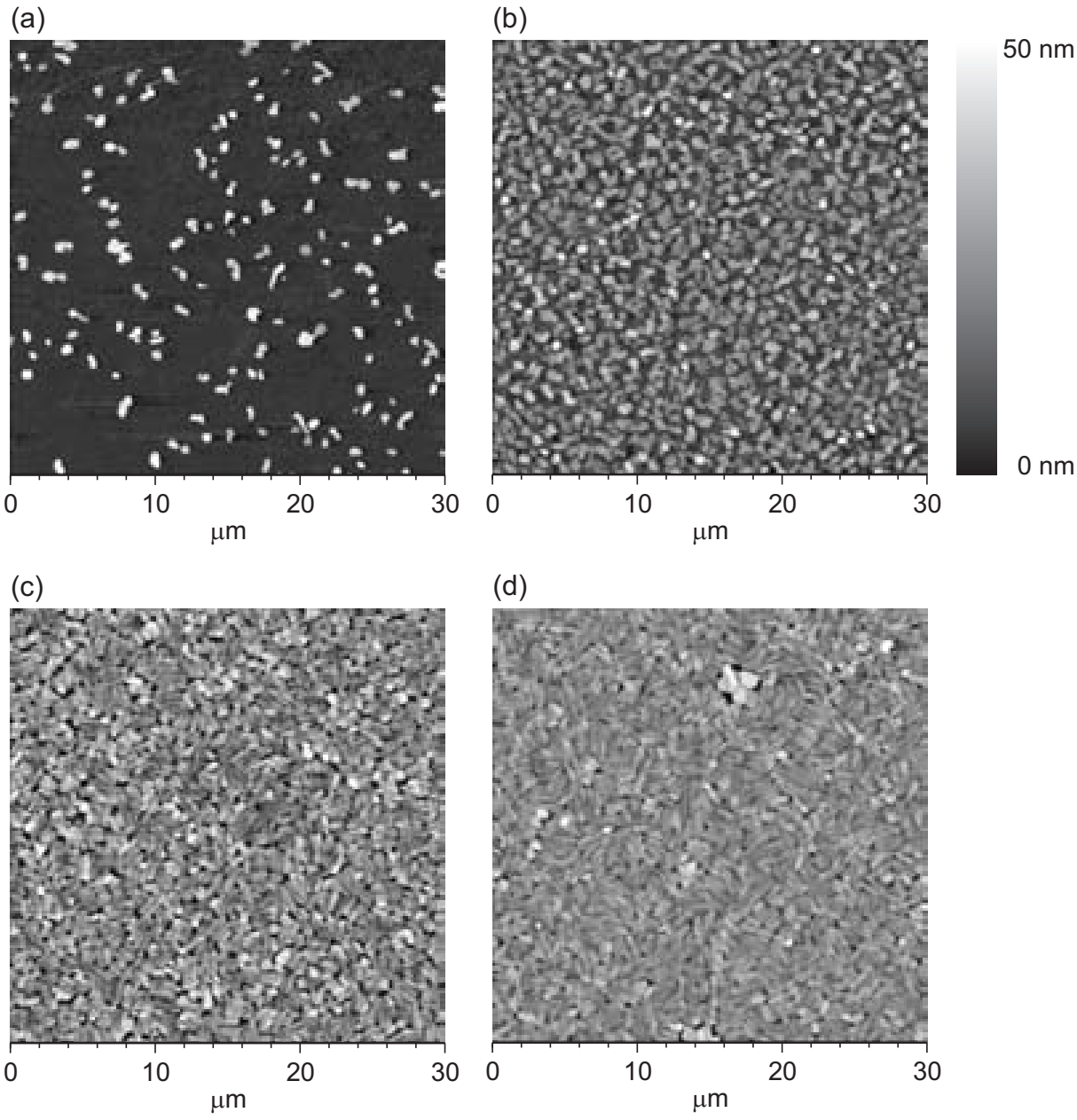

Figure 4.4: *AFM images of p-4P thin films on silicon oxide. The films have different nominal thicknesses of (a) 3 nm, (b) 5 nm, (c) 7 nm, and (d) 50 nm. The film growth starts from many nucleation islands and the film forms a granular structure. Therefore, it is assumed that the film close to the silicon interface has a high density of grain boundaries, resulting in trap states. The grey-scale bar quantifies the topology between 0 and 50 nm.*

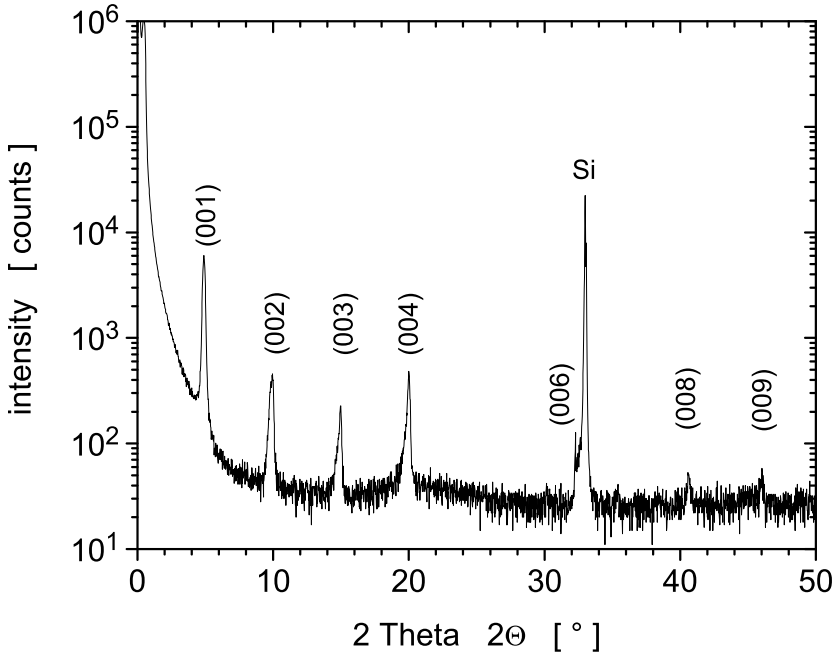

Figure 4.5: *Out-of-plane X-ray diffraction pattern of a p-4P thin film.*

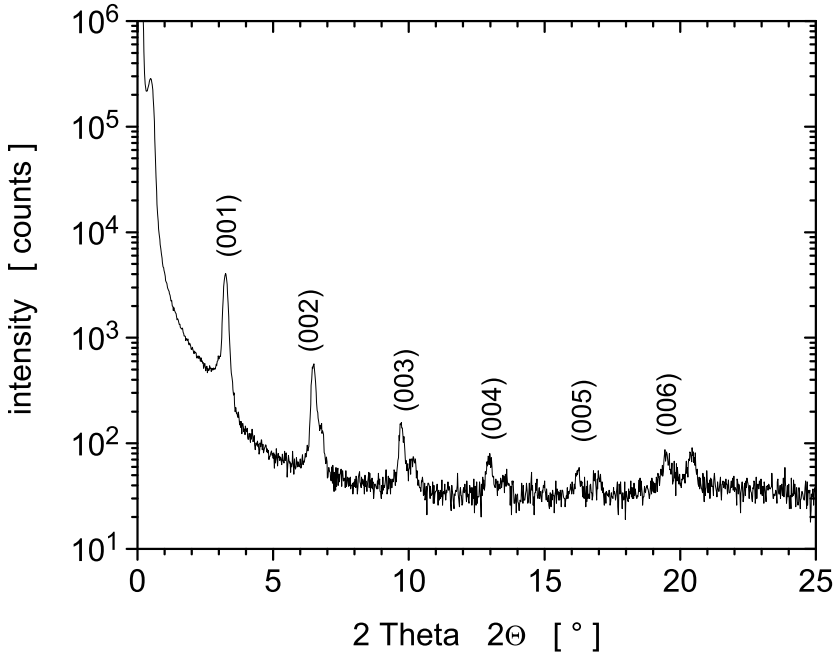

Figure 4.6: *Out-of-plane X-ray diffraction pattern of a p-6P thin film.*

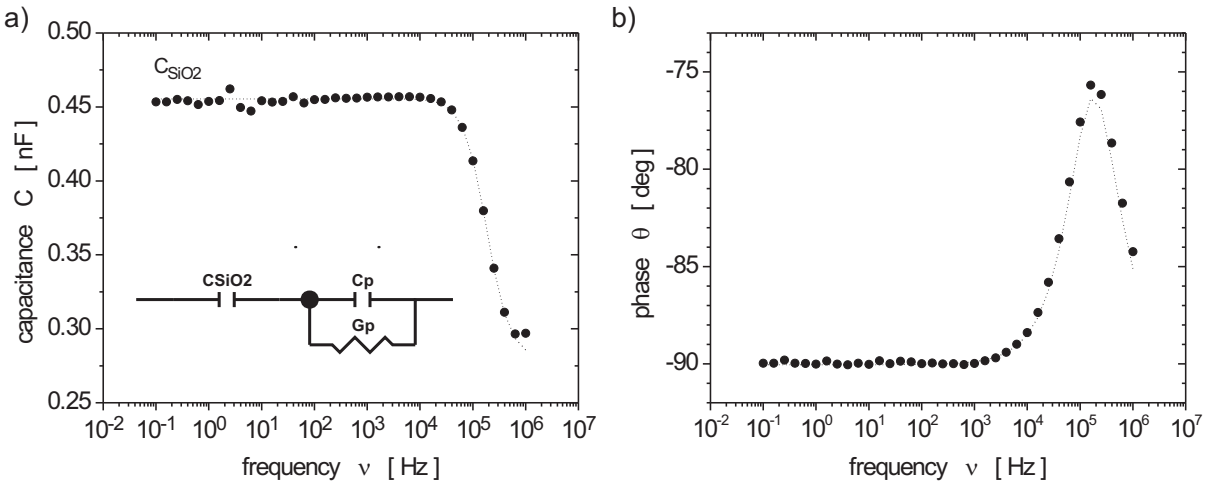

Figure 4.7: *Capacitance C and phase angle θ for the configuration Si/150 nm SiO_2/Au MOS diode. The contact area is 0.02 cm^2.*

spacing reveals a 2θ periodicity of 5.14°, which is equivalent to a lattice parameter of 17.67 Å in the (00l) direction. This value is in good agreement with previously reported cell parameters for the monoclinic unit cell of p-4P: a = 8.11 Å , b = 5.61 Å , and c = 17.91 Å [Del76, Bau78]. In contrast, in the diffractogram of a p-6P thin film, as shown in Figure 4.6, peak-splitting is observed, which indicates the coexistence of two phases, as it is also reported in [Gun97]. The 2θ periodicity is 3.24° and 3.40° with corresponding lattice parameters in the (00l) direction of 27.27 Å and 25.99 Å, respectively. These values are in good agreement with the reported d_{00l} spacing of 26.22 Å in p-6P single crystals [Gun97]. The results show that the molecules are oriented with the long axis perpendicular to the substrate surface.

4.2 Charge-Carrier Injection by CV-Measurements

In order to determine, whether an organic semiconductor is p-type, n-type or ambipolar, i.e. whether holes as well as electrons are transported, MIS diodes were studied by means of frequency- and bias-dependent impedance spectroscopy. Analyzing the capacitance as a function of the applied dc bias reveals, whether holes or electrons are accumulated at the insulator interface. Frequency-dependent studies give information about the dynamics.

Before the charge-carrier accumulation in organic thin films was studied by impedance spectroscopy, the capacitance of the Au contacted Si/150 nm SiO_2 substrate was measured, as shown in Figure 4.7, in order to account later for eventual artifacts. For low frequencies, the capacitance and the phase angle is constant at about 0.46 nF and −90°. However, for frequencies $\geq 10^4$ Hz, the capacitance is decreasing with increasing fre-

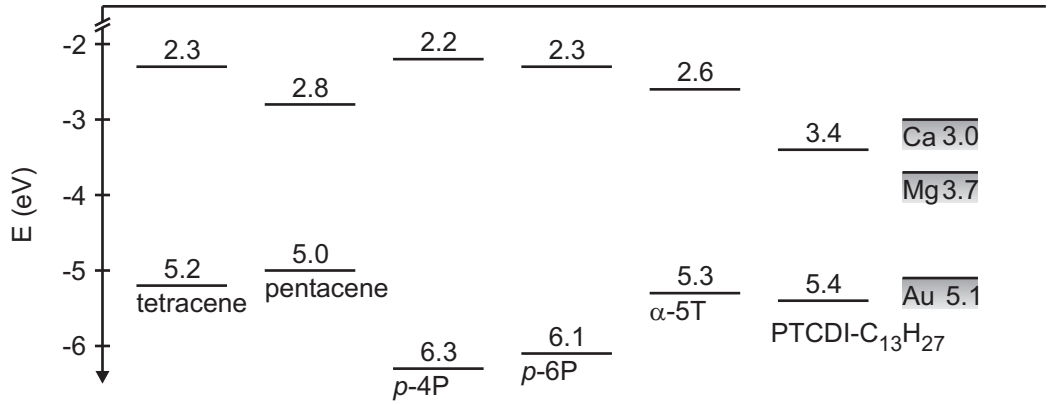

Figure 4.8: *HOMO and LUMO position of the organic materials tetracene, pentacene, p-4P, p-6P, α-5T and PTCDI-$C_{13}H_{27}$ together with the work function of metals used as source and drain contact: Au, Mg and Ca.*

quency and the phase value increases, having a maximum of $-75°$ at a frequency of 10^5 Hz. According to [Sze81] this behavior can be attributed to interface-trap charges at the silicon/silicon oxide interface and is modelled by the basic equivalent circuit shown in the inset of Figure 4.7(a). Hereby, C_{SiO2} is the SiO_2 capacitance and the frequency-dependent capacitance C_p and conductance G_p are associated with interface-traps. The simulated oxide capacitance C_{ox} is 4.54×10^{-10} F. This is in good agreement with the geometrical capacitance of 4.6×10^{-10} F calculated from a contact area of $A = 0.02$ cm^2 and a SiO_2 thickness of $d_{ox} = 150$ nm.

4.2.1 Influence of Contact Metal

Figure 4.8 shows the HOMO and LUMO position of organic hole-transport materials together with the work function of different contact metals. The data correspond to the values given in Table 1.1. The work function of Au seems to be suitable for hole injection into oligoacenes and oligothiophenes, an injection barrier is expected in case of combination with oligophenyls. Furthermore, Au appears to be not very well suited for electron injection into these materials. Alternative contact metals are Ca and Mg due to their low work function. The disadvantage of Ca is its fast oxidation, thus demanding for inert conditions. Mg appeared to have a low sticking coefficient on most organic materials and only on PTCDI-$C_{13}H_{27}$ top contacts could be formed.

For impedance spectroscopy, thermally evaporated pentacene thin films were structured by a shadow mask to yield 2×2 mm^2 pads which were top-contacted either by Au or Ca and measured without exposure to oxygen. The contact pad of 1×2 mm^2 was arranged in a way that 3/4 of its area covered the organic thin film and 1/4 was in direct contact with the SiO_2 insulator. The resulting capacitances were determined solely by the

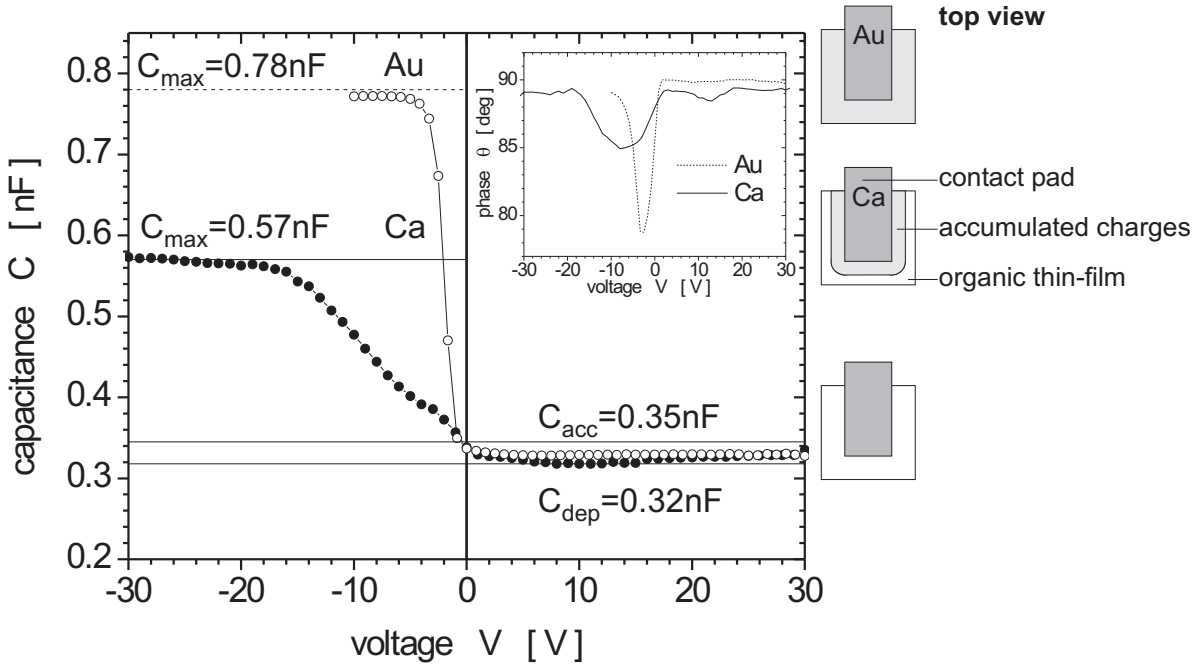

Figure 4.9: *Device capacitance as a function of applied bias voltage for pentacene with Au and Ca contacts. The inset shows the corresponding phase. C_{dep} is the depleted capacitance, C_{acc} is the capacitance measured for accumulated charge carriers below the contact pad, and C_{max} the maximum capacitance, corresponding to accumulated charges within the complete organic thin film. For further details see also Section 3.2.1.*

sample geometry, layer thicknesses and the dielectric constant according to Section 3.2.1. Here, for charge carriers accumulated below the contact pad an overall capacitance of $C_{acc} = 0.35$ nF is expected. In case of depletion, i.e. no charge carriers are injected, the capacitance is composed of the two parallel capacitances of the organic thin film and in series with the gate oxide below the organic thin film and the capacitance of the gate oxide below the overlapping contact pad. With the pentacene thin-film thickness of 20 nm, a depleted capacitance $C_{dep} = 0.32$ nF is expected.

Results

Figure 4.9 shows the capacitance as a function of applied bias between −30 and +30 V measured at a frequency of 1 Hz. For positive voltage, the capacitance is almost independent of the applied voltage and the contact metal. The measured value of 0.33 nF is in between the theoretically predicted depletion and accumulation capacitances. For negative bias voltage, the capacitance increases with increasing $|V_{bias}|$ and saturates. The maximum value of the capacitance is different for Au and Ca, whereas the onset of the increase is independent of the applied contact metal. The maximum capacitance obtained

contact metal	C_{max} [nF]	A_{tot} [cm^2]	d_{spread} [μm]	Q_{acc} cm^{-2}	$d_{average}$ [nm]
Au	0.78	0.045	500	5.8×10^{11}	13.1
Ca	0.57	0.033	290	1.8×10^{12}	7.4

Table 4.1: *Extracted values of maximum capacitance C_{max}, effective device area A_{tot}, spread distance for accumulated charge carriers d_{spread}, accumulated charge density Q_{acc} and average distance between accumulated charges $d_{average}$.*

for the Au contact is $C_{max} = 0.78$ nF and for the Ca contact $C_{max} = 0.57$ nF. The polarity indicates that the accumulated charges are holes.

The phase as a function of the applied bias voltage is shown in the inset of Figure 4.9. For the Au contact and positive bias, a purely capacitive behavior is observed, whereas for negative bias in the region of increasing capacitance the phase decreases, indicating a transition to conductive mode. As soon as the capacitance saturates, the device acts again purely capacitively. Thus, the increase of capacitance can be associated with a charging current. For the Ca contact, the capacitance shows a minimum for both negative and positive bias voltage. The minimum at negative voltage occurs at a larger bias than for the Au contact.

Discussion

The accumulation of holes is concluded from the increase of the capacitance with negative applied bias voltage. Since the measured capacitance exceeds the accumulated capacitance given by the size of the contact pad, it is assumed that charge carriers spread within the organic thin film, which is larger than the contact pad, and thus increase the effective area of the capacitor. It should be noted that the counter electrode formed by the highly doped silicon wafer is unstructured and therefore not limiting the device area. The maximum capacitance is therefore given by $C_{max} = \epsilon\epsilon_0 \cdot A_{tot}/d_{ox}$ and the total device area A_{tot} is derived from data to 0.045 cm^2 and 0.033 cm^2 for Au and Ca, respectively. For Au, the area corresponds to the overall device area composed of the organic thin film and the overlapping contact pad. Therefore, it can be concluded that charge carriers are accumulated over the complete organic thin film. In case of Ca, the area is smaller than the overall device area. Assuming a constant accumulated charge carrier density, the maximum spread distance d_{spread} for charge carriers is calculated to be 290 μm. The corresponding area is shaded light grey in the schematic top-view drawing of Figure 4.9.

Using the relation $C = Q/U$ the accumulated charge at the onset of saturation is estimated and used in conjunction with the effective device area to determine the average distance between accumulated charges. The resulting data are summarized in Table 4.1.

In case of Ca, an additional minimum in capacitance is observed at a bias voltage of 11 V, which is also reflected in a minimum of the phase, similar to the phase minimum for negative voltage and hole accumulation. Thus, it can be treated as indication for electron injection. The measured capacitance does not exceed C_{acc}, thus the injected electrons are only accumulated below the contact pad and do not spread laterally in the organic thin film. This effect could be only observed in films which where measured without exposure to oxygen. The observation of electron accumulation in pentacene is also reported in [Mei03].

4.2.2 Frequency-Dependent Capacitance

Results

Figure 4.10 shows the capacitance and phase of a Au/45 nm pentacene/150 nm SiO_2/n^+-Si MOS capacitor as a function of bias voltage between -40 and $+40$ V for different frequencies between 10^{-1} and 10^3 Hz and as a function of frequency between 10^{-1} and 10^6 Hz for several discrete bias voltages. In the voltage scan the capacitance is frequency-independent for positive bias voltage larger 35 V and shows a constant value of 3.8×10^{-10} F. At lower bias voltage, the capacitance is frequency dependent and its value is increasing with decreasing frequency. A first level of saturation is observed at a capacitance of 4.6×10^{-10} F, which corresponds to the geometric capacitance of the silicon oxide layer below the contact pad. Decreasing the bias voltage further below 0 V, a second level of saturation is observed at 1.04 nF for frequencies between 10^{-1} and 10^1 Hz. For higher frequencies, the capacitance increases for bias voltages below -5 V, but does not reach the saturation level of 1.04 nF. The corresponding phase shows pure capacitive behavior for bias voltages larger than 35 V. For bias voltages between 35 and 0 V, it shows a first minimum and for bias voltages between 0 and -40 V a second minimum. The positions of the minima coincide with the maximum slope of capacitance. The minimum in the phase is attributed to a resistive component in the device, i.e. the device does not react purely capacitive anymore. This can be interpreted as a charging process of the capacitor.

Considering the frequency scan in Figure 4.10(b), the capacitance is voltage-independent for frequencies larger than 10^5 Hz, with a value of 2.7×10^{-10} F. For lower frequencies, the capacitance increases and saturates in dependence on the applied bias voltage at three different levels at 3.8×10^{-10} F, 4.6×10^{-10} F and 1.04 nF. The increase in capacitance is strongest for an applied gate voltage of -40 V and decreasing with increasing bias voltage. Also in the frequency scan the corresponding phase is purely capacitive for saturated capacitances and shows a minimum for maximum slope in the capacitance. It should be noted that the voltage independent level at 2.7×10^{-10} F for high frequencies is also observed in the voltage scan. However, in order to increase the visibility within the phase

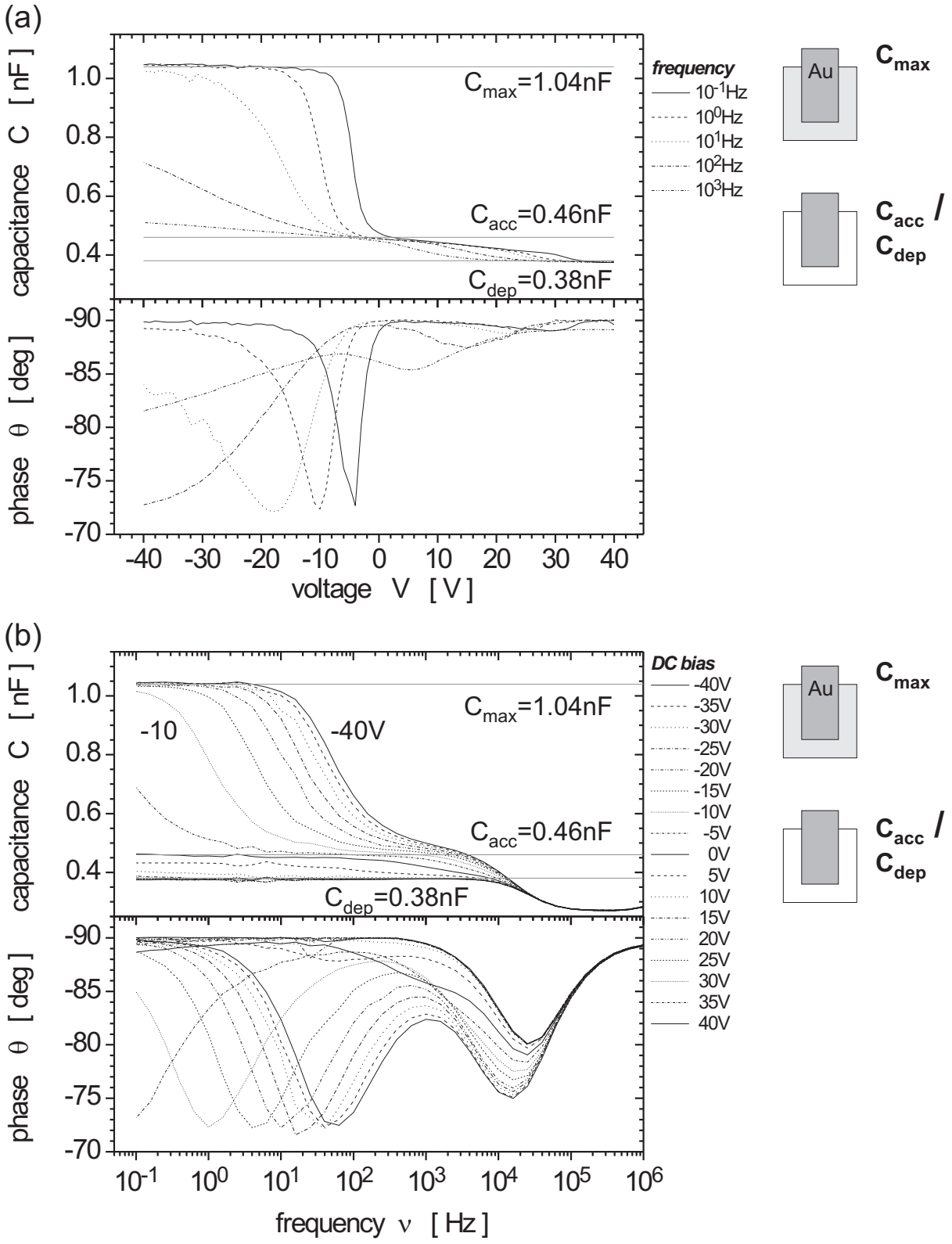

Figure 4.10: *Capacitance and phase versus frequency and voltage for a pentacene MIS diode with an oxide thickness d_{ox} = 150 nm and an organic thin-film thickness of d_{org} = 45 nm. C_{dep} is the depleted capacitance, C_{acc} is the capacitance measured for accumulated charge carriers below the contact pad, and C_{max} the maximum capacitance, corresponding to accumulated charges within the complete organic thin film. For further details see also Section 3.2.1.*

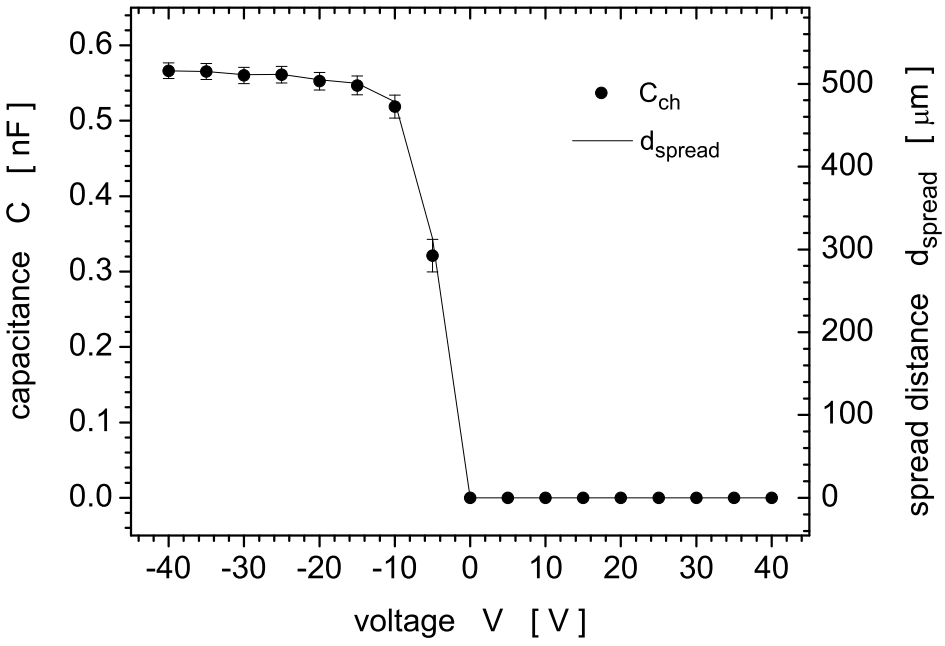

Figure 4.11: *Channel capacitance C_{ch} (symbols with corresponding error bars) and spread distance d_{spread} (line) as function of the applied bias voltage for the pentacene MIS diode with an oxide thickness d_{ox} = 150 nm and an organic thin-film thickness of d_{org} = 45 nm.*

diagram, the data for frequencies larger 10^3 have been omitted.

Discussion

The data of the frequency-dependent scan can be fitted for each applied bias voltage using the equivalent circuit introduced in Section 3.2.1. The voltage-independent capacitance of 2.7×10^{-10} F is attributed to to interface traps as discussed before and is taken into account for modelling the device by considering an additional parallel RC-circuit as shown in Figure 4.7. It is applied in series to the equivalent circuit of the organic MIS diode. The obtained channel capacitance and spread distance of charge carriers as a function of the applied gate voltage is shown in Figure 4.11. The onset of channel formation is at 0 V with an increase for negative gate bias. The maximum capacitance is reached at a bias voltage of -15 V. The maximum spread distance d_{max} obtained from the fitted data is 520 μm, which is slightly larger than the maximum spread distance according to the sample geometry, which is 500 μm. Here, it has to be noted that for the extraction of d_{spread} from the experimentally derived capacitance C an infinite organic thin film is assumed. Thus, the geometry of the additional contact area A_{ch} is not angular but shows round corners. In case of charge accumulation all over the limited contact pad, that model does not hold any more, due to charge accumulation also at the angular corners of the

material	μ **[cm^2/Vs]**
pentacene	1.3×10^{-1}
tetracene	3.4×10^{-3}
p-6P	1.9×10^{-2}
p-4P	2.5×10^{-4}
α-5T	1.1×10^{-2}
α-4T	4.0×10^{-5}
PTCDI-$C_{13}H_{27}$	4.9×10^{-3}

Table 4.2: *Charge-carrier mobility μ for the hole-transport materials pentacene, tetracene, p-6P, p-4P, α-5T, α-4T and the electron-transport material PTCDI-$C_{13}H_{27}$.*

organic thin film. Therefore, the extracted spread distance is slightly larger than the actual one.

Not shown are the data for the oligophenyls and oligothiophenes, for which also hole accumulation was observed. In PTCDI-$C_{13}H_{27}$ MIS diodes, electron accumulation was observed for both Mg as well as Au contacts.

4.3 Transport Properties at Room Temperature

4.3.1 Charge-Carrier Mobility

Single layer OFETs were prepared in order to extract the charge carrier mobility of the hole and electron-transport materials. Figure **??** shows the output and transfer characteristic of a single-layer pentacene transistor with symmetrical Au top contacts. The output characteristic, i.e. the drain current I_D as a function of drain-source voltage V_{DS}, exhibits a linear increase of $|I_D|$ vs. $|V_{DS}|$ for small $|V_{DS}|$ and a saturation region for large $|V_{DS}|$. The characteristics show a typical behavior with I_{Dsat} scaling quadratically with V_G. From the transfer characteristic, i.e. the square root of I_D as a function of V_G, a hole mobility of 0.13 cm^2/Vs can be extracted from the saturated drain current. The threshold voltage V_T is -43 V, and an on/off current ratio larger than 10^4 is obtained.

Typical output and transfer characteristics for OFETs prepared of tetracene, *p-4P*, *p*-6P, α-4T, α-5T and PTCDI-$C_{13}H_{27}$ are shown in Appendix A. The extracted field-effect mobilities for these materials are summarized in Table 4.2.

4.3.2 Influence of Contact Metal

Tetracene OFETs have been prepared using Au and Ca top contacts. Figure 4.13 shows the output characteristic of a tetracene OFET with Au and Ca top contacts. Both devices

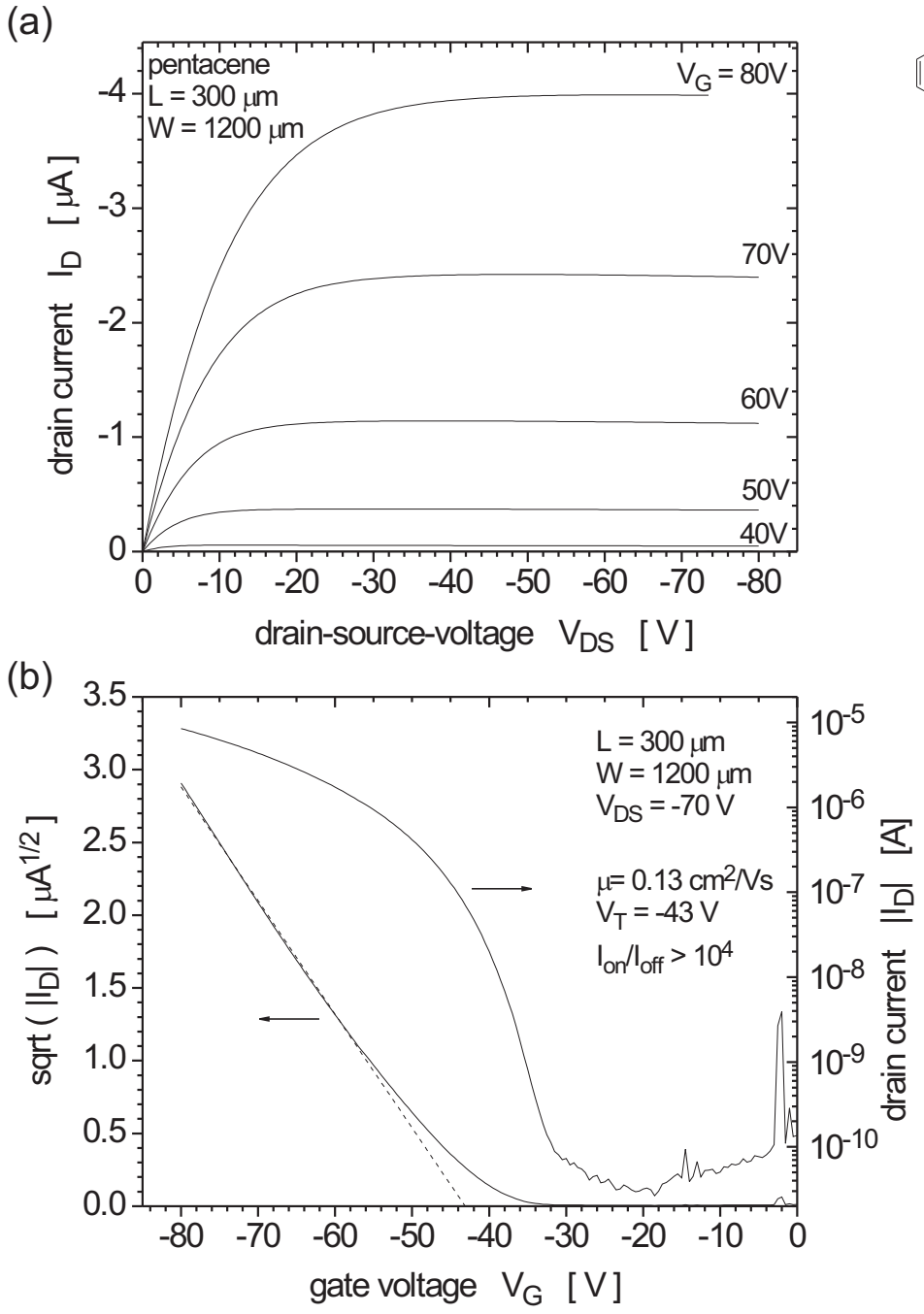

Figure 4.12: *(a) Output and (b) transfer characteristics of a 45 nm pentacene transistor with Au top contacts.*

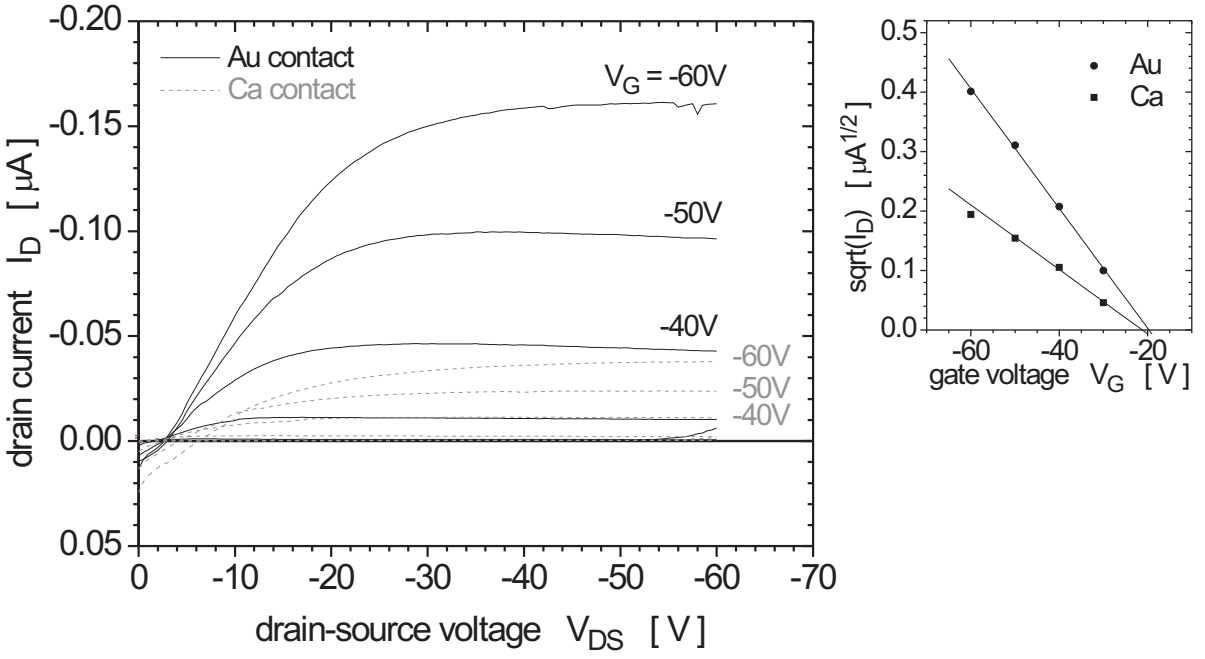

Figure 4.13: *Output characteristic for a tetracene OFET with Au and Ca top contacts. The inset shows the saturated drain current versus the threshold voltage (symbols) together with its linear fit (line).*

show a typical *p*-channel characteristic, however, the current density at equivalent bias voltage is lower for the device with Ca source contact. The inset shows the square root of the drain current in saturation for both devices. From the linear fit the threshold voltage can be derived to $V_T = 20(2)$ V for Au and $V_T = 21(4)$ V for Ca source contact. Due to the large error range, both values have to be treated as practically identical, i.e. the onset of current is independent of the contact metal. This result is in good agreement with the CV measurements using Ca and Au as hole injecting contact. Here, the onset of capacitance increase was also independent of the applied voltage. However, due to a larger contact resistance, the effective applied gate voltage is reduced and the saturated drain current decreases. This effect of source contact resistance on the saturated drain current has been described theoretically in [Sch03]. As a result, the extracted field-effect mobility is below the actual value, which is as an intrinsic material property independent of source and drain contact metal. It cannot be excluded that also Au does not form a purely ohmic contact, thus in case of contact resistances the extracted field-effect mobility is always smaller than the actual mobility, except the extracted mobility is corrected for the contact resistance.

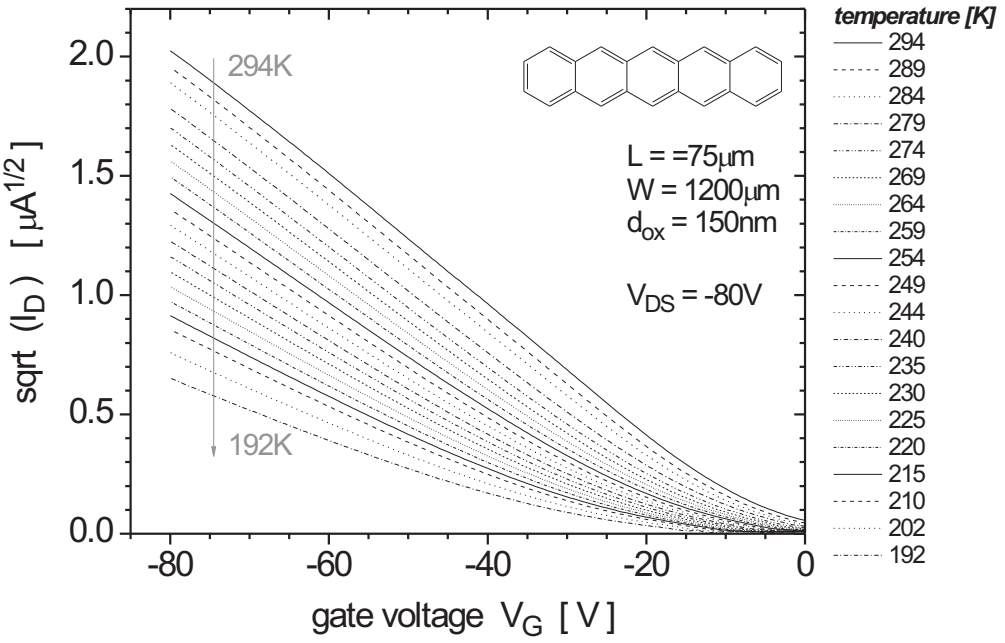

Figure 4.14: *Temperature dependence of the drain current at a drain-source voltage V_{DS} = -80 V for a pentacene OFET.*

4.4 Temperature-Dependence of Charge-Carrier Mobility

Figure 4.14 shows the transfer characteristic of a pentacene OFET at a drain-source voltage of $V_{DS} = -80$ V for temperatures ranging from 294 to 192 K. The square root of the drain current, which is decreasing with decreasing temperature, is plotted as a function of the gate voltage, allowing the extraction of field effect mobility and threshold voltage. Furthermore, the threshold voltage is shifted from $V_T = -4$ V at 294 K to $V_T = -28$ V at 192 K. A similar shift was also observed in other pentacene devices measured with decreasing temperature. In order to clarify whether the threshold voltage shift is simply due to degradation occurring with measurement repetition, the device was also characterized with increasing the temperature, i.e. starting at low temperatures. Here, the observed threshold voltage showed a positive shift of only 3 V, i.e. the shift occurred in the opposite direction, however, was nearly negligible. Thus it can be concluded that the observed shift in threshold voltage is a combination of degradation and temperature-dependent effects. In PTCDI-$C_{13}H_{27}$ OFETs, such a temperature dependence of the threshold voltage was not observed.

The extracted field effect mobility of the pentacene OFET is shown on a semi-logarithmic scale in Figure 4.15 as a function of the inverse temperature. At room temperature, the

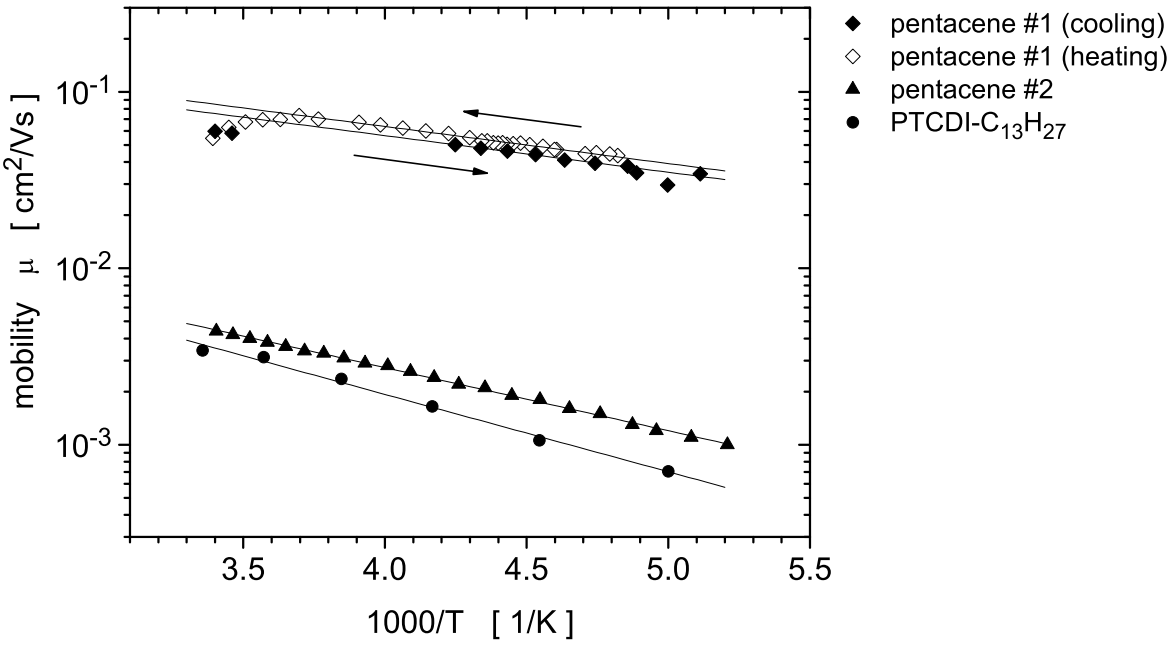

Figure 4.15: *Temperature dependence of the charge carrier mobility in pentacene and PTCDI-$C_{13}H_{27}$.*

device exhibits a hole mobility of 4.4×10^{-3} cm^2/Vs. Additionally, the data of a pentacene OFET exhibiting higher room temperature hole mobility (6×10^{-2} cm^2/Vs) and a PTCDI-$C_{13}H_{27}$ OFET are shown versus the inverse temperature. The room temperature electron mobility in PTCDI-$C_{13}H_{27}$ is 3.4×10^{-3} cm^2/Vs. All devices show a decrease of the extracted field-effect mobility with decreasing temperature. The activation energy of such a thermally activated process is described by the following equation [Hor98]:

$$\mu = \mu_0 exp(-E_a/kT) \tag{4.1}$$

and E_a is typically ascribed to trap states.

The values obtained for μ_0 and E_a are summarized in Table 4.3. The activation energy E_a and mobility pre-factor μ_0 for the high-mobility pentacene device (pentacene#1) were reproducible, independently of the scan direction. Comparing the pentacene#1 and #2 devices, the one with the higher hole mobility at room temperature shows the smaller activation energy, which is an expected result for the association of the activation energy with trap levels. The electron-transport material PTCDI-$C_{13}H_{27}$ exhibits the largest activation energy.

material	E_a [meV]	μ_0 [cm^2/Vs]
pentacene#1	41	0.38
pentacene#1	42	0.44
pentacene#2	71	0.07
PTCDI-$C_{13}H_{27}$	87	0.11

Table 4.3: *Activation energy and mobility prefactor μ_0 for the hole-transport material pentacene and the electron-transport material PTCDI-$C_{13}H_{27}$.*

4.5 Conclusion

Vacuum-deposited thin films of pentacene, *p*-4P and *p*-6P are polycrystalline. For pentacene, a perpendicular orientation of the molecules with respect to the substrate surface was found.

Au as well as Ca can be used to inject holes into pentacene thin films. The charge-carrier injection is more effective for Au, which results in a larger average spread distance of the accumulated charge carriers within the organic thin film. Furthermore, for Ca, indications of electron injection could be found; however, charges are accumulated only below the contact and thus, no channel is formed. Similarly, both Mg and Au can be used for electron injection into PTCDI-$C_{13}H_{27}$.

Functioning *p*-type OFETs based on tetracene could be demonstrated with both Au as well as Ca contacts. The increased contact resistance due to the injection barrier in the case of Ca leads to a lower saturated drain current for equal gate voltage. Thus, the extracted field-effect mobility is lower than the actual value. The threshold voltage is not influenced significantly by the injection barrier.

Temperature-dependent measurements revealed that the charge-carrier mobility is a thermally activated process: Both the hole mobility in pentacene as well as the electron mobility in PTCDI-$C_{13}H_{27}$ increase with increasing temperature, thus confirming that the model of hopping transport rather than band-like transport can be applied.

Chapter 5

Ambipolar Organic Field-Effect Transistor

Organic bilayer heterostructure FETs are presented as model structure for ambipolar transport, i.e. simultaneous *p*- and *n*-channel formation. The bilayer is prepared by subsequent evaporation of a hole-transport and an electron-transport material. The ambipolar transport characteristic is studied for different hole-transport materials, i.e. pentacene, *p*-4P [1], and α-5T [2] combined with the electron-transport material PTCDI-$C_{13}H_{27}$ [3]. The hole-transport materials differ in their HOMO-LUMO gaps and hole mobilities. Thus, the influence of different hole mobilities and contact resistances on the ambipolar characteristic is investigated. Au and Mg are used as injecting contacts, and the device characteristics are studied in forward and reverse bias, i.e. the characteristics of almost ohmic contacts and non-ohmic contacts are compared. Finally, two approaches for the theoretical simulation of the ambipolar current characteristic are introduced: an analytical model based on a modified version of the Schockley equation and a numerical calculation based on the drift-diffusion model.

5.1 Pentacene/PTCDI-$C_{13}H_{27}$ OFET

The preparation of a bilayer heterostructure consisting of the hole-transport material pentacene and the electron-transport material PTCDI-$C_{13}H_{27}$ leads to an OFET with pronounced ambipolar current-voltage characteristic, i.e. simultaneous *p*- and *n*-channel formation. An OFET structure is investigated that has been optimized for efficient charge-carrier injection by selecting Mg top and Au bottom contacts for injection of electrons and holes into the PTCDI-$C_{13}H_{27}$ and pentacene layers, respectively. This device architecture

[1] *para*-quaterphenyl
[2] α-quinquethiophene
[3] N,N'-ditridecylperylene-3,4,9,10-tetracarboxylic diimide

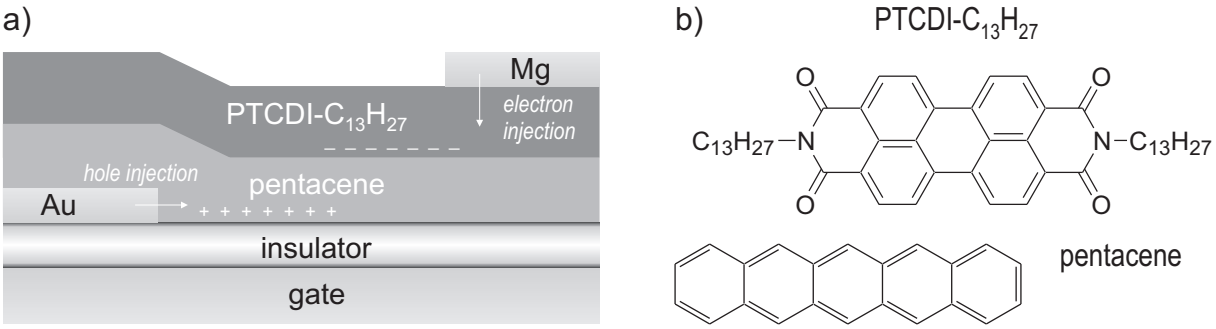

Figure 5.1: *(a) Schematic drawing of a bilayer heterostructure organic field-effect transistor combining 40 nm pentacene and 50 nm PTCDI-$C_{13}H_{27}$. A highly doped silicon wafer is used as substrate and gate contact, with 130 nm thick thermally grown SiO_2 layer as gate insulator. The device is bottom-contacted by Au (30 nm) and top-contacted by Mg (50 nm). (b) Molecular structure of PTCDI-$C_{13}H_{27}$ and pentacene. Reprinted from [Ros04a].*

serves as a model structure for ambipolar field-effect transistors, which are regarded as a requirement for efficient light-emitting field-effect transistors.

The schematic drawing of the pentacene/PTCDI-$C_{13}H_{27}$ bilayer heterostructure OFET together with the molecular structure of both organic semiconductors is shown in Figure 5.1. A heavily doped silicon wafer is used as substrate and gate contact, with a 130 nm thermally grown SiO_2 layer as gate insulator. Subsequently, a 30 nm Au contact for hole injection into pentacene, a 40 nm pentacene layer, a 50 nm PTCDI-$C_{13}H_{27}$ layer, and a 50 nm Mg top contact for electron injection into PTCDI-$C_{13}H_{27}$ have been thermally evaporated. The channel length and width are 140 μm and 2000 μm, respectively.

The energy levels of the highest occupied (HOMO) and the lowest unoccupied molecular orbital (LUMO) of pentacene and of PTCDI-$C_{13}H_{27}$ with respect to the work functions of Au and Mg are shown schematically as straight lines in Figure 5.2. The band diagram reflects only the situation between source and drain contact; the effect of the gate is not considered. The HOMO level of pentacene is 5.0 eV [Kar03], which is well-aligned with the work function of Au at 5.1 eV [Lid96], resulting in an efficient injection of holes into the pentacene layer. Mg was chosen for its work function of 3.7 eV [Lid96] to reduce the barrier for electron injection into the PTCDI-$C_{13}H_{27}$ LUMO level at 3.4 eV. The values for the relevant energy levels of PTCDI-$C_{13}H_{27}$ were estimated from [Hir95].

Results

As the device architecture itself is highly asymmetric with respect to source and drain electrodes and the two organic layers, it is necessary to differentiate not only between positive and negative gate bias, but also between the two cases of Au or Mg being defined as source contact. Figure 5.3 shows the transistor output characteristic of a heterostruc-

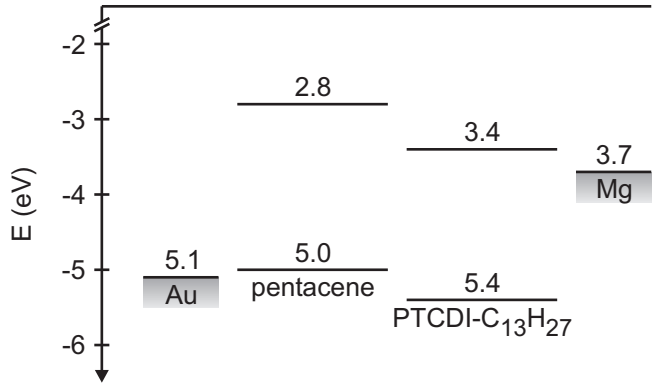

Figure 5.2: *Energy level diagram of HOMO and LUMO of pentacene [Kar03] and PTCDI-$C_{13}H_{27}$. The values for PTCDI-$C_{13}H_{27}$ are estimated values from [Hir95]. Also shown are the work functions of the two contact metals, Au and Mg [Lid96]. Reprinted from [Ros04a].*

ture transistor with the Au electrode biased as source (common) contact. The typical voltage range for gate and drain-source bias was ±50 V. Applying a negative gate bias V_G, typical *p*-channel characteristic is observed for negative drain-source voltages with $|V_{DS}| \leq |V_{onset}|$ as shown in Figure 5.3(a). For $|V_{DS}| > |V_{onset}|$ a steep increase in the drain current is observed, which is reproducible and not observed in the corresponding gate current. From the characteristic, the following empirical relation for V_{onset} is obtained: $V_{onset} \simeq V_G - 10$ V.

The drain current I_D for positive gate bias applied relative to the Au source contact is shown in Figure 5.3(b). For gate voltages between 0 and 10 V, the drain current increases with a positive curvature and shows no saturation. For gate voltages $V_G \geq 15$ V and small V_{DS} with $V_{DS} \leq V_{onset}$ the characteristic behaves like an *n*-channel device with a linearly increasing and saturating drain current. For $V_{DS} \geq V_{onset}$, again a pronounced increase of the drain current is observed. The magnitude of that additional current decreases with increasing V_G. The scale for the drain current in Figure 5.3(b) is two orders of magnitude lower than in (a).

The transistor output characteristic with Mg defined as source (common) contact and positive gate bias is shown in Figure 5.4(a). For $V_G \geq 15$ V, typical *n*-channel characteristic is observed, i.e. the magnitude of the saturated drain current I_D increases linearly with increasing V_G and saturates for $V_{DS} \geq V_{Dsat}$, as expected for normal transistor output characteristic. However, for $V_G \leq 10$ V, a pronounced increase of the drain current with increasing V_{DS} for large drain-source voltage values is observed. The current increases with decreasing V_G, and for $V_G \leq 5$ V no contribution of linearly increasing and saturating current is observed for small drain-source voltage V_{DS}.

Applying a negative gate bias $|V_G| \geq 10$ V with respect to the Mg source contact, the observed characteristic is typical for *p*-channel device operation, even though the

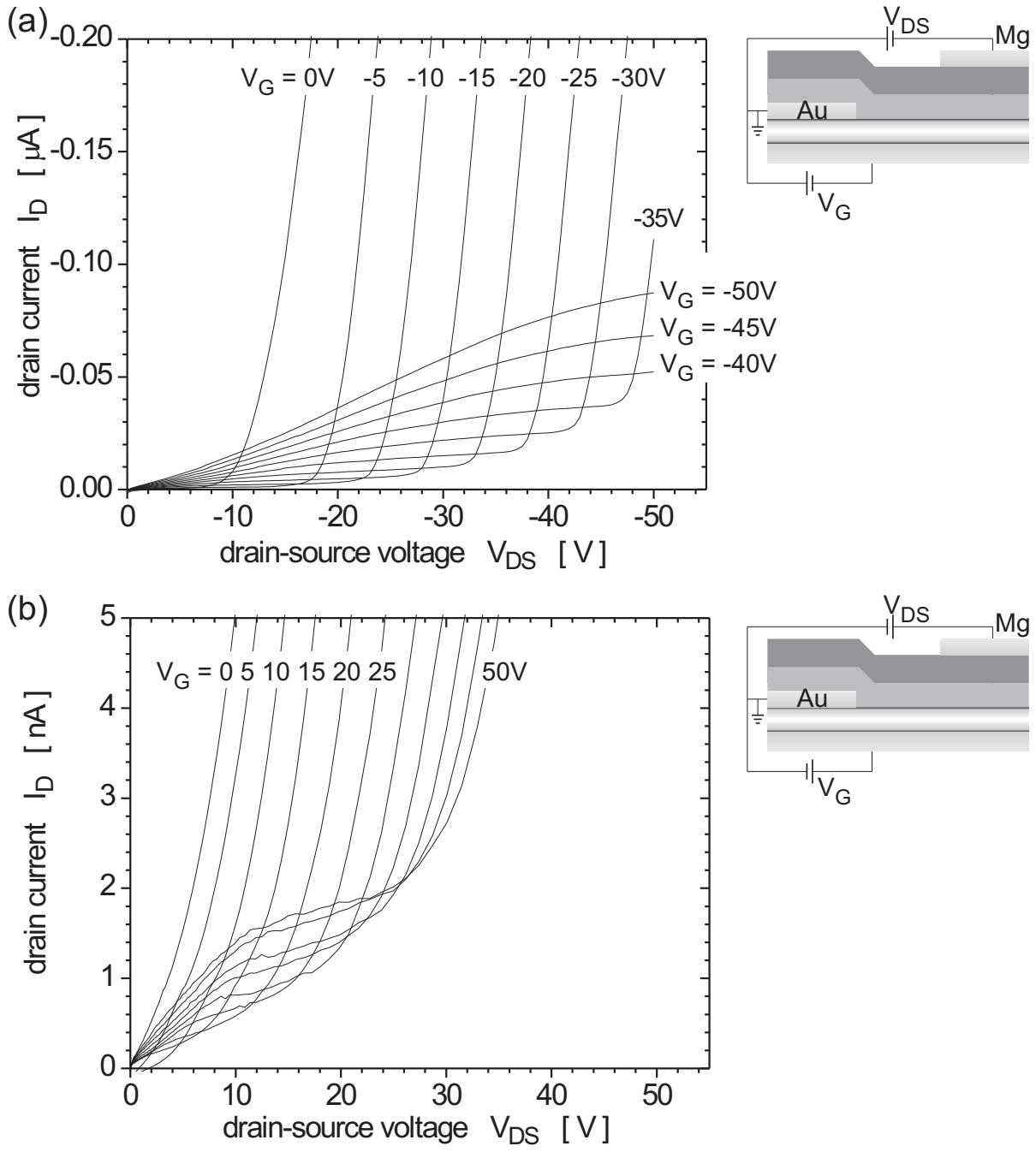

Figure 5.3: *Output characteristics of a pentacene/PTCDI-$C_{13}H_{27}$ bilayer heterostructure transistor with the Au electrode defined as source contact. The gate is biased (a) negative and (b) positive. The drain current is shown in μA and in nA for these two cases, respectively. Reprinted from [Ros04a].*

current increase for small $|V_{DS}|$ shows a rather positive curvature instead of being linear. The current increases with increasing gate bias and saturates for large V_{DS}, as shown in Figure 5.4(b). A tendency of saturation is observed for gate voltages with $|V_G| \leq 30$ V. For $|V_G| \geq 35$ V saturation occurs beyond the measurement range of $|V_{DS}| \leq 50$ V. For small negative V_G with $|V_G| \leq 5$ V, the additional current increase with positive curvature is observed for large $|V_{DS}|$. The current increases with decreasing $|V_G|$, resulting in a crossing of the $V_G = 0$ V and $V_G = -5$ V curves. Thus, in reverse-biasing the ambipolar characteristic is maintained, even though the current density is much lower.

Discussion

All four contact configurations of the pentacene/PTCDI-$C_{13}H_{27}$ bilayer heterostructure OFET show in the transistor characteristic additionally to the typical current increase and saturation an increase in drain current for large $|V_{DS}|$. In Figure 5.3(a), the typical *p*-channel characteristic for $|V_{DS}| \leq |V_{onset}|$ originates from an accumulation layer of holes formed at the pentacene/SiO_2 interface. For $|V_{DS}| = 0$ V holes are equally accumulated at both, source and drain contact. However, the charge-carrier concentration at the drain contact decreases with increasing $|V_{DS}|$ and for $|V_{DS}| = |V_G - V_{Tp}|$, with V_{Tp} being the threshold voltage for *p*-channel device operation, the gate bias at the drain contact is zero with no charges accumulated at the interface. Thus, the *p*-channel is in pinch-off and the drain current saturates. Increasing $|V_{DS}|$ further, the gate contact effectively exhibits a positive bias with respect to the drain contact. As the Mg contact energetically favors electron injection into PTCDI-$C_{13}H_{27}$, an accumulation layer of electrons is expected to form in the PTCDI-$C_{13}H_{27}$ layer on top of the pentacene layer. Therefore, the current increase is attributed to the injection of electrons into the PTCDI-$C_{13}H_{27}$ layer. Since the pentacence/PTCDI-$C_{13}H_{27}$ interface forms a barrier for electron injection from PTCDI-$C_{13}H_{27}$ into pentacene, the pentacene layer is expected to serve as an additional gate insulator for electron transport. Thus, the transport of electrons occurs in a channel formed close to the pentacene layer. The threshold voltage V_{Tn} for *n*-channel operation determines the onset of the additional electron current as follows: $|V_{onset}| = |V_G - V_{Tp} - V_{Tn}|$. From Figure 5.3(a) the empirical relation $V_{onset} \simeq V_G - 10$ V was obtained. Thus $V_{Tp} + V_{Tn} \simeq 10$ V. The non-linear current increase for small $|V_{DS}|$ originates from an additional series resistance most likely due to an injection barrier at the Au contact.

The ambipolar current characteristic in Figure 5.3(b) can be understood using similar arguments as before. Assuming, the observed *n*-channel characteristic originates from electrons being transported within the PTCDI-$C_{13}H_{27}$ thin film adjacent to the pentacene layer and the additional drain current is due to a *p*-channel formed within the pentacene layer, the ambipolar transport mechanism itself is unchanged. The significant difference

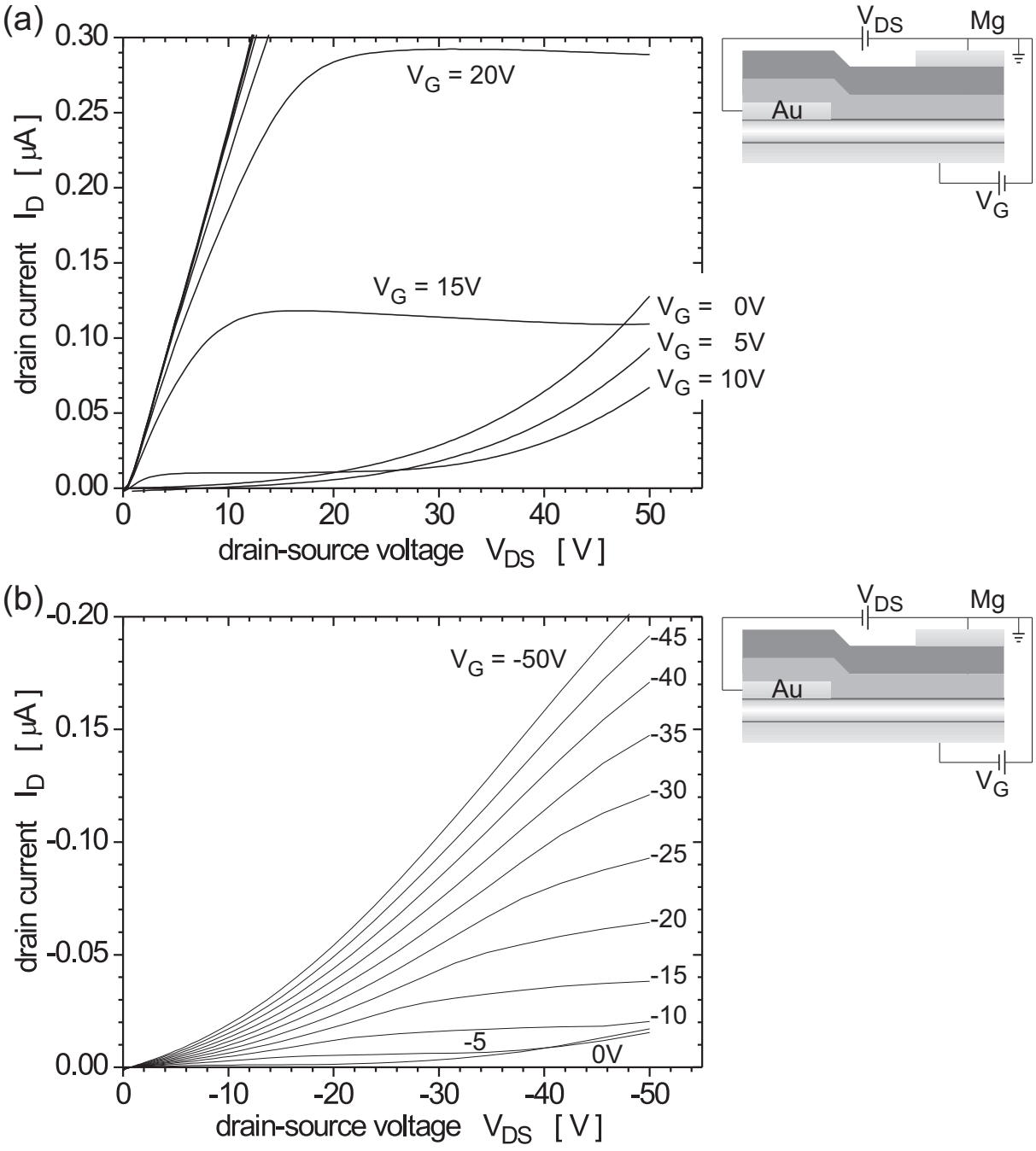

Figure 5.4: *Output characteristics of a pentacene/PTCDI-$C_{13}H_{27}$ bilayer heterostructure transistor with the Mg electrode defined as source contact. The gate is biased (a) positive and (b) negative. Reprinted from [Ros04a].*

between both cases is the injection of charge carriers. An electron channel, represented by the linearly increasing and saturating drain current, is formed only for $V_G \geq 15$ V. In this case, electrons are injected into the PTCDI-$C_{13}H_{27}$ layer from the Au source contact through the pentacene layer, i.e. with a large injection barrier. The additional nonsaturating drain current is observed already at $V_G = 0$ V. Since holes are injected from the Mg contact through the PTCDI-$C_{13}H_{27}$ layer, also the hole injection is dominated by a large barrier. Therefore the device characteristic is determined by high injection barriers (Fig. 5.2) and large contact resistances, which is reflected in the output characteristics (Fig. 5.3(b)). For example, the current density is reduced by one order of magnitude compared to the forward bias regime, where positive and negative charge carriers are directly injected from the metal contacts into the corresponding hole- and electron-transporting layer.

In Figure 5.4(a) the linearly increasing and saturating drain current is due to electrons injected from the Mg contact into the PTCDI-$C_{13}H_{27}$ thin film, which are expected to be transported adjacent to the pentacene layer. The formation of this *n*-channel occurs only for $V_G \geq 10$ V. The additional nonsaturating drain current is observed for drain source voltages up to to 50 V only for $V_G \leq 10$ V. In this voltage regime of $V_{DS} \geq V_{onset}$, the gate contact is negatively biased with respect to the drain contact and therefore the nonsaturating current originates from holes injected from the Au contact into the pentacene layer. The typical *p*-channel device characteristic in Figure 5.4(b) originates from holes which are injected from the Mg contact through the PTCDI-$C_{13}H_{27}$ layer into the pentacene thin film. This injection mechanism is associated with a high impedance, non-ohmic contact resistance, reflected in the positive curvature of the ideally linearly increasing drain current for small drain-source voltages. The additional drain current for $|V_G| \leq |-10|$ V and $|V_{DS}| \geq |V_{onset}|$ can be attributed to the injection of electrons since the gate contact is positively biased with respect to the drain contact, and therefore the nonsaturating current originates from electrons injected from the Au contact through the pentacene layer into the PTCDI-$C_{13}H_{27}$ thin film. The current in Figure 5.4(b) is again lower than in (a), which is caused by the large contact resistance due to the high injection barriers for hole injection from the low work function Mg source contact into the pentacene thin film through the PTCDI-$C_{13}H_{27}$ layer and for electron injection from the Au drain contact through the pentacene layer into the PTCDI-$C_{13}H_{27}$ thin film.

Conclusion

The pentacene/PTCDI-$C_{13}H_{27}$ bilayer heterostructure OFET shows for both contact configurations a typical transistor characteristic with an additional increase in the channel current, which is a typical feature of ambipolar device operation. From Figure 5.3(a) and

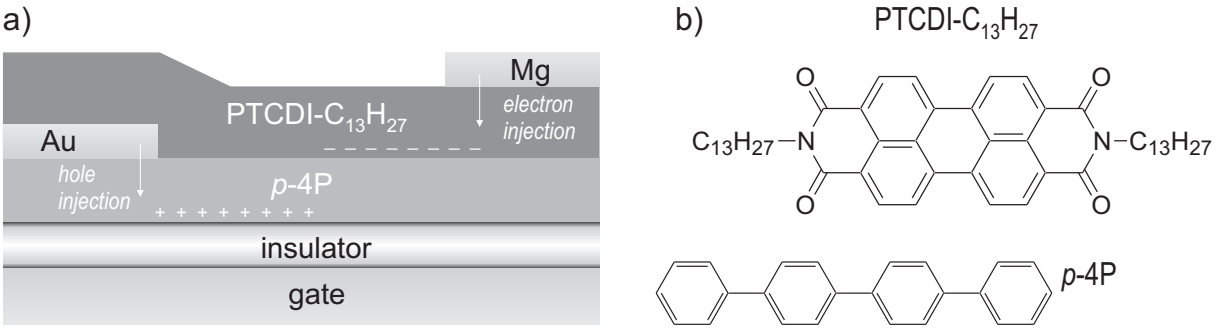

Figure 5.5: *Schematic drawing of a bilayer heterostructure OFET combining 35 nm p-4P and 45 nm PTCDI-$C_{13}H_{27}$. Highly doped silicon is used as substrate and gate contact, with a 130 nm thick thermally grown SiO_2 layer as gate insulator. The layers are top contacted by Au (30 nm) and Mg (50 nm). (b) Molecular structure of PTCDI-$C_{13}H_{27}$ and p-4P.*

5.4(a), it can be concluded consistently, that the electron mobility of the ambipolar device is higher than the hole mobility.

Even though the combination of pentacene and PTCDI-$C_{13}H_{27}$ results in a pronounced ambipolar current characteristic over a large range of bias voltages, no light emission is observed. The experimental results do not allow a prediction on the recombination rate of electrons and holes, which can either recombine between source and drain contact or pass each other in two independent parallel channels and leave the device at the other contact without recombination. Independent of that uncertainty, the energy levels are not matched for radiative recombination of electrons and holes of these two materials, as can be deducted from the energy level diagram in Figure 5.2.

5.2 *p*-4P/PTCDI-$C_{13}H_{27}$ OFET

In order to observe electroluminescence (EL) in an ambipolar heterostructure OFET, it seems to be favorable that HOMO and LUMO levels of both combined materials are chosen such a way that the HOMO and LUMO of the emitting material is within the HOMO and LUMO of the material with the larger gap. From these considerations one concludes that either pentacene or PTCDI-$C_{13}H_{27}$ should be replaced by a transport material with appropriate HOMO and LUMO levels. The choice of electron-transport materials is limited compared to the variety of hole-transport materials. Additionally, PTCDI-$C_{13}H_{27}$ is a fluorescent material with emission in the red, and thus a prospective emitter. Hence, a hole transporting material with HOMO and LUMO positions matching PTCDI-$C_{13}H_{27}$ as electron-transport material and emitter was searched, i.e. the band-gap of this new hole-transport material should be larger than the band-gap of PTCDI-$C_{13}H_{27}$ and the HOMO and LUMO levels of PTCDI-$C_{13}H_{27}$ should be within the ones of the

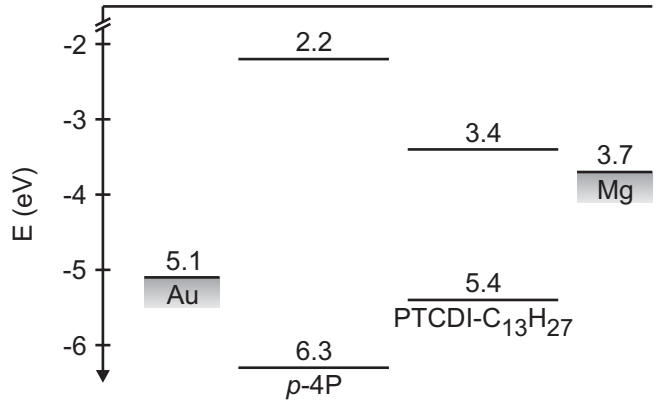

Figure 5.6: *Energy level diagram of HOMO and LUMO of p-4P and PTCDI-$C_{13}H_{27}$ and work function of the two contact metals, Au and Mg [Lid96]. The values for p-4P were estimated based on the HOMO and LUMO level of p-6P [Sch02b] and the singlet energy of p-4P [Pog02]. The values for PTCDI-$C_{13}H_{27}$ were estimated from [Hir95].*

hole-transport material. From an energetic point of view, *p*-4P is a promising candidate to be used due to its large band-gap of 3.9 eV and relatively good transport properties, which were described in Chapter 4. The device characteristic of a *p*-4P OFET is shown in Figure A.2.

The investigated device structure is shown schematically in Figure 5.5 together with the molecular structure of both organic compounds. The *p*-4P thin film is grown directly on top of the silicon oxide and top contacted by Au. The top contact was chosen in order to not disturb the growth of *p*-4P, which is very sensitive to parameters such as surface energy, substrate temperature and deposition rate. Thus, the top contact avoids growth defects that would be caused by a SiO_2/bottom Au contact interface. Subsequently, PTCDI-$C_{13}H_{27}$ is deposited, followed by a Mg top contact. The thicknesses of the organic layers are 35 nm and 45 nm for *p*-4P and PTCDI-$C_{13}H_{27}$, respectively. The metal contacts are 30 nm (Au) and 50 nm (Mg) thick. The channel length and channel width are 200 and 1200 μm, respectively. Due to the device architecture, PTCDI-$C_{13}H_{27}$ is directly contacted with Au and Mg, whereas the *p*-4P thin film is contacted with the Mg electrode only via the PTCDI-$C_{13}H_{27}$ layer.

The HOMO and LUMO levels of both organic transport materials and the work function of the metal contacts are shown in Figure 5.6. The work function of Mg matches the LUMO of PTCDI-$C_{13}H_{27}$, whereas the work function of Au does not exactly match the HOMO position of *p*-4P, however decent injection is still given. This device structure is again highly asymmetric with respect to the materials chosen as well as the energetic levels and the two cases of either Mg or Au being defined as source contact have to be distinguished for voltage scans in both directions.

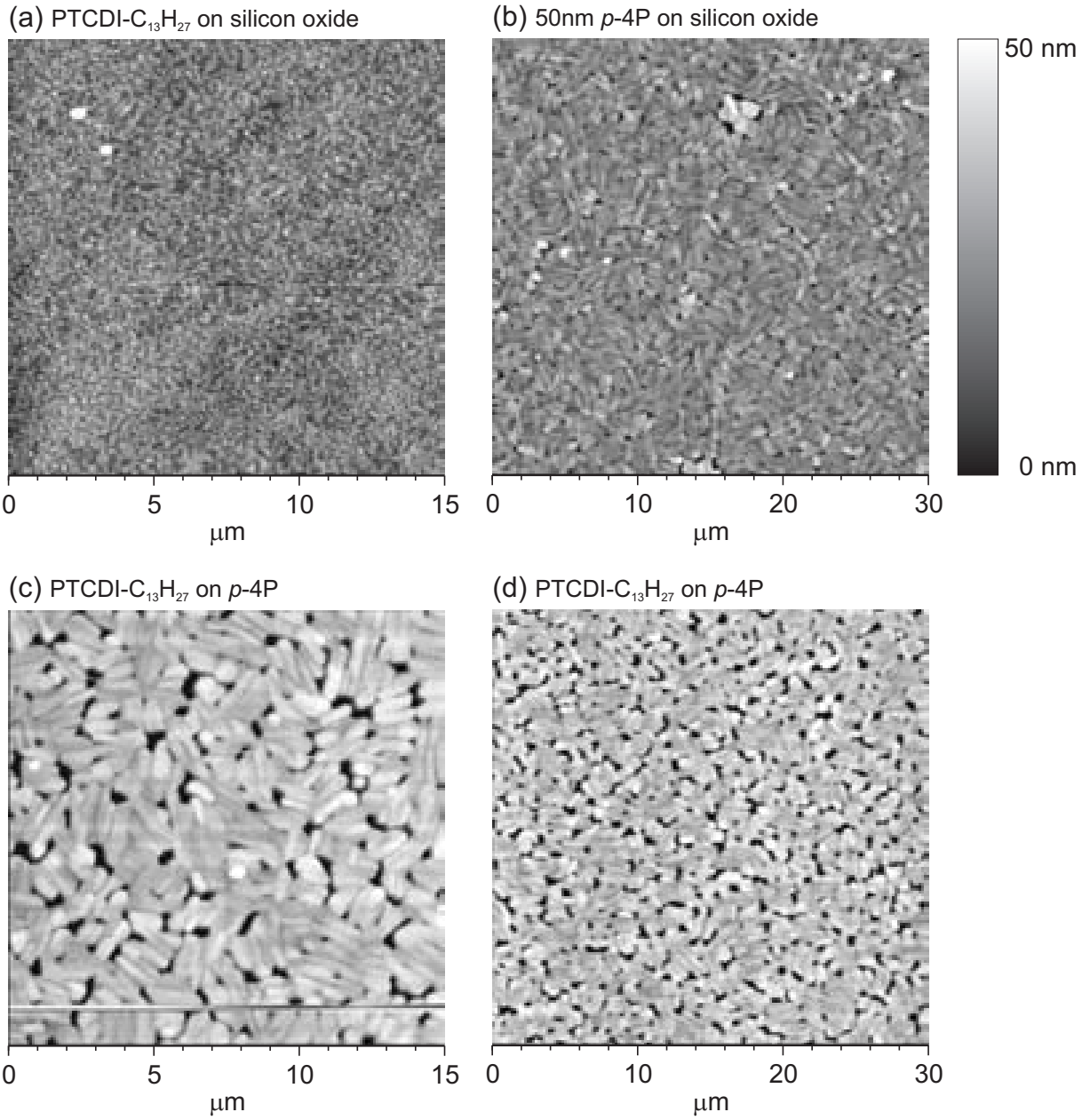

Figure 5.7: *AFM images of PTCDI-$C_{13}H_{27}$ on silicon (a) and on top of p-4P (c) and (d). For comparison, p-4P on silicon is shown as well (b). The scale of (a) and (c) is 15μm, the scale of (b) and (d) 30 μm. The grey-scale bar quantifies the topology between 0 and 50 nm.*

In order to control the growth of PTCDI-$C_{13}H_{27}$ and *p*-4P, AFM images were taken (Fig. 5.7). On SiO_2, PTCDI-$C_{13}H_{27}$ forms smooth films, while *p*-4P grows in quite large crystallites of $1-2$ μm. When PTCDI-$C_{13}H_{27}$ is deposited on *p*-4P, the morphology resembles the elongated large *p*-4P grains and is completely different to the one of PTCDI-$C_{13}H_{27}$ directly on silicon oxide. Therefore it can be concluded that PTCDI-$C_{13}H_{27}$ covers *p*-4P and a good contact between both materials is provided.

Results

The qualitative behavior of the output characteristic measured for positive and negative bias voltage $|V_{DS}|$ and $|V_G|$ up to 80 V resembles the characteristic features of ambipolar transport as discussed before. Figure 5.8(a) shows the output characteristic for the case of Mg defined as source contact. The graph is composed of two independent measurements, one for positive bias and one for negative bias voltage. Each scan was performed for increasing drain-source voltage $|V_{DS}|$ starting at 0 V. The characteristic for Au as source is shown in Figure 5.8(b). Additionally to the drain current, the measured gate current is shown in both graphs, and appears with being more than 2 orders of magnitude smaller than the drain current, to be almost zero on the drain-current scale. Only for Au as source and negative bias applied, the gate current appears to be noisy, which is also reflected in the corresponding drain current.

Similar to pentacene/PTCDI-$C_{13}H_{27}$ devices, for both positive and negative bias scans an almost linear current increase followed by saturation and an additional strong current increase with positive curvature are observed. In each of the four characteristics, the ideally linear increase of the drain current for small $|V_{DS}|$ shows here a positive curvature. In contrast to the previously discussed pentacene/PTCDI-$C_{13}H_{27}$ device, the saturated drain current is in the same order of magnitude for all four characteristics.

Also for the *p*-4P/PTCDI-$C_{13}H_{27}$ bilayer heterostructure OFET no light-emission could be observed. In order to investigate whether this is due to a mismatch of HOMO and LUMO level of *p*-4P and PTCDI-$C_{13}H_{27}$ or due to the bilayer heterostructure being an inappropriate device architecture, both materials have been combined in a bilayer OLED. Using Au as anode and Mg as cathode, red emission of PTCDI-$C_{13}H_{27}$ could be observed [Rost, unpublished]. Thus, the combination of the two materials can in principle emit light.

Discussion

Considering positive bias voltage, the saturated drain current in Figure 5.8(a) and (b) is due to accumulated electrons at the *p*-4P/PTCDI-$C_{13}H_{27}$ interface. The electrons are either injected from the Mg contact (a) or the Au contact (b), depending which of the

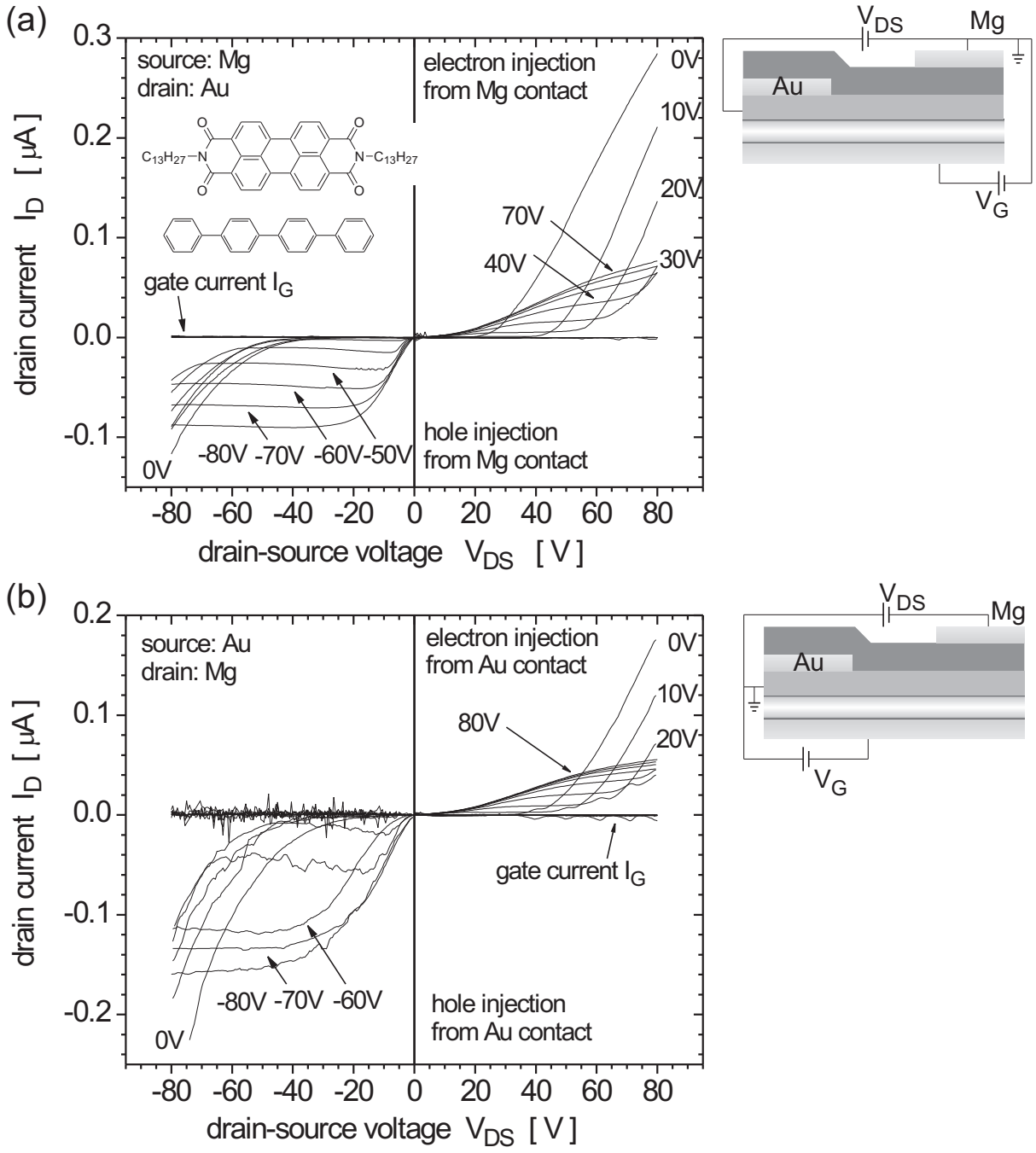

Figure 5.8: *Output characteristics of the p-4P/PTCDI-$C_{13}H_{27}$ bilayer heterostructure transistor. The bias voltage is either applied against the Mg contact (a) or the Au contact (b). I_D was measured for negative and positive values of V_{DS}, respectively. the values of V_G are indicated in the diagram.*

two contacts is defined as source. The pronounced increase in current, which is gate-voltage-dependent, is due to hole injection from opposite drain contact. Contrary, for negative bias voltage, holes are injected from the source contact, either Mg or Au, and accumulated at the *p*-4P/SiO_2 interface. The pronounced, gate-voltage-dependent current is due to electron injection from either Au or Mg, respectively.

Comparing the magnitude of the drain current for either positive or negative voltage bias in Figure 5.8(a) and (b), a difference between injection of electrons and holes from either Au or Mg is observed. Considering the accumulation of electrons, the saturated drain current for injection from Mg is 1.5 times larger than the saturated drain current for injection from Au. Consistently, for the accumulation of holes, the saturated drain current for injection from Au is even 1.8 times larger than the saturated drain current for injection from Mg, which is through the PTCDI-$C_{13}H_{27}$ layer into the *p*-4P thin film. Regarding the band diagram in Figure 5.6, the band offset for hole injection from Au is 1.1 eV, for hole injection from Mg via PTCDI-$C_{13}H_{27}$ it is composed of two barriers with the energies 1.7 and 0.8 eV. The electron injection into PTCDI-$C_{13}H_{27}$ from Mg can be associated with a barrier of 0.3 eV, from Au with a barrier of 1.7 eV, respectively.

Conclusion

The bilayer heterostructure OFET of *p*-4P and PTCDI-$C_{13}H_{27}$ shows an almost symmetric pronounced ambipolar characteristic. Even though both mobilities seem to be in the same order of magnitude, the hole mobility appears to be slightly larger than the electron mobility. The quantitative mobility values will be discussed in detail in Section 5.4.1. No light emission is observed from the bilayer heterostrcucture OFET, although EL could be observed in bilayer OLED devices composed of *p*-4P and PTCDI-$C_{13}H_{27}$. The emission spectrum could be allocated to emission from PTCDI-$C_{13}H_{27}$. Therefore, a mismatch of the energy levels of the two organic materials can be excluded as the limiting factor for the EL from an OFET structure. It is assumed that either the electron and hole channels are formed parallel to each other and thus no recombination takes place, or the current densities and recombination rate are too low, and thus the EL intensity is below the detection limit of the photodiode.

5.3 α-5T/PTCDI-$C_{13}H_{27}$ OFET

An increase in ambipolar current densities can either be achieved by decreasing the channel length and increasing the channel width, or by replacing *p*-4P with a hole-transport material having considerably higher mobilities, such as α-5T. The HOMO and LUMO levels of α-5T are in between the ones of *p*-4P and pentacene, whereas the HOMO level of

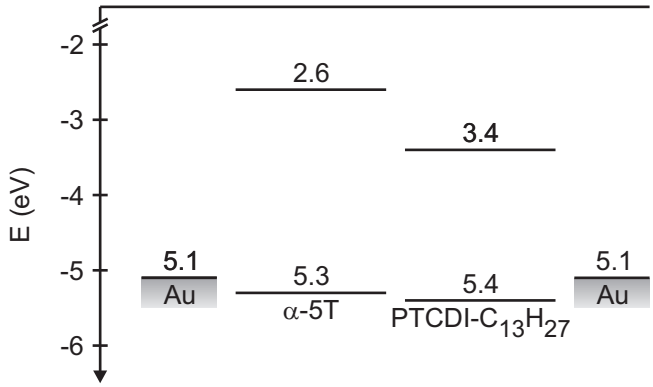

Figure 5.9: *Energy level diagram of HOMO and LUMO of α-5T and PTCDI-$C_{13}H_{27}$ and work function of the two contact metals, Au and Mg [Lid96]. The values for α-5T are based on its HOMO level [Jon90] and singlet energy [dM99]. The values for PTCDI-$C_{13}H_{27}$ were estimated from [Hir95].*

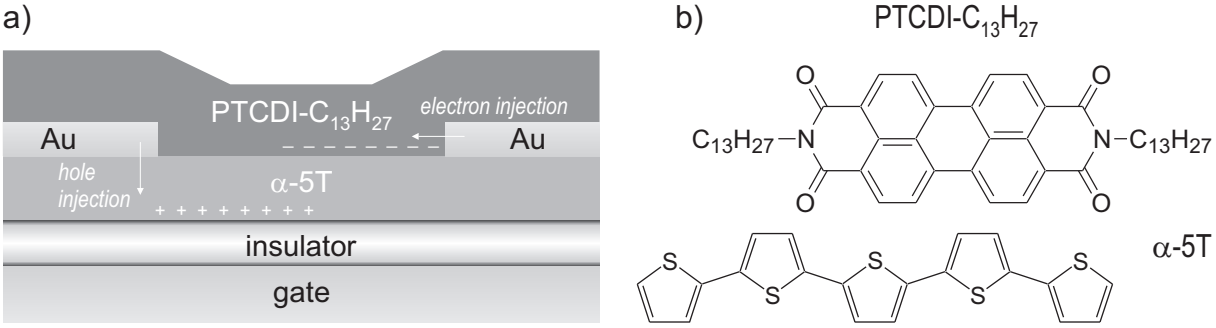

Figure 5.10: *Schematic drawing of a bilayer heterostructure OFET combining 50 nm α-5T and 45 nm PTCDI-$C_{13}H_{27}$. Highly doped silicon is used as substrate and gate contact, with a 150nm thick thermally grown SiO_2 layer as gate insulator. The device is symmetrically contacted by Au. (b) Molecular structure of PTCDI-$C_{13}H_{27}$ and α-5T.*

α-5T is with 5.3 eV [Jon90] similar to the one of PTCDI-$C_{13}H_{27}$, as shown in Figure 5.9 . The investigated device structure is shown in Figure 5.10. The thin film of α-5T is grown directly on silicon oxide and top contacted by Au, in order to avoid growth defects at the SiO_2/bottom contact interface. PTCDI-$C_{13}H_{27}$ is deposited as the top layer. For this device Mg could not be employed as contact metal due to processing limitations.

This device structure is symmetric with respect to source and drain contacts as can be seen from the schematic drawing in Figure 5.10. The symmetry in device architecture comes along with an asymmetry with respect to contact resistance, as it is shown in the energy level diagram in Figure 5.9. The gold contact forms an almost ohmic contact for hole injection into α-5T, however, the contact is clearly non-ohmic for electron injection into PTCDI-$C_{13}H_{27}$. This leads to a higher contact resistance and therefore smaller elec-

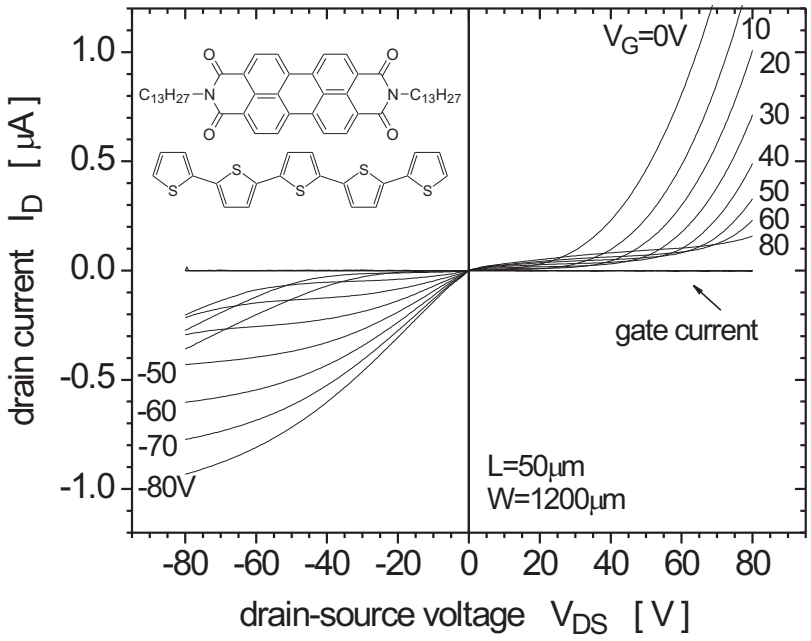

Figure 5.11: *Output characteristic of the α-5T/PTCDI-$C_{13}H_{27}$ bilayer heterostructure transistor. The gate has been either biased positive or negative. I_D was measured for positive and negative values of V_{DS} varied between 0 and ± 80 V, respectively.*

tron currents than expected from the electron mobility in PTCDI-$C_{13}H_{27}$. Both organic layers are directly contacted with both electrodes, excluding additional contact resistances due to charge-carrier injection via an organic layer.

Results

Due to the device symmetry with respect to source and drain contacts, only the two cases of positive and negative bias have to be considered, independent on which of the two top contacts are defined as source. Figure 5.11 shows the output characteristics of two independent measurements, one for positive bias and one for negative bias voltage. They were performed starting from 0 V and increasing the drain-source voltage V_{DS} to ±80 V for discrete gate bias of the same sign, also varied from 0 to ±80 V. For both polarities, typical transistor characteristics are observed with a saturation region for the *n*-channel regime as well as for the *p*-channel regime. Also in both cases, for large $|V_{DS}| \geq |V_{onset}|$ the additional nonsaturating current characteristic for ambipolar device operation is observed.

Figure 5.12 shows the ambipolar transfer characteristics of the device, whereas in (a) the drain current is plotted semilogarithmic versus the gate voltage for drain-source voltages from 0 to ±100 V and in (b) the square root of the drain current for $|V_{DS}| = 100$ V is shown, from which the electron and hole mobility can be extracted. Each graph is

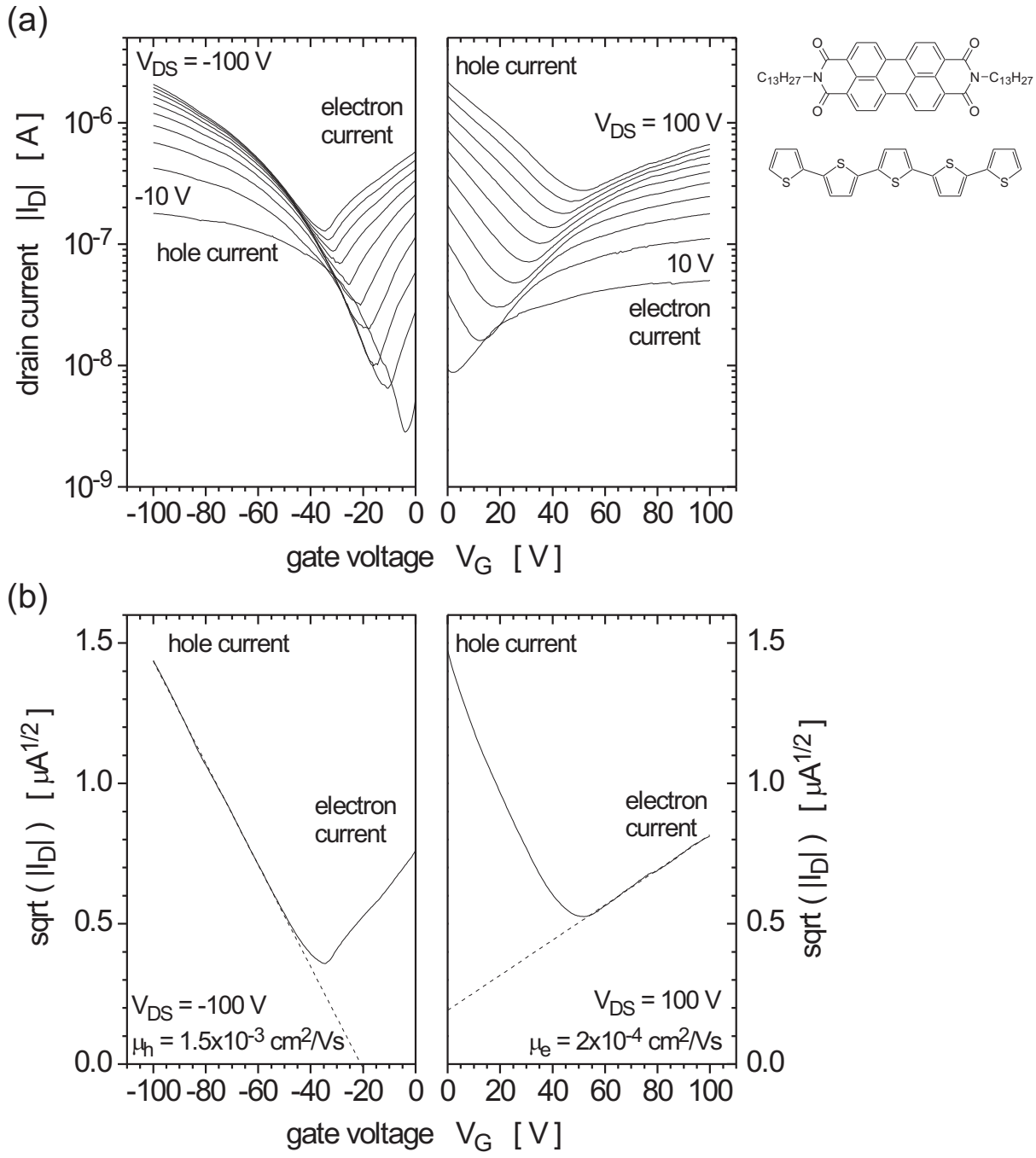

Figure 5.12: *Transfer characteristic of the α-5T/PTCDI-$C_{13}H_{27}$ bilayer heterostructure OFET. (a) Semilogarithmic plot for the drain current I_D versus the gate voltage V_G. (b) Square root of the drain current I_D versus the gate voltage V_G for $|V_{DS}| = 100$ V. The dotted line is the linear fit in the unipolar limit at large gate bias, from which electron and hole mobilities can be extracted to $\mu_n = 2 \times 10^{-4}\ cm^2/Vs$ and $\mu_p = 1.5 \times 10^{-3}\ cm^2/Vs$, respectively.*

composed of two independent measurements, one for positive and one for negative bias voltages. The scan direction was chosen in each case with start at 0 V and increasing the bias voltage up to ±100 V. In the transfer characteristic of unipolar devices only for gate voltages above threshold a drain current is observed, which is increasing with both the drain-source and gate bias. This current is also observed for. However, whereas unipolar devices are in the "off"-state for gate voltages below threshold, for which only gate leakage is observed, here a drain current is observed also for gate voltages below threshold. This drain current is increasing with increasing drain-source voltage, but decreasing with increasing gate voltage. Thus for each applied drain-source voltage, a minimum in the drain-current versus gate voltage curve is observed.

Discussion

For positive voltage scans, electrons are injected from the source contact and the observed saturation region of the current is due to accumulated electrons at the PTCDI-$C_{13}H_{27}$/α-5T interface. The strong increase in current, which is gate voltage dependent, is due to hole injection from the drain contact. Contrary for negative bias voltages, holes are injected from the source contact and the observed saturation region of the current is due to accumulated holes at the α-5T/SiO_2 interface. The strong increase in current, which is gate voltage dependent, is due to electron injection from the drain contact.

The ambipolar transfer characteristic shows an "on-off-on"transition, whereas the drain current in the "on"-state for large $|V_G|$ is identical to the unipolar drain current, i.e. a hole current for negative gate bias and an electron current for positive bias. From the slope of that current, hole and electron mobility can be extracted as 1.5×10^{-3}cm^2/Vs and 2×10^{-4}cm^2/Vs, respectively. Around the minimum region of the drain current, electron and hole transport overlap and the transistor operates ambipolar.

Conclusion

The bilayer heterostructure OFET of α-5T and PTCDI-$C_{13}H_{27}$ shows an ambipolar characteristic, that is not as symmetric as the one of *p*-4P and PTCDI-$C_{13}H_{27}$, due to the larger hole mobility of α-5T. The hole current is approximately one order of magnitude larger than in the case of *p*-4P applied as hole transport matrial, whereas the electron current is unchanged. Also for this device, no light emission is observed. Thus it is assumed that even in case of emitted light the intensity is still below the detection limit of the silicon photodiode. From the ambipolar transfer characteristics, hole and electron mobility of 1.5×10^{-3} cm^2/Vs and 2×10^{-4}cm^2/ Vs could be extracted.

5.4 Simulation of Ambipolar OFET Characteristic

Modelling the ambipolar device characteristic is motivated by the idea of describing the ambipolar current in a similar way as the unipolar transistor characteristic is described by the Shockley equation. There, the device characteristic is described by the charge-carrier mobility μ as the only material parameter, the threshold voltage V_T describing the interface properties and the device dimensions channel length L and channel width W and the insulator capacitance C_i. In a first approach, the Shockley equation is modified for the quantitative description of ambipolar transport. However, this approach neither considers recombination nor eventual modifications in the effective channel length. Therefore in a second approach, the ambipolar device characteristic is simulated analytically applying the drift-diffusion model and considering only material parameters and the device geometry. This approach delivers not only the current-voltage characteristic, but also the potential distribution and charge-carrier concentration between source and drain contact. Additionally, charge-carrier recombination is considered.

5.4.1 Model Based on a Modified Shockley Equation

The observed characteristic of an ambipolar transistor can be understood in a qualitative manner as a superposition of the characteristics of two unipolar organic field-effect transistors. This requires the analysis of the complete characteristic with a voltage scan for gate and drain-source bias not only in the typical operating regime, but also in the reverse voltage regime, i.e for example the measurement of the drain current for a *n*-channel device not only for positive gate and drain-source voltages, but also for negative gate and drain-source voltages.

Regarding an OFET where electrons are the majority charge carriers, the typical operating regime, characterized by the linear region for small drain bias and the saturation region for large drain bias, is hereby for a *n*-channel device located in the first quadrant of an I_D versus V_{DS} diagram. The reverse scan, which features no saturation, is located in the third quadrant, as it is shown in Figure 5.13(a). Whereas I_D in the first quadrant increases with the gate bias V_G, the current in the third quadrant decreases with increasing gate voltage. In the first quadrant, the drain current dependence on the gate voltage is theoretically described as a quadratic one, however, the experimental curve shows a subquadratic increase of the saturated drain current with the applied gate voltage. This deviation from theory is most likely due to traps within the organic thin film [Ref].

Considering the *n*-channel device for the stationary case in which no drain-source-voltage, but a negative gate voltage is applied, electrons are depleted at the gate-insulator interface. Consequently, applying a small negative drain-source voltage with $|V_{DS}| \leq$

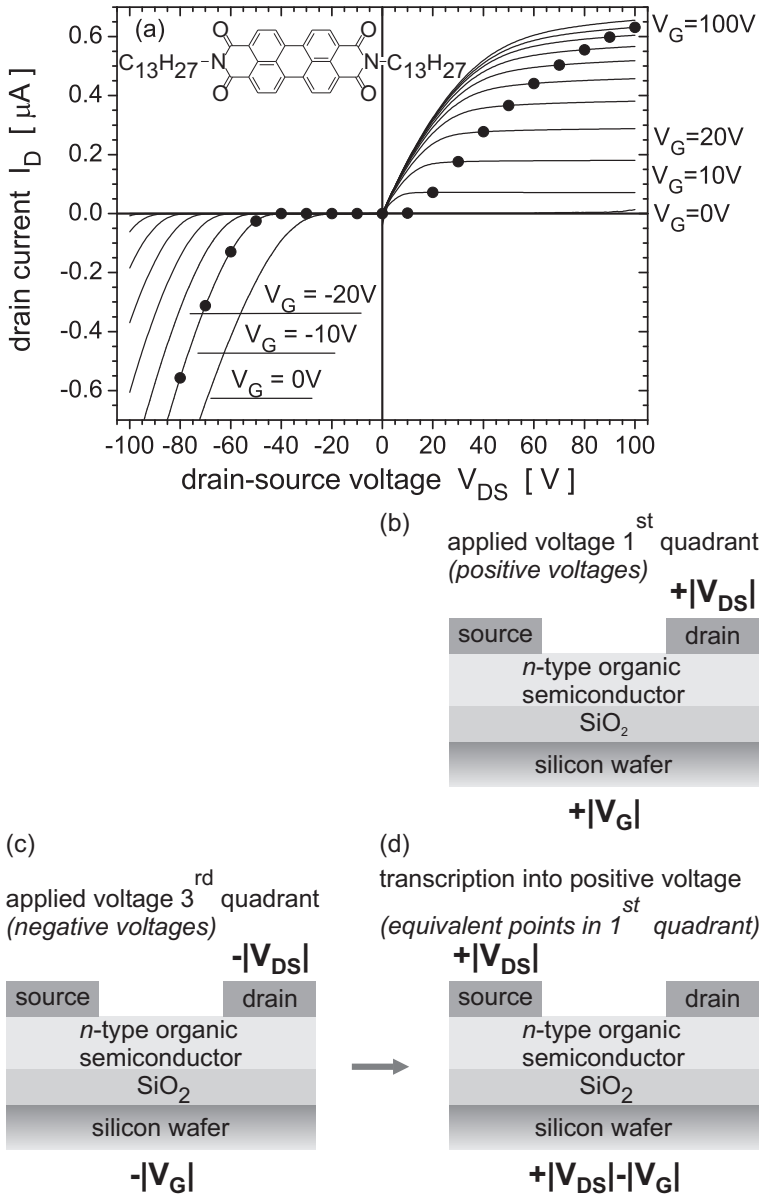

Figure 5.13: *(a) Measured output characteristic of a unipolar, n-channel single-layer transistor in the complete bias range of positive and negative drain-source and gate voltages. The drain current in the first quadrant of the I_D versus V_{DS} diagram shows saturation, whereas in the third quadrant no saturation is observed. (b) Schematic drawing for the drain-source and gate voltage bias that leads to an electronic current flow in the first quadrant. (c) Schematic drawing for drain-source and gate voltage bias that leads to electronic current flow in the third quadrant. In this case, a negative drain-source and negative gate voltage is applied with respect to the source contact. (d) Redefining the drain contact as common contact. This notation is equivalent to a positive drain-source voltage and a positive gate voltage (for $|V_{DS}| > |V_G|$), being applied with respect to the drain contact. The effective gate voltage is then $V_G - V_{DS}$. Therefore, for each data point in the third quadrant, an equivalent data point in the first quadrant can be found. However, the scan of V_{DS} for discrete V_G is then a simultaneous scan of the effective drain-source and gate voltage, resulting in a nonsaturating current. Reprinted from [Ros04a].*

$|V_G - V_T|$, no current flow is observed. V_T is the threshold voltage for n-channel transistor operation. Increasing the magnitude of the drain-source bias above values of $|V_G - V_T|$, the drain contact is biased more negative than the gate contact, i.e. with respect to the drain contact a positive net gate bias is applied. Consequently, electrons are injected from the drain contact and accumulated at the interface close to the gate insulator. A drain-source current is observed as a consequence of the drain-source field.

Since the drain contact is now acting as injecting contact and only electrons are considered, it is convenient to redefine it as common or source contact, i.e. express the voltages applied to the source and gate contact with respect to the drain contact, as schematically shown in Figure 5.13(b)-(d). The resulting net source-drain voltage V'_{SD} is therefore given by:

$$V'_{SD} = -V_{DS} \tag{5.1}$$

and the net gate voltage V'_{GD} is given by:

$$V'_{GD} = V_G - V_T - V_{DS} \tag{5.2}$$

For negative V_{DS} with $|V_{DS}| \geq |V_G - V_T|$, both V'_{SD} and V'_{GD} are positive values. Whereas for the typical output characteristic with injection from source contact the applied drain-source voltage and gate voltage are independent, for the reverse characteristic, the effectively applied gate voltage is a composition of the applied drain-source and gate voltage. Therefore the transistor output characteristic in reverse direction is not a drain-source voltage scan for discrete gate voltages. Rather, with increasing drain-source voltage, not only the net source-drain voltage V'_{SD} is increasing, but also the net gate voltage V'_{GD}, resulting in a non-saturating drain current. Increasing the magnitude of the negative applied gate voltage V_G leads for a constant applied negative drain-source voltage V_{DS} according to Equation 5.2 to a decreasing positive gate voltage V'_{GD}. Therefore, the reverse drain current is decreasing with increasing V_G.

The previously discussed OFETs featuring ambipolar device characteristic are bilayer heterostructures of a hole and an electron transport-material, i.e. a combination of a p-channel and a n-channel device. In a first approximation, the ambipolar current is composed of a hole and an electron current. Therefore, regardless of whether the device is scanned in the positive or negative bias regime, one of these currents saturates, whereas for the other one no saturation is observed. In the heterostructure transistor we therefore always measure a superposition of both, the saturating and the nonsaturating characteristic, independent of the applied voltage regime (positive or negative bias), leading to the characteristic features of the ambipolar current.

In a simple approach, the ambipolar current characteristic can therefore be modelled as a superposition of a hole and an electron current. The effective applied drain-source

and gate voltages for one of the charges have to be adapted from Equation 2.7 and 2.9 using Equation 5.1 and 5.2.

Considering positive gate bias V_G with $V_G - V_{Tn} \geq 0$ and positive drain-source voltage V_{DS} with $V_{DS} \leq V_G - V_{Tn}$, the electron current I_{Dn} is given by

$$I_{Dn} = \frac{W}{L}\mu_n C_i \left[(V_G - V_{Tn})V_{DS} - \frac{1}{2}{V_{DS}}^2 \right]; \text{ for } V_{DS} \leq V_G - V_{Tn} \tag{5.3}$$

Here, μ_n is the field-effect mobility for electrons and V_{Tn} the threshold voltage for n-channel operation. For large V_{DS} with $V_{DS} \geq V_G - V_{Tn}$, the drain current I_{Dn} saturates and depends only on V_G:

$$I_{Dnsat} = \frac{W}{2L}\mu_n C_i (V_G - V_{Tn})^2; \text{ for } V_{DS} \geq V_G - V_{Tn} \tag{5.4}$$

The corresponding hole current I_{Dp} is zero for $V_{DS} \leq V_G - V_{Tp}$ and is for $V_{DS} \geq V_G - V_{Tp}$ with $0 \leq V_G - V_{Tp}$ given by

$$I_{Dp} = \frac{W}{L}\mu_p C_i \left[(V_G - V_{Tp} - V_D)(-V_{DS}) - \frac{1}{2}{V_{DS}}^2 \right]; \text{ for } 0 \leq V_G - V_{Tp} \tag{5.5}$$

Here, μ_p is the field-effect mobility for holes and V_{Tp} the threshold voltage for p-channel operation. For $0 \geq V_G - V_{Tp}$, the drain current I_{Dp} is given by

$$I_{Dpsat} = \frac{W}{2L}\mu_p C_i (V_G - V_{Tp} - V_{DS})^2; \text{ for } 0 \geq V_G - V_{Tp} \tag{5.6}$$

Similar expressions hold for the electron and hole current under negative drain-source and gate bias. The total ambipolar current I_{Damb} is the sum of electron and hole current. The analytical expression for the total ambipolar current I_{Damb} used for simulation with Mathcad© can be found in Appendix B. Free parameters are the electron mobility μ_n, the hole mobility μ_p, and the threshold voltages for n- and p-channel device operation, V_{Tn} and V_{Tp}, respectively. The model does not account for any contact resistances and injection barriers, change in effective channel length and the modified gate insulator capacitance for the top layer.

The simulated and measured data for the pentacene/PTCDI-$C_{13}H_{27}$ device (Figure 5.3(a) and 5.4(a)) are shown in Figure 5.14. The values for the channel length L, the channel width W, and the capacitance C_i are fixed parameters and the values are set according to the device geometry to $L = 140\ \mu$m, $W = 1200\ \mu$m, and $C_i = 2.3 \times 10^{-8}$ F/cm^2.

First, the threshold voltages for p- and n-channel operation have been extracted from the experimental data with $V_{Tp} = -4$ V and $V_{Tn} = 8$ V. Subsequently, the mobilities have been adjusted to fit the experimental data. Hereby, the weakness of the model due to not taking contact resistance and injection barriers into account is obvious. In the linear region of the measured data of Figure 5.14(a) the drain current shows a concave

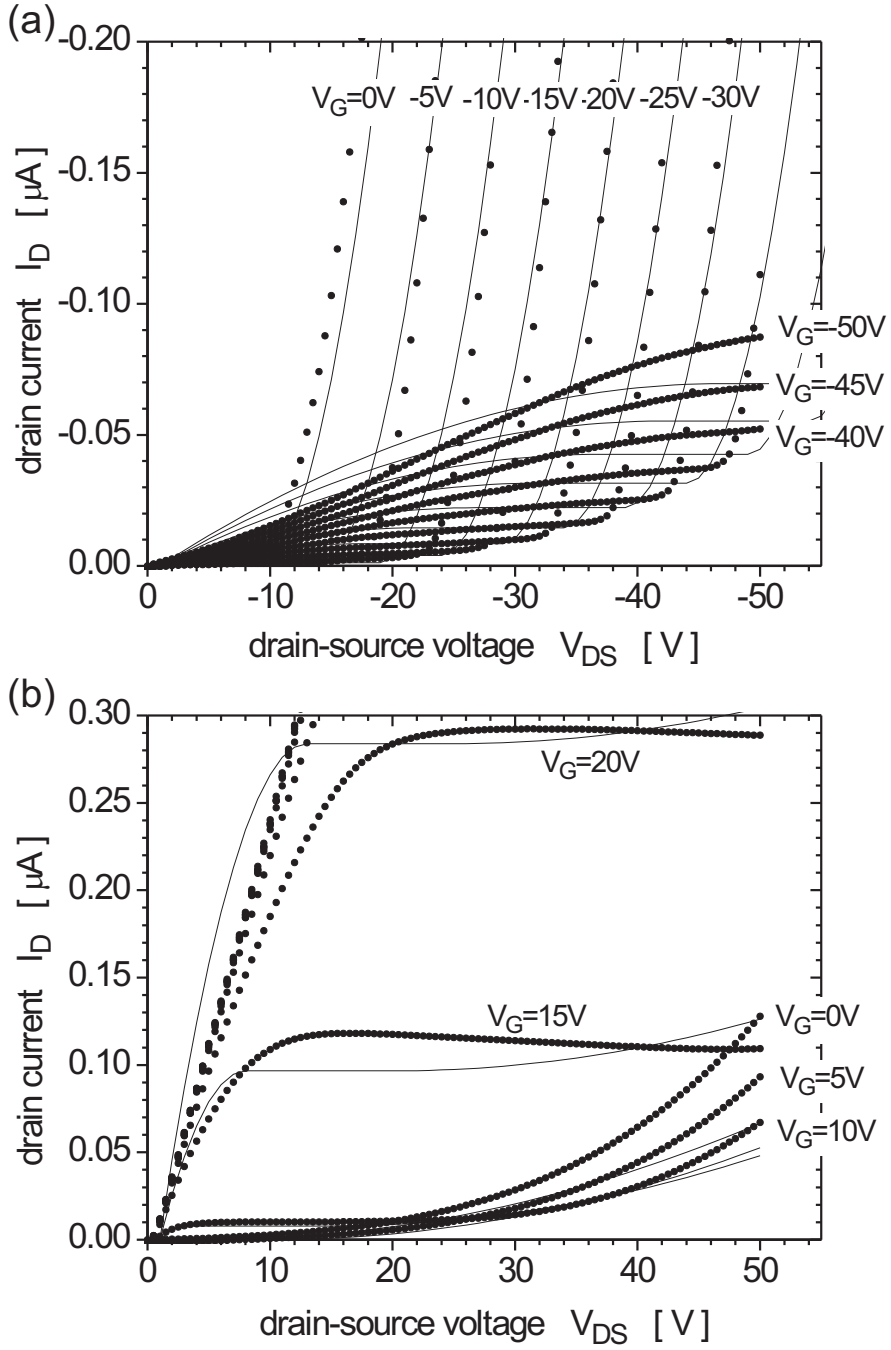

Figure 5.14: *Simulated (line) and measured (symbols) output characteristic of the pentacene/PTCDI-$C_{13}H_{27}$ bilayer heterostructure transistor. (a) Au is defined as source contact, (b) Mg is defined as source contact. The best fit is obtained for threshold voltages V_{Tn} = -8 V and V_{Tp} = 4 V and mobilities of $\mu_n = 1.2 \times 10^{-2}$ cm^2/Vs and $\mu_p = 2 \times 10^{-4}$ cm^2/Vs.*

device structure	contact metal	V_{Tn} [V]	μ_n [cm^2/Vs]	contact metal	V_{Tp} [V]	μ_p [cm^2/Vs]
pentacene/PTCDI-$C_{13}H_{27}$	Mg	8	1.2×10^{-2}	Au	-4	2×10^{-4}
p-4P/PTCDI-$C_{13}H_{27}$	Mg	15	4×10^{-4}	Au	-25	8×10^{-4}
α-5T/PTCDI-$C_{13}H_{27}$	Au	15	4×10^{-4}	Au	-15	1.5×10^{-3}

Table 5.1: *Fitted values for V_{Tn} and V_{Tp} and electron and hole mobilities μ_n and μ_p for the different bilayer heterostructure OFETs obtained by the modified Shockley approximation. Influences of contact resistance and modified gate capacitance and channel length have been neglected.*

increase with increasing drain-source voltage instead of a linear one. Consequently, the saturated drain current is smaller than it would be without contact resistances. Since contact resistances are neglected in the model, the fitted values for the electron and hole mobility reflect only the correct order of magnitude, but not the correct value of the actual mobility. Furthermore, the saturated drain-current in Figure 5.14(b) shows a non-quadratic dependence on the gate voltage, which is also omitted in the model, leading only to an approximation for the mobility. Nevertheless, the best fit has been obtained for electron and hole mobilities of $\mu_n = 1.2 \times 10^{-2}$ cm^2/Vs and $\mu_p = 2 \times 10^{-4}$ cm^2/Vs for that particular device.

For the *p*-4P/PTCDI-$C_{13}H_{27}$ and the α-5T/PTCDI-$C_{13}H_{27}$ bilayer heterostructure OFETs, threshold voltages for *n*- and *p*-channel operation and electron and hole mobilities are obtained with the same approach. The results are summarized in Table 5.1.

Due to the discussed disadvantages of the model and its inability to make predictions about the voltage distribution, charge-carrier densities between source and drain contact and recombination, a more advanced model based on numerical two-dimensional simulations has been applied.

5.4.2 Advanced Simulation using the Drift-Diffusion Model

To investigate the basic ambipolar effects without the additional influences of the special bilayer heterostructure, a single layer model structure is considered. Thus, the additional influence of mixed bottom and top contacts, an additional organic/organic interface and modified gate capacitance for the top layer are neglected. An electron as well as a hole mobility is ascribed to the organic transport material and the HOMO and LUMO levels have been chosen to the ones of pentacene. Source and drain electrodes are bottom contacts of Au and Mg, thus having different work functions. The thickness of the organic thin film and the metal contacts is 30 nm. The SiO_2 gate insulator has a thickness of $d_{\mathrm{ox}} = 150$ nm with a relative dielectric constant of $\epsilon_{\mathrm{ox}} = 3.9$. The channel length is

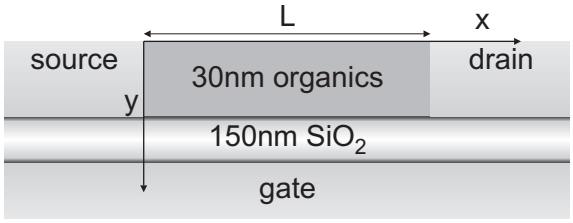

Figure 5.15: *Single layer model structure with an organic thin-film thickness of 30 nm and a channel length of 140 µm.*

$L = 140$ µm and the channel width W is for simplicity chosen as 1 µm. The simulated channel length including contact regions is 160 µm. The monolayer model structure is shown in Figure 5.15.

Simulations have been carried out using the drift-diffusion model in combination with the two-dimensional device simulation programm ISE-TCAD [AG99]. Its applicability to organic materials has been shown in detail in [Sch00, Ngu01, Nes02]. The program simultaneously solves the Poisson equation for the electrical potential ϕ and the continuity equations for the hole and electron densities p and n, respectively. In the non degenerate limit, they are connected with the hole and electron quasi-Fermi potentials $\phi_{\mathrm{F_p}}$ and $\phi_{\mathrm{F_n}}$ by $p = n_{\mathrm{i}} \exp[\mathrm{e}(\phi_{\mathrm{F_p}} - \phi)/\mathrm{k_B}T]$ and $n = n_{\mathrm{i}} \exp[\mathrm{e}(\phi - \phi_{\mathrm{F_n}})/\mathrm{k_B}T]$. The intrinsic density n_i is related to the gap energy E_{g} and the effective densities of states N_{V} and N_{C} in the valence and conduction band by $n_{\mathrm{i}} = \sqrt{N_{\mathrm{V}} N_{\mathrm{C}}} \exp[-E_{\mathrm{g}}/2\mathrm{k_B}T]$. For a molecular material, the molecular or monomer density has to be used rather than the effective density of states [Ngu01].

Material parameters of the organic thin film have been chosen equivalent to pentacene: relative dielectric constant $\epsilon_{\mathrm{s}} = 3.5$, electron affinity $\chi = 3.22$ eV, band gap $E_{\mathrm{g}} = 1.85$ eV [Sch02a], and effective density of states $N_{\mathrm{C}} = N_{\mathrm{V}} = 10^{21}$ cm^{-3} (monomer density). Constant mobilities for electrons and holes are assumed, but the absolute values are varied. Unless otherwise noted, $\mu_{\mathrm{n}} = 1.2 \times 10^{-3}$ cm^2/Vs and $\mu_{\mathrm{p}} = 1.2 \times 10^{-4}$ cm^2/Vs are used as standard values. The material is assumed to be intrinsic. In addition direct recombination was taken into account. For an organic material with low mobility the bimolecular rate R_{direct} described by the Langevin form: [Pop82, Blo98] is

$$R_{\mathrm{direct}} = k \left[np - n_{\mathrm{i}}^2 \right], \tag{5.7}$$

with

$$k = \frac{\mathrm{e}}{\epsilon_0 \epsilon_{\mathrm{r}}} \left(\mu_{\mathrm{n}} + \mu_{\mathrm{p}} \right). \tag{5.8}$$

The source, drain and gate contact materials are described as metals. The gate contact material is characterized solely by its work function, which has been chosen to 4.08 eV,

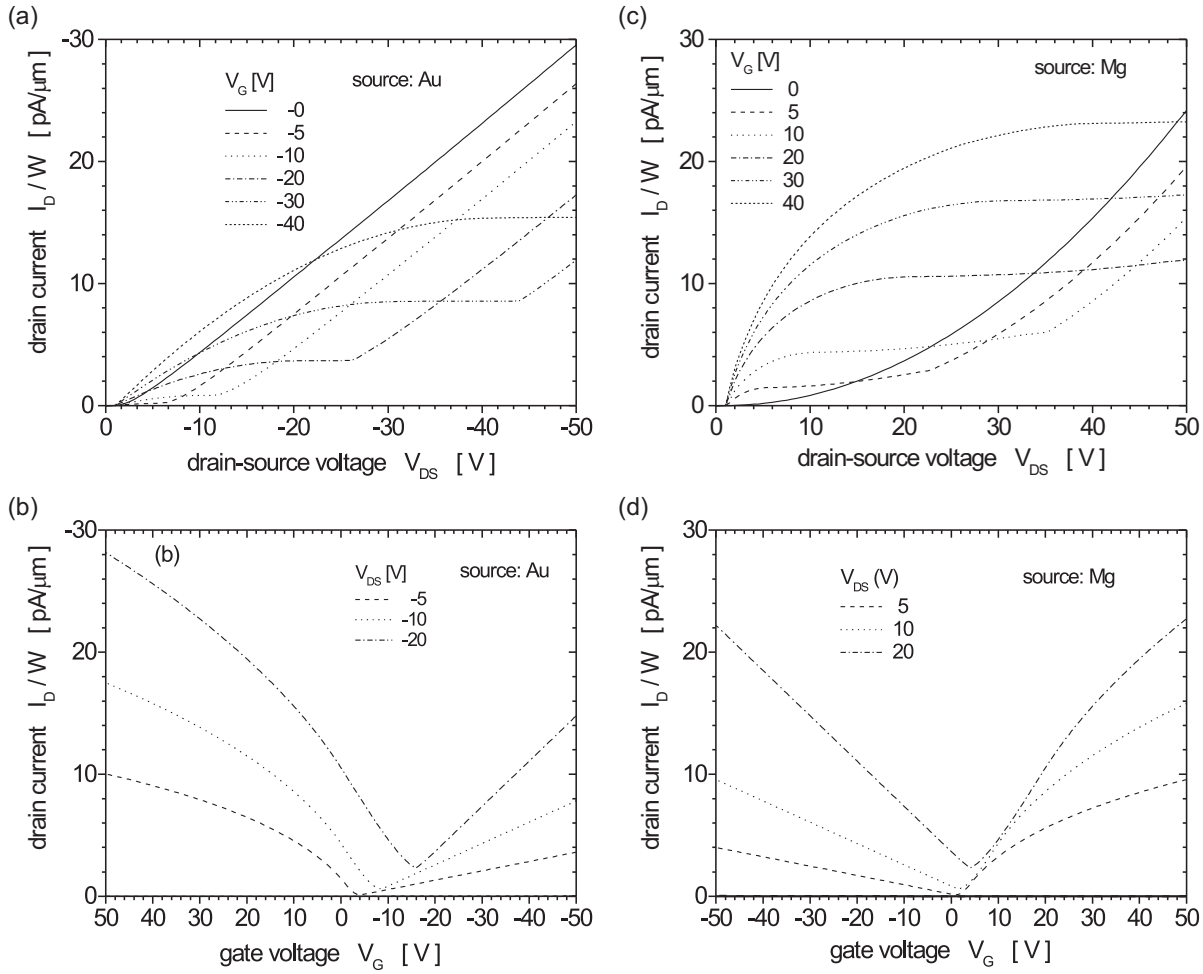

Figure 5.16: *Simulated output (a) and (c) and transfer characteristic (b) and (d) for the monolayer model structure shown in Figure 5.15. The two cases of Au (a) and (b) and Mg (c) and (d) defined as source contact are distinguished.*

corresponding to $n^+ - Si$ with a doping concentration of $N_\mathrm{D} = 8 \times 10^{18}$ cm^{-3}. The exact value is not really of interest because only the flat band voltage is directly influenced. In contrast, the work functions of the source and drain contacts are crucial quantities. These work functions differ to enable hole injection from one and electron injection from the other contact. Thus, for the Au contact we have chosen 5.0 eV, which is close to the HOMO level of pentacene. For the Mg contact 3.635 eV is used as standard value. The difference between these metal work functions and the energy of the transport states, i.e. χ for electrons and $(\chi + E_\mathrm{g})$ for holes, where χ is the electron affinity acts as barrier at the contacts. Possible dipole layers or Fermi-level pinning can be modelled by choosing a corrected work function. For any given set of parameters, one simulation with the Au contact as source and one with Mg as source have been carried out. All results correspond to a temperature of 300 K.

For the standard barriers, the hole density at the Au contact is 6.6×10^{19} cm^{-3}, whereas the electron density at the Mg contact is rather low, i.e. 1.0×10^{14} cm^{-3} . Therefore, the Au contact will be an accumulation contact for holes. Its properties remain unchanged for small variation of its work function. On the other hand, at the Mg contact, depletion exists as far as the electron channel is formed and the electron current depends sensitively on small variations in the value of the Mg work function. Additionally, the ambipolar current consisting of an electron current injected at Mg and a hole current injected at Au depends on the ratio of the electron and hole mobilities. The standard parameters used have been chosen such that the device clearly exhibits ambipolar properties.

Results and Discussion

Current-voltage characteristics simulated with the standard parameters defined above are shown in Figure 5.16 for both cases of Au defined as source and Mg defined as source. The output characteristic in Figure 5.16(a) and (c) qualitatively exhibits the same characteristics of ambipolar behavior as the experimental dependencies do for the asymmetric bilayer heterostructure in Figure 5.3(a) and 5.4(a), however, there are also some differences. The simulated transfer characteristics are shown in Figure 5.16(b) and (d) on a linear scale.

In the simulated output characteristic with Au as source (Fig. 5.16(a)), typical *p*-channel characteristic is observed for negative gate and drain-source voltage up to where saturation sets in. In contrast to the experimental data (Fig. 5.3(a)), which show a soft onset of the drain current with positive curvature, in the simulated data the current increase is linear. For higher $|V_{DS}|$ the steep almost linear increase of the current begins abruptly, with a gate source voltage dependence that indicates an electron current, and an almost equidistant parallel shift with V_G. The onset of this increase is clearly at a lower drain-source voltage than in Figure 5.3(a). A shift of this onset voltage can be caused by interface charges [Paa05]. The transfer characteristic with Au as source shows the normal linear dependence of the active region for low negative drain-source voltage and negative gate voltage for the *p*-channel. If the gate voltage is changed in the positive direction, the onset of the electron current injected from the Mg drain contact occurs. This electron current becomes larger than the hole current for increasing positive gate voltage due to the higher electron mobility. On the other hand, the gate voltage dependence of this current becomes then sublinear as expected from a nonohmic electron injecting contact. Although the current exhibits a minimum, there is no real off-state.

The simulated output characteristic for Mg as source shows, in addition to the *n*-channel formation at low drain-source voltages, the additional current for large drain-source voltages arising from hole injection at the Au drain. Similar to the experimental

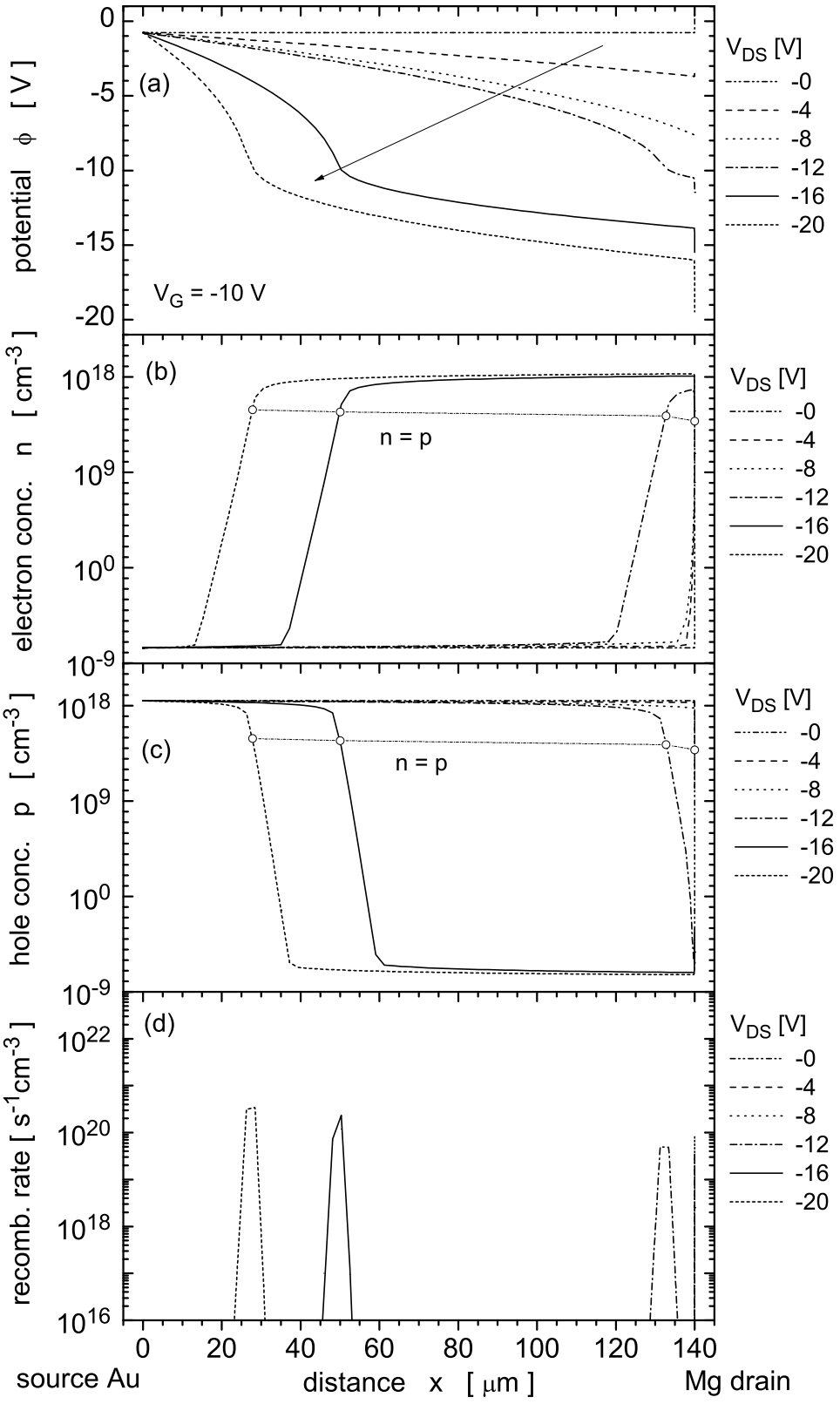

Figure 5.17: *(a) Simulated internal field distribution, (b) concentration profile for holes and (c) electrons, and (d) recombination rate per unit volume for the monolayer model structure shown in Figure 5.15 under different bias conditions for the case of Au defined as source contact.*

data shown in Figure 5.4(b), the onset is visible only for low gate voltages within the considered drain-source voltage range up to +50 V. In good agreement with the experiments, the drain-voltage dependence of the additional hole current is almost quadratic. Also, the electron current increases in saturation almost linearly with the gate-source voltage, in contrast to the normal quadratic dependence. This is also observed in the simulated transfer characteristic (Fig. 5.16(d)), which here becomes sublinear for large positive gate voltage. The hole current again exhibits a linear gate-source voltage dependence.

To summarize, the simulated model system indeed qualitatively shows the characteristics typical of ambipolar operation, which have been measured at the asymmetric heterostructure device. The two deviations of the measured characteristics from the theoretical description at low drain-source voltages, i.e. the soft onset of the current with a positive curvature for Au as source and the rather weak gate-voltage dependence of the drain current for Mg as source do not occur in the simulations due to the simplified description of the contacts. Further insight can only be obtained by an inspection of the internal field and concentration profiles.

The internal device physics is described by three variables, the electrical potential ϕ, the electron concentration n and the hole concentration p. They are shown in Figure 5.17(a) to (c) for Au as source contact along the channel at the interface to the gate oxide. The gate voltage V_G is -10 V and the negative drain-source voltage V_{DS} is varied between 0 and -20 V. The corresponding current-voltage characteristics is shown in Figure 5.16(a). For low $-V_{DS} \leq 8$ V, the potential drops linearly, as the transistor operates in the active transistor region, the electron concentration is negligible, and only the p-channel is formed with a carrier concentration $\approx 3 \times 10^{18}$ cm^{-3}, which is less than the concentration at the Au contact. At $V_{\mathrm{DS}} = -12$ V the potential starts to decrease towards the Mg contact, as in the transition into saturation, but then the curvature changes, indicating the formation of the electron channel with an extension of ≈ 6 μm. In this voltage range the hole channel has vanished. Already for $V_{DS} = -16$ V the electron channel extends for more than ≈ 90 μm and the hole channel is getting correspondingly shorter. At $V_{DS} = -20$ V the onset of the electron channel is further shifted towards the source contact. The occurrence of the electron channel at $V_{\mathrm{DS}} = -12$ V is reflected in the corresponding output characteristic by the onset of the electron current (Fig. 5.16(a)). As expected, recombination occurs at the transition between the two channels, i.e. for $n \approx p$, as depicted in Figure 5.17(d). Thus with increasing drain-source voltage the recombination zone is shifted through the channel towards the Au source, and increases slightly with increasing drain-source voltage. The length of the recombination zone is only few micrometers.

For Mg defined as source contact, the corresponding dependencies are shown in Figure 5.18. A significant difference to the case of Au defined as source exists. because of the

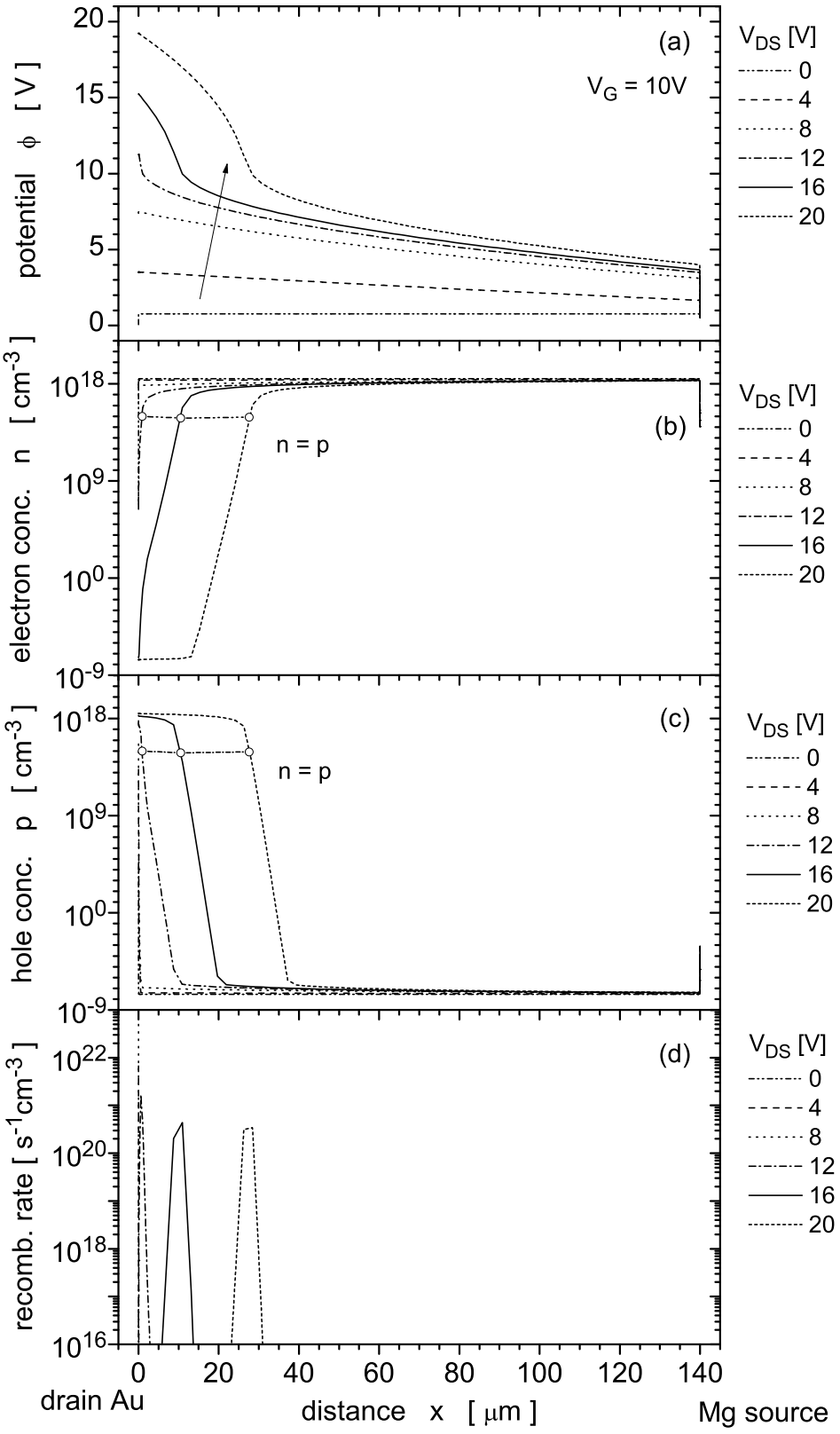

Figure 5.18: *(a) Simulated internal field distribution, (b) concentration profile for holes and (c) electrons, and (d) recombination rate per unit volume for the monolayer model structure shown in Figure 5.15 under different bias conditions for the case of Mg defined as source contact.*

higher electron mobility, the n-channel is longer than the region of the injected holes near the drain, even at $V_{DS} = 20$ V. Therefore, in the output characteristic for $V_G = 10$ V, the hole current begins to predominate only above $V_{DS} \approx 35$ V at $V_G = 10$ V. For the same reason, the location of the recombination moves only to a lesser degree from drain to source. Moreover, recombination is largest near the hole-injecting Au electrode, at a drain-source voltage at which the hole current is not yet visible in the current characteristic, and then decreases with the further increase of V_{DS}.

The simulation shows another remarkable difference between the Mg and the Au contact. Directly at the Mg contact, independent of whether it is defined as source or as drain, there is an abrupt potential drop that increases with $|V_{DS}|$. No such a potential drop occurs at the Au contact. The hole concentration at the Au contact is larger than in the accumulation channel, as discussed before. Thus the Au contact yields an excess of holes. For holes, the Mg contact is a forward-biased Schottky contact. Therefore, if Au is defined as source, the normal p-channel transistor characteristic is obtained for small V_{DS}, as shown in Figure 5.16(a). With Au defined as drain and for sufficiently large $|V_{DS}|$, i.e. when the hole channel predominates, the device operates similarly as a forward-biased diode under space-charge-limited condition, leading to the quadratic $|V_{DS}|$ dependence.

The situation is rather different at the Mg contact, which provides electron injection. For Mg as source, the n-channel is formed because of the applied gate voltage, and, owing to the Mg work function, this contact is a reverse-biased Schottky contact for electrons, with a depletion zone growing with increasing V_{DS}. This depletion at the source limits the n-channel transistor current, and is also responsible for the nonquadratic dependence of the current on the gate voltage. This effect of a Schottky-type source has already been described in [Lin04b]. For Mg defined as drain, the electron-injecting contact is again a reverse-biased Schottky contact. The n-channel is formed only for large $|V_{DS}|$, and the narrow depletion zone increases slightly with increasing $|V_{DS}|$. Nevertheless, with a width of only about 100 nm, the narrow depletion zone acts effectively as ohmic resistance in series with the rather extended accumulation channel, resulting in a linear dependence of I_D on the drain-source voltage.

5.5 Conclusion

Ambipolar transport is observed for the combination of different hole-transport materials, i.e. pentacene, p-6P and α-5T, with the fluorescent electron-transport material PTCDI-$C_{13}H_{27}$ in a bilayer heterostructure OFET. However, no light emission could be detected, even in the case of energetically matched HOMO and LUMO levels of both transport materials. The absence of light emission is probably due to the bilayer heterostructure device

architecture, in which both channels, the electron and the hole channel, are localized in different layers, parallel to each other along the entire channel length and with only little or no charge recombination taking place.

The ambipolar current characteristic is modelled under the assumption that the total current is a superposition of independent electron and hole currents. It could be shown for the first time that a modified Shockley equation leads to an analytical expression of the ambipolar current that qualitatively resembles the experimental data. The electron and hole mobilities and the threshold voltages for n- and p-channel operation are used as free parameters. The approach does not account for contact resistances at source and drain, a reduced gate capacitance for the top organic thin film, and an effective channel length. Therefore, the extracted electron and hole mobilities and threshold voltages can be considered only as approximate values showing tendencies.

Numerical two-dimensional simulations for a single-layer model system yield current-voltage characteristics with similar characteristic features of ambipolar operation as observed experimentally in double-layer structures with an electron-injecting top contact. The origin of the typical ambipolar transport characteristic has been clarified by analyzing the internal field distribution, the electron and hole densities, and by considering recombination. The ambipolar properties depend on the barriers at the injecting contacts and on the ratio of the electron and the hole mobility. According to the simulations, effective recombination occurs only in a narrow region with $n \approx p$. For small $|V_{DS}|$, this recombination zone is located at the drain contact. Increasing the drain-source bias shifts the recombination zone towards the source contact, which is in agreement with recently published results on infrared emission of an ambipolar carbon nanotube FET [Fre04].

Chapter 6

Light-Emitting Organic Field-Effect Transistor

Light-emitting organic field-effect transistors (OFETs) were the scope of the ILO[1] project and this work. The first publications on light-emitting OFETs based on thin films of small molecules were published within the ILO consortium [Hep03, San04]. These devices consisted of a single-layer tetracene thin film, which was bottom-contacted with Au and showed only a unipolar *p*-type characteristic. It is assumed that in these devices the less mobile electrons are trapped and recombine with mobile holes in close vicinity of the drain contact at which they are injected. The EL efficiency is determined by, among other things, the low fluorescence efficiency of tetracene. Therefore, in parallel, the EL properties of *p*-6P [2] and *p*-4P [3] were investigated in unipolar OFETs. Both materials have a larger bandgap than tetracene and are therefore suitable for doping with an efficient phosphorescent emitter, as it was one of the goals of the ILO project. In the following, the electro-optical properties of *para*-oligophenyl based light-emitting OFETs will be discussed.

Unipolar light-emitting OFETs do not offer any advantages compared to existing OLED devices, as recombination is pinned to the drain contact. More flexibility is expected from ambipolar light-emitting OFETs. However, ambipolar OFETs based on a bilayer heterostructure discussed in Chapter 5 did not exhibit light emission. The problem is most likely the low recombination rate between two spatially separated conduction channels. In this chapter, a concept is introduced that allows, for the first time, the realization of an ambipolar light-emitting OFET by coevaporation of a hole-transport and an electron-transport material. The influence of the ratio of these two materials on the electron and hole mobilities as well as the EL properties are investigated.

[1] EU project: **I**njection **L**asing in **O**rganic Thin Films; contract number IST-2001-33057

[2] *para*-sexiphenyl

[3] *para*-quaterphenyl

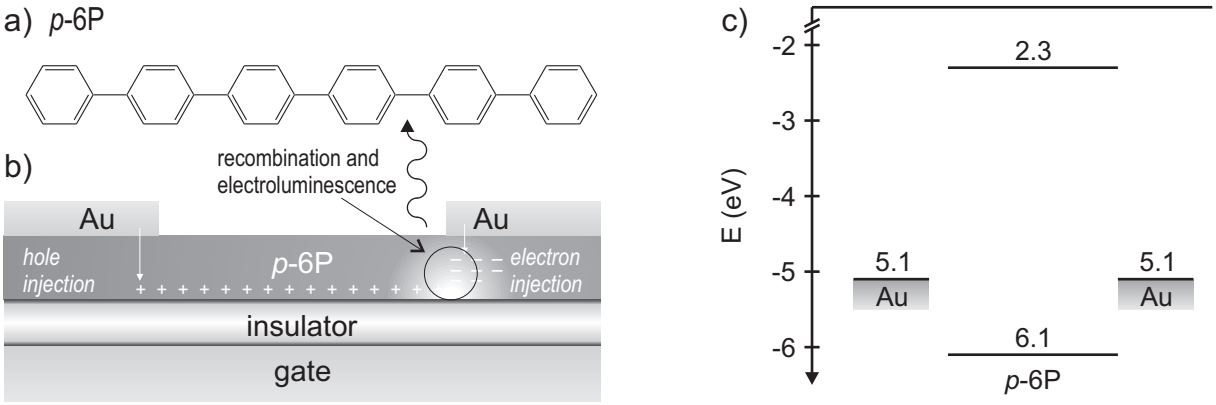

Figure 6.1: *(a) Molecular structure of p-6P, (b) schematic drawing of the Au/p-6P/Au OFET, and (c) energy-level diagram of the device showing the source and drain contact metal work functions [Lid96] and the p-6P HOMO and LUMO levels, taken from [Sch02b].*

Furthermore, a theoretical description of the EL of unipolar and ambipolar OFETs based on a modified Shockley equation and Langevin recombination is given.

6.1 Unipolar Light-Emitting OFETs

Unipolar light-emitting OFETs based on the oligophenyl compounds *p*-4P and *p*-6P have been prepared. *p*-6P is used as both the transport material and emitter, whereas the bandgap of *p*-4P is too large for EL in the visible spectral region. Therefore, it has been doped with an efficient phosphorescent dye and a modified drain contact has been used for efficient electron injection. Thus, the location of the recombination zone could be determined.

6.1.1 p-6P Light-Emitting OFET

p-6P films have been utilized successfully as emissive layer in single-layer [Yan02] and multilayer [Yan02, Yan97, Era95] OLED structures. The bandgap of *p*-6P is 3.8 eV [Sch02b], and the maximum of its blue fluorescence spectrum is at 423 nm, equivalent to 2.9 eV. The optical properties, i.e. the absorption spectrum together with the photoluminescence emission and excitation spectra of *p*-6P, are shown in Appendix B. Its good hole-transport properties allow the application of *p*-6P in field-effect devices. Figure 6.1 shows the molecular structure of *p*-6P, together with the schematic OFET device architecture and the energy-level diagram of source and drain contacts with the HOMO and LUMO levels of *p*-6P [Sch02b]. The device is designed as a top contact architecture in order to ensure a film growth that is as defect-free as possible. The *p*-6P film has a

thickness of 49 nm. Au has been used as source and drain contact, resulting in injection barriers for holes and electrons of 1.1 eV and 2.1 eV, respectively. Attempts to use Mg as top contact were not successful, due to its apparently low sticking coefficient on *p*-6P.

Results

The output characteristic of the *p*-6P transistor is shown in Figure 6.2, together with the gate leakage current and the EL intensity. The EL is measured as the photodiode current of a Si photodiode placed on top of the transistor structure, thus shown in units of pA. The drain current follows a typical unipolar characteristic for *p*-channel device operation. For negative gate and drain-source bias, an active region with increasing current and an saturation region for large $|V_{DS}|$ is observed. The current increase at small drain-source bias is not linear as expected, but shows a concave characteristic, indicating a contact resistance due to the large injection barriers formed between Au and *p*-6P. For positive bias voltage, drain current is observed only for large V_{DS}, and the onset shifts to even larger V_{DS} with increasing gate bias V_G. The magnitude of the current is decreasing with increasing V_G. The gate leakage current is three orders of magnitude smaller than the drain current, thus gate leakage can be excluded as source for EL.

For positive bias voltage, the onset of EL is in good agreement with the onset of the drain current, and is therefore easy to be allocated. For negative bias voltage, the onset of EL coincids with the onset of saturation of the drain current I_D, which is denoted by square symbols in the output characteristic of Figure 6.2(a).

Plotting the photodiode current versus the drain current, as shown in Figure 6.3(a), provides further insight into characteristic features of the device. For negative gate voltages, the onset of EL is very sharp and shifts towards higher drain currents with increasing gate voltage. Contrary, for positive gate voltages, the onset of EL appears independent on the applied gate bias. It occurs already at a current of only 1 μA, as shown in the semilogarithmic plot of the EL intensity as a function of drain current in Figure 6.3(b).

Discussion

The output characteristic with the observed saturation for negative bias voltage is due to hole transport in the channel. No electron transport is observed. As the device shows EL, electrons must be injected at the drain contact. The observed EL and its relation to the drain current is explained by analyzing the charge carrier accumulation in the channel formed between source and drain contact.

For negative gate bias and no drain-source voltage applied, a conductive channel is formed by hole accumulation at the SiO_2/*p*-6P interface. The charge-carrier density is the same at source and drain. Applying a negative drain-source bias, the charge-carrier

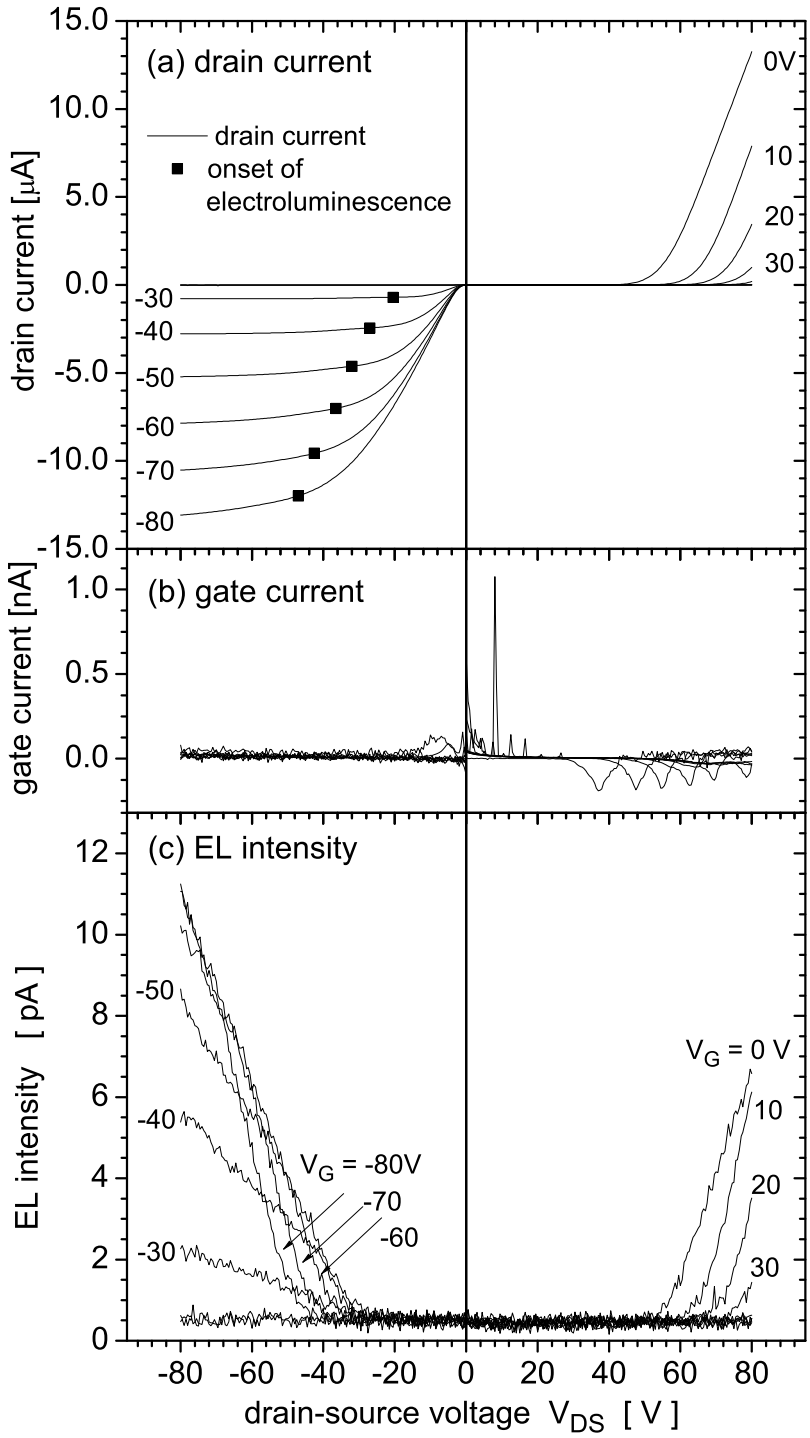

Figure 6.2: *(a) Output characteristic, (b) gate current, and (c) EL intensity of a p-6P field-effect transistor. The symbols in (a) denote the onset drain-source voltage and corresponding drain current for EL.*

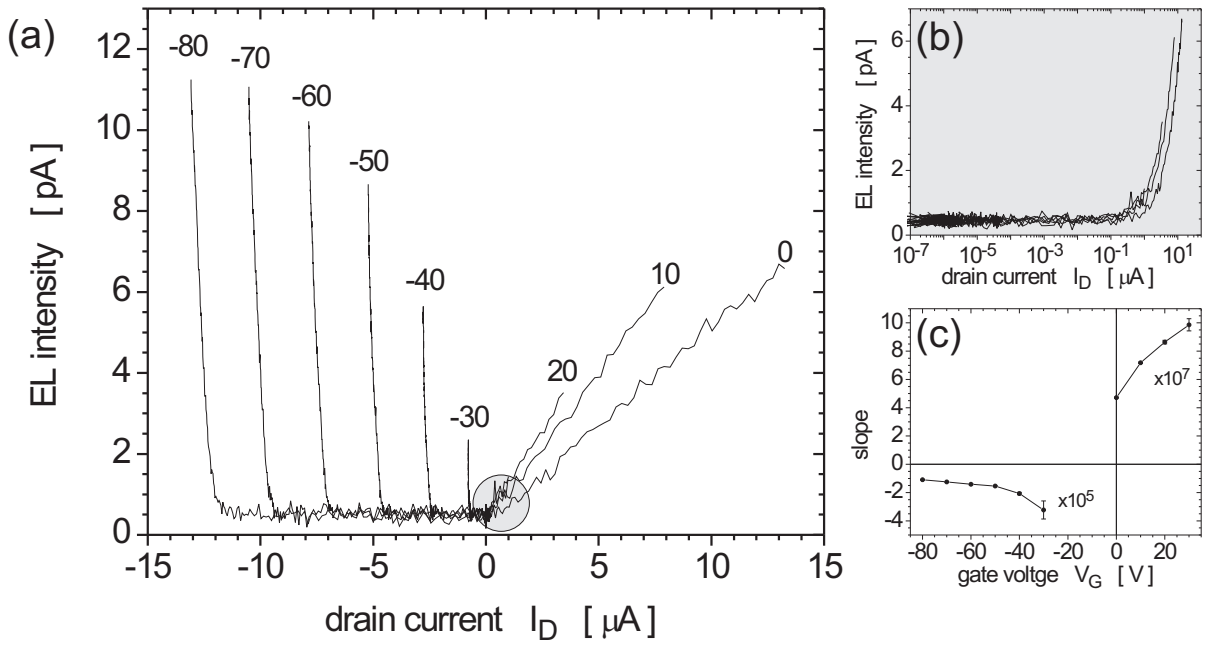

Figure 6.3: *(a) EL intensity as a function of drain current I_D. (b) Semi-logarithmic plot of EL intensity versus drain current I_D. (c) Slope of the linear fit of the EL intensity as function of the drain current versus the applied gate bias.*

density nearby the drain contact decreases and is zero for drain source voltages with $|V_{DS}| = |V_G - V_T|$. For this voltage, the channel is in transition to pinch-off. Increasing $|V_{DS}|$ further, the additionally applied voltage drops at the drain contact, which is then negatively biased with respect to the gate contact, resulting in injection of electrons at the drain contact. No additional electron current is observed, thus, the electron mobility in *p*-6P is negligible and the current does not increase significantly with increasing $|V_{DS}|$, but saturates. However, transported holes and injected electrons recombine and EL is observed. For positive gate bias, electrons are injected from the source contact into the *p*-6P layer, however, even in case of an applied positive drain-source voltage, no current flow is observed due to the low mobility of electrons in *p*-6P. Increasing V_{DS} further with $V_{DS} \geq V_G - V_T$, the drain contact is positively biased with respect to the gate, and holes can be injected at the drain into the *p*-6P thin film. Due to the non-zero hole mobility, a drain current is observed as shown in Figure 6.2. These holes recombine close to the source contact with the injected electrons, resulting in EL observed directly proportional with the drain current.

Therefore, in Figure 6.3 the onset of EL intensity for positive drain current occurs at a hole current of 1 μA, since electrons are injected already at low drain-source voltage. The current threshold for EL of about 1 μA is given by the threshold for the photodiode. The

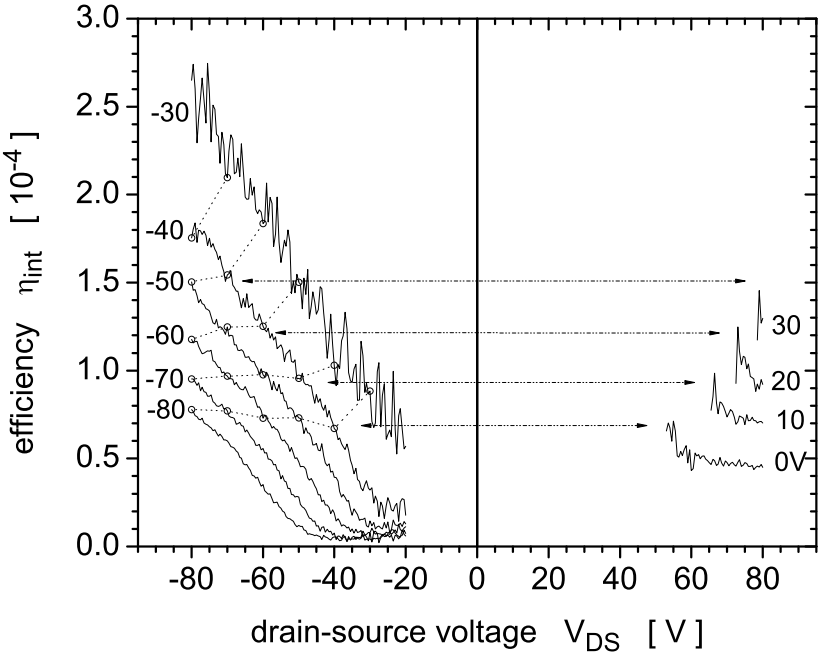

Figure 6.4: *Internal quantum efficiency η_{int} versus the drain-source voltage V_{DS} of the p-6P OFET shown in Figure 6.1 for different gate voltages. The symbols for negative drain-source and gate voltage indicate the equivalent data for the positive bias voltage.*

slope is determined by the number of electrons injected into the device, which depends on the applied gate voltage. For negative drain current, electrons are injected at the onset of saturation but do not contribute to the net current through the device. Therefore, the onset of EL is equivalent to the corresponding saturated drain current, which is almost constant for a defined gate voltage. Thus the slope appears to be very steep. For negative bias voltages, the slope varies between -3.2×10^{-5} and -1.1×10^{-5} for gate voltages between -30 and -80 V, respectively. Contrary, for positive gate voltages, the slope dependence on the applied gate voltage is more distinct, varying between 4.7×10^{-7} and 9.9×10^{-7} for gate voltages between 0 and 30 V, respectively. The slope as a function of the applied gate voltage is shown in Figure 6.3(c). From this plot it can be concluded that electrons are injected even at 0 V gate voltage, which is most likely due to positive interface charges resulting in a shift of the effective gate voltage.

The measured external efficiency of the device is obtained by the ratio of the EL intensity I_{EL} and the drain current I_D and taking the geometry factor of the setup, determined by the area and position of the photodiode, into account:

$$\eta_{ext} = \frac{I_{EL}}{I_D} \cdot \frac{A_{hemisphere}}{A_{photodiode}} \tag{6.1}$$

with $A_{photodiode}$ being the area of the photodiode, and $A_{hemisphere}$ being the surface area of

the hemisphere formed around the emitting device with a radius of the device-photodiode-distance.

The internal quantum efficiency η_{int} can be derived by additionally taking into account the absorption of half the intensity in the silicon substrate, the outcoupling efficiency of $1/n^2$, the photodiode sensitivity S_{ph} and the photon energy E_{ph} according to the emitted wavelength:

$$\eta_{int} = \frac{I_{EL}}{I_D} \cdot \frac{A_{hemisphere}}{A_{photodiode}} \cdot 2 \cdot n^2 \cdot \frac{1}{S_{ph} \cdot E_{ph}} \tag{6.2}$$

Here, n denotes the refractive index of the organic material. The internal quantum efficiency is equivalent to the number of emitted photons per charge. For the emission spectrum of *p*-6P, as shown in Figure B.1, the photodiode sensitivity S_{ph} is about 0.2 A/W and the photon energy E_{ph} can be set to 3 eV. With $n = 1.7$, $A_{hemisphere} = 9.4$ cm^2, $A_{photodiode} = 1$ cm^2 it is $\eta_{int} = 91 \cdot I_{EL}/I_D$. The internal quantum efficiency as a function of the applied drain-source voltage is shown in Figure 6.4. For negative bias voltages, the efficiency depends on both the gate voltage and the drain-source voltage. For positive gate bias, the efficiency is almost constant for a given gate voltage. The applied drain-source and gate voltage in case of positive bias can be transcribed into negative bias voltage according to the method described in Chapter 5. This is shown by the symbols connected with dotted lines.

Conclusion

The *p*-6P OFET is a unipolar device, emitting light for positive and negative bias voltages. The observation of EL is not correlated with the gate leakage current but requires pinch-off of the hole channel and consequently the injection of electrons at the drain contact. The internal efficiency of the device is in the order of 10^{-4}, whereas the measured external efficiency is two orders of magnitude smaller. The absolute intensity is too low for optical allocation of the position of the recombination zone. Thus, an additionally doped device structure will be discussed in the following section.

6.1.2 *p*-4P/*p*-4P:Ir(btp)$_2$acac Light-Emitting OFET

p-4P is an organic hole-transport material with a relatively large bandgap of 4.1 eV [Pog02]. Thus in order to emit in the visible spectrum it has to be doped with an efficient emitter. Doped *p*-4P films, however, show poor transport properties, because the dopant does not only compromise the film growth and decrease the molecular order within the thin film, the dopant molecules act also as trap sites, therefore additionally decreasing the mobility. Thus, the transistor is designed as a bilayer heterostructure of an undoped

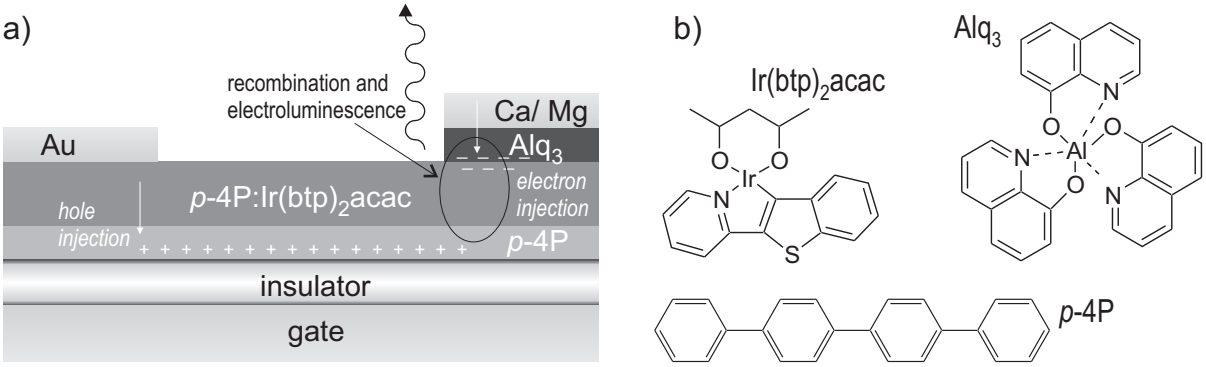

Figure 6.5: *(a) Schematic drawing of a heterostructure OFET combining an undoped p-4P and an Ir(btp)$_2$acac doped p-4P layer. The undoped p-4P layer has a thickness of 10 nm, the doped layer is 30 nm thick. Au (40 nm) is used for hole injection and an Alq$_3$ (20 nm)/Ca (15 nm)/Mg (8 nm) contact for electron injection. (b) Molecular structures of Ir(btp)$_2$acac, Alq$_3$ and p-4P.*

p-4P layer for charge-carrier transport and a doped *p*-4P layer on top. As dopant the phosphorescent dye Ir(btp)$_2$acac [4] has been used, which is known as efficient emitter in OLED devices [Ada01, Che03a].

The schematic device structure of the Ir(btp)$_2$acac doped *p*-4P OFET is shown in Figure 6.5(a). The transistor consists of an undoped *p*-4P thin film in order to optimize the charge-carrier transport close to the SiO_2 interface. This undoped *p*-4P thin film is covered with an Ir(btp)$_2$acac doped *p*-4P thin film. The doping density is $5 - 10\%$. The device is top contacted to ensure defect-free film growth. Au is used for efficient hole injection and a Ca/Mg contact for efficient electron injection. In order to improve the electron injection and thus increase the EL efficiency, an Alq$_3$ [5] intermediate layer is introduced. Figure 6.5 shows the molecular structure of Ir(btp)$_2$acac, *p*-4P and Alq$_3$. The layer thicknesses are 150 nm for the gate insulator SiO_2, 10 nm for the undoped *p*-4P layer, 30 nm for the Ir(btp)$_2$acac doped *p*-4P thin film and 20 nm for Alq$_3$. The channel length and width of the device are 60 μm and 2000 μm, respectively.

The energy level diagram for the device between source and drain contact is shown in Figure 6.6. Since charge carrier transport takes place at the insulator interface, the transported charges have to pass the Ir(btp)$_2$acac doped *p*-4P thin film twice. Hence, the energetic levels of this layer are shown at the source as well as at the drain contact. Additionally, the work function of the contact metals Au and Ca are shown. The Ir(btp)$_2$acac doped *p*-4P layer contributes an additional series resistance at both contacts.

[4] iridium(III)bis(2-(2.-benzothienyl)pyridinato-N,C^3)(acetylacetonate)
[5] tris(8-hydroxyquinoline) aluminum

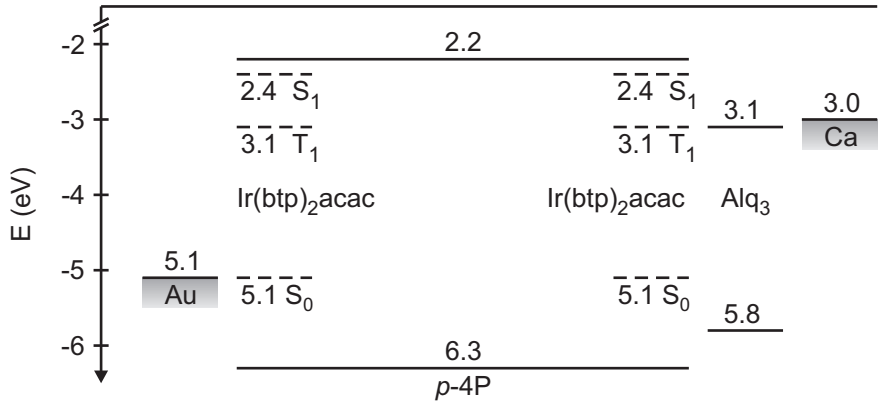

Figure 6.6: *Energy level diagram between source and drain contact of a heterostructure OFET combining an undoped p-4P and an Ir(btp)$_2$acac doped p-4P layer, as in Figure 6.5. At both contacts, injected charge carriers cross the Ir(btp)$_2$acac doped p-4P layer prior to accumulation within the p-4P thin film. At the Ca/Mg contact, an additional Alq$_3$ layer is sandwiched in between the metal contact and the Ir(btp)$_2$acac doped p-4P layer. The energetic values for p-4P were estimated based on the HOMO and LUMO levels of p-6P [Sch02b] and the singlet energy of p-4P [Pog02]. The levels of Ir(btp)$_2$acac are taken from [Che03a], of Alq$_3$ from [Che01].*

Results

Figure 6.7 shows the output characteristic for the device for negative gate and drain-source bias. The characteristic can be devided in an active region with linear current increase for low $|V_{DS}|$ and a second region at higher $|V_{DS}|$, for which no clear saturation is observed. Additionally, the gate current is plotted as dotted lines to exclude EL caused by gate leakage. Even though the Alq$_3$ thin film assists efficient electron injection from Mg into the organic thin film, no electron transport is observed.

Figure 6.8(a) is a top view photograph of the device, which shows both source and drain contacts, the organic thin film and the contact needles. The contact pads are highlighted by a thin white borderline and the channel length L is indicated. Operating the device, EL is be observed by eye as a bright line close to the drain contact, as shown in Figure 6.8(b). The EL appears rather white and its intensity is increasing with increasing drain-source voltage, but was not intense enough to record an emission spectrum.

The photoluminescence (PL) excitation and emission spectrum of the undoped *p*-4P and the Ir(btp)$_2$acac doped *p*-4P film on quartz are shown in Figure B.2. The emission spectrum of *p*-4P peaks at 400 nm. Doped films show the typical Ir(btp)$_2$acac emission with its maximum at 621 nm and a remaining contribution of *p*-4P emission. The excitation spectrum taken between 200 and 600 nm reveals that the Ir(btp)$_2$acac emission is most intense for excitation of *p*-4P, instead of direct excitation of Ir(btp)$_2$acac.

In order to investigate the EL properties of an Ir(btp)$_2$acac doped *p*-4P thin film, an

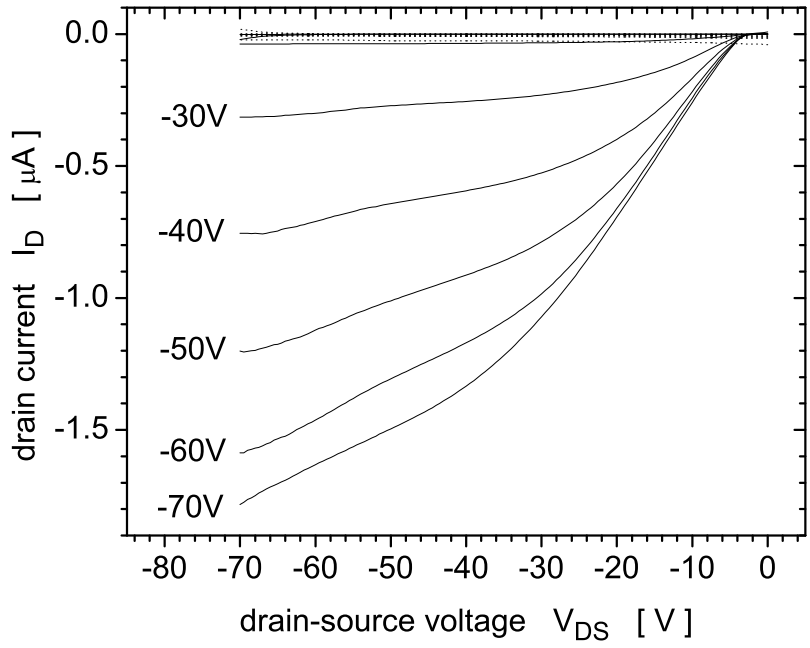

Figure 6.7: *Output characteristic of a heterostructure OFET combining an undoped p-4P and an Ir(btp)$_2$acac doped p-4P layer.*

OLED structure has been prepared. Single layer devices could not be prepared without short-circuit, attributed to pinholes in the organic film, which are filled by the electrode metal. Therefore, an additional Alq_3 film has been sandwiched between the doped *p*-4P film and the Ca/Mg cathode. The film does not only prevent short-circuits, but also improves electron injection. The device structure is shown as inset in Figure 6.9(b). The normalized EL spectrum of the device is shown in Figure 6.9(a) for different current densities between 0.1 and 20 mA/cm^2. For low current densities, the Ir(btp)$_2$acac emission is dominating with only a small contribution of Alq_3 emission. With increasing current densities, Alq_3 emission increases and becomes the dominating one for current densities larger than 10 mA/cm^2. The shift of emission from Ir(btp)$_2$acac to Alq_3 is also observed in the color coordinates, which are shown in Figure 6.9(c).

The electrical characteristic of the OLED is shown in Figure 6.10 for an applied bias voltage between −4 to 8 V. The current voltage characteristic is rectifying with moderate leakage for reverse bias. The onset of light-emission is at 2.2 V, in good agreement with the onset of forward-bias current at 2.0 V. The onset of light-emission appears shifted to slightly higher voltage due to the dark current of the diode.

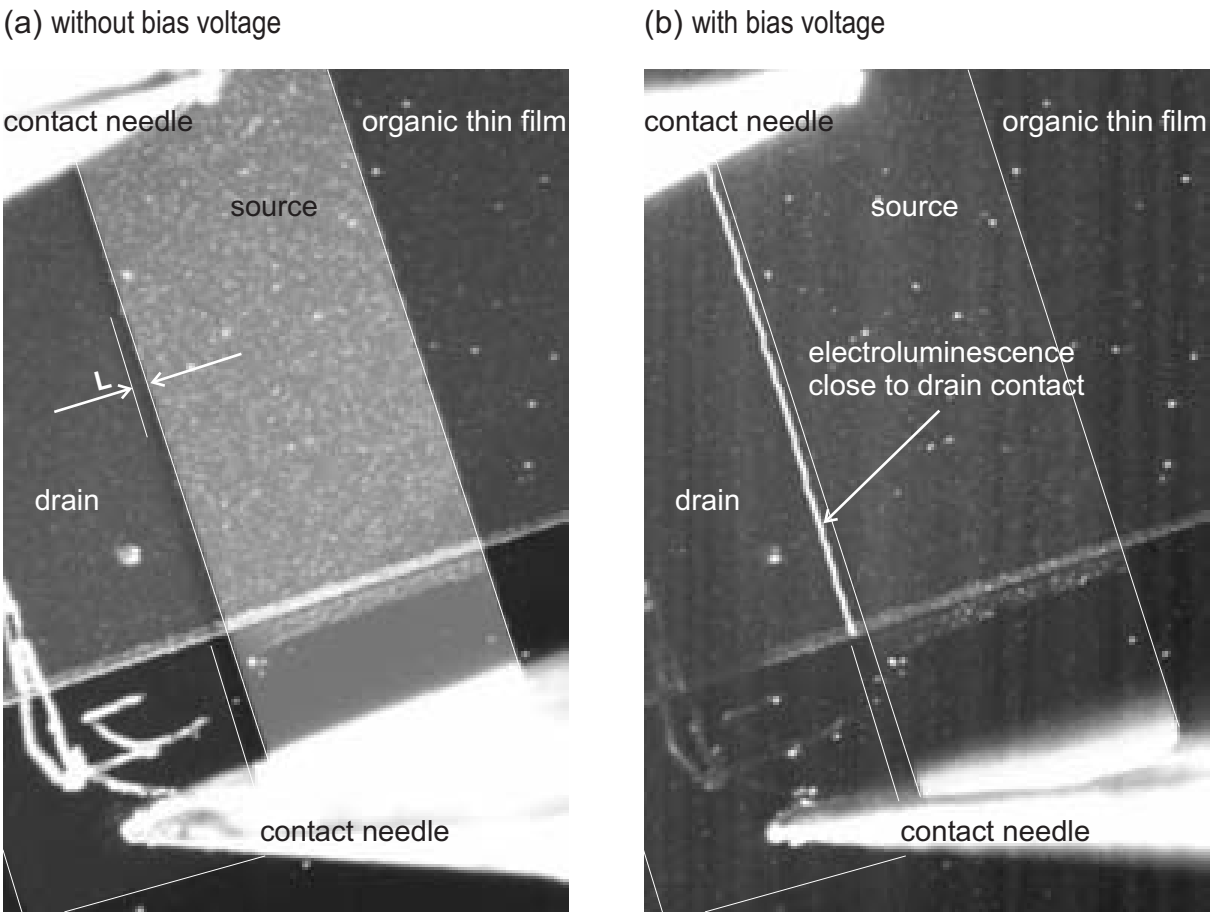

Figure 6.8: *Microscopic top view of the p-4P / p-4P:Ir(btp)$_2$acac OFET without (a) and with (b) applied negative bias voltage. The outline of source and drain contact are marked with thin white lines for better recognition. L indicates the channel length of 60 µm. The EL under bias voltage is observed as a bright line close to the drain contact.*

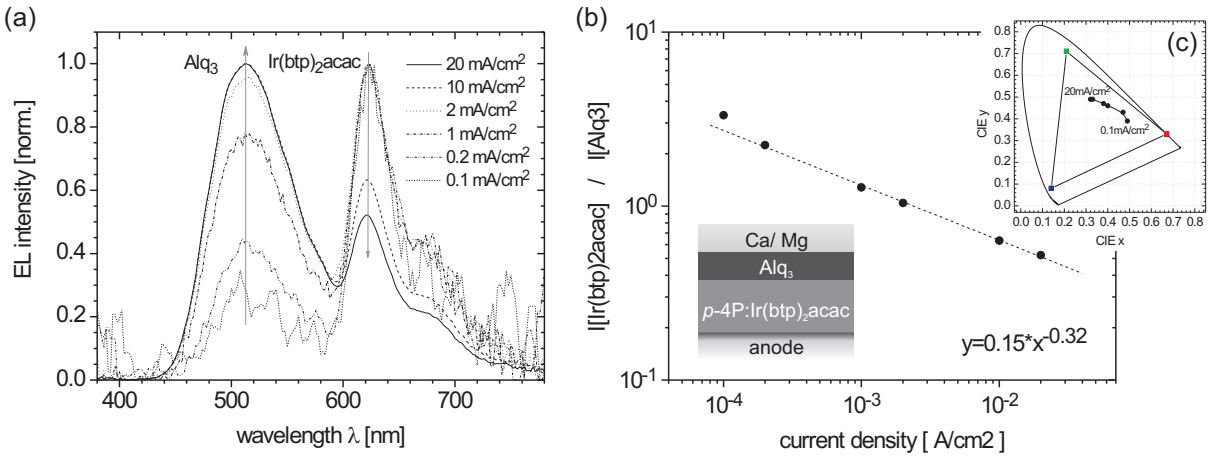

Figure 6.9: *(a) Emission spectrum of the anode/45 nm p-4P:Ir(btp)$_2$acac/20 nm Alq$_3$/Ca/Mg device for different current densities. The doping concentration is 5-10 %. (b) Intensity ratio of Ir(btp)$_2$acac and Alq$_3$ emission versus the current density. The device structure is shown in the inset. (c) Shift of the CIE1931 color coordinates with increasing current densities from red to green.*

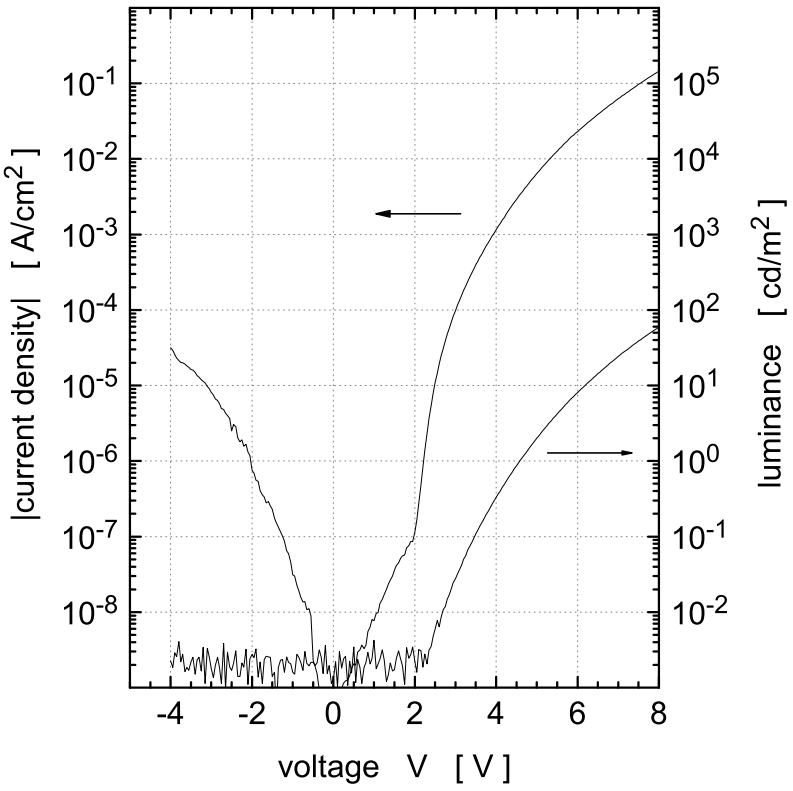

Figure 6.10: *IV characteristics and luminance of the OLED structure shown in Figure 6.9.*

Discussion

The nonlinear onset of the drain current in the output characteristic of Figure 6.7 indicates high contact resistance for the injection of holes. Saturation occurs only for large drain-source voltages, however, even for small gate bias, no electron transport could be observed. This interpretation is consistent with the top view photograph of the emitting OFET, where emission takes place in close vicinity of the drain contact. The PL excitation spectrum indicates energy transfer between *p*-4P and $Ir(btp)_2acac$. The peak intensity ratio of $Ir(btp)_2acac$ and Alq_3 emission as a function of the the current density in the OLED structure is shown on a double-logarithmic plot in Figure 6.9(b). From the linear fit, which is plotted as dotted line, a slope of -1/3 is obtained. The shift from red $Ir(btp)_2acac$ to green Alq_3 emission with increasing current density is also reflected in the shift of the CIE1931 color coordinates, as can be seen in Figure 6.9(c). The color coordinates are not located at the periphery of the NTSC color triangle, but rather grouped not far from the center white point, which is in agreement with the observation of a rather white emission.

Conclusion

Unipolar light-emitting field-effect transistors prove that the injection is not the limiting parameter for ambipolar transport in organic thin films, even in the case of high injection barriers. Rather the transport itself is truly unipolar. Consequently, recombination, exciton formation and radiative decay occurs close to the metallic drain contact.

6.2 Ambipolar Light-Emitting OFET

A definite drawback of a bilayer heterostructure is the small interface area between the electron and the hole transport layers and thus the low recombination rate of electrons and holes. According to the simulation of ambipolar devices in Section 5.4.2, recombination occurs in the region of equal electron and hole concentration. At this position the gate field between source and drain contact is zero. Therefore, the recombination of electrons and holes in a bilayer heterostructure relies only on Coulomb interaction. With a separation of the hole and electron channel of 30 nm, the electric field is according to $E = e/4\pi\epsilon\epsilon_0 r^2 \simeq 10^4$ V/cm. In an OLED, EL is observed only for electric fields larger 10^5 V/cm. Therefore, the distance between both channels has to be reduced by an order of magnitude. However, from single layer experiments it is known that a thin film of only 3 nm is not well connected and therefore shows no charge-carrier mobility. An approach to decrease the distance between both channels with keeping the original film thickness of several 10 nm is to mix electron- and hole-transporting moieties in a single layer, a bulk heterostructure.

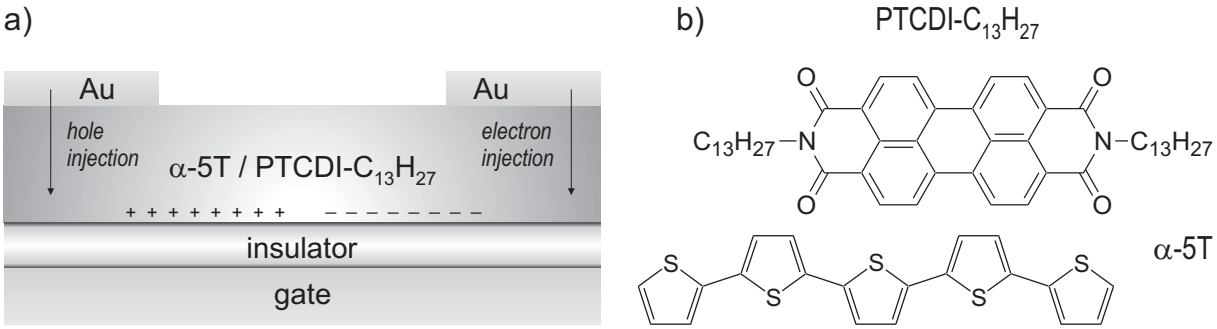

Figure 6.11: *Device structure of a coevaporated thin-film transistor consisting of 50 nm α-5T and PTCDI-$C_{13}H_{27}$. The device is top-contacted with Au. The gate insulator is a 150 nm thick thermally grown SiO_2 on top of a highly doped silicon wafer, used also as gate contact. Reprinted from [Ros04b].*

Additionally, the interface area of both materials is increased. An ambipolar OFET based on a bulk heterostructure has been demonstrated with solution-processed polymer OFETs recently [Gee00, Mei03]. However, the mixing thought to be not suitable for small molecules, since mixing reduces the order within the organic thin film and thus reduces the charge-carrier mobility.

6.2.1 α-5T/PTCDI-$C_{13}H_{27}$ Light-Emitting OFET

With the coevaporation of α-5T [6] and PTCDI-$C_{13}H_{27}$ [7] the principle of an ambipolar light-emitting field-effect transistor was demonstrated for the first time. α-5T was chosen as hole-transport material in order to match PTCDI-$C_{13}H_{27}$ as an electron-transport material with considerably high mobility and fluorescent properties. Among the series of oligothiophenes, α-5T is distinguished by its combination of band-gap and mobility. In order to avoid the formation of charge transfer excitons the HOMO and LUMO levels of PTCDI-$C_{13}H_{27}$ should lie within the levels of the hole-transport material. Thus, tetracene, pentacene and α-6T can be excluded energetically. From an energetic point of view, α-4T would be even more preferable than α-5T, however, the hole mobility in α-4T devices is two orders of magnitude lower than in α-5T, as summarized in Chapter 4. Compared to oligophenyls like *p*-6P or *p*-4P, the field-effect mobility in oligothiophenes was found to be less sensitive to variations in deposition parameters or impurities. Thus, α-5T has been chosen as hole-transport material to be combined with PTCDI-$C_{13}H_{27}$.

The molecular structure of α-5T and PTCDI-$C_{13}H_{27}$ and the schematic device architecture are shown in Figure 6.11. A heavily doped, *n*-type Si wafer (doping level:

[6] α-quinquethiophene
[7] N,N'-ditridecylperylene-3,4,9,10-tetracarboxylic diimide

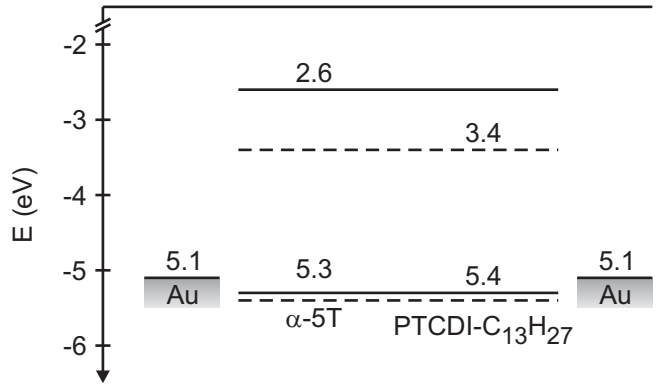

Figure 6.12: *Energy levels (HOMO and LUMO) of α-5T (solid lines) and PTCDI-$C_{13}H_{27}$ (dashed lines) and work function of the Au contact. The values for α-5T are based on its HOMO level [Jon90] and singlet energy [dM99]. The values for PTCDI-$C_{13}H_{27}$ were estimated from [Hir95].*

10^{18} cm^{-3}) with an aluminum back contact acts as gate electrode and substrate. The gate insulator consists of a thermally grown SiO_2 layer with a thickness of 150 nm. Prior to processing, the oxidized wafer was cleaned with a standard wet-cleaning procedure, comprising ultrasonic cleaning in acetone and isopropanol. The organic thin film used in this study was prepared by coevaporation of α-5T and PTCDI-$C_{13}H_{27}$ with ratios of 9:1, 3:1, 1:1, 1:3, 1:9. Additionally, pure α-5T and PTCDI-$C_{13}H_{27}$ OFETs were prepared The deposition rate was 0.3 Å/s for the coevaporated thin film having a final thickness of 50 nm. The Au source and drain contacts were thermally evaporated and had a thickness of 40 nm. The lateral dimensions were defined by shadow masks. The channel length and width of the coevaporated OFET were 40 μm and 55.1 mm, respectively.

The relevant value for charge-carrier injection is the work function of source and drain, as it is shown in Figure 6.12. Au with its work function of 5.1 eV matches the HOMO level of α-5T for efficient hole injection. Even though the combination of Au and PTCDI-$C_{13}H_{27}$ results in a high barrier for electron injection, decent injection is still given, as discussed for single layer devices in Chapter 4.

Results

The study of the morphology of the coevaporated thin films by means of atomic force microscopy is not feasible due to the liquid crystalline properties of PTCDI-$C_{13}H_{27}$ and its high mobility on the substrate, which did not allow to record morphological mappings. Therefore, the structure and phase composition of the coevaporated thin films were studied by laser scanning confocal microscopy. The maxima of PL emission of α-5T and PTCDI-$C_{13}H_{27}$ are well separated with 550 nm and 690 nm, respectively. Therefore, it is possible

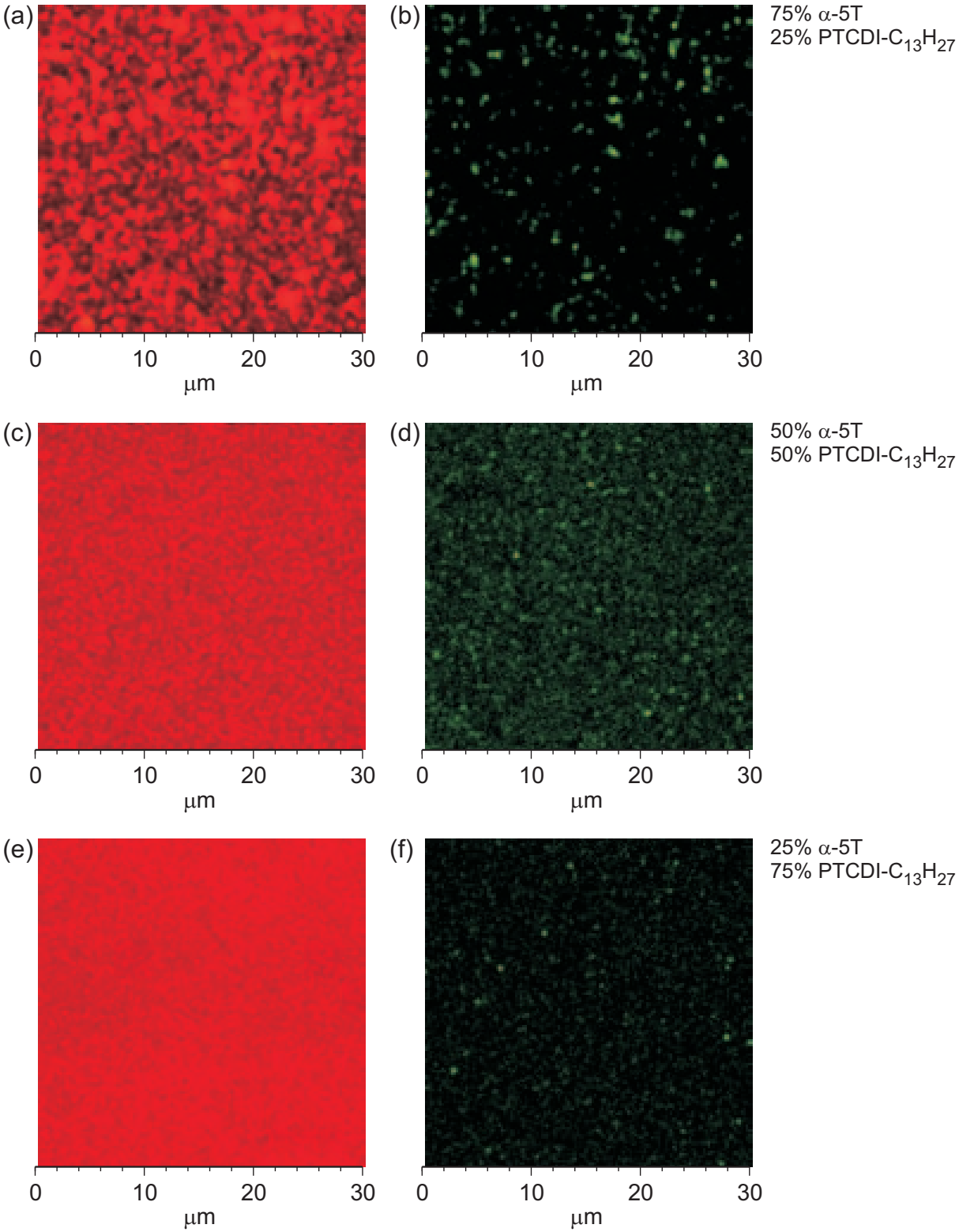

Figure 6.13: *Laser scanning confocal micrograph images (30 μm × 30 μm) of coevaporated thin films of α-5T and PTCDI-$C_{13}H_{27}$ with the respective volume ratio of 3:1 (a,b), 1:1 (c,d) and 1:3 (e,f). The red channel for PTCDI-$C_{13}H_{27}$ emission is shown in (a,c,e) and the green channel for α-5T emission in (b,d,f). The images in (a) and (b) have been taken with 5 times higher intensity.*

to study the phase separation in the bulk heterojunction by selectively recording the spectral ranges related to each material. Figure 6.13 shows the laser scanning confocal microscopy (LSCM) images of coevaporated films of α-5T and PTCDI-$C_{13}H_{27}$ of different ratios 3:1, 1:1 and 1:3 from top to bottom. The left images show the red emission of PTCDI-$C_{13}H_{27}$, whereas the right images show the green emission of α-5T. It should be kept in mind that the quantum yield of PTCDI-$C_{13}H_{27}$ is much higher than the one of weakly emitting α-5T. The coverage for PTCDI-$C_{13}H_{27}$ increases from top to bottom, whereas the coverage of α-5T decreases.

Detailed analysis of the charge-carrier accumulation at the gate insulator was performed by capacitance-voltage (CV) measurements on a metal-oxide-semiconductor (MOS) capacitor structure as described in Section 3.2.1. Applying a DC bias voltage of ± 40 V, an accumulation layer of electrons or holes is formed, respectively. The superimposed AC voltage is modulated with a frequency between 10^4 and 1 Hz. Films with a α-5T to PTCDI-$C_{13}H_{27}$ volume ratio of 3:1 and 1:1 have been selected exemplarily because they show the transition from dominating hole mobility to dominating electron mobility (Fig. 6.14). Three distinct values of the capacitance are determined by the sample geometry. First, the lowest capacitance the system exhibits is its depleted capacitance C_{dep}, for which no carriers at all are injected. It is composed of the capacitance of the gate insulator below the contact pad in parallel with the serial capacitance of the gate insulator and the organic thin film below the top contact. Second, the accumulated capacitance C_{acc}, which is equivalent to charge carriers accumulated below the contact. It is given by the geometric capacitance of the gate insulator for the area of the whole contact. The third capacitance C_{max} originates from the fact that the organic thin film is larger than the contact pad and together with the substrate as an even larger second electrode charge carriers can spread over the whole area of the organic thin film, thus increasing the effective geometric capacitance of the gate insulator. C_{max} describes the maximum capacitance obtained by the geometric gate insulator capacitance determined by both, the contact area and the organic thin-film area.

For the sample with a ratio of 3:1 (Fig. 6.14(a)), the capacitance at 1 and 10 Hz is larger for hole accumulation than for electron accumulation. The capacitance surpasses C_{acc} for 1 Hz at -5 and $+15$ V, and for 10 Hz at -14 and $+26$ V for hole and electron accumulation, respectively. For frequencies larger than 100 Hz, electron accumulation below the contact yields to larger capacitances than hole accumulation. The sample with equal proportions of α-5T and PTCDI-$C_{13}H_{27}$ (Fig. 6.14(b)) shows for each frequency stronger electron accumulation. The electron accumulation reaches at a frequency of 1 Hz almost the maximum value of C_{max}, and the hole accumulation is still strong enough for a channel accumulation. The capacitance surpasses C_{acc} for electron accumulation at -7, -3, $+3$ and $+17$ V for frequencies of 1, 10, 100 and 10^4 Hz. For hole accumulation,

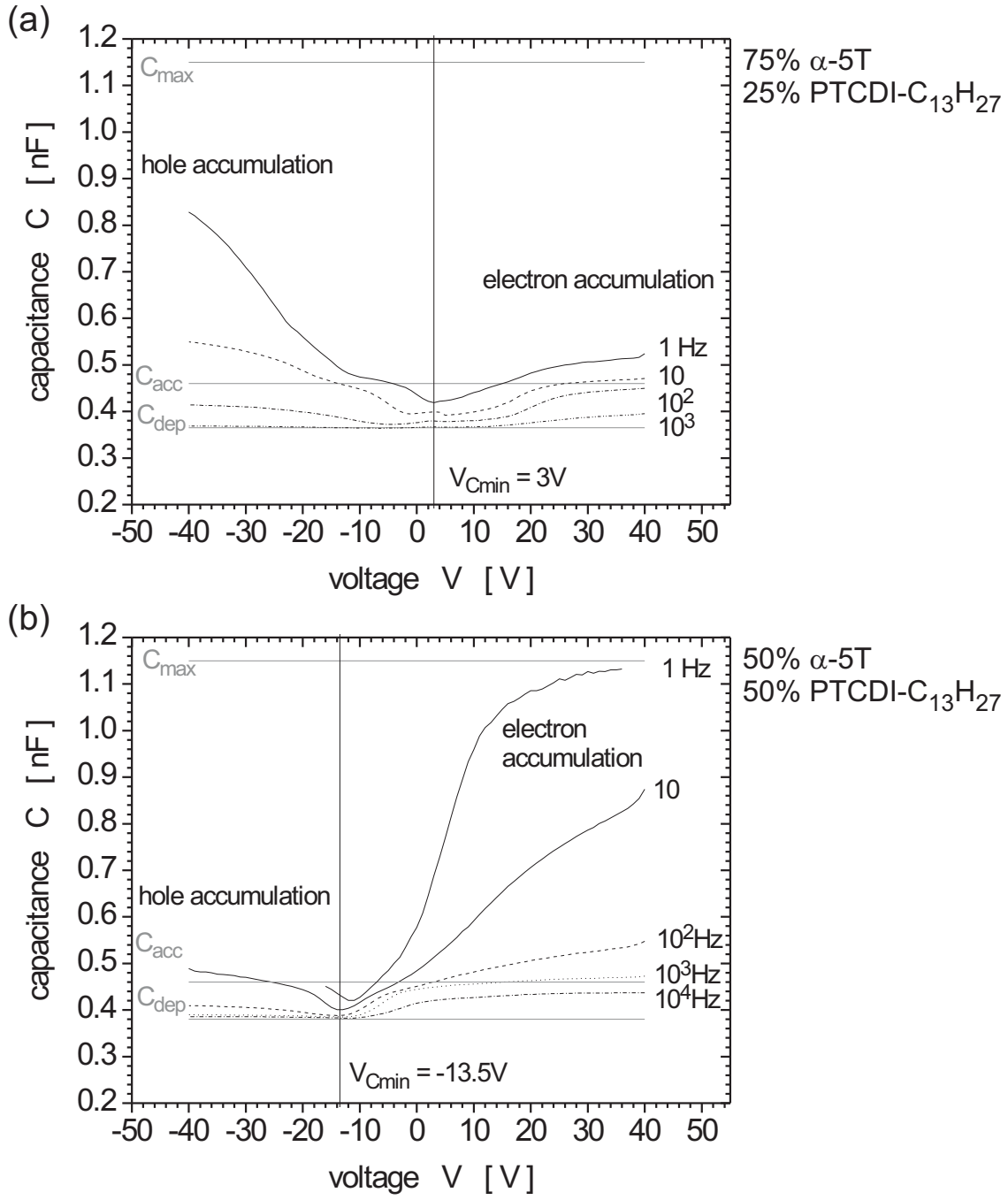

Figure 6.14: *CV measurement for coevaporated thin films with an α-5T to PTCDI-$C_{13}H_{27}$ volume ratio of (a) 3:1 and (b) 1:1. The bias voltage was scanned from -40 to +40 V for frequencies between 1 and 10^4 Hz.*

the capacitance surpasses C_{acc} at -26 V for a frequency of 10 Hz.

Figure 6.15 to 6.18 show the output and transfer characteristics of coevaporated thin-film transistors of α-5T and PTCDI-$C_{13}H_{27}$ with different ratios of both materials. The corresponding EL intensity is shown in units of the photodiode current. Each figure is composed of two independent measurements, one for positive and one for negative gate bias, whereas all scans were performed starting at 0 V.

The devices with a α-5T to PTCDI-$C_{13}H_{27}$ ratio of 3:1 and 1:1 show ambipolar output and transfer characteristic (Fig. 6.15 and 6.16), for which the current in the output characteristic is classified into a region of linear or sublinear increase, a region of saturation and a region of an additional pronounced current increase. In Figure 6.15, i.e. for the device with a α-5T to PTCDI-$C_{13}H_{27}$ ratio of 3:1, the saturated drain current is larger for negative bias voltage, in Figure 6.16 it is larger for positive bias voltage. The transfer characteristic shows the semilogarithmic plot of I_D versus V_G as dashed lines and the square root of I_D at a drain-source bias $V_{DS} = \pm 80$ V as solid lines. Additionally, the linear fit to the square root of I_D as a function of gate bias for large bias voltage is shown as dotted line. Extracted values such as electron and hole mobility μ_n and μ_p, the ratio of EL intensity I_{EL} to drain current I_D, and the drain current at the onset of EL, I_{Donset}. The semilogarithmic plot of I_D from $V_G = 0$ V, features a decreasing current which turns for further increasing $|V_G|$ into an increasing one. In between, the drain current shows a minimum I_{Dmin}. The corresponding gate voltage V_{Gmin} is a function of V_{DS} and the value of $|I_{Dmin}|$ is increasing with increasing $|V_{DS}|$. The most striking feature, however, is the light emission monitored by the photocurrent of the photodiode, as shown in Figure 6.16. In the output characteristic for negative V_{DS} and V_G, the light output is apparently correlated with the nonsaturating drain current. The highest brightness is achieved for $V_G = 0$ V and $V_{DS} = -50$ V and the intensity decreases with increasing $|V_G|$. The onset and magnitude correlates well with the drain current, whereas for positive bias voltages only weak emission is observed and no obvious correlation with the drain current seems to exist. To verify that light emission indeed originates in the recombination of electrons and holes injected at drain and source, the gate current has been measured simultaneously. Even though a small gate leakage current was observed, no correlation between light emission and gate current could be found. For the device with a α-5T to PTCDI-$C_{13}H_{27}$ ratio of 3:1 no EL is observed.

The output and transfer characteristics for devices with an excess of PTCDI-$C_{13}H_{27}$, i.e. an α-5T to PTCDI-$C_{13}H_{27}$ ratio of 1:3 and 1:9, is shown in Figure 6.17 and 6.18. For both devices, a unipolar current with saturation in the positive bias regime is observed. The saturated drain current is larger for the device containing a higher ratio of PTCDI-$C_{13}H_{27}$. The transfer characteristic for positive bias voltage shows the typical unipolar features with leakage current only for small applied gate voltage with $V_G < V_T$ and a

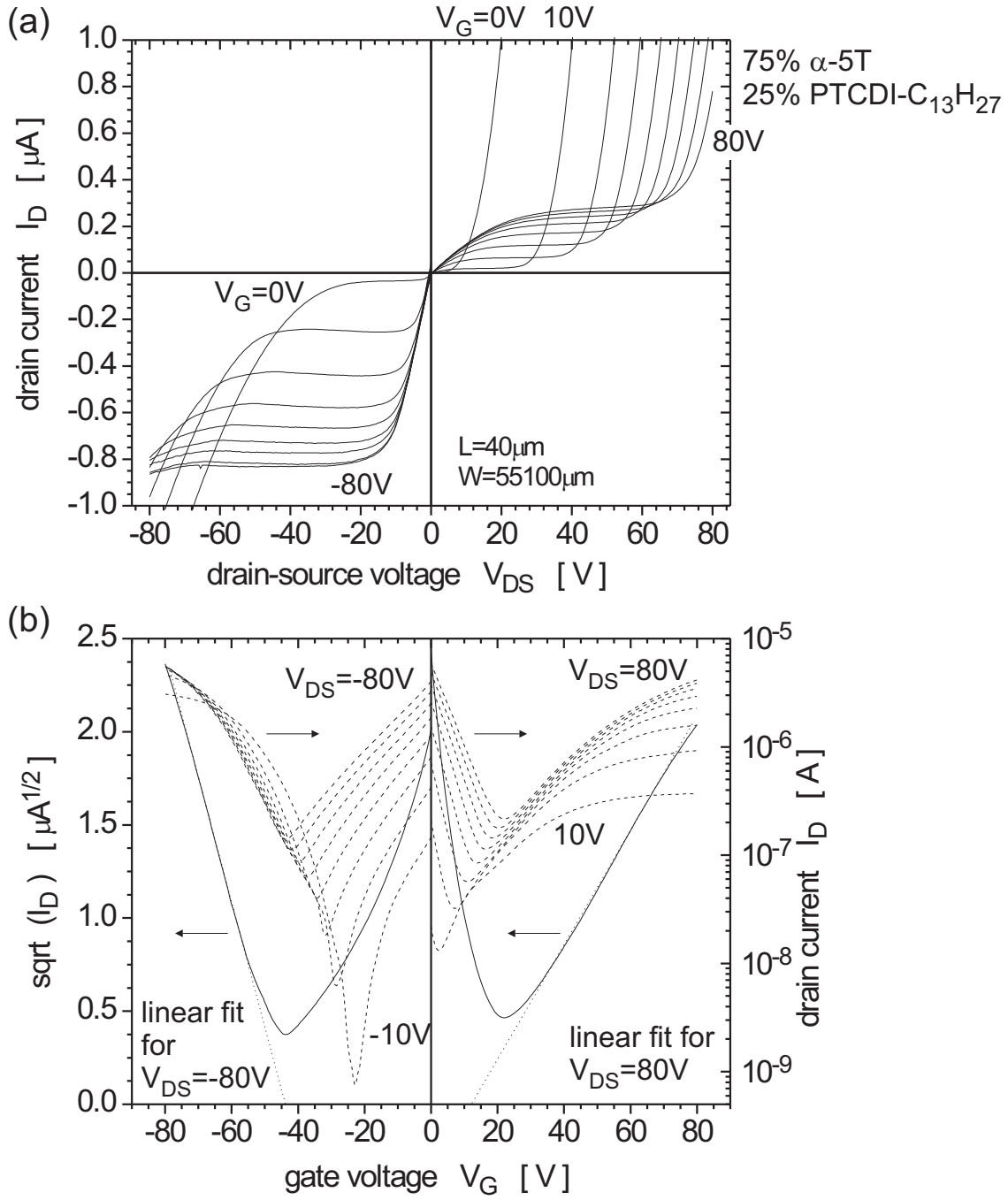

Figure 6.15: *(a) Output and (b) transfer characteristic for the coevaporated α-5T/PTCDI-$C_{13}H_{27}$ thin film with a ratio of 3:1. The solid lines in (b) denote the square root of the drain current at a drain-source voltage of ±80 V. The linear fit for the saturated region is shown as dotted line. Its slope is used to extract the hole and electron mobility. The dashed lines in (b) correspond to the semilogarithmic plot of the drain-current versus the gate voltage.*

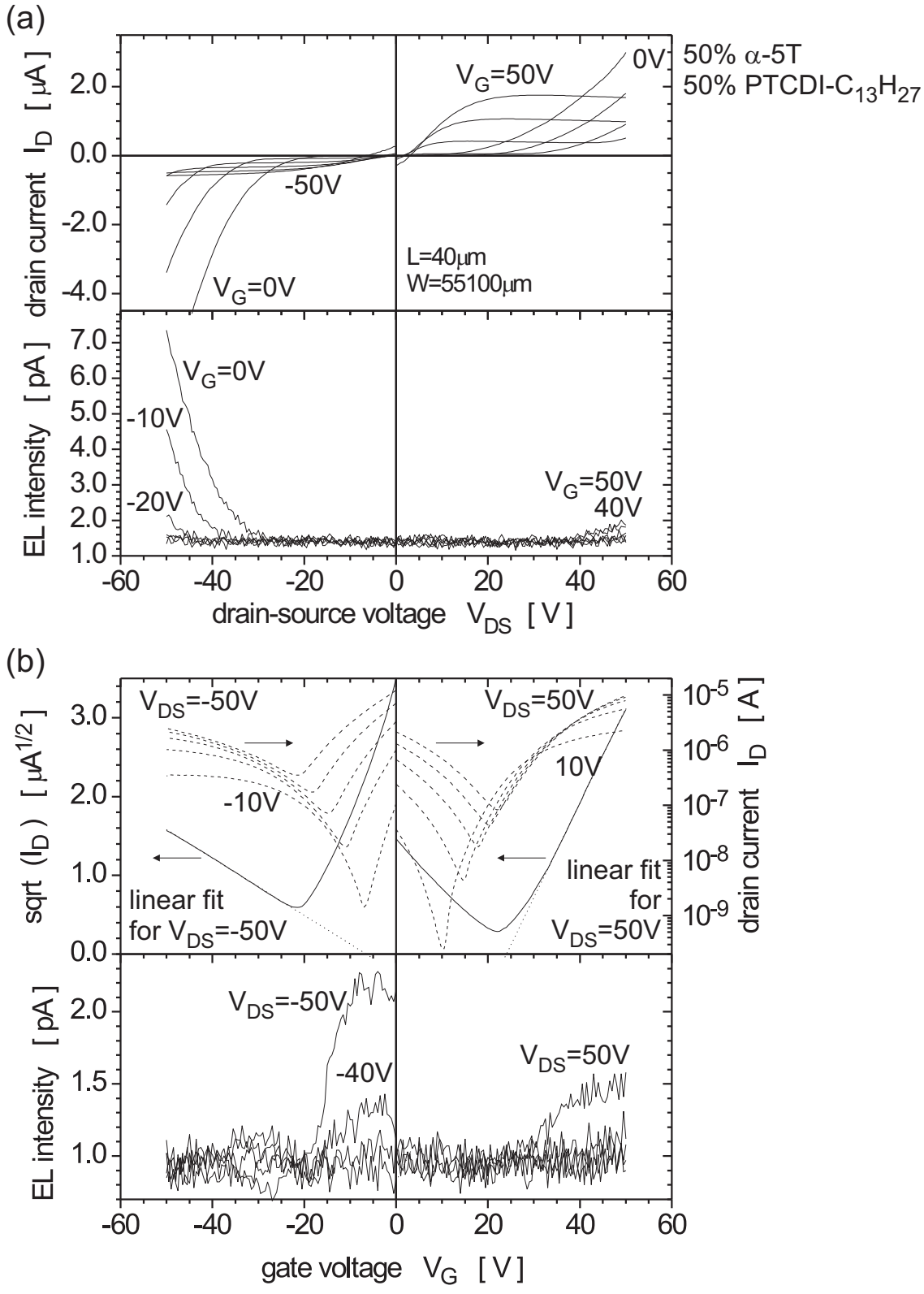

Figure 6.16: *(a) Output and (b) transfer characteristic showing the drain current and EL intensity for the coevaporated α-5T/PTCDI-$C_{13}H_{27}$ thin film with a ratio of 1:1. The solid lines in (b) denote the square root of the drain current at a drain-source voltage of ±50 V. The linear fit for the saturated region is shown as dotted line. Its slope is used to extract the hole and electron mobility. The dashed lines in (b) correspond to the semilogarithmic plot of the drain-current versus the gate voltage. Reprinted from [Ros04b].*

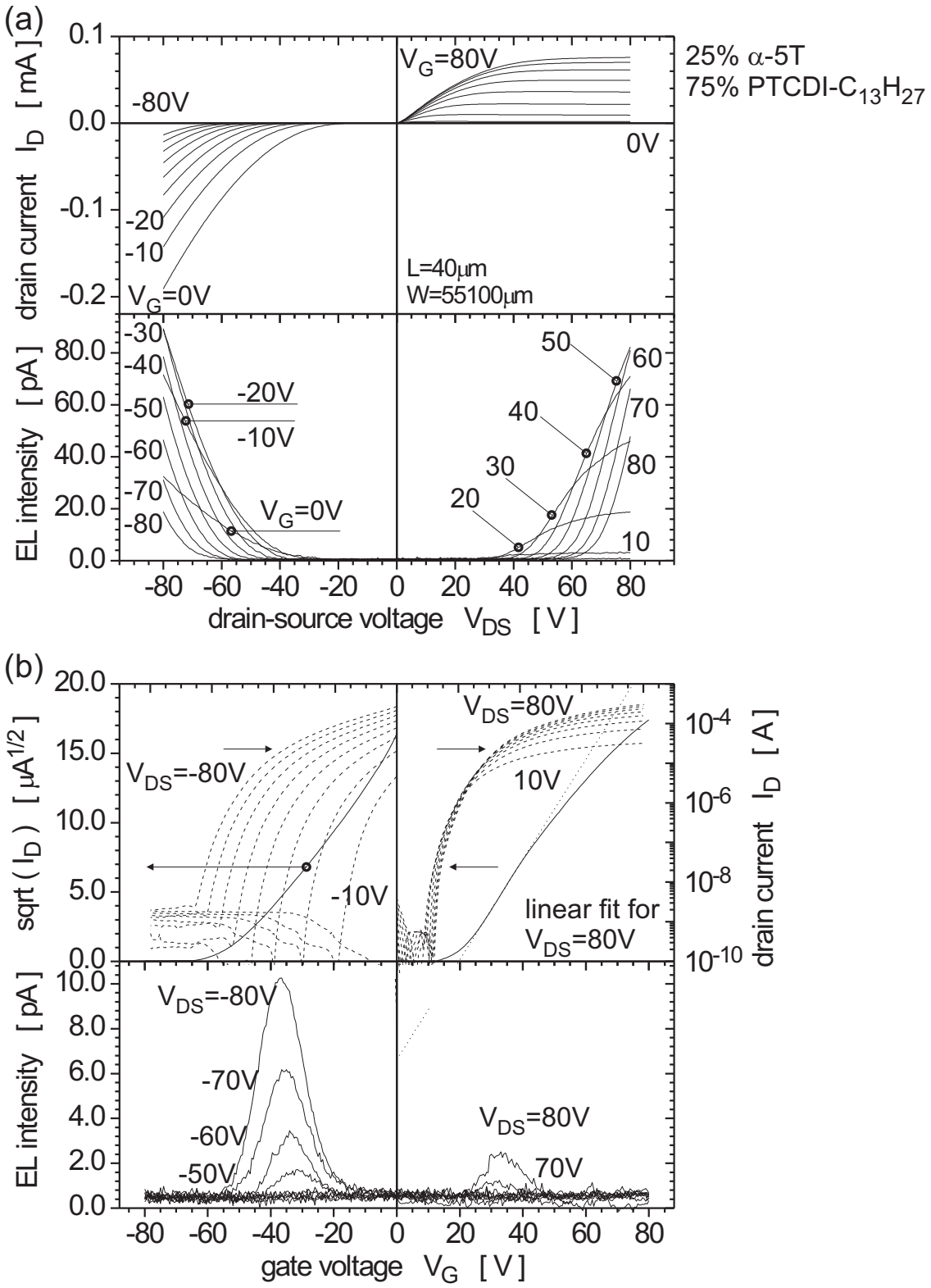

Figure 6.17: *(a) Output and (b) transfer characteristic showing the drain current and EL intensity for the coevaporated α-5T/PTCDI-$C_{13}H_{27}$ thin film with a ratio of 1:3. The solid lines in (b) denote the square root of the drain current at a drain-source voltage of ±80 V. The linear fit for the saturated region is shown as dotted line. Its slope is used to extract the hole and electron mobility. The dashed lines in (b) correspond to the semilogarithmic plot of the drain-current versus the gate voltage.*

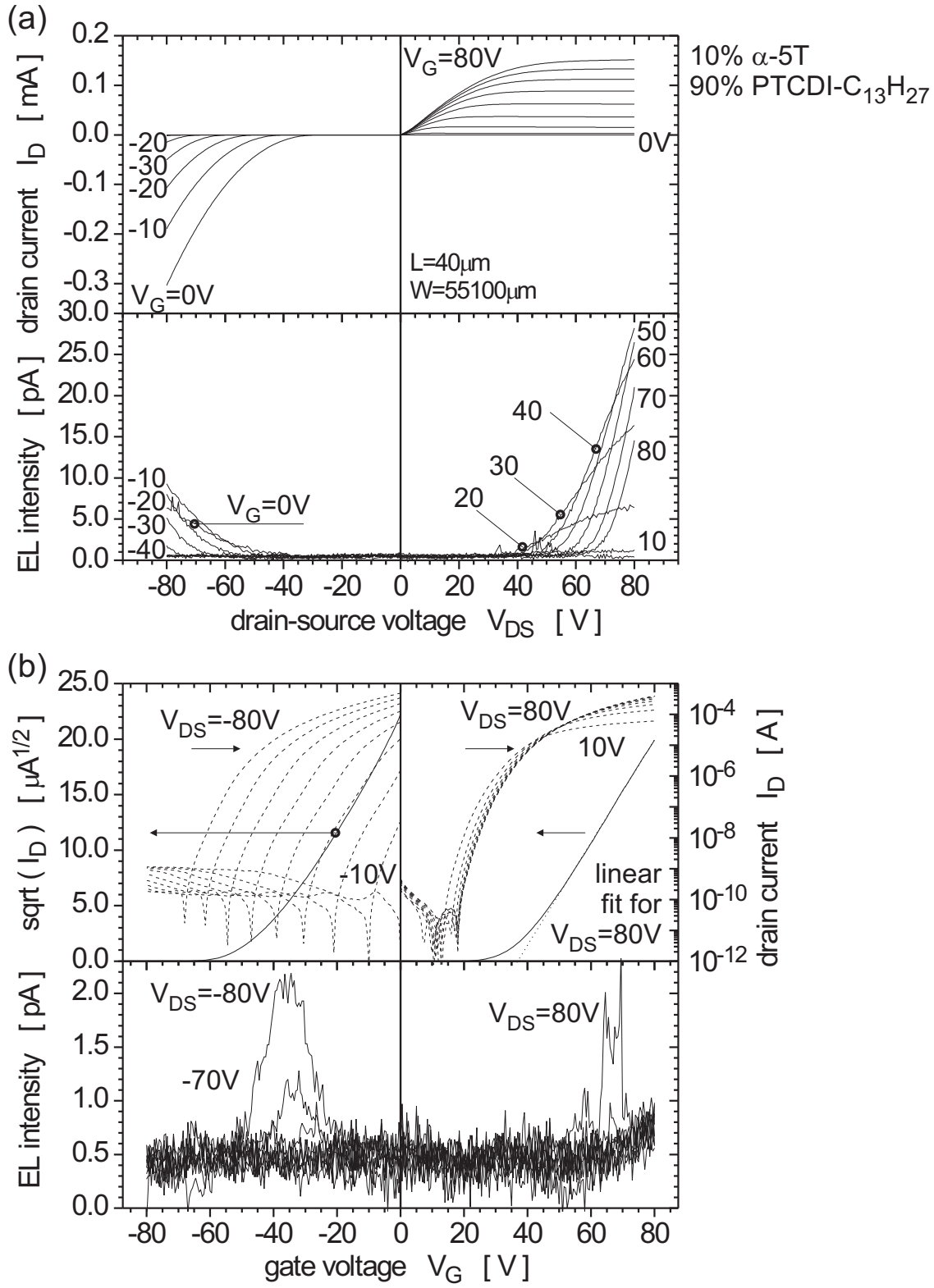

Figure 6.18: *(a) Output and (b) transfer characteristic showing the drain current and EL intensity for the coevaporated α-5T/PTCDI-$C_{13}H_{27}$ thin film with a ratio of 1:9. The solid lines in (b) denote the square root of the drain current at a drain-source voltage of ±80 V. The linear fit for the saturated region is shown as dotted line. Its slope is used to extract the hole and electron mobility. The dashed lines in (b) correspond to the semilogarithmic plot of the drain-current versus the gate voltage.*

ratio α-5T : PTCDI-$C_{13}H_{27}$	μ_p [cm^2/Vs]	μ_n [cm^2/Vs]	$\frac{\partial I_{EL}}{\partial I_D}$ $V_{DS} = 0$V	$\frac{\partial I_{EL}}{\partial I_D}$ $V_{DS} = -10$V	I_{Donset} $V_{DS} = 40$V	I_{Donset} $V_{DS} = 50$V
3 : 1	2.2×10^{-3}	5.5×10^{-4}	n/a	n/a	n/a	n/a
1 : 1	8.6×10^{-4}	9.0×10^{-4}	9.2×10^{-7}	1.2×10^{-6}	1 μA	1.7 μA
1 : 3	n/a	3.6×10^{-3}	1.7×10^{-7}	5.1×10^{-7}	36 μA	49 μA
1 : 9	n/a	6.7×10^{-3}	2.1×10^{-8}	4.7×10^{-8}	63 μA	88 μA

Table 6.1: *Summary of the current characteristic and EL properties of α-5T and PTCDI-$C_{13}H_{27}$ coevaporated OFETs with different ratios of both materials.*

sharp current increase above threshold voltage. Contrary, the drain current for negative bias voltage is decreasing with increasing $|V_G|$ and the onset voltage is not constant, but a function of V_{DS}. For both devices, EL is observed. In the output characteristic, EL occurs only at large drain-source bias, whereas the onset voltage $|V_{DSonset}|$ is increasing with increasing $|V_G|$, as does the slope, resulting in a crossing of curves corresponding to different V_G. In the transfer characteristic, no EL is observed for $V_G = 0$ V and large gate voltages with $|V_G| \geq 60$ V. In between, the EL shows a maximum. The position of the maximum shifts with increasing $|V_{DS}|$ to larger $|V_G|$ and the intensity is increasing with increasing $|V_{DS}|$. Whereas in the output characteristic for negative bias voltage the EL correlates with I_D, for positive bias voltage and also for the transfer characteristic, no obvious relation seems to exist.

Figure 6.19 shows the EL intensity of the output characteristic of devices with an α-5T to PTCDI-$C_{13}H_{27}$ ratio of 1:1, 1:3 and 1:9 as a function of the drain current. A striking feature of all three graphs is the fact that for negative drain bias, the onset of EL is at virtually zero drain current with the slope varying with the applied gate bias. Contrary for positive gate bias, the onset shifts with the applied gate bias, however, the slope is almost constant.

Discussion

The morphology of the α-5T/PTCDI-$C_{13}H_{27}$ thin film with a material ratio of 3:1 in Figure 6.13(a,b) appears to be rather granular. Whereas PTCDI-$C_{13}H_{27}$ seems to form an interconnected network, α-5T seems to form clusters of about 1 μm. The observation of cluster formation and phase segregation is further confirmed with the observation of bulk emission in PL spectra of the coevaporated thin film. Thus, both materials are not mixed homogenously on a molecular level, but instead a bulk heterojunction is formed in contrast to a bilayer heterojunction discussed in Chapter 5. The observation of isolated clusters contradicts with the observed ambipolar characteristic of the device, since the occurrence of both, electron and hole mobility would require not only the PTCDI-$C_{13}H_{27}$ thin film

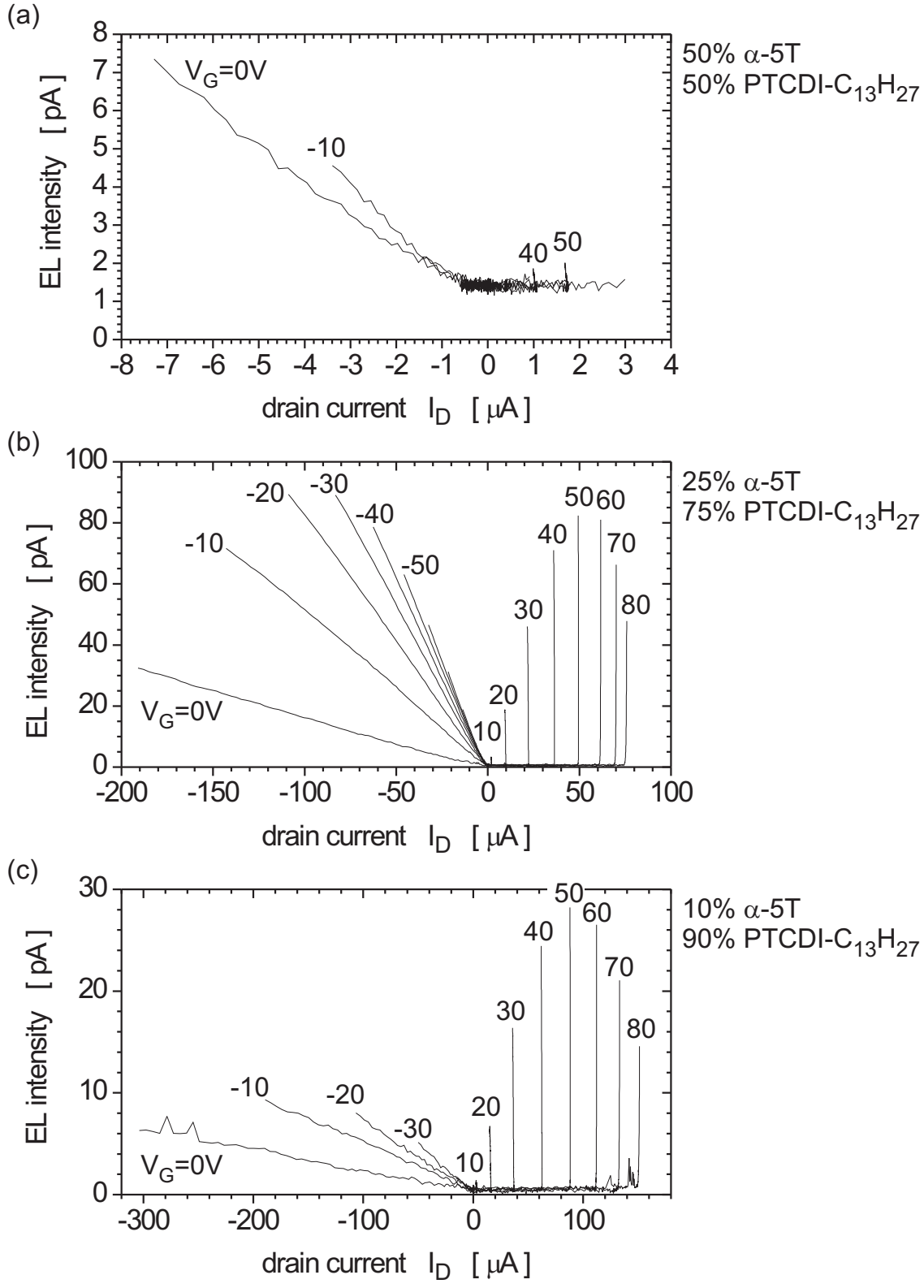

Figure 6.19: *EL intensity as a function of drain current for devices with different ratios of α-5T and PTCDI-$C_{13}H_{27}$: (a) 1:1, (b) 1:3, and (c) 1:9.*

to be interconnected, but also the α-5T thin film. CV measurements confirm that both films are interconnected, since holes as well as electrons are not just accumulated below the contact, but spread within the organic thin film, which is necessary for the channel formation in an OFET device structure. Thus, the α-5T clusters must be interconnected, even though that is not clearly visible in the LSCM images.

Coevaporated thin films with increasing PTCDI-$C_{13}H_{27}$ content as shown in Figure 6.13(c,d,e,f) appear to be rather homogenously mixed. The clusters of α-5T are smaller and seem to be quite homogenously distributed within the film. For the device with a material ratio of 1:1, as shown in (c,d), an ambipolar characteristic is observed (Fig. 6.16), which is also confirmed by CV measurements, as shown in Figure 6.14(b). Thus it can be concluded that the α-5T clusters are interconnected, whereas for the coevaporated thin film with a material ratio of 1:3 they are isolated and enclosed by an interconnected PTCDI-$C_{13}H_{27}$ layer.

Detailed analysis of the CV scans reveal the electron and hole injection for positive and negative bias applied to the silicon wafer. The accumulated charge depends on the concentration of each material within the coevaporated thin film. The CV data are in agreement with the transistor characteristic, from which for an excess or equal ratio of α-5T an ambipolar characteristic is observed, whereas for an excess of PTCDI-$C_{13}H_{27}$, only unipolar transport has been found. Thus, the mobility of α-5T is stronger affected by coevaporation than the one of PTCDI-$C_{13}H_{27}$. It can be assumed that the thin film growth and crystallinity of PTCDI-$C_{13}H_{27}$ is less affected by coevaporation than the one of α-5T. Additionally, the interconnectivity of islands of PTCDI-$C_{13}H_{27}$ might me better than the one of the observed α-5T clusters, as it was concluded already from the LSCM images.

Whereas the devices containing an excess of PTCDI-$C_{13}H_{27}$ show only unipolar electron current, the devices with an equal ratio of both compounds or an excess of α-5T function as ambipolar OFETs. The discontinuity in the output characteristic of Figure 6.16 at $V_{DS} = 0$ V originates from gate leakage at large gate bias. The magnitude of the gate leakage is the same for positive and negatives voltages.

The transfer characteristic, which features an "on-off-on"behavior in ambipolar devices, is used for the extraction of charge-carrier mobility. The "on"state for small gate bias originates from charge-carrier injection at the drain contact, i.e. for negative gate bias, it is an electron current, for positive gate bias a hole current. The residual drain current around the "off"-state is ambipolar, i.e. is composed of both types of charge carriers, whereas the drain current at large gate bias is carried by charges injected at the source contact, equivalent to unipolar devices. A detailed description of the ambipolar transfer characteristic can be found in Chapter 5. From the linear fit to the square root of this region, charge-carrier mobilities in ambipolar devices can be extracted. The ex-

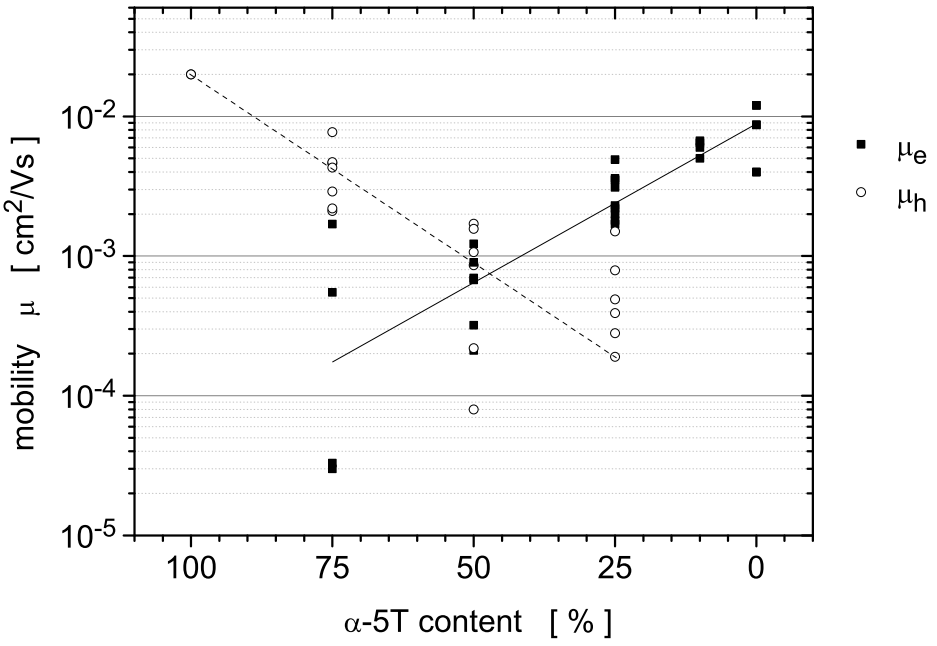

Figure 6.20: *Tuning of the electron and hole mobility in the coevaporated α-5T/PTCDI-$C_{13}H_{27}$ thin film depending on the ratio of both materials.*

tracted electron and hole mobilities for different ratios of α-5T and PTCDI-$C_{13}H_{27}$ are shown in Figure 6.20. The data include the values shown in Table 6.1, together with the mobilities extracted from a larger number of samples to indicate the reproducability of film formation. Additionally, the electron and hole mobility of pure reference devices of PTCDI-$C_{13}H_{27}$ and α-5T are included. The hole mobility in α-5T is 2.5×10^{-2} cm^2/Vs and the electron mobility in PTCDI-$C_{13}H_{27}$ is 5×10^{-3} cm^2/Vs.

For a defined gate voltage, the EL intensity is increasing with increasing $|V_{DS}|$ for $|V_{DS}| \geq |V_{DSonset}|$. However, for a defined drain-source voltage, a maximum value for the EL intensity exists. Figure 6.21(a) compares the EL intensity as a function of the drain current for devices with different material ratios at $V_{DS} = 0$ and -10 V. The data are taken from the outpput characteristics in Figure 6.16 to 6.18. Since the device geometry is the same for all three devices, the absolute EL intensity can be compared. For 0 V as well as for -10 V, the device with a ratio of both materials of 1:1 shows the highest EL intensity. Although it is not the device with the overall highest charge-carrier density, it is the one with the most balanced electron and hole mobility. The higher the PTCDI-$C_{13}H_{27}$ content, the lower is the EL intensity and the more unbalanced are the charge-carrier mobilities. Even though the main emission is expected to origin from PTCDI-$C_{13}H_{27}$, as it can be deduced from PL data in Figure B.3(a), the absolute EL intensity is observed to be rather a direct function of the mobilities than of the content

of the electroluminescent material.

The internal quantum efficiency, as defined in Equation 6.2, is plotted versus the drain-source voltage in Figure 6.21(b). According to the PL spectrum of the coevaporated film of α-5T and PTCDI-$C_{13}H_{27}$, the photodiode sensitivity S_{ph} is 0.4 A/W and the photon energy is about 2 eV. Thus, the internal quantum efficiency is $\eta_{int} = 68 \cdot I_{EL}/I_D$. The data refer again to the output characteristics in Figure 6.16 to 6.18. The curves are restricted to gate voltage of 0, -10 and -20 V, since the data for the device having a α-5T to PTCDI-$C_{13}H_{27}$ ratio of 1:1 are available only for these gate voltages. Again, the device with balanced electron and hole mobility shows the highest efficiency and the one with the most unbalanced mobilities shows the lowest efficiency. The efficiencies obtained from the transfer characteristic cannot be compared in such a way, since EL occurs for different gate and drain-source voltages, i.e. at different internal fields.

Conclusion

With the coevaporation of the hole-transport material α-5T and the electron-transport material PTCDI-$C_{13}H_{27}$, an ambipolar light-emitting field-effect transistor could be demonstrated for the first time. The light intensity is controlled by both the drain-source voltage V_{DS} and the gate voltage V_G. Moreover, the latter can be used to adjust the charge-carrier balance for a given V_{DS} in such a way, that the EL intensity is maximized.

The simultaneous formation of an electron and a hole channel combined with ambipolar transport shows that even though the two materials are coevaporated, they form interconnected thin films. The charge-carrier mobilities can be tuned by the ratio of both materials and varied over three orders of magnitude. Thus the ambipolar bulk-heterostructure OFET demonstrates the general concept of adjusting electron and hole mobilities by coevaporation of two different organic semiconductors.

Regarding EL, the advantage of a bulk heterostructure over a bilayer heterostructure is the increased recombination rate compared to bilayer devices due to shorter distances and thus stronger Coulomb interaction. Furthermore, the effective interface between both materials is increased. The recombination rate depends on the mobility and accumulated charge of both materials in the bulk heterostructure. Thus, the efficiency depends directly on the ratio of both materials. The efficiency is maximal for the material ratio of 1:1, i.e. for balanced mobilities, according to Figure 6.20. The system can still be improved regarding its EL efficiency by the choice of a more efficient emitting material than PTCDI-$C_{13}H_{27}$

The bulk heterostructure requires the two materials to be deposited in a way that the mixing does not occur on a molecular scale, but rather on a nanoscale to microscale, in order to obtain defect free growth and simultaneously increase the interface area of the

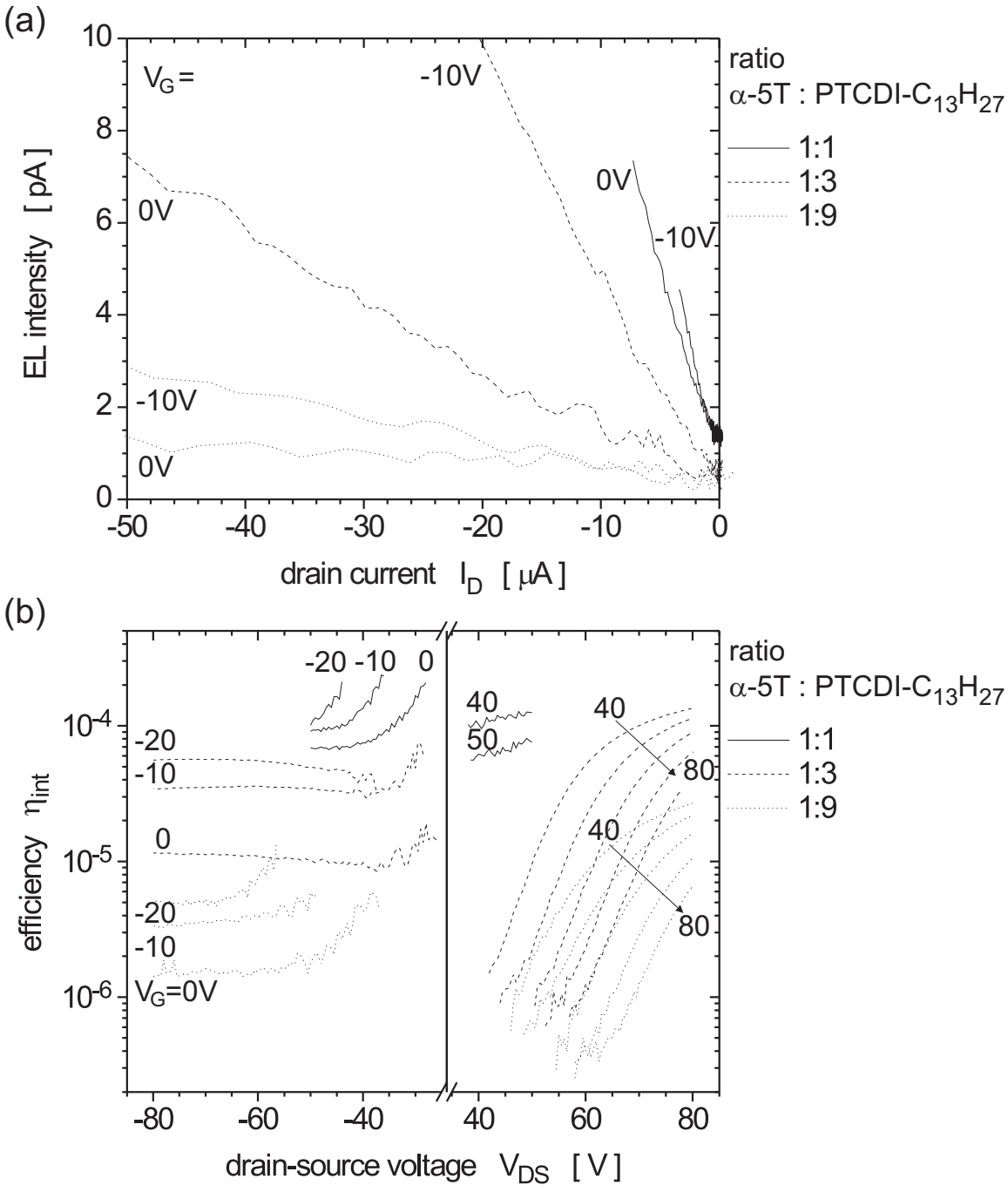

Figure 6.21: *(a) Comparison of the EL intensity versus the drain current at a gate voltage of 0 and −10 V and different ratios of α-5T and PTCDI-$C_{13}H_{27}$. (b) Comparison of the internal quantum efficiency η_{int} as a function of the applied drain-source voltage V_{DS} at a gate voltage of 0 and −10 and −20 V and different ratios of α-5T and PTCDI-$C_{13}H_{27}$.*

heterojunction.

The device structure serves as a model system for ambipolar light-emitting OFETs and demonstrates the flexibility given by the bias voltage and ratio of both materials, as demonstrated in the next section.

6.2.2 Modelling the Electroluminescence of Ambipolar OFETs

In the following, a basic analytical model for the EL of an ambipolar OFET will be derived. It is based on the modified Shockley equation for the ambipolar drain current as derived in Section 5.4.1, which is a superposition of an electron current and a hole current. Furthermore, Langevin recombination is assumed [Lam70], thus the EL intensity and recombination rate of electrons and holes between source and drain electrode can be expressed as:

$$I_{EL} \propto \int_0^L \frac{e}{\varepsilon_r \varepsilon_0} \cdot (\mu_n(x) + \mu_p(x)) \cdot n(x) \cdot p(x) \cdot dx \,, \tag{6.3}$$

with ε_r the dielectric constant of the coevaporated organic layer, $n(x)$ and $p(x)$ the electron and hole densities, and $\mu_n(x)$ and $\mu_p(x)$ the electron and hole mobilities along the channel, respectively. It can be rewritten to:

$$I_{EL} \propto \int_0^L \frac{e}{\varepsilon_r \varepsilon_0} \cdot (\mu_n(x) \cdot n(x) \cdot p(x) + \mu_p(x) \cdot n(x) \cdot p(x)) dx \,, \tag{6.4}$$

With $I_{Dn} = e \cdot \mu_n(x) \cdot n(x)$ and $I_{Dp} = e \cdot \mu_p(x) \cdot p(x)$, it can be rewritten as

$$I_{EL} \propto \int_0^L \frac{1}{\varepsilon_r \varepsilon_0} \cdot (I_{Dn}(x) \cdot p(x) + I_{Dp}(x) \cdot n(x)) dx \,, \tag{6.5}$$

Assuming that the recombination current is much smaller than the drain current, thus recombination can be neglected, it is $I_{Dn}(x) = \text{const} = I_{Dn}$ and $I_{Dp}(x) = \text{const} = I_{Dp}$ with I_{Dn} and I_{Dp} being the superimposed electron and hole current resulting in an ambipolar characteristics as described previously in Equation 6.3 to 6.6. Furthermore, also the accumulated charge is assumed to be constant, which can be done since recombination is restricted to a narrow region between source and drain contact, in which the charge-carrier density in a first approximation can be considered to be constant. Thus the EL can be expressed as:

$$I_{EL} \propto \frac{1}{\varepsilon_r \varepsilon_0} \cdot (I_{Dn} \cdot p + I_{Dp} \cdot n) \,, \tag{6.6}$$

With $n = I_{Dn}/e\mu_n$ and $p = I_{Dp}/e\mu_p$. The overall expression for the EL intensity I_{EL} used for simulation with Mathcad© can be found in Appendix C. It is obtained by inserting Equation 5.3 to 5.6 into Equation 6.6. Free parameters are the electron mobility μ_n,

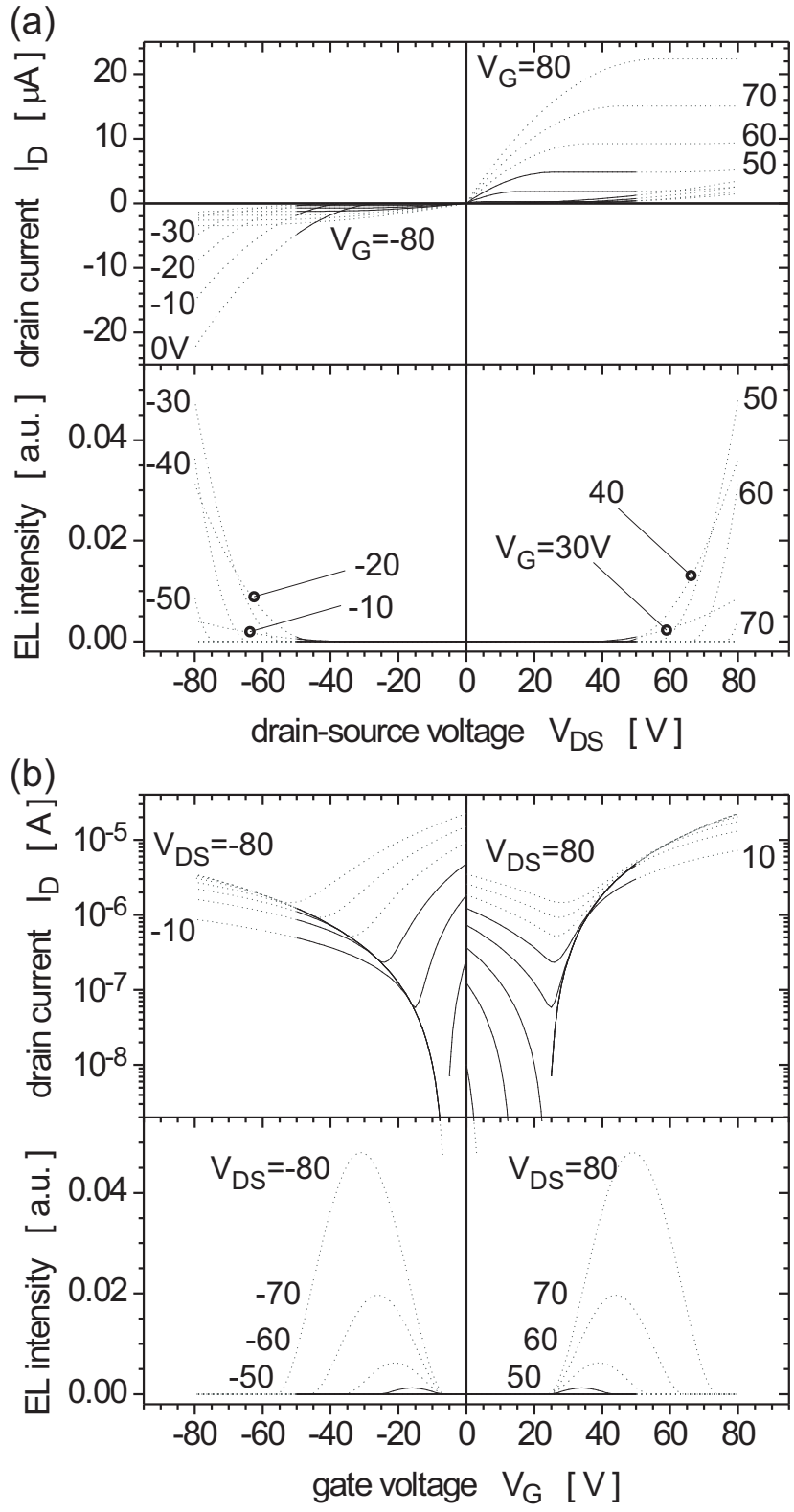

Figure 6.22: *Drain current and EL intensity for the simulated output and transfer characteristic. The electron and hole mobility are chosen to* $\mu_n = 4.5 \times 10^{-4}\ cm^2/Vs$ *and* $\mu_p = 4 \times 10^{-5}\ cm^2/Vs$*, respectively. All other parameters are described in the text.*

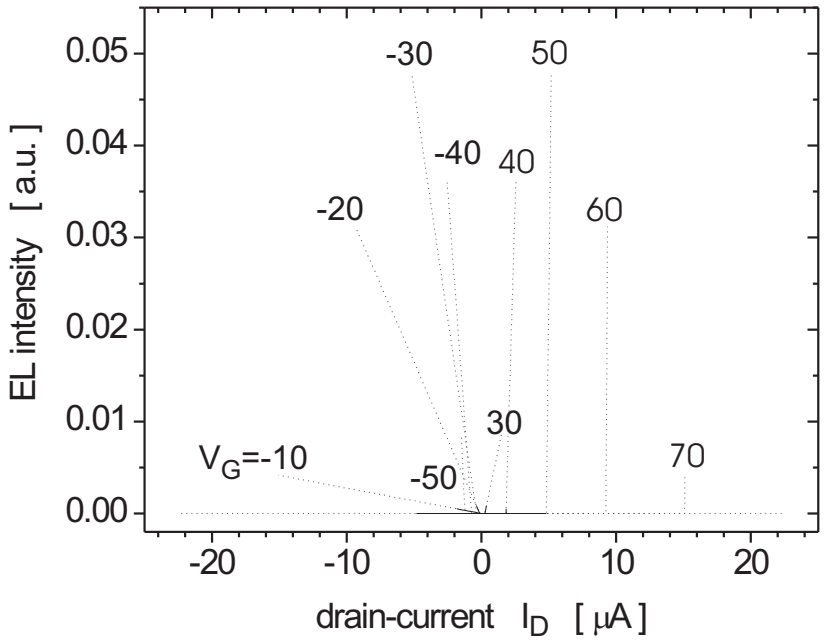

Figure 6.23: *Simulated EL intensity as a function of the drain current for an ambipolar light-emitting OFET with different ratios of electron and hole mobility.*

the hole mobility μ_p, and the threshold voltages for n- and p-channel device operation, V_{Tn} and V_{Tp}, respectively. The model does not account for any contact resistances, injection barriers and eventual change in effective channel length. Furthermore, the recombination rate is only described by the charge-carrier mobilities and the accumulated charge. It does not account for the separation of both charges in the bulk heterojunction and the fluorescence efficiency.

The parameters have been chosen for the device with an α-5T to PTCDI-$C_{13}H_{27}$ ratio of 1:1 and thus according to the experimental data in Figure 6.16(b), i.e. the electron mobility is $\mu_n = 4.5 \times 10^{-4}$ cm^2/Vs, the hole mobility is $\mu_p = 4 \times 10^{-5}$ cm^2/Vs, the threshold voltage for n-channel device operation is $V_{Tn} = 24$ V, the equivalent threshold voltage for p-channel operation is $V_{Tp} = -6$ V, the channel length is $L = 40$ μm, and channel width is $W = 55100\mu$m.

Results

The simulated drain current and EL intensity for output and transfer characteristic are shown in Figure 6.22(a) and (b). The simulation has been performed for a drain-source and gate voltage range between 0 to ± 80 V and is shown as dotted line. Since the simulated device of Figure 6.16 has been characterized only for a voltage range between 0 to ± 50 V, the simulated data referring to the latter voltage range are shown as solid

lines. The drain current shows all characteristic features of an ambipolar characteristic as discussed in detail in Chapter 5. Thus, the emphasis will be put on the description of the EL intensity.

For a defined gate voltage, the EL intensity increases with $|V_{DS}|$, whereas the onset of EL shifts with increasing $|V_G|$ towards larger $|V_{DS}|$. The slope of the EL as a function of $|V_{DS}|$ also increases. In contrast, in the transfer characteristic for defined drain-source voltage, a maximum exists in the EL intensity. The onset of EL at $|V_{Gonset}|$ does not depend on the applied drain-source voltage and is determined by the threshold voltages V_{Tn} and V_{Tp}. For a gate bias larger than $|V_{Gonset}|$, the EL intensity first increases, then reaches a maximum value $I_{ELmax}(V_{DS})$ and decreases again until turn-off is reached at $|V_{Goff}|$, the value of which depends on the applied drain-source voltage, as does the position of the maximum EL intensity. The maximum value increases with increasing $|V_{DS}|$, as expected from the output characteristic.

Figure 6.23 shows the EL intensity as a function of the drain current for different applied gate voltages. As before, the simulated data for the applied bias range of ±50 V referring to the device shown in Figure 6.16 are shown as straight lines and the simulated data for the full bias range of ±80 V are shown as dashed lines. For negative bias voltage and $|V_G| \leq 30$ V, the onset is independent of $|V_G|$, and the slope increases with increasing $|V_G|$. For gate voltages of −40 and −50 V, the onset shifts towards larger $|I_{DS}|$. Increasing the gate bias further, the EL intensity is zero within the given drain-source voltage range. For positive gate bias below a gate voltage of 30 V and above 70 V, the EL intensity is zero within the drain-source voltage range given . In between, the onset shifts towards larger drain currents with a constant slope for increasing gate bias .

Discussion

Considering the simulation for a voltage range of ±50 V, the simulation qualitatively represents the experimental data, even though some significant differences have to be mentioned: For negative gate bias the experiment shows EL already at 0 V gate bias. This is in agreement with the experimental transfer characteristic, for which the EL onset appears to be at positive gate voltage. The discrepancy to the theoretical simulation originates from the treatment of the threshold voltage versus charge-carrier injection. The experimentally derived threshold voltage is the onset voltage for charge-carrier transport in a channel in which a sufficiently large number of charges are accumulated. This value has been used in the theoretical description for the onset of charge-carrier injection, for which however the threshold is actually smaller. Even if a corrected threshold voltage were introduced, such a constant value would not describe the charge carrier injection over an injection barrier correctly.

In the transfer characteristic, the EL is observed in a region that is attributed to the ambipolar current, i.e. the region where the transition from a unipolar electron current to a unipolar hole current or vice versa takes place. For gate voltages outside this range, the current is unipolar, carried either by electrons or by holes. The position of the maximum in EL intensity shifts with the observed minimum in drain current in the transfer characteristic, for which the current is ambipolar.

For the EL as a function of the drain current, a general statement can be derived from the simulation, which is in agreement with the experimental data obtained on both the *p*-6P and the coevaporated thin films:

- If the applied bias voltage is such that the charge carrier of higher mobility is injected at the source contact and the one of lower mobility at the drain, the onset of EL shifts with increasing $|V_G|$ towards larger $|I_D|$.

- In contrast, if the applied bias voltage is such that the charge carrier of lower mobility is injected at source and the one of higher mobility at the drain contact, the onset of EL as function of the drain current is close to zero and independent of the applied gate voltage. The EL intensity increases linearly with I_D and the slope increases with increasing $|V_G|$. Only for very large gate bias and for a nonzero mobility of the charge carrier injected at source, will the EL onset also shift with further increasing $|V_G|$ towards higher drain currents.

This can be understood because in the first case charge carriers at the drain contact are injected only for gate voltages at which a gate-voltage-dependent current exists between source and drain contact. In the second case, even though charge carriers are injected at the source already for small gate bias, they do not contribute to the current owing to their low mobility. However, if the gate voltage exceeds the threshold for injection of the more mobile charge carrier at the drain, the drain current increases and EL is observed.

Conclusion

It could be shown for the first time that the EL observed in ambipolar and unipolar OFETs can be modelled based on a modified Shockley equation combined with Langevin recombination. Even though the model does not account for contact resistances, injection barriers, reduced effective channel length in ambipolar devices, recombination radii and fluorescence efficiency, it qualitatively describes the characteristic features of EL from OFET devices in good agreement with the experimental data.

6.3 Conclusion

Unipolar light-emitting OFETs based on oligophenyl compounds have been demonstrated. The EL observed in unipolar OFETs requires a pinch-off of the conductive channel and the injection of the opposite charge at the drain contact. The internal efficiency of the unipolar light-emitting OFET based on *p*-6P is in the order of 10^{-4}; the external efficiency is even two orders of magnitude smaller. An $Ir(btp)_2acac$-doped *p*-4P unipolar transistor, emitting with higher intensities, thus allowing inspection by optical microscopy, revealed that the emission is indeed localized in close vicinity of the drain contact. Thus, unipolar light-emitting field-effect transistors prove that injection is not the limiting parameter for ambipolar transport in organic thin films, even in the case of high injection barriers. Rather the transport itself is truly unipolar.

For the first time, a light-emitting OFET based on a coevaporated thin film of α-5T and PTCDI-$C_{13}H_{27}$ that exhibits pronounced ambipolar conduction over a wide range of bias conditions accompanied by light emission has been demonstrated. Light emission is correlated with the drain current, and can be modulated by both the drain-source voltage V_{DS} and the gate voltage V_G. Moreover, the latter can be used to tune the balance of charge carriers for a given V_{DS} in such a way that the EL intensity can be maximized.

The simultaneous formation of an electron and a hole channel combined with ambipolar transport shows that even though the two materials are coevaporated, they form interconnected thin films. The device serves as an excellent model structure for light-emitting OFETs. By coevaporation of two different organic semiconductors, an electron- and a hole-transport material, the electron and hole mobilities can be adjusted, i.e. the resulting ambipolar characteristic is controlled by the stoichiometry of the two materials. The efficiency is maximum for a material ratio of 1:1, where the mobilities have equal values of about 5×10^{-4} cm^2/Vs.

A model based on the modified Shockley equation and Langevin recombination has been introduced to describe the EL observed in ambipolar and unipolar OFETs. Even though the model does not account for contact resistances, injection barriers, reduced effective channel length in ambipolar devices, recombination radii and fluorescence efficiency, it qualitatively describes the characteristic features of EL from OFET devices in good agreement with the experimental data.

Summary

The goal of this thesis was the fabrication and characterization of a light-emitting ambipolar organic field-effect transistor (OFET). In the literature, light-emitting ambipolar field-effect transistors (FET) based on small molecules, which are of interest for novel electro-optical devices, have not yet been described. For the realization of such a light-emitting ambipolar OFET, three different strategies were pursued: Firstly, conventional single-layer OFETs were investigated in terms of their electroluminescent properties. Secondly, bilayer heterostructures based on an electron- and a hole-transport material were prepared. Thirdly, a novel concept based on coevaporated, i.e. mixed films consisting of an electron- and a hole-transport material, has been realized. Although the single-layer structures were light-emitting, the unipolar transport properties of the organic materials restrict light emission to a region close to one contact. In contrast, in bilayer heterostructures an ambipolar transport characteristics was measured, but no electroluminescence (EL) observed. Finally, with the novel concept of a coevaporated bulk heterostructure, EL in an ambipolar OFET could be observed for the first time.

Within the scope of this work various organic semiconducting materials were investigated with respect to their transport properties in single-layer structures : tetracene, pentacene, *p*-4P [1], *p*-6P [2], α-4T [3], α-5T [4] and PTCDI-$C_{13}H_{27}$ [5]. Thereby, charge-carrier injection and the formation of a conducting channel due to accumulated charge carriers was studied in metal-insulator-semiconductor (MIS) capacitor structures. For the oligoacene, α-oligothiophene and *para*-oligophenyl compounds, hole injection was observed, whereas for the perylene derivative electron injection was found. Varying the work function of the contact metal yielded the following conclusions: (i) Charge carriers are injected despite high barriers of up to 2 eV at the injecting contact. (ii) In organic films with spacial extension larger than the contact pad, charge carriers are accumulated, and thus a conductive channel is formed, also in those regions of the organic film that are not directly contacted with the metal electrode. (iii) For higher contact barriers, the spacial exten-

[1] *para*-quaterphenyl
[2] *para*-sexiphenyl
[3] α-quaterthiophene
[4] α-quinquethiophene
[5] N,N'-ditridecylperylene-3,4,9,10-tetracarboxylic diimide

sion of the channel formed is smaller. (iv) Indications of inversion of charge carriers in organic semiconductors could only be observed for pentacene measured under inert atmosphere in combination with Ca as contact metal. However, the inversion of charge carriers occurs only directly below the contact, i.e. no extended channel is formed. The metal-oxide-semiconductor (MOS) capacitor structures could be modelled on the basis of frequency-dependent capacitance-voltage (CV) measurements using an appropriate equivalent circuit. From functional analysis the extended channel capacitance and the channel length as function of the applied voltage are extracted. In investigating the transport properties in organic materials in OFETs, special emphasis was put on the parameter mobility. The charge-carrier mobility in an organic thin film strongly depends on its molecular order, which in turn depends on the deposition parameters, such as substrate temperature and deposition rate. Therefore, a topology analysis of the evaporated films was performed by means of X-ray diffraction (XRD) to investigate the crystallinity of the films. Films consisting of pentacence, a planar molecule, exhibit strong crystallinity with a molecular orientation almost perpendicular to the substrate. Even films of *para*-oligophenyl, which are non-planar molecules and thus produce films that are less well ordered, exhibit structures in the XRD spectrum that indicate textured, polycrystalline films. As *p*-4P reacts most sensitively to variations in the deposition parameters, the dependence of the charge-carrier mobility on the substrate temperature was investigated using *p*-4P. Temperature-dependent measurements of the transistor characteristics yield information on charge-carrier transport. Both the hole mobility in pentacene and the electron mobility in PTCDI-$C_{13}H_{27}$ are thermally activated, and in both materials the mobility decreases with decreasing temperature, starting at room temperature. Assuming thermally activated hopping transport, activation energies of $E_a = 41$ meV and 71 meV for the hole mobility in pentacene for room temperature mobilities of 6×10^{-2} cm^2/Vs and 4.4×10^{-3} cm^2/Vs, respectively, could be determined. The electron mobility in PTCDI-$C_{13}H_{27}$ shows an activation energy of 87 meV.

In all investigated materials unipolar transport was found. Therefore, OFETs consisting of a bilayer heterostructure combining an electron- and a hole-transport material, were prepared and their transport properties investigated. Metals with different work functions were used for the source and the drain contact to ensure efficient charge-carrier injection. The electron-transport material PTCDI-$C_{13}H_{27}$ was combined with each of the following hole-transport materials: pentacene, *p*-4P and α-5T. In each combination ambipolar transport was observed. For the electrical simulation of this characteristic two different approaches were chosen: Firstly, the characteristic has been simulated based on a modified Schockley equation with the free parameters electron and hole mobility as well as the threshold voltages for *n*- and *p*-channel device operation. Secondly, the characteristic has been simulated under the assumption of the drift-diffusion model. Both

approaches explain the qualitative characteristics of the curves. The numerical simulation also yields, in addition to mobility and threshold voltage, information on the gradient of the potential and the charge-carrier density between source and drain as well as the recombination in the case of ambipolar transport. In none of the bilayer heterostructure OFETs, light-emission could be observed, which can most likely be ascribed to the weak Coulomb interaction between the accumulated charges in the two layers. Therefore, unipolar OFETs were investigated in terms of their EL properties. Either efficiently emitting transport materials, such as *p*-6P, or doped films, such as $Ir(btp)_2acac$ [6] doped *p*-4P films, were employed. For the latter case, light emission could be demonstrated in close vicinity of the drain contact, which is in agreement with the numerical simulation.

Only by using the novel approach of coevaporating an electron- and a hole-transport material could light emission be observed for the first time in an ambipolar OFET. The electron-transport material PTCDI-$C_{13}H_{27}$ was combined with the hole-transport material α-5T. Decisive for the selection of α-5T were the energy gap and the planarity of the molecule, which ensures an ordered film growth on the molecular scale even in coevaporated thin films. It could be demonstrated that the electron and the hole mobility in the coevaporated thin film can be tuned systematically by varying the ratio of the two materials in the coevaporated film. The hole mobility in coevaporated films could be varied between 2.2×10^{-3} cm^2/Vs and 4×10^{-5} cm^2/Vs, the electron mobility between 6.7×10^{-3} cm^2/Vs und 5.5×10^{-4} cm^2/Vs. The EL intensity in OFETs has been modelled using a modified Schockley equation under the assumption of Langevin recombination.

Moreover, within the scope of this thesis, an integrated UV deposition and characterization chamber as well as an electro-optical characterization setup for OFETs were designed and set up. The electro-optical characterization of the films was performed in a glove box under argon atmosphere. The investigated OFETs were all prepared on silicon substrates, i.e. a highly doped silicon wafer was used as substrate and conductive gate electrode. The gate insulator SiO_2 was prepared by thermal oxidation.

The light-emitting ambipolar OFET based on a coevaporated thin film of an electron- and a hole-transport material is a promising concept. The thesis has been performed within the scope of the EU project ILO[7]. Based on the results of the discussed light-emitting ambipolar OFET a followup project has been applied for.

[6] iridium(III)bis(2-(2.-benzothienyl)pyridinato-N,C^3)(acetylacetonate)

[7] **I**njection **L**asing in **O**rganic Thin Films; contract number IST-2001-33057

A

Appendix A

Transistor Characteristics - Experimental Data

In Chapter 4, single layer OFETs based on different organic semiconductors have been discussed and the output and transfer characteristic of a pentacene OFET was studied in detail. For the other materials, i.e. tetracene, *p*-4P, *p*-6P, α-4T, α-5T and PTCDI-$C_{13}H_{27}$, the extracted field-effect mobilities were summarized. Here, the original experimental data of these devices are shown, whereas typical characteristics have been selected.

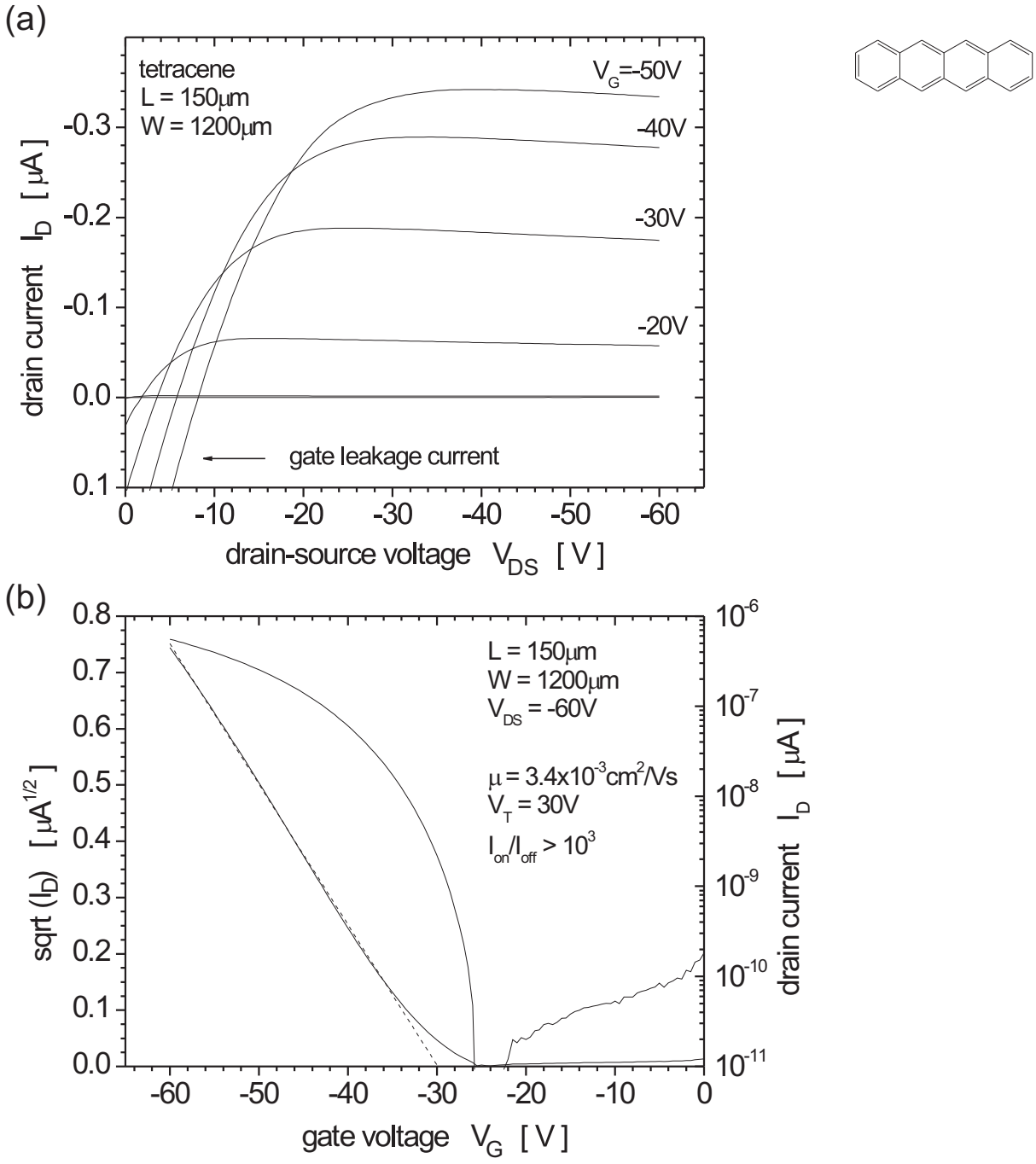

Figure A.1: *(a) Output and (b) transfer characteristics of a 80 nm tetracene transistor with Au top contacts. The organic thin film was not patterned, but deposited over the entire substrate, resulting in high leakage currents.*

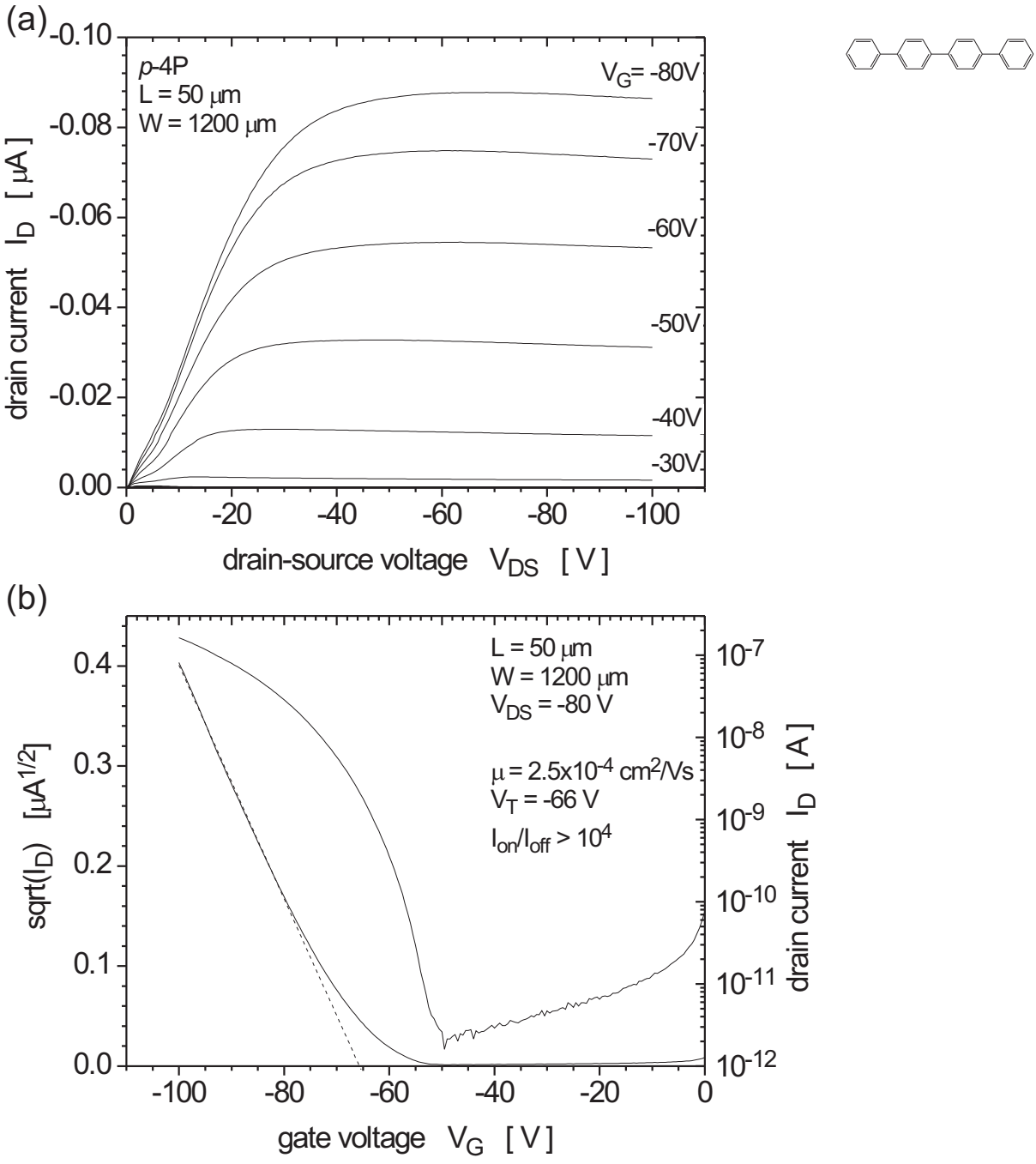

Figure A.2: *(a) Output and (b) transfer characteristics of a 20 nm p-4P transistor with Au top contacts.*

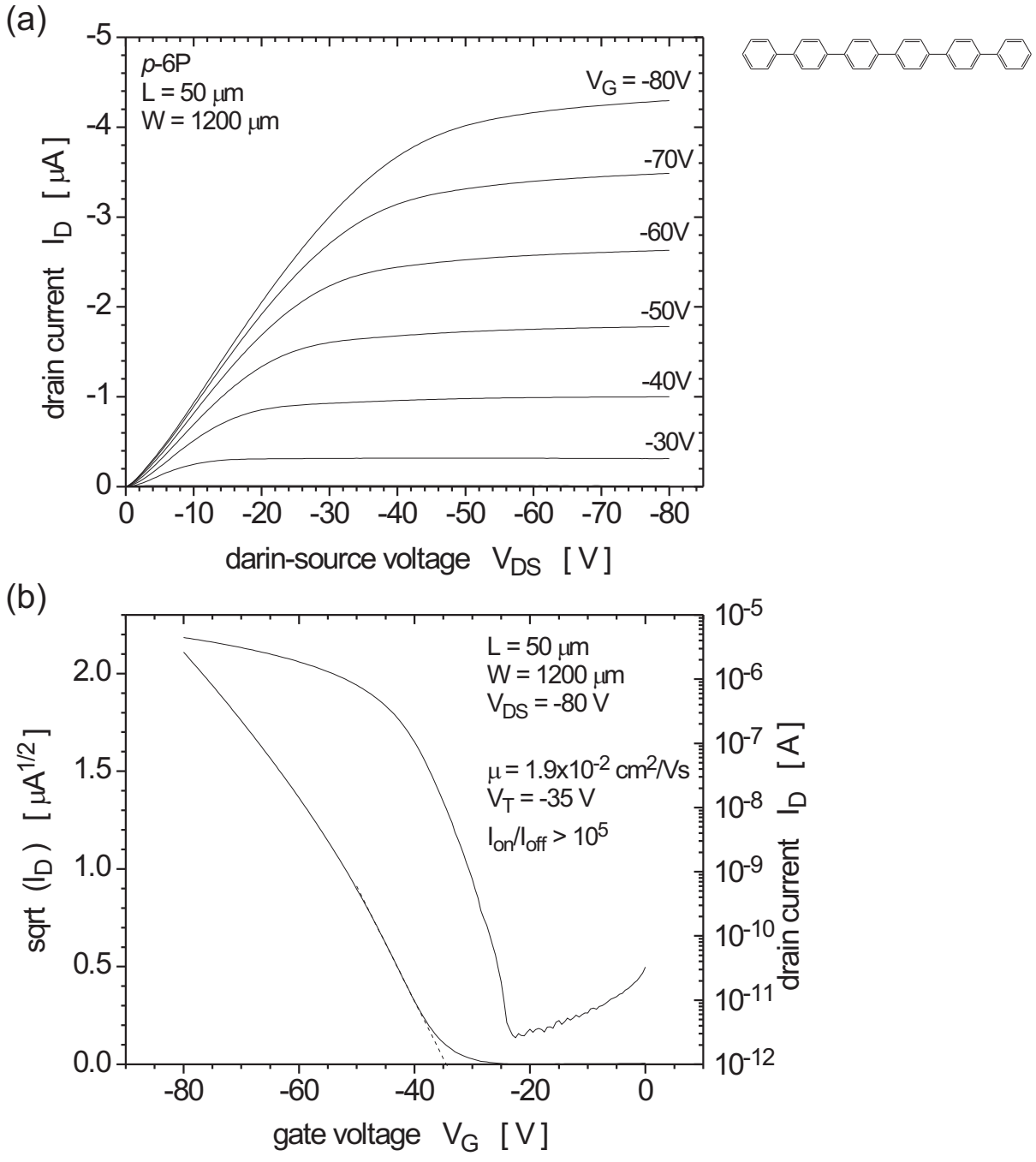

Figure A.3: *(a) Output and (b) transfer characteristics of a 60 nm p-6P transistor with Au top contacts.*

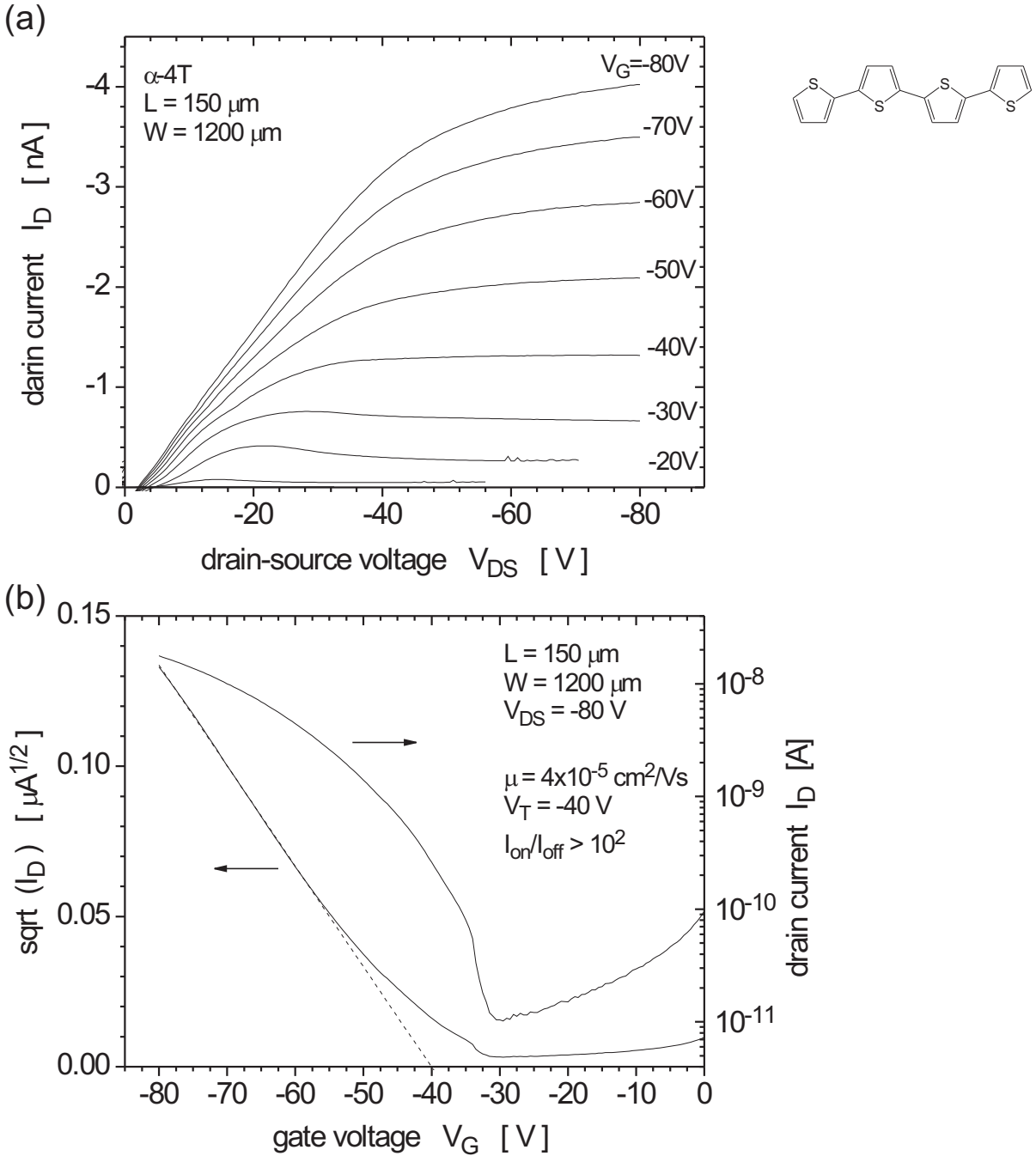

Figure A.4: *(a) Output and (b) transfer characteristics of an α-4T transistor with Au top contacts.*

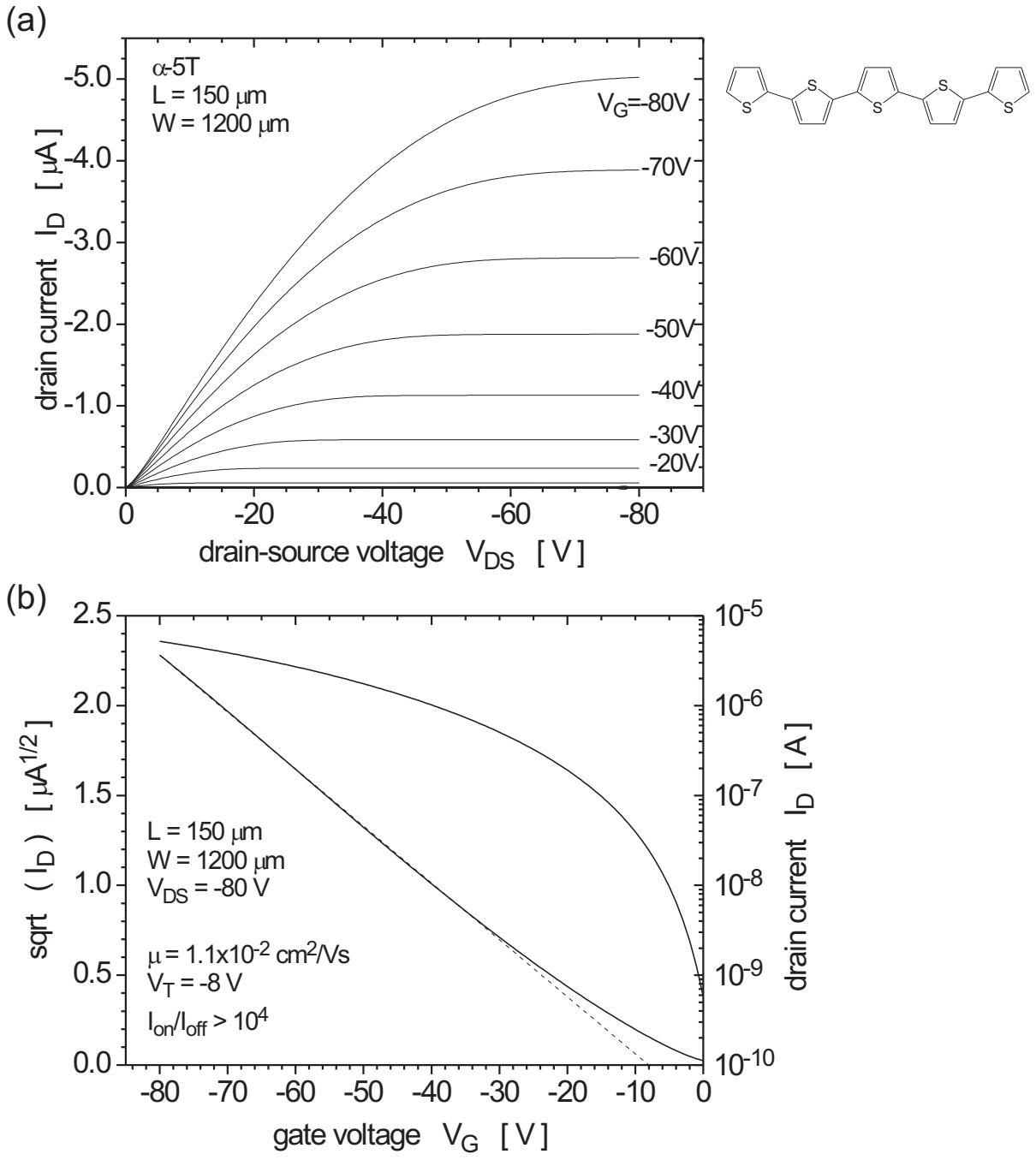

Figure A.5: *(a) Output and (b) transfer characteristics of an α-5T transistor with Au top contacts.*

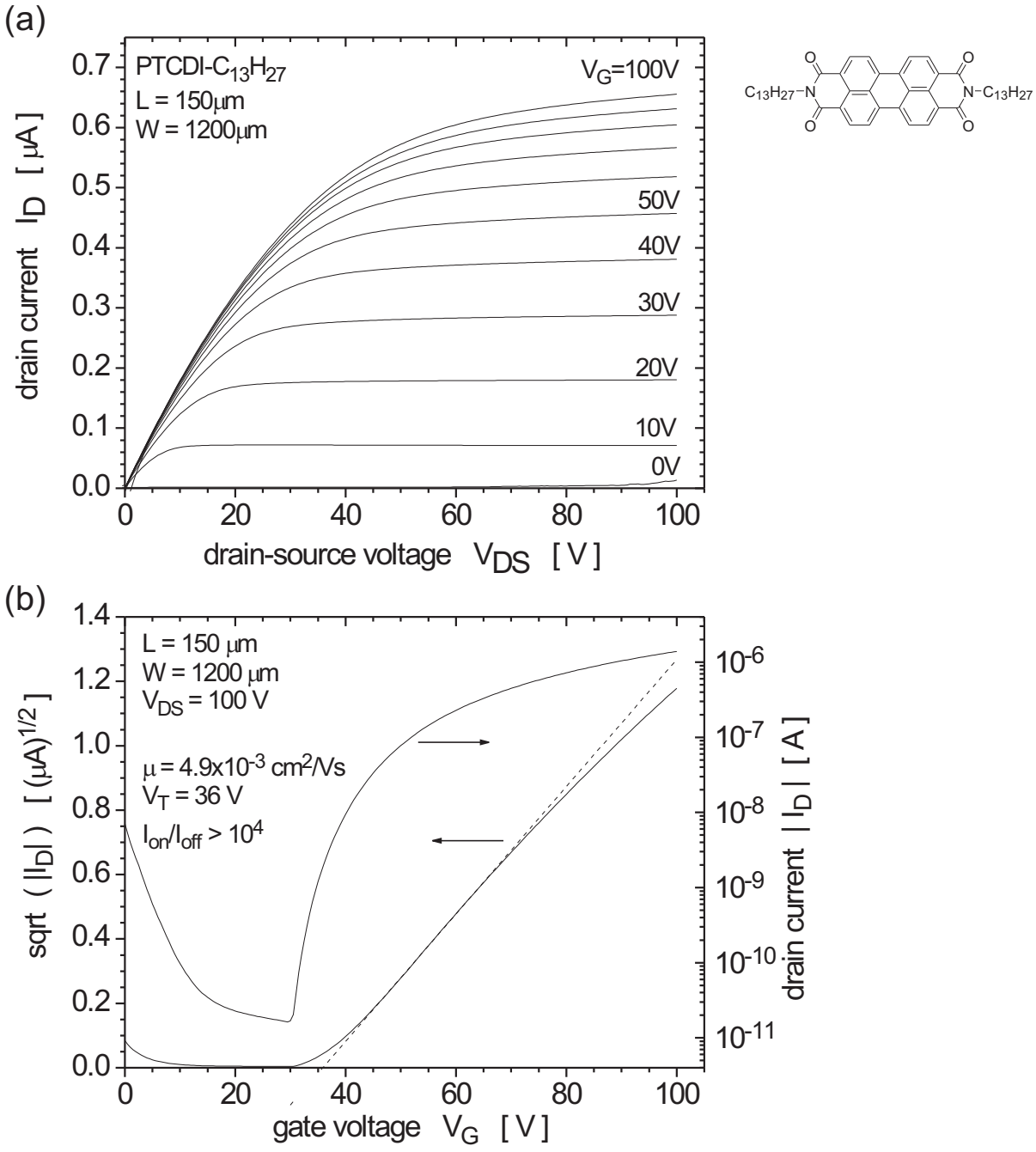

Figure A.6: *(a) Output and (b) transfer characteristics of a 50 nm PTCDI-$C_{13}H_{27}$ transistor with Mg bottom contacts.*

Appendix B

Optical Properties - Experimental Data

In Chapter 5, light-emitting OFETs based on *p*-4P, *p*-6P and coevaporated thin films of α-5T and PTCDI-C_{13}-H_{27} have been discussed. In the following, the optical properties, i.e. the absorption and emission spectra of thin films, are presented as a reference.

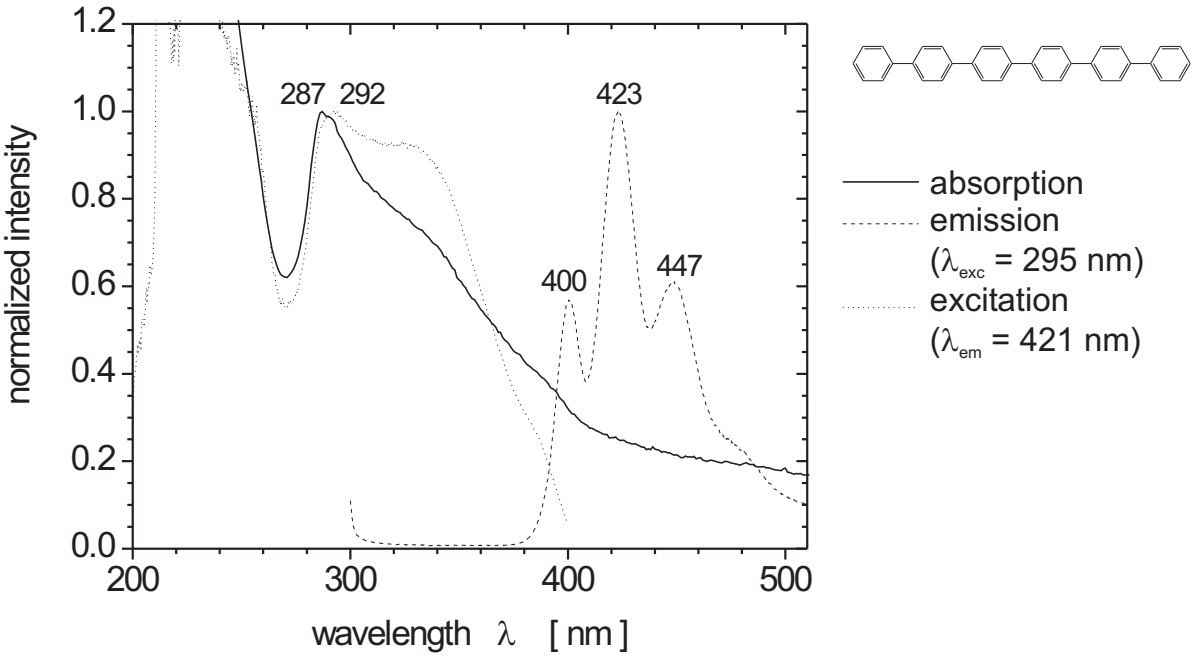

Figure B.1: *Absorption, emission and excitation spectrum of p-6P on quartz.*

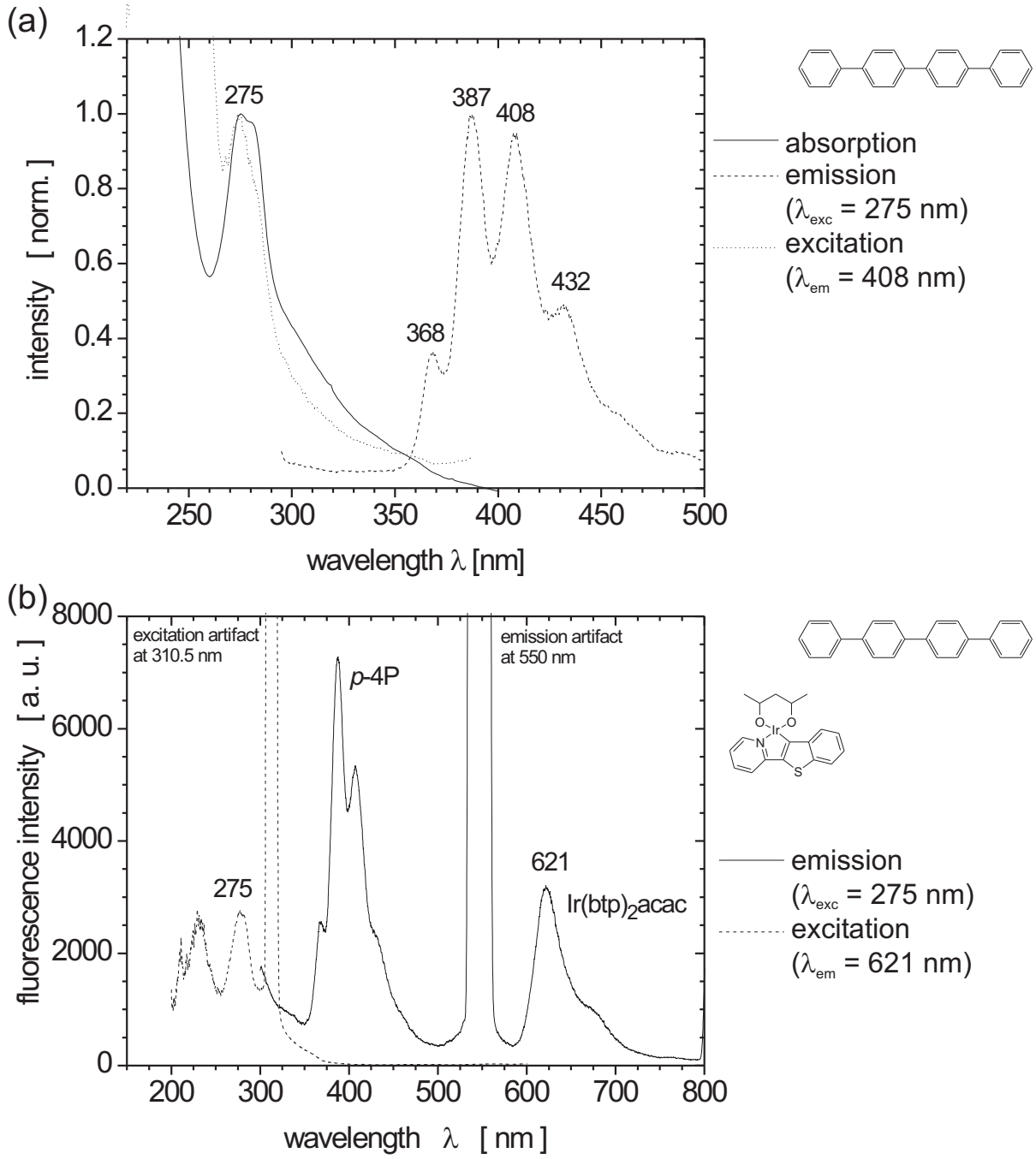

Figure B.2: *(a) Absorption, emission and excitation spectrum of p-4P on quartz. (b) PL emission and excitation spectrum of an $Ir(btp)_2acac$ doped p-4P thin film. Emission and excitation artifacts are due to higher-order excitation. $Ir(btp)_2acac$ emission is excited only via excitation of p-4P. The p-4P emission is not completely quenched by the dopant.*

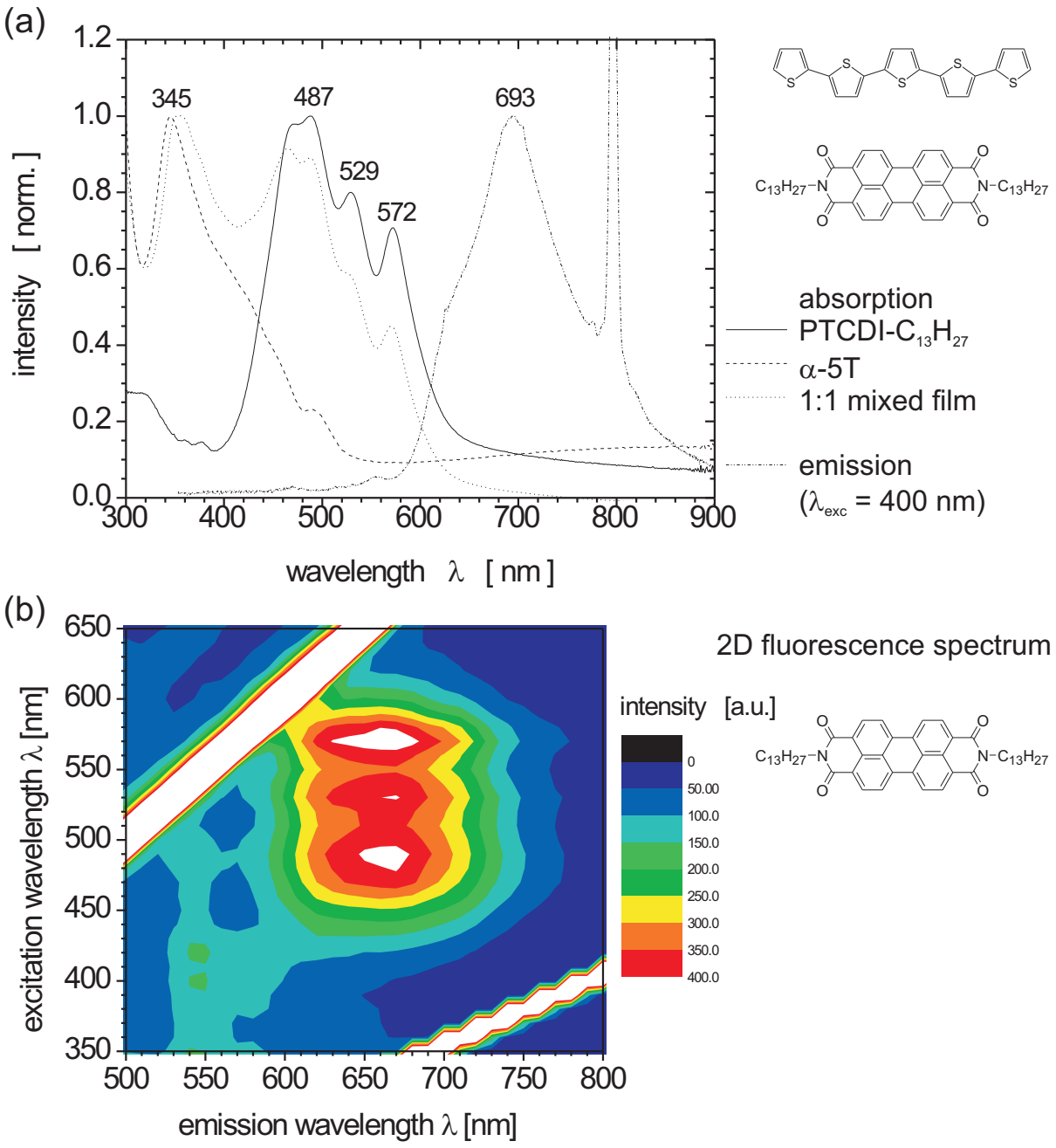

Figure B.3: *(a) Absorption spectra of PTCDI-C_{13}-H_{27}, α5-T, and a 1:1 coevaporated film of the two materials on quartz. In addition, the PL emission spectrum of the coevaporated film is shown. Even though the excitation wavelength is chosen for α-5T, mainly PTCDI-C_{13}-H_{27} emission is observed, indicating an efficient exciton transfer. (b) 2D fluorescence spectrum of PTCDI-C_{13}-H_{27}.*

Appendix C

Simulation of Ambipolar Transistor Characteristic

As previously described in Chapter 5.4.1, the current characteristics of an ambipolar OFET can be modelled in a first approximation by the sum of the electron and hole current according to the Shockley model. The analytical expression obtained from Equations 5.3 to 5.6 used for simulation with Mathcad is as following for positive values of V_G and V_{DS}:

$I_{Damb} =$

$$\begin{aligned}
&\frac{W}{L}\mu_n C_i\left[(V_G - V_{Tn})V_{DS} - \frac{1}{2}{V_{DS}}^2\right]\frac{V_G - V_{Tn}+ \mid V_G - V_{Tn} \mid}{2(V_G - V_{Tn})}\,\frac{V_G - V_{Tn} - V_{DS}+ \mid V_G - V_{Tn} - V_{DS} \mid}{2(V_G - V_{Tn} - V_{DS})}\\
&+\frac{W}{L}\mu_n C_i\left[(V_G - V_{Tn})^2\right]\frac{V_G - V_{Tn}+ \mid V_G - V_{Tn} \mid}{2(V_G - V_{Tn})}\,\frac{V_G - V_{Tn} - V_{DS}- \mid V_G - V_{Tn} - V_{DS} \mid}{2(V_G - V_{Tn} - V_{DS})}\\
&+\frac{W}{L}\mu_p C_i\left[(V_G - V_{Tp} - V_{DS})(-V_{DS}) - \frac{1}{2}{V_{DS}}^2\right]\frac{V_G - V_{Tp} - V_{DS}- \mid V_G - V_{Tp} - V_{DS} \mid}{2(V_G - V_{Tp} - V_{DS})}\,\frac{V_G - V_{Tp}- \mid V_G - V_{Tp} \mid}{2(V_G - V_{Tp})}\\
&+\frac{W}{L}\mu_p C_i\left[(V_G - V_{Tp} - V_{DS})^2\right]\frac{V_G - V_{Tp} - V_{DS}- \mid V_G - V_{Tp} - V_{DS} \mid}{2(V_G - V_{Tp} - V_{DS})}\,\frac{V_G - V_{Tp}+ \mid V_G - V_{Tp} \mid}{2(V_G - V_{Tp})}
\end{aligned} \tag{C.1}$$

and as following for negative values of V_G and V_{DS}:

$I_{Damb} =$

$$\begin{aligned}
&-\frac{W}{L}\mu_p C_i\left[(V_G - V_{Tp})V_{DS} - \frac{1}{2}{V_{DS}}^2\right]\frac{V_G - V_{Tp}- \mid V_G - V_{Tp} \mid}{2(V_G - V_{Tp})}\,\frac{V_G - V_{Tp} - V_{DS}- \mid V_G - V_{Tp} - V_{DS} \mid}{2(V_G - V_{Tp} - V_{DS})}\\
&-\frac{W}{L}\mu_p C_i\left[(V_G - V_{Tp})^2\right]\frac{V_G - V_{Tp}- \mid V_G - V_{Tp} \mid}{2(V_G - V_{Tp})}\,\frac{V_G - V_{Tp} - V_{DS}+ \mid V_G - V_{Tp} - V_{DS} \mid}{2(V_G - V_{Tp} - V_{DS})}\\
&-\frac{W}{L}\mu_n C_i\left[(V_G - V_{Tn} - V_{DS})(-V_{DS}) - \frac{1}{2}{V_{DS}}^2\right]\frac{V_G - V_{Tn} - V_{DS}+ \mid V_G - V_{Tn} - V_{DS} \mid}{2(V_G - V_{Tn} - V_{DS})}\,\frac{V_G - V_{Tn}+ \mid V_G - V_{Tn} \mid}{2(V_G - V_{Tn})}\\
&-\frac{W}{L}\mu_n C_i\left[(V_G - V_{Tn} - V_{DS})^2\right]\frac{V_G - V_{Tn} - V_{DS}+ \mid V_G - V_{Tn} - V_{DS} \mid}{2(V_G - V_{Tn} - V_{DS})}\,\frac{V_G - V_{Tn}- \mid V_G - V_{Tn} \mid}{2(V_G - V_{Tn})}
\end{aligned} \tag{C.2}$$

Appendix D

Simulation of Electroluminescence from OFETs

As previously described in Chapter 6.2.2, the electroluminescence of a light emitting OFET can be modelled qualitatively in a first approximation by using the expression for the ambipolar electron and hole current according to Equation C.1 and C.2 and assuming Langevin recombination. The analytical expression used for simulation with Mathcad is as following for positive values of V_G and V_{DS}:

$$
\begin{aligned}
I_{EL} = \\
&\left(\frac{W}{L}\mu_n C_i\left[(V_G - V_{Tn})V_{DS} - \frac{1}{2}{V_{DS}}^2\right]\frac{V_G - V_{Tn} + \mid V_G - V_{Tn} \mid}{2(V_G - V_{Tn})}\frac{V_G - V_{Tn} - V_{DS} + \mid V_G - V_{Tn} - V_{DS} \mid}{2(V_G - V_{Tn} - V_{DS})}\right. \\
&\left.+\frac{W}{L}\mu_n C_i\left[(V_G - V_{Tn})^2\right]\frac{V_G - V_{Tn} + \mid V_G - V_{Tn} \mid}{2(V_G - V_{Tn})}\frac{V_G - V_{Tn} - V_{DS} - \mid V_G - V_{Tn} - V_{DS} \mid}{2(V_G - V_{Tn} - V_{DS})}\right) \\
&\left(\frac{W}{L}C_i\left[(V_G - V_{Tp} - V_{DS})(-V_{DS}) - \frac{1}{2}{V_{DS}}^2\right]\frac{V_G - V_{Tp} - V_{DS} - \mid V_G - V_{Tp} - V_{DS} \mid}{2(V_G - V_{Tp} - V_{DS})}\frac{V_G - V_{Tp} - \mid V_G - V_{Tp} \mid}{2(V_G - V_{Tp})}\right. \\
&\left.+\frac{W}{L}C_i\left[(V_G - V_{Tp} - V_{DS})^2\right]\frac{V_G - V_{Tp} - V_{DS} - \mid V_G - V_{Tp} - V_{DS} \mid}{2(V_G - V_{Tp} - V_{DS})}\frac{V_G - V_{Tp} + \mid V_G - V_{Tp} \mid}{2(V_G - V_{Tp})}\right) \\
&+\left(\frac{W}{L}C_i\left[(V_G - V_{Tn})V_{DS} - \frac{1}{2}{V_{DS}}^2\right]\frac{V_G - V_{Tn} + \mid V_G - V_{Tn} \mid}{2(V_G - V_{Tn})}\frac{V_G - V_{Tn} - V_{DS} + \mid V_G - V_{Tn} - V_{DS} \mid}{2(V_G - V_{Tn} - V_{DS})}\right. \\
&\left.+\frac{W}{L}C_i\left[(V_G - V_{Tn})^2\right]\frac{V_G - V_{Tn} + \mid V_G - V_{Tn} \mid}{2(V_G - V_{Tn})}\frac{V_G - V_{Tn} - V_{DS} - \mid V_G - V_{Tn} - V_{DS} \mid}{2(V_G - V_{Tn} - V_{DS})}\right) \\
&\left(\frac{W}{L}\mu_p C_i\left[(V_G - V_{Tp} - V_{DS})(-V_{DS}) - \frac{1}{2}{V_{DS}}^2\right]\frac{V_G - V_{Tp} - V_{DS} - \mid V_G - V_{Tp} - V_{DS} \mid}{2(V_G - V_{Tp} - V_{DS})}\frac{V_G - V_{Tp} - \mid V_G - V_{Tp} \mid}{2(V_G - V_{Tp})}\right. \\
&\left.+\frac{W}{L}\mu_p C_i\left[(V_G - V_{Tp} - V_{DS})^2\right]\frac{V_G - V_{Tp} - V_{DS} - \mid V_G - V_{Tp} - V_{DS} \mid}{2(V_G - V_{Tp} - V_{DS})}\frac{V_G - V_{Tp} + \mid V_G - V_{Tp} \mid}{2(V_G - V_{Tp})}\right)
\end{aligned}
\tag{D.1}
$$

and as following for negative values of V_G and V_{DS}:

$$
\begin{aligned}
I_{EL} = \\
&(-\frac{W}{L}\mu_p C_i\Big[(V_G - V_{Tp})V_{DS} - \frac{1}{2}{V_{DS}}^2\Big]\frac{V_G - V_{Tp} - \mid V_G - V_{Tp} \mid}{2(V_G - V_{Tp})}\frac{V_G - V_{Tp} - V_{DS} - \mid V_G - V_{Tp} - V_{DS} \mid}{2(V_G - V_{Tp} - V_{DS})} \\
&-\frac{W}{L}\mu_p C_i\Big[(V_G - V_{Tp})^2\Big]\frac{V_G - V_{Tp} - \mid V_G - V_{Tp} \mid}{2(V_G - V_{Tp})}\frac{V_G - V_{Tp} - V_{DS} + \mid V_G - V_{Tp} - V_{DS} \mid}{2(V_G - V_{Tp} - V_{DS})}) \\
&(-\frac{W}{L}C_i\Big[(V_G - V_{Tn} - V_{DS})(-V_{DS}) - \frac{1}{2}{V_{DS}}^2\Big]\frac{V_G - V_{Tn} - V_{DS} + \mid V_G - V_{Tn} - V_{DS} \mid}{2(V_G - V_{Tn} - V_{DS})}\frac{V_G - V_{Tn} + \mid V_G - V_{Tn} \mid}{2(V_G - V_{Tn})} \\
&-\frac{W}{L}C_i\Big[(V_G - V_{Tn} - V_{DS})^2\Big]\frac{V_G - V_{Tn} - V_{DS} + \mid V_G - V_{Tn} - V_{DS} \mid}{2(V_G - V_{Tn} - V_{DS})}\frac{V_G - V_{Tn} - \mid V_G - V_{Tn} \mid}{2(V_G - V_{Tn})}) \\
&(-\frac{W}{L}C_i\Big[(V_G - V_{Tp})V_{DS} - \frac{1}{2}{V_{DS}}^2\Big]\frac{V_G - V_{Tp} - \mid V_G - V_{Tp} \mid}{2(V_G - V_{Tp})}\frac{V_G - V_{Tp} - V_{DS} - \mid V_G - V_{Tp} - V_{DS} \mid}{2(V_G - V_{Tp} - V_{DS})} \\
&-\frac{W}{L}C_i\Big[(V_G - V_{Tp})^2\Big]\frac{V_G - V_{Tp} - \mid V_G - V_{Tp} \mid}{2(V_G - V_{Tp})}\frac{V_G - V_{Tp} - V_{DS} + \mid V_G - V_{Tp} - V_{DS} \mid}{2(V_G - V_{Tp} - V_{DS})}) \\
&(-\frac{W}{L}\mu_n C_i\Big[(V_G - V_{Tn} - V_{DS})(-V_{DS}) - \frac{1}{2}{V_{DS}}^2\Big]\frac{V_G - V_{Tn} - V_{DS} + \mid V_G - V_{Tn} - V_{DS} \mid}{2(V_G - V_{Tn} - V_{DS})}\frac{V_G - V_{Tn} + \mid V_G - V_{Tn} \mid}{2(V_G - V_{Tn})} \\
&-\frac{W}{L}\mu_n C_i\Big[(V_G - V_{Tn} - V_{DS})^2\Big]\frac{V_G - V_{Tn} - V_{DS} + \mid V_G - V_{Tn} - V_{DS} \mid}{2(V_G - V_{Tn} - V_{DS})}\frac{V_G - V_{Tn} - \mid V_G - V_{Tn} \mid}{2(V_G - V_{Tn})})
\end{aligned}
\tag{D.2}
$$

Abbreviations

Symbols

A	device area
A_{ch}	channel area
A_{con}	contact area
A_{inj}	area of organic thin film below injecting contact
A_{tot}	total device area
C_i	capacitance per unit area
C_{ox}	oxide capacitance
C_{org}	capacitance of organic thin film
C_{con}	contact capacitance
C_{inj}	capacitance of organic thin film and insulating layer below injecting contact
C_{ch}	channel capacitance
C_{dep}	capacitance for depleted device
C_{acc}	capacitance for accumulated charges
C_{spread}	capacitance for strong accumulation
C_{min}	minimum capacitance for depleted charges
C_{max}	maximum capacitance for accumulated charges
C_s	capacitance of the depleted semiconductor
C_{it}	capacitance due to interface traps
C_d	depletion layer capacitance
C_{FB}	capacitance at flat band condition
d	film thickness
d_{ox}	thickness of gate insulator, gate oxide
d_{org}	thickness of organic thin film
d_s	thickness of semiconductor thin film
d_{spread}	spread distance of accumulated charge carriers
$d_{average}$	average distance of accumulated charge carriers

E	electric field
E_a	activation energy
E_{ph}	photon energy
E_F	Fermi level
E_V	top of valence band
E_C	bottom of conduction band
E_g	energy band gap
E_i	intrinsic Fermi level
E_S	singlet energy
E_T	triplet energy
F	electric field
I_D	drain current
I_{Dsat}	saturated drain current
I_{Dn}	drain electron current
I_{Dnsat}	saturated drain electron current
I_{Dp}	drain hole current
I_{Dpsat}	saturated drain hole current
I_{Damb}	ambipolar drain current
I^-_{Damb}	ambipolar drain current for negative applied bias
I^+_{Damb}	ambipolar drain current for positive applied bias
I_{Donset}	onset current for electroluminescence
I_{EL}	photodiode current
I_{on}	drain current in on-state
I_{off}	drain current in off-state
L	channel length
m_{sat}	slope of square root of saturated drain current versus gate voltage
m_{lin}	slope of linear drain current versus gate voltage
n	electron density; refractive index
N_A	acceptor impurity density
N_C	density of states in the conduction band
N_V	density of states in the valence band
n_i	intrinsic charge carrier density
p	hole density
Q_{it}	interface charges
R	resistance
R_{ch}	channel resistance
R_p	parasitic resistance
R_{direct}	bimolecular recombination rate

R_{org1}	parallel resistance in equivalent circuite
R_{org2}	serial resistance in equivalent circuite
r_c	coulomb capture radius
S	subthreshold swing
S_{ph}	photodiode sensitivity
T	temperature
V	voltage
V_{DS}	drain-source voltage
V_G	gate voltage relative to source contact
V_G, eff	effective gate voltage relative to source contact
V'_{SD}	net source-drain voltage relative to drain contact
V'_{GD}	net gate voltage relative to drain contact
V_T	threshold voltage
V_{Tn}	threshold voltage for *n*-channel device operation
V_{Tp}	threshold voltage for *p*-channel device operation
V_{onset}	onset drain-source voltage for ambipolar current
$V_{DSonset}$	onset drain-source voltage for electroluminescence
V_{Dsat}	drain-source voltage at onset of saturated drain current
V_{min}	voltage corresponding to minimum device capacitance
V_{FB}	flat band voltage
V_{bias}	bias voltage
W	channel width
x	width overlap of the metal contact in capacitor device structures
x_d	width of depletion zone
x_{dmax}	maximum depletion width
ϵ_{ox}	relative dielectric constant of gate insulator
ϵ_s	relative dielectric constant of the semiconductor
η	efficiency
η_{int}	internal quantum efficiency
η_{ext}	external quantum efficiency
μ	field-effect mobility
μ_n	electron mobility
μ_p	hole mobility
μ_{sat}	field-effect mobility extracted from saturated drain-current
μ_{lin}	field-effect mobility extracted from linear drain-current
σ	conductivity
Φ_M	metal work function
Φ_B	contact barrier hight

ϕ	electrical potential
ϕ_{Fp}	hole quasi-Fermi potential
ϕ_{Fn}	electron quasi-Fermi potential
ϕ_{fl}	fluorescence quantum yield
ϕ_T	triplet quantum yield
χ	electron affinity
χ_S	electron affinity of the semiconductor
Ψ_B	potential difference between E_F and E_i

Devices and Methods

OFET	organic field-effect transistor
OLED	organic light-emitting diode
FET	field-effect transistor
TFT	thin-film transistor
MOS	metal-oxide-silicon
MIS	metal-insulator-semiconductor
CV	capacitance voltage
IV	current voltage
PL	photoluminescence
EL	electroluminescence
HOMO	highest occupied molecular orbital
LUMO	lowest unoccupied molecular orbital
AFM	atomic force microscopy
XRD	X-ray diffraction
LSCM	laser scanning confocal microscopy
VASE	variable angle spectroscopic ellipsometry
XPS	x-ray photoelectron spectroscopy
UPS	ultraviolet photoelectron spectroscopy
ILO	injection lasing in organic thin films

Materials

p-4P	*para*-quaterphenyl
p-6P	*para*-sexiphenyl
α-4T	α-quaterthiophene
α-5T	α-quinquethiophene
PTCDI-$C_{13}H_{27}$	N,N'-ditridecylperylene-3,4,9,10-tetracarboxylic diimide
Alq_3	tris(8-hydroxyquinoline) aluminum
$Ir(btp)_2acac$	iridium(III)bis(2-(2.-benzothienyl)pyridinato-N,C^3)(acetylacetonate)

Bibliography

[Ada01] C. Adachi, M. A. Baldo, S. R. Forrest, S. Lamansky, M. E. Thompson, and R. C. Kwong. High-efficiency red electrophosphorescence devices. *Appl. Phys. Lett.*, 78(11):1622–1624, 2001.

[AG99] Integrated Systems Engineering AG. Zurich, Switzerland, 1995-1999.

[Ahl04] M. Ahles, A. Hepp, R. Schmechel, and H. von Seggern. Light emission from a polymer transistor. *Appl. Phys. Lett.*, 84(3):428–430, 2004.

[Bab04] A. Babel, J. D. Wind, and A. Jenekhe. Ambipolar charge transport in air-stable polymer blend thin-film transistors. *Adv. Funct. Mater.*, 14(9):891–894, 2004.

[Bao96] Z. Bao, A. J. Lovinger, and A. Dodabalapur. Organic field-effect transistors with high mobility based on copper phthalocyanine. *Appl. Phys. Lett.*, 69(20):3066–3068, 1996.

[Bao98] Z. Bao, A. J. Lovinger, and J. Brown. New air-stable n-channel organic thin film transistors. *J. Am. Chem. Soc.*, 120:207–208, 1998.

[Bar70] D. F. Barbe and C. R. Westgate. Surface state parameters of metal-free phthalocyanine single crystals. *J. Phys. Chem. Solids*, 31:2679–2687, 1970.

[Bau78] J. L. Baudour, Y. Delugeard, and P. Rivet. Structural phase transition in polyphenyls. vi. crystal structure of the low-temperature ordered phase of p-quaterphenyl at 110 k. *Acta Cryst.*, B34:625–628, 1978.

[Bei02] T. A. Beierlein, H.-P. Ott, H. Hofmann, H. Riel, B. Ruhstaller, B. Crone, S. Karg, and W. Riess. Combinatorial device fabrication and optimization of multilayer organic leds. *Proc. SPIE Int. Soc. Opt. Eng.*, 178:4464, 2002.

[Bei03] T. Beierlein. *Combinatorial methods for Organic Light-Emitting Materials and Devices*. PhD thesis, University of Bayreuth, 2003.

[Blo98] P. W. M. Blom and M. J. M. De Jong. Device operation of polymer light-emitting diodes. *Philips J. Res.*, 51(4):479–494, 1998.

[Bre04] D. W. Breiby, I. S. Theis, O. Bunk, and M. M. Nielsen. Grazing incidence measurements of pentacene thin-films. *manuscript in preparation*, 2004.

[Bri03] M. Brinkmann, S. Graff, C. Straupé, J.-C. Wittmann, C. Chaumont, F. Nuesch, A. Aziz, M. Schaer, and L. Zuppiroli. Orienting tetracene and pentacene thin films onto friction-transferred poly(tetrafluoroethylene) substrate. *J. Phys. Chem. B*, 107(38):10531–10539, 2003.

[Bro97] A. R. Brown, D. M. De Leeuw, M. Matters, and C. P. Jarrett. Field-effect transistors made from solution-processed organic semiconductors. *Synth. Met.*, 88(1):37–55, 1997.

[Bul01] Bulović. *Organic Electronic Materials*, volume 41, chapter 11. Springer, Berlin, 2001. edited by R. Farchioni and G. Grosso.

[Bur90] J. H. Burroughes, D. D. C. Bradley, A. R. Brown, R. N. Marks, K. Mackay, R. H. Friend, P. L. Burns, and A. B. Holmes. Light-emitting diodes based on conjugated polymers. *Nature*, 347:539 – 541, 1990.

[Bus89] H. H. Busta, J. E. Pogemiller, R. W. Standley, and K. D. Mackenzie. Self-aligned bottom-gate submicrometer-channel-length a-si:h thin-film transistors. *IEEE Trans. El. Dev.*, 36(12):2883–2888, 1989.

[Che01] B. Chen, X. Lin, L. Cheng, C. Lee, W. A. Gambling, and S. Lee. Improvement of efficiency and colour purity of red-dopant organic light-emitting diodes by energy levels matching with the host materials. *J. Phys. D*, 34:30–35, 2001.

[Che03a] X. Chen, J.-L. Liao, Y. Liang, M. O. Ahmed, H.-E. Tseng, and S.-A. Chen. High-efficiency red-light emission from polyfluorenes grafted with cyclometalated iridium complexes and charge transport moiety. *J. Am. Chem. Soc.*, 125:636–637, 2003.

[Che03b] R. J. Chesterfield, C. R. Newman, T. M. Pappenfus, P. C. Ewbank, M. H. Haukaas, K. R. Mann, L. L. Miller, and C. D. Frisbie. High electron mobility and ambipolar transport in organic thin-film transistors based on a π-stacking quinoidal terthiophene. *Adv. Mater.*, 15(15):1278–1282, 2003.

[Cro01] B. K. Crone, A. Dodabalapur, R. Sarpeshkar, R. W. Filas, Y.-Y. Lin, Z. Bao, J. H. O'Neill, W. Li, and H. E. Katz. Design and fabrication of organic complementary circuits. *J. Appl. Phys.*, 89(9):5125–5132, 2001.

[Del76] Y. Delugeard, J. Desuche, and J. L. Baudour. Structural transition in polyphenyls. ii. the crystal structure of the high-temperature phase of quaterphenyl. *Acta Cryst.*, B32:702–705, 1976.

[Dim01] C. D. Dimitrakopoulos and D. J. Mascaro. Organic thin-film transistors: A review of recent advances. *IBM J. Res. Develop.*, 45(1):11–27, 2001.

[Dim02] C. D. Dimitrakopoulos and P. R. L. Malenfant. Organic thin film transistors for large area electronics. *Adv. Mater.*, 14(2):99–117, 2002.

[dM99] J. S. de Melo, L. M. Silva, L. G. Arnaut, and R. S. Becker. Singlet and triplet energies of a-oligothiophenes: A spectroscopic, theoretical, and photoacoustic study: Extrapolation to polythiophene. *J. Chem. Phys.*, 111(12):5427–5433, 1999.

[Dod95] A. Dodabalapur, H. E. Katz, L. Torsi, and R. C. Haddon. Organic field-effect bipolar transistors. *Science*, 269:1560, 1995.

[Dod96] A. Dodabalapur, H. E. Katz, L. Torsi, and R. C. Haddon. Organic field-effect bipolar transistors. *Appl. Phys. Lett.*, 68(8):1108–1110, 1996.

[Ebi83] F. Ebisawa, T. Kurokawa, and S. Nara. Electrical properties of polyacetylene/polysiloxane interface. *J. Appl. Phys.*, 54(6):3255–3259, 1983.

[Era95] M. Era, T. Tsutsui, and S. Saito. Polarized electroluminescence from oriented p-sexiphenyl vacuum-deposited film. *Appl. Phys. Lett.*, 67(17):2436–2438, 1995.

[Fac00] A. Facchetti, Y. Deng, A. Wang, Y. Koide, H. Sirringhaus, T. J. Marks, and R. H. Friend. Tuning the semiconducting properties of sexithiophene by α,ω-substitution – α,ω-diperfluorohexylsexithiophene: the first n-type sexithiophene for thin-film transistors. *Angew. Chem. Int. Ed.*, 39(24):4547–4551, 2000.

[Fac03] A. Facchetti, M. Mushrush, H. E. Katz, and T. J. Marks. n-type building blocks for organic electronics: A homologous family of fluorocarbon-substituted thiophene oligomers with high carrier mobility. *Adv. Mater.*, 15(1):33–38, 2003.

[Fre04] M. Freitag, J. Chen, J. Tersoff, J. C. Tsang, Q. Fu, J. Liu, and P. Avouris. Mobile ambipolar domain in carbon nanotubes infrared emitters. *Phys. Rev. Lett.*, 93(7):076803–1/4, 2004.

[Gar89] F. Garnier, G. Horowitz, X. Peng, and D. Fichou. A field-effect transistor based on conjugated alpha-sexithienyl. *Solid State Commun.*, 72(4):381–384, 1989.

[Gee00] W. Geens, S. E. Shaheen, C. J. Brabec, J. Poortmans, and N. S. Sariciftci. Field-effect mobility measurements of conjugated polymer/fullerene photovoltaic blends. *AIP Conf. Proc.*, 544:516, 2000.

[Gmb04] PolyIC GmbH. press release. http://www.polyic.com/en/info/press/PolyIC200411-001de.pdf, 2004.

[Gui89] G. Guillaud, R. Madru, M. A. Sadoun, and M. Maitrot. Thin-film transistors based on nickel phthalocyanine. *J. Appl. Phys.*, 66(9):4554–4556, 1989.

[Gun97] D. J. Gundlach, Y.-Y. Lin, T. N. Jackson, and D. G. Schlom. Oligophenyl-based organic thin film transistors. *Appl. Phys. Lett.*, 71(26):3853–3855, 1997.

[Hac86] M. Hack, M. Shur, and W. Czubatyi. Double-injection field-effect transistor: A new type of solid-state device. *Appl. Phys. Lett.*, 48(20):1386–1388, 1986.

[Hal03] M. Halik, H. Klauk, U. Zschieschang, G. Schmid, S. Ponomarenko, S. Kirchmeyer, and W. Weber. Relationship between molecular structure and electrical performance of oligothiophene organic thin film transistors. *Adv. Mater.*, 15(11):917–922, 2003.

[Has04] T. Hasegawa, K. Mattenberger, J. Takeya, and B. Batlogg. Ambipolar field-effect carrier injections in organic mott insulators. *Phys. Rev. B*, 69:245115–1/6, 2004.

[Hei00] S. B. Heidenhain, Y. Sakamoto, T. Suzuki, A. Miura, H. Fujikawa, T. Mori, S. Tokito, and Y. Taga. Perfluorinated oligo(*p*-phenylene)s: Efficient n-type semiconductors for organic light-emitting diodes. *J. Am. Chem. Soc.*, 122:10240–10241, 2000.

[Hep03] A. Hepp, H. Heil, W. Weise, M. Ahles, R. Schmechel, and H. von Seggern. Light-emitting field-effect transistor based on a tetracene thin film. *Phys. Rev. Lett.*, 91(15):157406–1/4, 2003.

[Hir95] M. Hiramoto, K. Ihara, H. Fukusumi, and M. Yokoyama. Conduction type control from n to p type for organic pigment films purified by reactive sublimation. *J. Appl. Phys.*, 78(12):7153–7157, 1995.

[Hor89] G. Horowitz, D. Fichou, X. Peng, Z. Xu, and F. Garnier. A field-effect transistor based on conjugated alpha-sexithienyl. *Solid State Commun.*, 72(4):381–384, 1989.

[Hor90] G. Horowitz. Organic semiconductors for new electronic devices. *Adv. Mater.*, 2(6-7):287–292, 1990.

[Hor98] G. Horowitz. Organic field-effect transistors. *Adv. Mater.*, 10(5):365–377, 1998.

[Jac98] T. N. Jackson, Y. Y. Lin, D. J. Gundlach, and H. Klauk. Organic thin-film transistors for organic light-emitting flat-panel display backplanes. *IEEE J. Sel. Top. Quantum Electron.*, 4(1):100–104, 1998.

[Jon90] D. Jones, M. Guerra, L. Favaretto, A. Modelli, M. Fabrizio, and G. Distefano. Determination of the electronic structure of thiophene oligomers and extrapolation to polythiophene. *J. Phys. Chem.*, 94:5761–5766, 1990.

[Kar01a] N. Karl. *Organic Electronic Materials*, volume 41, chapter 6, page 231. Springer, Berlin, 2001. edited by R. Farchioni and G. Grosso.

[Kar01b] N. Karl. *Organic Electronic Materials*, volume 41, chapter 6, page 223. Springer, Berlin, 2001. edited by R. Farchioni and G. Grosso.

[Kar03] N. Karl. *Synth. Met.*, 133-134:649, 2003.

[Kat97] H. E. Katz. Organic molecular solids as thin film transistor semiconductors. *J. Mater. Chem.*, 7:369, 1997.

[Koe87] H. Koezuka, A. Tsumura, and T. Ando. Field-effect transistor with polythiophene thin film. *Synth. Met.*, 18(1-3):699–704, 1987.

[Kud84] K. Kudo, M. Yamashina, and T. Moriizumi. Field-effect measurement of organic dye films. *Jpn. J. Appl. Phys.*, 23(1):130–130, 1984.

[Kuw04] E. Kuwahara, Y. Kubozono, T. Hosokawa, T. Nagano, K. Masunari, and A. Fujiwara. Fabrication of ambipolar field-effect transistor device with heterostructure of C_{60} and pentacene. *Appl. Phys. Lett.*, 85(20):4765–4767, 2004.

[Lam70] M. A. Lampert and P. Mark. *Current Injection in Solids.* Academic Press, New York, 1970.

[Lid96] D. R. Lide. *CRC handbook of Chemistry and Physics.* CRC, Boca Raton, FL, 77 edition, 1996.

[Lil30] J. E. Lilienfeld. U.s. patent 1,745,175, 1330.

[Lin97] Y.-Y. Lin, D. J. Gundlach, S. F. Nelson, and T. N. Jackson. *IEEE Trans. El. Dev.*, 44:1325, 1997.

[Lin03] H.-C. Lin, M.-F. Wang, C.-Y. Lu, and T.-Y. Huang. Ambipolar schottky barrier silicon-on-insulator metal-oxide-semiconductor transistors. *Solid State Electronics*, 47(2):247–251, 2003.

[Lin04a] Y.-M. Lin, J. Appenzeller, and Ph. Avouris. Ambipolar-to-unipolar conversion of carbon nanotube transistors by gate structure engineering. *Nano Lett.*, 4(5):947–950, 2004.

[Lin04b] T. Lindner, G. Paasch, and S. Scheinert. Influence of distributed trap states on the characteristics of top and bottom contact organic field-effect transistors. *J. Mater. Res.*, 19(7):2014–2027, 2004.

[Lua92] S. Luan and G. W. Neudeck. An experimental study of the source/drain parasitic resistance effects in amorphous silicon thin film transistors. *J. Appl. Phys.*, 72(2):766–772, 1992.

[Mac87] J. R. Macdonald. *Impedance Spectroscopy - emphasizing solid materials and systems.* Wiley, New York, 1987.

[Mal02] P. R. L. Malenfant, C. D. Dimitrakopoulos, J. D. Gelorme, L. L. Kosbar, T. O. Graham, A. Curioni, and W. Andreoni. N-type organic thin-film transistor with high field-effect mobility based on a n,n'-dialkyl-3,4,9,10-perylene tetracarboxylic diimide derivative. *Appl. Phys. Lett.*, 80(14):2517–2519, 2002.

[Mar01] R. Martel, V. Derycke, C. Lavoie, J. Appenzeller, K. K. Chan, J. Tersoff, and Ph. Avouris. Ambipolar electrical transport in semiconducting single-wall carbon nanotubes. *Phys. Rev. Lett.*, 87(25):256805–1/4, 2001.

[Mat01] C. C. Mattheus, A. B. Dros, J. Baas, A. Meetsma, J. L. D. Boer, and T. T. M. Palstra. Polymorphism in pentacene. *Acta Cryst. C*, 57:939–941, 2001.

[Mei03] E. J. Meijer, D. M. de Leeuw, S. Setayesh, E. van Veenendaal, B.-H. Huisman, P. W. M. Blom, J. C. Hummelen, U. Scherf, and T. M. Klapwijk. Solution-processed ambipolar organic field-effect transistors and inverters. *Nature Materials*, 2:678–682, 2003.

[Mue01] M. Muench. *Strukturelle Beeinflussung der elektrischen transporteigenschaften dünner organischer Schichten.* PhD thesis, Universität Stuttgart, 2001.

[Mur93] S. L. Murov, I. Carmichal, and G. L. Hug. *Handbook of Photochemistry.* Marcel Dekker, Inc., New York, 2 edition, 1993.

[Nel98] S. F. Nelson, Y.-Y. Lin, D. J. Gundlach, and T. N. Jackson. Temperature-independent transport in high-mobility pentacene transistors. *Appl. Phys. Lett.*, 72(15):1854–1856, 1998.

[Nes02] A. Nesterov, G. Paasch, S. Scheinert, and T. Lindner. Simulation study of the influence of polymer modified anodes on organic led performance. *Synth. Met.*, 130(2):165–175, 2002.

[Neu75] G. W. Neudeck and A.K. Malhotra. Field effect conductance modulation in vacuum-evaporated amorphous silicon films. *J. Appl. Phys.*, 46(1):239–246, 1975.

[Neu87a] G. W. Neudeck, H. F. Bare, and K. Y. Chung. Modeling of ambipolar a-si:h thin-film transistors. *IEEE Trans. El. Dev.*, ED-34(2):344350, 1987.

[Neu87b] G. W. Neudeck, K. Y. Chung, and H. F. Bare. *IEEE Trans. El. Dev.*, ED-34:866–871, 1987.

[Ngu01] P. H. Nguyen, S. Scheinert, S. Berleb, W. Brütting, and G. Paasch. The influence of deep traps on transient current-voltage characteristics of organic light-emitting diodes. *Org. Electronics*, 2(3-4):105–120, 2001.

[Pac03] R. Pacios, J. Nelson, D. D. C. Bradley, and C. J. Brabec. Composition dependence of electron and hole transport in polyfluorene:[6,6]-phenyl C_{61}-butyric acid methyl ester blend films. *Appl. Phys. Lett.*, 83(23):4764–4766, 2003.

[Pet70] L. D. Petrova and L. D. Rozenshtein. Field effect in an organic semiconductor chloranil. *Fiz. Tverd. Tela (Sov.Phys. - Solid State)*, 12(3):961–962, 1970.

[Peu03] P. Peumans, S. Uchida, and S. R. Forrest. Efficient bulk heterojunction photovoltaic cells using small-molecular-weight organic thin films. *Nature*, 425:158–162, 2003.

[Pfl85a] H. Pfleiderer, W. Kusian, and B. Bullemer. An ambipolar amorphous-silicon field-effect transistor. *Siemens Forsch.- u. Entwickl. Ber.*, 14(3):114–119, 1985.

[Pfl85b] H. Pfleiderer, W. Kusian, and B. Bullemer. An ambipolar field-effect transistor model. *Siemens Forsch.- u. Entwickl. Ber.*, 14(2):69–75, 1985.

[Pfl86a] H. Pfleiderer. Elementary ambipolar field-effect transistor model. *IEEE Trans. El. Dev.*, ED-33(1):145–147, 1986.

[Pfl86b] H. Pfleiderer and W. Kusian. Ambipolar field-effect transistor. *Solid State Electronics*, 29(3):317–319, 1986.

[Pod03] V. Podzorov, S. E. Sysoev, E. Loginova, V. M. Pudalov, and M. E. Gershenson. Single-crystal organic field effect transistors with the hole mobility ∼8 cm^2/vs. *Appl. Phys. Lett.*, 83(17):3504–3506, 2003.

[Pod04] V. Podzorov, E. Menard, A. Borissov, V. Kiryukhin, J. A. Rogers, and M. E. Gershenson. Intrinsic charge transport on the surface of organic semiconductors. *Phys. Rev. Lett.*, 93(8):086602–1/4, 2004.

[Pog02] A. Pogantsch, G. Heimel, and E. Zojer. Quantitative prediction of optical excitations in conjugated organic oligomers: A density functional theory. *J. Chem. Phys.*, 117(12):5921–5928, 2002.

[Pop82] M. Pope and C. E. Swenberg. *Electronic processes in organic crystals*. Oxford University Press, New York, 1982.

[Rad02] M. Radosavljevic, M. Freitag, K. V. Thadani, and A. T. Johnson. Nonvolatile molecular memory elements based on ambipolar nanotube field effect transistors. *Nano Lett.*, 2(7):761–764, 2002.

[Raj00] G. Rajeswaran, M. Itoh, M. Boroson, S. Barry, T. K. Hatwar, K. B. Kahen, K. Yoneda, R. Yokoyama, T. Yamada, N. Komiya, H. Kanno, and H. Takahashi. Active matrix low temperature poly-si tft / oled full color displays: Development status. *SID 2000 Technical Digest*, 40:1, 2000.

[Rey04] J. Reynaert, D. Cheyns, D. Janssen, R. Müller, V. I. Arkhipov, J. Genoe, G. Borghs, and P. Heremans. Ambipolar injection in a submicron channel light-emitting tetracene transistor with distinct source and drain contacts. *Appl. Phys. Lett.*, submitted, 2004.

[Rie02] H. Riel. *Optimization of Multilayer Organic Light-Emitting Devices*. PhD thesis, University of Bayreuth, 2002.

[Rie03] H. Riel, S. Karg, T. Beierlein, W. Riess, and K. Neyts. Tuning the emission characteristics of top-emitting organic light-emitting devices by means of a dielectric capping layer: An experimental and theoretical study. *J. Appl. Phys.*, 94(8):5290–5296, 2003.

[Rie04] W. Riess, T. A. Beierlein, and H. Riel. Optimizing oled structures for a-si display applications via combinatorial methods and enhanced outcoupling. *Phys. Stat. Sol. A*, 201(6):13601371, 2004.

[Ros04a] C. Rost, D. J. Gundlach, S. Karg, and W. Riess. Ambipolar organic field-effect transistor based on an organic heterostructure. *J. Appl. Phys.*, 95(10):5782–5787, 2004.

[Ros04b] C Rost, S. Karg, W. Riess, M. A. Loi, M. Murgia, and M. Muccini. Ambipolar light-emitting organic field-effect transistor. *Appl. Phys. Lett.*, 85(9):1613–1615, 2004.

[Sak04] T. Sakanoue, E. Fujiwara, R. Yamada, and H. Tada. Visible light emission from polymer-based field-effect transistors. *Appl. Phys. Lett.*, 84(16):3037–3039, 2004.

[San04] C. Santato, R. Capelli, M. A. Loi, M. Murgia, F. Cicoira, V. A. L. Roy, P. Stallinga, R. Zamboni, C. Rost, S. F. Karg, and M. Muccini. Tetracene-based organic light-emitting transistors: optoelectronic properties and electron injection mechanism. *Synth. Met.*, 146(3):329–334, 2004.

[Sch99] A. Schoonveld. *Transistors based on ordered organic semiconductors.* PhD thesis, Rijksuniversiteit Groningen, 1999.

[Sch00] S. Scheinert, G. Paasch, P. H. Nguyen, S. Berleb, and W. Brütting. Transient i-v characteristics of oled with deep traps. In *Proceedings ESSDERC00, Edition Frontiers*, pages 444–447, Paris, 2000.

[Sch02a] P. G. Schroeder, C. B. France, J. B. Park, and B. A. Parkinson. Energy level alignment and two-dimensional structure of pentacene on aun111o surfaces. *J. Appl. Phys.*, 91(5):3010–3014, 2002.

[Sch02b] P. G. Schroeder, C. B. France, B. A. Parkinson, and R. Schlaf. Orbital alignment at p-sexiphenyl and coronene/layered materials interfaces measured with photoemission spectroscopy. *J. Appl. Phys.*, 91(11):9095–9107, 2002.

[Sch03] R. Schmechel, A. Hepp, H. Heil, M. Ahles, W. Weise, and H. von Seggern. Light emitting field-effect transistor: simple model and underlying functional mechanisms. *Proc. SPIE*, 5217:101, 2003.

[Sha01] S. E. Shaheen, C. J. Brabec, N. S. Sariciftci, F. Padinger, T. Fromherz, and J. C. Hummelen. 2.5% efficient organic plastic solar cells. *Appl. Phys. Lett.*, 78(6):841–843, 2001.

[Shi04] T. Shimada, T. Sugai, Y. Ohno, S. Kishimoto, T. Mizutani, H. Yoshida, T. Okazaki, and H. Shinohara. Double-wall carbon nanotube field-effect transistors: Ambipolar transport characteristics. *Appl. Phys. Lett.*, 84(13):2412–2414, 2004.

[Sir98] H. Sirringhaus, N. Tessler, and R. H. Friend. Integrated optoelectronic devices based on conjugated polymers. *Science*, 280:1741–1744, 1998.

[Sta04] A. F. Stassen, R. W. I. de Boer, N. N. Iosad, and A. F. Morpurgo. Influence of the gate dielectric on the mobility of rubrene single-crystal field-effect transistors. *Appl. Phys. Lett.*, 85(17):3899–3901, 2004.

[Sze81] S. M. Sze. *Physics of Semiconductor Devices.* Wiley, New York, 2 edition, 1981.

[Tad00] H. Tada, H. Touda, M. Takada, and K. Matsushige. Quasi-intrinsic semiconducting state of titanyl-phthalocyanine films obtained under ultrahigh vacuum conditions. *Appl. Phys. Lett.*, 76(7):873–875, 2000.

[Tan87] C. W. Tang and S. A. VanSlyke. Organic electroluminescent diodes. *Appl. Phys. Lett.*, 51(12):913–915, 1987.

[Ter03] S. Terada, G. Izumi, Y. Sato, M. Takahashi, M. Tada, K. Kawase, K. Shimotoku, H. Tamashiro, N. Ozawa, S. Takanori, C. Sato, T. Nakadaira, Y. Iwase, T. Sasaoka, and T. Urabe. A 24-in. am-oled display with xga resolution by novel seamless tiling technology. *SID 2003 Technical Digest*, 54:5L, 2003.

[Tsu86] A. Tsumura, H. Koezuka, and T. Ando. Macromolecular electronic device: Field-effect transistor with a polythiophene thin film. *Appl. Phys. Lett.*, 49(18):1210–1212, 1986.

[Tsu03] T. Tsujimura, Y. Kobayashi, K. Murayama, A. Tanaka, M. Morooka, C.-T. Chung, R.-M. Chen, C.-C. Yang, W. Riess, and F. R. Libsch. A 20-in. oled display driven by super-amorphous-silicon technology. *SID 2003 Technical Digest*, XXXIV(1):6, 2003.

[Yan97] H. Yanagi and S. Okamoto. Orientation-controlled organic electroluminescence of p-sexiphenyl films. *Appl. Phys. Lett.*, 71(18):2563–2565, 1997.

[Yan02] H. Yanagi, T. Morikawa, and S. Hotta. Electroluminescence from low-dimensionally confined crystals of thiophene/p-phenylene co-oligomers. *Appl. Phys. Lett.*, 81(8):1512–1514, 2002.

List of Publications

1. C. Rost, S. Karg, W. Riess, M. A. Loi, M. Murgia, M. Muccini. Light-emitting ambipolar organic heterostructure field-effect transistor. *Synthetic Metals*, 146(3), 237-241, 2004.

2. C. Santato, R. Capelli, M. A. Loi, M. Murgia, F. Cicoira, V. A. L. Roy, P. Stallinga, R. Zamboni, C. Rost, S. F. Karg, M. Muccini. Tetracene based organic light-emitting transistors: optoelectronic properties and electron injection mechanism. *Synthetic Metals*, 146(3), 329-334, 2004.

3. C. Rost, S. Karg, W. Riess, M. A. Loi, M. Murgia, M. Muccini. Ambipolar light-emitting organic field-effect transistor. *Applied Physics Letters* 85(9), 1613-15, 2004.

4. C. Rost, D. J. Gundlach, S. Karg, W. Riess. Ambipolar organic field-effect transistor based on an organic heterostructure. *Journal of Applied Physics* 95(10), 5782-5787, 2004.

5. T. A. Beierlein, B. Ruhstaller, D. J. Gundlach, H. Riel, S. Karg, C. Rost, W. Riess. Investigation of internal processes in organic light-emitting devices using thin sensing layers. *Synthetic Metals* 138(1-2), 213-221, 2003.

6. I. Kaiser, K. Ernst, C. Fischer, R. Könenkamp, C. Rost, I. Sieber, M. C. Lux-Steiner. The eta-solar cell with $CuInS_2$: A photovoltaic cell concept using an extremely thin absorber (eta). *Solar Energy Materials and Solar Cells*, 67(1-4), 89-96, 2001.

7. R. Könenkamp, K. Ernst, C. Fischer, M. C. Lux-Steiner, C. Rost. Semiconductor growth and junction formation within nano-porous oxides. *Physica Status Solidi A* 182(1), 151-155, 2000.

8. C. Rost, I. Sieber, C. Fischer, M. C. Lux-Steiner, R. Könenkamp. Semiconductor growth on porous substrates. *Materials Science and Engineering B*, 69, 570-573, 2000.

9. C. Rost, I. Sieber, S. Siebentritt, M. C. Lux-Steiner, R. Könenkamp. Spatially distributed p-n heterojunction based on nanoporous TiO_2 and CuSCN. *Applied Physics Letters* 75(5), 692-694, 1999.

Patents

1. Tuning optical characteristics of organic light emitting devices.
   S. Karg, W. Riess, H. Riel, C. Rost, H. Nakamura.
   CH9-2003-0010-EP1; Patent filed 11/2004.

2. Proton conductor and its manufacturing method, proton conductive polymer and its manufacturing method, proton conductive polymer composition, and electrochemical device.
   K. Fukushima, B. Nuber, C. Rost, Y. Uetake, B. Pietzak, T. Tsunenaga, S. Takizawa.
   JP2003303513; Patent filed 06/2002; Patent published 10/2003

3. Functional material or functional element and method of manufacturing the same.
   H. Matsumura, C. Rost, T. Enomoto, R. Ugajin.
   JP2003285299; Patent filed 03/2002; Patent published 10/2003

4. Proton conducting material and method of preparing the same, and electrochemical device using the same.
   K. Hinokuma, M. Ata, B. Pietzak, C. Rost
   WO2000JP0004864; Patent filed 07/2000; Patent published 01/2001.

5. Festkörperbauelement, seine Verwendung und Verfahren zu seiner Herstellung.
   R. Könenkamp, C. Rost, K. Ernst, C. Fischer, M. C. Lux-Steiner, S. Siebentritt.
   DE1999019910155; Patent filed 02/1999; Patent published 09/2000.

Acknowledgements

First of all, I would like to thank Prof. Markus Schwoerer for the supervision of my thesis as an external Ph.D. student and his continued confidence in my work. I really benefitted from the interesting discussions we had during my visits in Bayreuth and at the Spring Meeting of the DPG in Regensburg.

I also thank Prof. Werner Köhler for readily accepting as a second reviewer.

Substantial contributions to the success of this work came from Dr. habil. Walter Rieß, whom I would like to thank for giving me the opportunity to work at the IBM Research Laboratory as well as for his continued support of my work.

Special thanks go to Dr. Siegfried Karg, whom I not only owe the ILO project, but also many shared hours in the lab, interesting and fruitful discussions on my work and a theoretical introduction into the world of golf.

I would like to express my gratitude to my former colleagues Dr. Brian Crone, now at Los Alamos National Laboratory and Dr. David Gundlach, now at ETH Zürich, for their introduction into the field of small molecule OFETs.

Within the Science and Technology department of IBM, I would like to thank Ute Drechsler for her support in the cleanroom, Meinrad Tschudy for the "gold-plating"of my samples as well as for his support on assembling the vacuum chamber and manufacturing urgently needed parts and pieces, Dr. Ingmar Meijer for oxidizing the silicon wafers, Hanspeter Ott for his many ideas on and the realization of the sample holder for the deposition chamber, Dr. Peter Müller for AFM measurements and Marilyne Sousa for taking X-ray diffraction data and having the patience of sharing the office with me.

I also would like to thank the other members of the Display group, namely Dr. Heike Riel, Dr. Tilman Beierlein, and Dr. Santos Alvarado, who all gave me an excellent introduction into the field of OLEDs, and Thomas Brunschwiler not only for taking care of the ski week-ends in Davos.

I would like to express my gratitude to the team at the ISMN-CNR in Bologna, Italy, namely Dr. Michele Muccini for his professional coordination of the ILO project, many interesting and fruitful discussions as well as inviting me to Bologna for a short research visit. Furthermore, I specially thank Dr. Maria Antonietta Loi for the optical characterization of the coevaporated films as well as being my contact person for the sample and data exchange with Bologna, Dr. Mauro Murgia for the deposition of tetracene thin films as well as the coevaporated films of α-5T and PTCDI-$C_{13}H_{27}$, and Dr. Franco Dinelli for his assistance with AFM images. It was my pleasure to meet Dr. Giovanna Barbarella at the EMRS in Strasbourg, whom I owe the synthesis of α-5T.

I also would like to thank Dr. Gernot Paasch and Dr. Thomas Lindner from the IWF in Dresden, Germany for their collaboration with simulating the experimental data on ambipolar OFETs. My thanks go also to Dr. Dag Werner Breiby from the Danish Polymer Centre at the Risø National Laboratory, Roskilde, Denmark for taking X-ray diffraction data. Finally, I would like to thank Dr. Roland Schmechel from the TU Darmstadt, Germany for encouraging discussions within the scope of the ILO EU project. I should not forgett Prof. Toshiyasu Suzuki from the Institute of Molecular Science in Okazaki, Japan and his effort in supplying me with perfluorinated quaternaphthalene as electron-transport material, even though I was not able to prepare functional devices.

My compliments are also given to the IBM's Publication Department, namely Charlotte Bolliger and Lilli-Marie Pavka for proof-reading, to Eliska Kron and Nicola Gustafsson from the Library, as well as to the Intellectual Property Team, lead by Peter Klett. Thanks to him I managed at least sometimes to join the weekly IBM Hobby Club fitness classes.

Most of all, I deeply thank my parents - without their continuous support throughout my study this work would not have been possible - and my husband Alexander for his endless patience.

Curriculum Vitae

Name	:	Constance Rost-Bietsch, geb. Rost
Date of Birth	:	May 17, 1975
Place of Birth	:	Erlabrunn/Erzgeb., Germany
Nationality	:	German

Doctoral Thesis

2001 - 2004 Ph.D. research in the Display Group
at the IBM Zurich Research Laboratory, Switzerland.
Thesis advisors: Dr. W. Riess and Prof. Dr. M. Schwoerer.

Work Experience

1999 - 2001 Research scientist
Sony Research Laboratory, Yokohama, Japan.

Study of Physics

1998 - 1999 Diploma Thesis at the Hahn-Meitner-Institute, Berlin.
Title: *CuI and CuSCN as p-type semiconductors for a solar cell with extremely thin absorber.* Thesis advisor: Prof. Dr. M. C. Lux-Steiner.

1996 - 1999 Free University of Berlin, "Diplom" in Physics, grade "sehr gut".

1995 - 1996 University of St. Andrews, Scotland.

1993 - 1995 University of Göttingen, "Vordiplom" in Physics, grade "gut".

Education

1989 - 1993 Spezialschule math.-naturw.-techn. Richtung Karl-Marx-Stadt /
Johannes-Kepler-Gymnasium Chemnitz.

1981 - 1989 Primary School, Erlabrunn.

Awards

2004 IBM Research Division Award
for Active Matrix OLED Display (AMOLED) Technology.

1999 Studienförderpreis of the Heraeus-Foundation.

Ich erkläre hiermit, dass ich die vorliegende Arbeit selbständig verfasst und nur die angegebenen Quellen und Hilfsmittel verwendet habe.

Rüschlikon, den 17.12.2004